LEAD-ACID BATTERY RESPONSE TO VARIOUS FORMATION LEVELS AND METHODS: DETERMINING THE OPTIMAL FORMATION LEVEL FOR OFF-GRID SOLAR APPLICATIONS

by

Justin Deveau

Submitted in partial fulfilment of the requirements
for the degree of Master of Applied Science

at

Dalhousie University
Halifax, Nova Scotia
August 2015

© Copyright by Justin Deveau, 2015

Table of Contents

List of Tables

List of Figures

Abstract

A significant number of people in the world are without electricity service, the majority of which are located in rural areas where extending the electricity grid is not economically feasible. Off-grid solar photovoltaic technology has been identified as the most prominent option to electrify these rural areas, of which lead-acid storage batteries are a major component.

The manufacture of lead-acid batteries requires an electrochemical activation process called “formation”. Formation is poorly defined in the public literature as it is considered confidential by battery manufacturers, and because solar storage batteries are only now a significant market. Thus, the objective of this thesis project is to determine the optimal formation level and method for the manufacturing of lead-acid batteries intended for the off-grid solar storage market. In order to determine the optimal formation level, ELG15 lead-acid battery cells with a rated capacity of 231 Ah and positive plate thicknesses of 4.32 mm were formed using two different formation algorithms in a laboratory setting to formation levels ranging from 0.70 to 7.04 times the theoretical capacity of the cell. Following the completion of 10 deep-cycles per cell, the ideal formation level for this cell was determined to be between 2.75 and 3.55 times its theoretical capacity. This newly recommended formation range for off-grid solar applications was found to be complementary to the range recommended in literature for conventional applications of 1.30 to 2.50 times the theoretical capacity of the cell.

In order to determine the optimal formation method, ELG15 cells were formed using the floor container, submerged container, circulated electrolyte, and tank formation methods used interchangeably at Surrette Battery Company, and to three formation levels equivalent to 80 %, 100 %, and 120 % of the standard formation algorithm for each respective formation method. Subsequently, three cells per formation level (i.e., a module) were deep-cycled simultaneously using a series configuration. By comparing the initial discharge capacity results of the 12 different modules as a function of theoretical capacity, the modules obtained using the circulated electrolyte formation method outperformed all other formation methods, and showed no disadvantages with respect to total formation time when compared to the other formation methods. The optimal formation method was determined to be the circulated electrolyte formation method, at a level equivalent to 2.89 times the theoretical capacity of the cell.

List of Abbreviations and Symbols Used

Acronyms

AC	Alternating current
CC	Constant-current
CV	Constant-voltage
DC	Direct current
DFE	Discharge formation efficiency
IR	Internal resistance
LAB	Lead-acid battery
LO	Leady oxide
NAM	Negative active material
NF	Normal-formed
OCV	Open-circuit voltage
OF	Over-formed
PAM	Positive active material
PV	Photovoltaic
RC	Resistor-capacitor
RESL	Renewable Energy Storage Laboratory
SBC	Surrette Battery Company
SG	Specific gravity
TC	Theoretical capacity
UF	Under-formed

Symbols

$C_{25\,°C}$	Corrected capacity at 25 °C
$a_{H_2SO_4}$	Activity coefficient of sulfuric acid
a_{H_2O}	Activity coefficient of water
A	Atomic mass
C	Measured discharge capacity
e	Voltage
F	Faraday constant
i	Current
N	Valency
n	Number of moles of electrons
R	Ideal gas constant
T	Temperature
TC	Theoretical capacity
θ	Cell temperature immediately prior to discharge
λ	Discharge rate factor

Chemical Compounds

1BS	1PbO × PbSO4
3BS	3PbO × PbSO4 × H_2O
4BS	4PbO × PbSO4
H_2SO_4	Sulfuric acid
Pb	Lead
PbO	Lead oxide
PbO_2	Lead dioxide
$PbSO_4$	Lead sulfate

Acknowledgements

I would like to express my sincere gratitude and appreciation to my supervisor Dr. Lukas Swan, who has been a tremendous mentor for me, and without whom this research would not have been possible. Your continuous support and guidance throughout my time here at Dalhousie University was instrumental to my success as a research engineer. I would also like to thank my supervisory committee members, Dr. Dominic Groulx and Dr. Uday Venkatadri, for your great comments and suggestions throughout my thesis project. Furthermore, I would like to express my thanks to the faculty, administration, and staff of the Department of Mechanical Engineering at Dalhousie University for all your support along the way. Moreover, a special thank you goes to the rest of the Renewable Energy Storage Laboratory team, and especially to Chris White, who had to endure countless hours working by my side, and whose contributions to this thesis project cannot be overstated.

Thank you to everyone at Surrette Battery Company, and especially to Pascal Ferron, who graciously answered my tireless questions regarding the manufacturing processes of the lead-acid battery, and helped to ensure that I was able to collect all the necessary data for my thesis project in a timely matter. Furthermore, additional thanks are reserved for Surrette Battery Company, who through a collaborative research and development grant with the Natural Sciences and Engineering Research Council of Canada, made this research possible.

Finally, I would like to thank my family and my friends, whose love and support kept me motivated and balanced.

Chapter 1: Introduction

There are presently over one billion people in the world without electricity service. More than 95 % of these people are either in sub-Saharan Africa or developing Asia, of which a further 84 % are located in rural areas [1]. The International Energy Agency [1] has stated that national governments must make "modern energy access a political priority", and have estimated that an annual investment of $48 billion per year is needed to achieve modern energy access for the global population. This represents an opportune market for the development of off-grid technologies in rural areas of these aforementioned continents, as extending the electricity grid to sparsely populated, remote, or mountainous areas is not economically feasible [1]. Off-grid solar photovoltaic (PV) technology has been identified as the most prominent option to electrify rural areas, and is comprised of a PV module as the energy harvesting technology, a battery as a storage device, a charge controller as a control unit, and a direct current/alternating current (DC/AC) converter for AC loads [2]. It is important to note that batteries for energy storage systems have a high capital cost [2], thus ensuring optimal battery performance is of utmost importance. The lead-acid battery (LAB) is the most widely used energy storage medium for off-grid systems due to its low cost compared to other battery types, its wide availability, and its maturity [3, 4].

This initiative to develop rural electricity services using off-grid solar PV systems provides new business opportunities for LAB manufacturers, where companies that reduce cost while providing an optimized product using advanced manufacturing techniques will be advantaged. The formation process is a time and energy intensive charging process by which manufacturers electrochemically activate the battery [4]. As such, the main objective of this thesis project was to identify the optimal LAB formation level and method for off-grid solar power applications. This research project was completed in conjunction with Surrette Battery Company (SBC), a LAB manufacturer located in Springhill, Nova Scotia, who devote over 50 % of their battery production to the off-grid solar market. SBC, who interchangeably uses four different formation methods for the production of LABs, provided the battery samples for this research project. The scope of this project is primarily focused on applied engineering energy storage research, which will make use of an

evidence-based approach using real battery production data, and battery performance results.

This thesis is divided into six chapters. Chapter 2 is divided into three sections, the first covering the fundamentals of the LAB, the second providing an overview of the LAB formation, and the third discussing the recent LAB developments as pertaining to this research project. Chapter 3 reiterates the main objective of this research project, and introduces the two independent phases of this research project which were used to address the main objective. Specifically, the first phase of this research project, *Lead-acid Battery Formation Optimization – Laboratory Study*, will determine the optimal LAB formation level for off-grid solar applications, whereas the second phase of this research project, *Lead-acid Battery Formation Optimization – Industrial Study*, will determine the optimal LAB formation method for off-grid solar applications. It is important to note that these two phases were used to structure the remainder of the document. To this point, the methodology which was used to address these two phases is presented in Chapter 4, with the results for both phases presented in Chapters 5 and 6, respectively. Finally, Chapter 7 concludes the work and provides recommendations guiding the formation of the LAB in industry, and recommendations to further this research.

Chapter 2: Literature Review

The following literature review is separated into three main sections. Although the LAB is a mature technology, it encompasses one of the most complicated battery chemistries, explained by the fact that the electrolyte (i.e., sulfuric acid, H_2SO_4) participates directly in the electrochemical reactions [4]. As such, the first section of this literature review will provide a brief background on the key components of the LAB, and the required manufacturing steps before battery formation can occur.

The second section of this literature review will present the formation characteristics of the LAB. Within this section, the concept of the formation level, and a description of the four different battery formation methods used at SBC will also be presented. The four different battery formation methods at SBC are the floor container formation, submerged container formation, circulated electrolyte formation, and tank formation methods.

The third section of this literature review will present recent developments with respect to the LAB, and its joint operation with off-grid solar systems.

The following terms, within the context of the LAB, will be used throughout this thesis:

Module: A module is comprised of multiple battery *cells*. For a LAB, each cell has an open-circuit voltage (OCV) of 2.041 volts (V) + (RT/nF) ln ($a^2{}_{H_2SO_4}/a^2{}_{H_2O}$), where R is the ideal gas constant (8.314 J K^{-1} mol^{-1}), T is the temperature in K, n is the number of moles of electrons exchanged in the electrochemical reaction (i.e., 2 for a LAB), F is the is the Faraday constant (96,485 C mol^{-1}), and where $a_{H_2SO_4}$ and a_{H_2O} are the activity coefficients of sulfuric acid and water, respectively [5]. Cells can be connected in series or in parallels, depending on the desired voltage and current output of the battery.

Capacity: Measured in ampere-hours (Ah), the capacity of the LAB is defined as the integral of current with respect to time. It should be noted that a *charging capacity* corresponds to the usage of a positive current, whereas a *discharging capacity* corresponds to the usage of a negative current. As an example, a cell subjected to a current of -60 A over a span of 2 hours results in a discharging capacity of 120 Ah.

Power: Instantaneous electrical power is measured in watts (W). It is calculated based on the product of current and voltage.

State-of-Charge: The state-of-charge of a LAB is defined as its available capacity (in Ah) with respect to its rated capacity (in Ah), the latter defined by the manufacturer at nominal operating conditions [6]. In other words, it is defined as the remaining capacity of a LAB, and is best determined by performing a deep-discharge test [6, 7]. The reliability of the deep-discharge test in determining the state-of-charge of a LAB is further illustrated in Wagner and Sauer [8], who used this method to determine the full state-of-charge (i.e., discharge capacity) of LABs in different solar power systems.

2.1. Fundamentals of the Lead-acid Battery

Figure 1 shows the details of construction for a LAB.

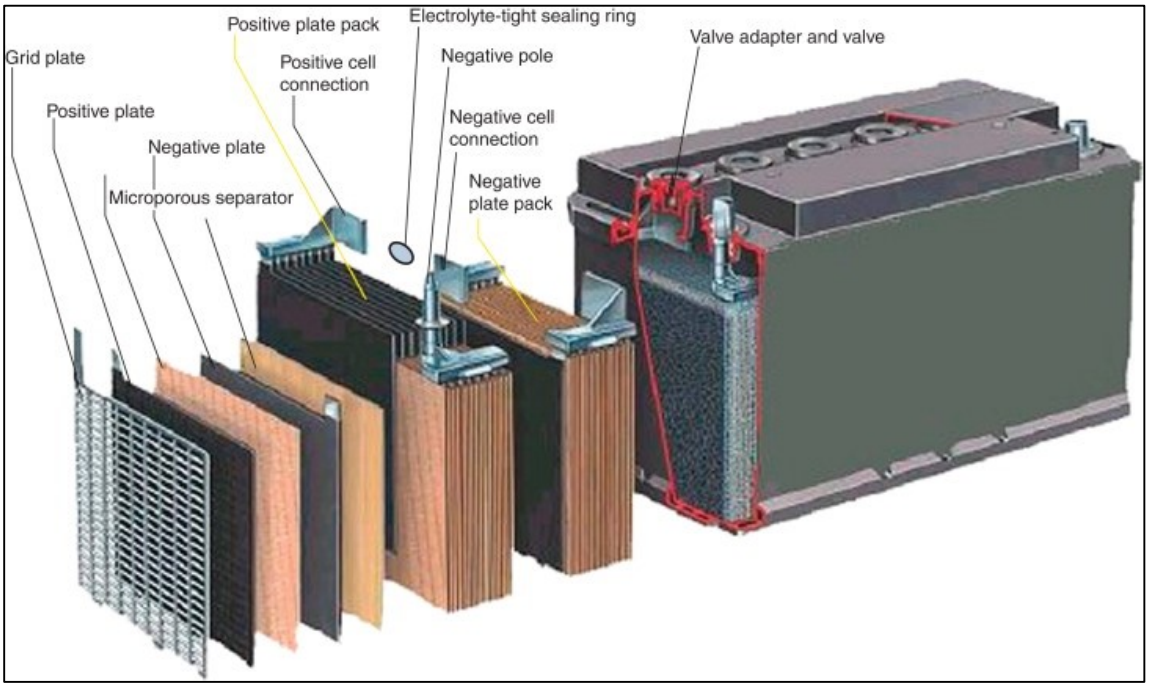

Figure 1 Construction of a Lead-Acid Battery (Reprinted from [9], with permission from Elsevier)

As shown in Figure 1, the key components of the LAB can be identified as the positive and negative plates (i.e., electrodes), the separator, and the electrolyte.

Lead grids are necessary for the production of the positive and negative plates, which are differentiated by the pasted active material (i.e., positive active material (PAM), and negative active material (NAM), respectively) which coat the grids. It is these positive and negative plates, acting as electrodes, that are responsible for the discharging and charging reactions of the LAB. Grids are produced either through casting, or through rolling and

expansion techniques, where lead-antimony or lead-tin-calcium alloys are typically used [4]. In order to prepare the paste, pure lead ingots are melted and oxidized at ambient air conditions, creating leady oxide (LO). To ready the paste for the positive plates, fine polymer fibers, along with measured amounts of water and H_2SO_4, are added to the LO. This mixing process, which typically lasts between 10 to 20 minutes, results in the formation of basic lead sulfates (i.e., yPbO × $PbSO_4$, where y varies based on the mixing conditions). On the other hand, the paste for the negative plates is prepared by mixing lignosulfonate (i.e., an organic expander), barium sulfate, carbon, and lead oxidation inhibitors to the LO [4, 10, 11]. The addition of the lignosulfonate is an important component in the paste of the negative plates, as it reduces the formation time of the NAM, increases the discharge capacity of the plates, and improves the life of the LAB [10]. Once the paste for the PAM and NAM have reached their respective desired density and consistency values, it is spread onto the grids, which are then readied for the curing process. The curing process, where the PAM and NAM particles are interconnected to form an uninterrupted strong porous mass tightly bound to the grids, is the last step before the LAB formation [12]. This oxidizing process is performed in a controlled environment taking into account temperature, humidity, and time, in order to ensure optimal skeleton size for the formation process [4]. Specifically, paste comprised of 3BS (i.e., 3PbO × $PbSO_4$ × H_2O) particles is obtained when it is prepared and cured with temperatures ranging from 30 °C to 60 °C, while paste comprised of 4BS (i.e., 4PbO × $PbSO_4$) particles is obtained when it is prepared and cured with temperatures ranging from 80 °C to 95 °C [12]. If the paste is prepared and cured at a temperature of 70 °C, a mixture comprised of 3BS and 4BS particles is obtained [13]. It is important to note that the lignosulfonate which is added to the paste of the NAM suppresses the creation of 4BS particles. Thus, following the completion of the curing stage, the NAM is typically comprised of 3BS particles regardless of the operating temperature [10]. Different formation and performance characteristics are attributed to these three different mass structures. Specifically, as 4BS lead sulfate crystals are larger than 3BS lead sulfate crystals, the resulting formation process for the 4BS crystal structure is more difficult. This typically results in lower initial discharge capacity performance results, unless a significantly longer formation time is employed. On the other hand, a 4BS crystal structure offers advantages when compared to a 3BS crystal structure

with respect to improved mechanical strength and cycle life. A mix of 4BS and 3BS particles is commonly employed by LAB manufacturers in order to maximize the advantages of the two different crystal structures [14].

Separators, often enclosing the positive plates, have one primary function. They prevent the electronic conductance between the positive and negative electrodes, which could otherwise result in short circuits through physical contact between the electrodes. Although, as the electrolyte participates directly into the electrochemical reactions of a LAB, the separator must also allow ionic conductance so that the redox reactions can proceed [15].

Lead-acid batteries have different classifications based on the quantity and physical state of the electrolyte. The scope of this project is limited to flooded electrolyte batteries, typically referred to as flooded batteries [5]. The electrolyte of the LAB is usually comprised of a 36 % by weight H_2SO_4 solution. This solution has a high electrical conductivity, a relatively low freeing point, and a low reaction rate with lead grids. It is important to note that on the completion of battery discharge, a surplus quantity of H_2SO_4 must remain to ensure ionic conductivity [5]. Furthermore, the state-of-charge of a flooded LAB can be estimated by taking specific gravity (SG) measurements of the electrolyte in the battery. Using a reference density of water at 25 °C, the SG of flooded batteries typically range between 1.10 (fully discharged) to 1.28 (fully charged), with the cell voltage at open circuit conditions increasing linearly as a function of acid concentration [16, 17].

Once the battery is activated, it is the combination of the positive and negative plates (plates with same polarity assembled in parallel), the separators, and the electrolyte that generate and accumulate electric energy. Equations (1) and (2) show the electrochemical discharge reactions at the positive and negative plates, respectively. One should note that the charging reactions for the positive and negative plates are simply the reverse of those shown in equations (1) and (2), respectively [18]. Equation (3) shows the overall reaction that occurs during discharge (left to right) and charge (right to left) of a LAB [17].

Positive plate discharge: $PbO_2 + 3H^+ + HSO_4^- + 2e^- \rightarrow PbSO_4 + 2H_2O$ (1)

Negative plate discharge: $Pb + HSO_4^- \rightarrow PbSO_4 + H^+ + 2e^-$ (2)

$$\text{Overall reaction: } Pb + PbO_2 + 2H_2SO_4 \leftrightarrow 2PbSO_4 + 2H_2O \quad (3)$$

As shown in equations (1) and (2), a solid conductor of electrons, PbO_2 (i.e., lead dioxide) for the positive plate, and Pb (i.e., lead) for the negative plate, reacts with H_2SO_4, to form a non-conductive solid, $PbSO_4$ (i.e., lead sulfate). This results in an increase in volume of the solid phase for both electrodes [18].

2.2. Lead-acid Battery Formation

Once the aforementioned curing process has been completed, the plates are electrochemically activated through a process called formation. The first part of the formation process is the soaking period. For all four aforementioned formation techniques, the plates are soaked in H_2SO_4 electrolyte, which reacts with the cured material to form $PbSO_4$ (i.e., material sulfation) [14]. It is important to note that the results of the soaking procedure are impacted by different factors: the concentration of the electrolyte, the duration of the soaking period, and the crystal structure of the cured paste. Specifically, when electrolyte with a low concentration of H_2SO_4 is used (i.e., 1.06 SG), Dreier *et al.* [13] have shown there to be minimal differences in the progress of material sulfation when comparing plates comprised of 3BS crystals to ones comprised of 4BS crystals, regardless of soaking time. This was determined by measuring the acid density surrounding the plates. On the other hand, when electrolyte with a high concentration of H_2SO_4 is used (i.e., 1.20 SG), the authors have shown that a crystal structure comprised of 3BS reacts much more intensively than one comprised of 4BS, while the progress of material sulfation for a crystal structure comprised of a mix of 3BS and 4BS was shown to be between those of the 3BS and 4BS crystal structures.

Dreier *et al.* [13] determined the specific soaking material conversion ratios for plates comprised of a 4BS crystal structure (i.e., about 80 % 4BS) to be as follows. With respect to soaking electrolyte with an SG of 1.20, most of the sulfation reaction occurred within the first 0.5 hour, as relatively similar conversion ratios were found on the plates after 24 hours, with about 50 % $PbSO_4$, 20 % 1BS (i.e., $1PbO \times PbSO_4$), and 20 % 4BS. With respect to soaking electrolyte with an SG of 1.06, the authors showed that much less material had reacted with the H_2SO_4 after 0.5 hour (e.g., 20 % vs. 40 % conversion to $PbSO_4$ for 1.06 SG electrolyte and 1.20 SG electrolyte, respectively). Furthermore, after a

soaking period of 24 hours, it was determined that the plates were still comprised of about 35 % 4BS.

Specific soaking material conversion ratios for plates comprised of a 3BS crystal structure (i.e., 50 % 3BS) were determined to be as follows. With respect to soaking electrolyte with an SG of 1.20, 80 % $PbSO_4$ was found after a soaking time of 0.5 hour. After a soaking period of 24 hours, more than 95 % of the plate material was found to be $PbSO_4$. With respect to soaking electrolyte with an SG of 1.06, about 60 % $PbSO_4$ was found after a soaking time of 0.5 hour and 24 hours [13].

Thus, the authors determined that the faster reaction rate for the crystal structure comprised of 3BS when compared to 4BS when soaked in 1.20 SG electrolyte was due to the finer crystalline structure of the former. This was not the case when 1.06 SG soaking electrolyte was used, due to its low concentration of H_2SO_4, limiting the conversion reaction of the material [13].

Following the soaking period, the originally inactive positive and negative plates are then charged using a predetermined amount of formation capacity, converting the inactive materials to PbO_2 for the positive plates, and to Pb for the negative plates [4]. The concept of the predetermined amount of formation capacity, or formation level, is explored in more details in section 2.2.2, while the following section (2.2.1) will discuss the LAB formation characteristics of the PAM and NAM.

2.2.1. Formation Characteristics

Positive Active Material

Following the completion of the curing process, the PAM is comprised mainly of either 3BS, 4BS, or a mix of 3BS/4BS particles, as a result of the different curing temperatures, along with a quantity of lead oxide (i.e., PbO). Pavlov [19] has divided the formation process into two stages. The first stage is defined by the oxidation (i.e., loss of electrons) of the PbO and basic lead sulfates to α-PbO_2, and small amounts of β-PbO_2. It should be noted that during the first stage of formation, the solution filling the paste pores is of a neutral to slightly alkaline pH, causing the paste to react with the H_2SO_4, thus also forming $PbSO_4$. On the other hand, the second stage of formation is defined by the oxidation of the $PbSO_4$ to β-PbO_2 [19]. It is important to note that the α-PbO_2 crystals form

the active mass skeleton, which allows for the conduction of current, whereas the β-PbO_2 crystals are electrochemically active, and determine the capacity of the positive plates [20]. With respect to PAM comprised of 3BS particles, the first formation stage is deemed to be completed when the 3BS, 1BS, and PbO phases in the paste are no longer present, which coincides with the maximum content of $PbSO_4$ in the plate [19]. As the grid is the only electron conductor in the cured plate, formation starts at the grid bars, where the subsequent formation of PbO_2 zones is dependent on the amount of H_2SO_4 in the paste. Specifically, zones of PbO_2 will initially be created on the surface of the plates and then move to its interior if the paste is prepared with 0 % H_2SO_4, while the opposite will occur if the paste is prepared with more than 8 % H_2SO_4. These zonal reactions are slow, resulting in the long process of the LAB formation [19].

As stated in section 2.1, 4BS lead sulfate crystals are larger than 3BS lead sulfate crystals, resulting in a different and more difficult formation process for the former. Thus, with respect to PAM comprised of 4BS particles, Pavlov [19] has shown it to be virtually impossible to prove the presence of α-PbO_2 crystals at the start of the formation process, with the main product of the electrochemical reaction being β-PbO_2 crystals. Specifically, he has noted that the oxidation of the paste, originally comprised mainly of 4BS, α-PbO, and β-PbO, proceeds relatively quickly until a 70 % by weight of PbO_2 is reached. While the formation of α-PbO_2 for PAM comprised of 4BS is not as clear as when PAM is comprised of 3BS, Pavlov [19] has nonetheless concluded the presence of α-PbO_2 at the end of the formation process.

The efficiency of the formation process is defined as the percentage of PbO_2 at the end of the LAB activation, as the negative plates are formed more quickly than the positive plates [21]. The maximum degree of formation for plates comprised of 4BS cured paste is 70 % after a formation time of 30 hours, whereas plates comprised of 3BS cured paste can reach a degree of formation exceeding 90 % after a formation time of 18 hours [19]. Thus, Pavlov [19] concludes that plates comprised of 4BS crystal structure can only complete their formation process following the completion of five to ten deep-discharge cycles due to ion transport difficulties during the formation process.

Negative Active Material

As stated above, the lignosulfonate added to the paste of the NAM suppresses the creation of 4BS particles. Thus, the paste of cured negative plates is typically comprised of 3BS, PbO, and residual Pb [10]. Like the formation process of the PAM, the formation process for the NAM is divided into two stages. The first stage is defined by the reduction (i.e., gain of electrons) of 3BS and PbO to Pb. As was the case for the PAM, the paste also reacts with the H_2SO_4 to form $PbSO_4$. On the other hand, the second stage of formation for the NAM is defined by the reduction of $PbSO_4$ to Pb. Pavlov [10] has shown that this formation process starts on the surface of the plate. Specifically, zones of Pb and $PbSO_4$ will first cover the whole surface of the plate, and then grow towards the interior of the plate until formation is complete. With this in mind, the first formation stage is deemed to be completed when the amount of $PbSO_4$ on the surface layer of the plates begins to decrease. At this stage, the reduction of 3BS and PbO to Pb is still occurring within the inner layers of the plate. Thus, these two aforementioned reduction reactions will occur simultaneously during the formation process of the NAM.

Formed NAM consists of a primary lead crystal skeleton, obtained during the first stage of formation, covered with small secondary lead crystals, obtained during the second stage of formation [10]. As stated by Pavlov [10], the primary lead crystal skeleton serves as the current-collector for NAM, while the capacity of the negative plate is determined by the secondary lead crystals. This is very similar in nature to the α-PbO_2 and β-PbO_2 crystal structures, respectively, formed on the PAM. Thus, in order for the negative plates to obtain good performance characteristics, one should ensure an optimal ratio between these two structures.

Important Formation Parameters

In addition to the above formation characteristics, Pavlov [21] considers the following parameters to play an important role in the formation process of the LAB: the formation current, the formation temperature, the battery voltage during formation, the formation level, the concentration of H_2SO_4 for the formation process, and the H_2SO_4/LO ratio in the paste. The formation current dictates the rate at which the electrochemical reactions discussed above occur on the positive and negative plates, and the rate at which the chemical reactions (i.e., no transfer of electrons), caused by the electrochemical reactions,

occur. Specifically, during the first stage of formation, the aforementioned reactions of sulfation dominate, which causes a reduction in the concentration of H_2SO_4, an increase in cell temperature, and a decrease in cell voltage. One should note that the increase in cell temperature is due to the exothermic chemical reactions between the PbO, basic lead sulfates, and H_2SO_4 when the plates are first immersed into the electrolyte, while the decrease in cell voltage is due to the low equilibrium potential of the electrodes. During the second stage of formation, H_2SO_4 is released from the plates due to the reduction of $PbSO_4$ to Pb at the negative plates, and to the oxidation of $PbSO_4$ to PbO_2 at the positive plates. These redox reactions in turn cause the cell voltage to increase, while the cell temperature now decreases due to the endothermic nature of these two redox reactions [21]. Taking into account these reactions, the chosen formation current profile should thus yield optimal performance parameters of the plates, while also ensuring high formation efficiency. Pavlov [21] has defined two ranges of formation current densities. A "normal range" of 2 to 10 mA per cm^2 of plate surface (i.e., total surface area of positive plates), and an "accelerated range" of 10 to 15 mA per cm^2 of plate surface. A formation current density of 2 to 10 mA per cm^2 of plate surface is considered normal as higher values are typically limited by cell temperature and voltage restrictions.

With respect to the formation temperature, Pavlov [21] has stated that the optimum temperature range for the formation process is between 30 °C and 50 °C. The formation of batteries below this temperature range should be avoided due to the significant reduction in formation efficiency [14]. On the other hand, formation temperatures above 60 °C result in a large β/α-PbO_2 ratio in the PAM. While this leads to higher initial discharge capacity values, the active mass skeleton is weak (i.e., α-PbO_2) resulting in reduced cycle life for the LAB. Furthermore, high formation temperatures also reduces the capacity of the negative plates due to expander degradation, reduces the efficiency of formation due to the acceleration in water decomposition, and quickens the corrosion of the positive grids [21].

With respect to the battery voltage during formation, Pavlov [21] recommends an upper voltage limit of 2.60 to 2.65 V per cell, in order to limit intense hydrogen and oxygen evolution (i.e., electrolysis). Water electrolysis is a normal battery process where hydrogen and oxygen gases are released through the vent cap of a LAB when electric current is passed through water [22].

The concept of the formation level is explored in section 2.2.2.

As alluded to above, Pavlov [19] has confirmed that a high concentration of H_2SO_4 (i.e., 1.15 SG) in the formation process results in a shorter duration for the first stage of the formation process, additional formation of $PbSO_4$ in the first stage of the formation process, and an increase in the content of β-PbO_2 in the PAM. On the other hand, a lower initial concentration of H_2SO_4 (i.e., 1.05 SG) during the formation process generally results in equal amounts of α-PbO_2 and β-PbO_2, and in a shorter overall formation time due to an increase in formation efficiency (i.e., due to the higher solubility of $PbSO_4$ [16]). As stated above, an increase in the β/α-PbO_2 ratio results in higher overall discharge capacity values, but at the expense of reduced cycle life for the LAB [14, 19].

With respect to the H_2SO_4/LO ratio in the paste, Pavlov [19] has stated that the β/α-PbO_2 ratio in the PAM has a positive correlation to the H_2SO_4/LO ratio for both 3BS and 4BS cured pastes. This correlation has a larger impact on plates comprised of a 3BS crystal structure when compared to plates comprised of a 4BS crystal structure. Similarly to the PAM, the NAM is also impacted by the H_2SO_4/LO ratio in the cured paste. Specifically, a high H_2SO_4/LO ratio in the cured paste leads to a more apparent secondary lead crystal structure in the NAM [10]. Thus, a proper H_2SO_4/LO ratio must be selected in order to obtain optimal performance with respect to both the positive and negative plates.

Finally, it is important to note that there are two significant differences between the formation process of the LAB and its charging process within deep-cycling operation. Firstly, the current profiles between the formation process and the charging process of the LAB are vastly different. Specifically, relatively high charging currents are recommended during the initial stages of the charging process, whereas as stated above, small formation currents are typically employed in order to limit the chemical reactions [21]. Secondly, as the active mass skeletons comprised of α-PbO_2 for the PAM and primary lead crystals for the NAM are formed during the first stage of the formation process, these skeleton structures already exist during battery charging. Thus, during the discharging and charging operation of the LAB, the β-PbO_2 and secondary lead crystal structures are simply consumed/rebuilt over the already existing skeleton of the positive and negative plates, respectively. One should note that the primary structures of the positive and negative plates

do change throughout the cycle-life of the battery, but at a much slower rate than the secondary structures [10, 21].

2.2.2. Formation Level

Pavlov [21] states that in practice, the quantity of electricity flowing through the plates during formation should amount to between 1.70 and 2.50 times the theoretical capacity of the plates. The additional energy is required due to side reactions, such as gassing, during the formation process [14]. These multipliers are dependent on the thickness of the plates, the phase composition of the cured paste, the size of the particles which constitute the individual phases, and the current and voltage algorithms of formation [21]. The theoretical capacity of the LAB, 240 Ah per kilogram of PbO, is obtained by multiplying the valency of PbO by the Faraday constant, and then dividing this value by the atomic weight of PbO. This is shown in equation (4).

$$TC = \frac{N \times F}{A} = \frac{2 \times 26.801 \text{ Ah mol}^{-1}}{223.199 \text{ g mol}^{-1}} = 240 \text{ Ah [kg PbO]}^{-1} \quad (4)$$

where TC is the theoretical capacity, N is the valency, F is the Faraday constant, and A is the atomic mass. As such, the formation level is defined as the formation input in Ah of a respective cell divided by the TC of the cell (e.g., 2000 Ah (formation input) / 710 Ah (TC) = 2.82 (formation level)).

Similar ranges of formation levels have been recommended in [14, 23-25]. Wagner [14] states that practical formation conversion factors are between 1.30 and 2.50 times the theoretical capacity of the plates.

Nelson [23] states that 1.50 to 2.50 times the theoretical capacity of the plates must be put into the plates for complete formation, and that the best level of PbO_2 conversion depends on the application. For instance, it is stated that for automotive batteries with a short distribution time, PbO_2 levels of 75 % to 85 % can be allowed, as it is assumed that this conversion factor will increase due to battery usage [23]. In other words, battery manufacturers may strategically under-form batteries, saving them time and energy, with the expectation that clients complete the formation process.

Prout [24] states that in practice, formation input levels are based on the thickness of the plates. By dividing his recommended formation input values given as a function of Ah per kilogram of wet positive paste by the theoretical minimum formation input of 186.2

Ah per kilogram of wet paste [24], one obtains formation levels between 1.61 and 2.15 times the theoretical capacity of the plates for plate thicknesses varying between 1.15 mm and 4.50 mm, respectively.

Finally, Lin *et al.* [25] experimentally determined the formation level of tubular positive electrodes to be 1.50 times the theoretical capacity of the plates. However, it should be noted that only three different formation levels were considered, these being 1.50, 2.50, and 3.50 times the theoretical capacity of the plates [25].

While there appears to be some agreement between Pavlov, Wagner, Nelson, Prout, and Lin *et al.* regarding the recommended formation levels for LABs (see Table 1), this component is poorly defined as shown by the variation in the recommended values. Furthermore, an in-depth analysis of this matter supported by experimental work has proven to be difficult to find in the literature, with only one paper stating experimental evidence, as formation practices are considered confidential by battery manufacturers.

Table 1 Recommended Formation Levels (Ratio of Theoretical Capacity)

Author	Minimum	Maximum	Details
Pavlov [21]	1.70	2.50	from Best Practice
Wagner [14]	1.30	2.50	from Best Practice
Nelson [23]	1.50	2.50	from Best Practice
Prout [24]	1.61	2.15	from Best Practice
Lin *et al.* [25]	1.50	1.50	Experimentally Established

Finally, it is important to note that the formation process of batteries for the off-grid solar market is especially challenging because they may be placed into immediate discharge service (e.g., a cloudy installation day). While conventional markets such as transportation or uninterruptible power supply can provide a high-voltage, and long overcharge because of their strong charging systems, such a strong initial charge is generally not available in off-grid solar systems. Consequently, battery performance may be less than expected by the off-grid client if conventional formation practices are applied [8, 26].

2.2.3. Formation Method

As stated, there are four different LAB formation methods used interchangeably at SBC. The floor container, submerged container, and circulated electrolyte formation methods are considered to be within the same classification of formation methods, the

container formation classification, due to their similar formation procedures. On the other hand, the tank formation method is independently characterized as the *tank formation* classification [4].

Container Formation Classification

The general formation procedure for the three formation methods within the container formation classification is as follows [4]:

1) Cell assembly
2) Filling cell with electrolyte
3) Soaking of plates
4) Formation of cell
5) Finishing procedures
6) Cell ready for operation.

These three methods are only differentiated by the specifics of step 4, each having unique characteristics. It should be noted that these three methods form pre-assembled cells connected in series. During step 4 of the floor container formation, the simplest formation method, the cell is connected to a current source, and formation commences based on a predefined algorithm. The SBC floor container formation is shown in Figure 2, with cells connected in series to a current source. Condensing tubes are installed on top of the cells during the formation process in order to reduce the concentration of hydrogen in the air by recombining and condensing the gases as they exit the cells, while lead bars are used to connect the cells in series.

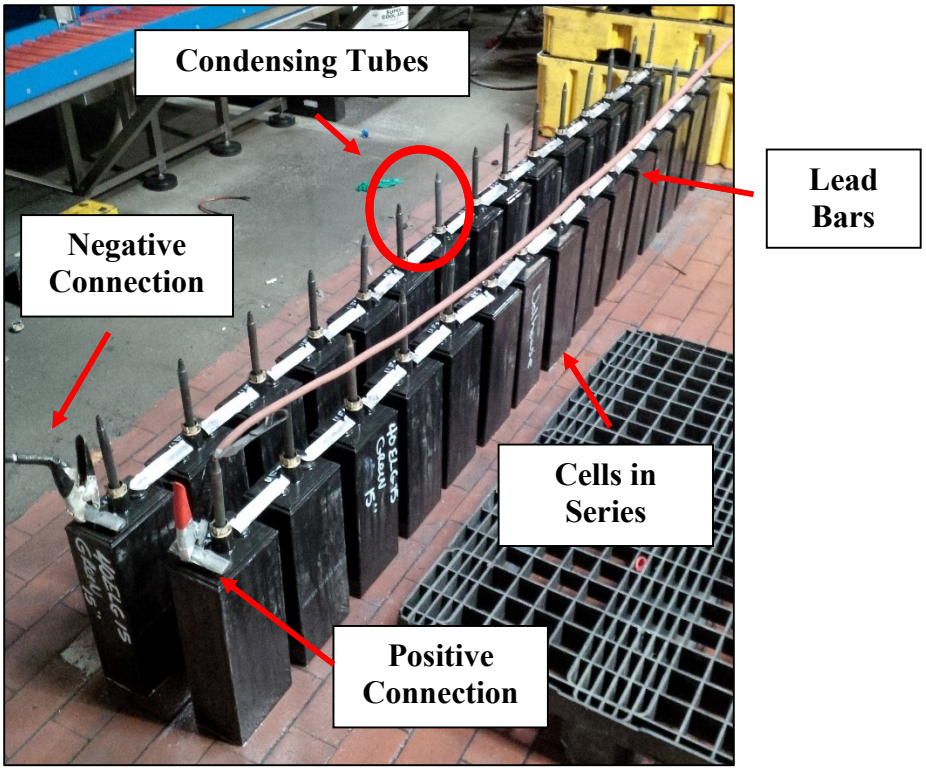

Figure 2 SBC Floor Container Formation

In most cases, formation is accomplished under constant-current conditions, although several current algorithms, such as multi-step current algorithms, can be used in battery formation [4, 21]. As the reactions between PbO, basic lead sulfates, and H_2SO_4 are exothermic, the temperature of the battery during formation rises [21]. Specifically with the floor container formation method, a great amount of heat is generated due to the combination of a small cell heat capacity, and a high concentration of H_2SO_4 [21]. This can lead to battery temperatures exceeding 60 °C, again accelerating the corrosion of the positive plates, and in time, resulting in a shorter battery cycle life due to expander degradation in the NAM [4, 21, 27]. As such, current densities for the floor container formation method are generally limited to a range between 2 and 10 mA per cm^2 of plate surface, which in turn leads to an extended formation time [21].

The submerged container formation method, shown in Figure 3, is one of two techniques used to mitigate the temperature rise of the battery during the formation process. Interconnects are used to connect the modules in series.

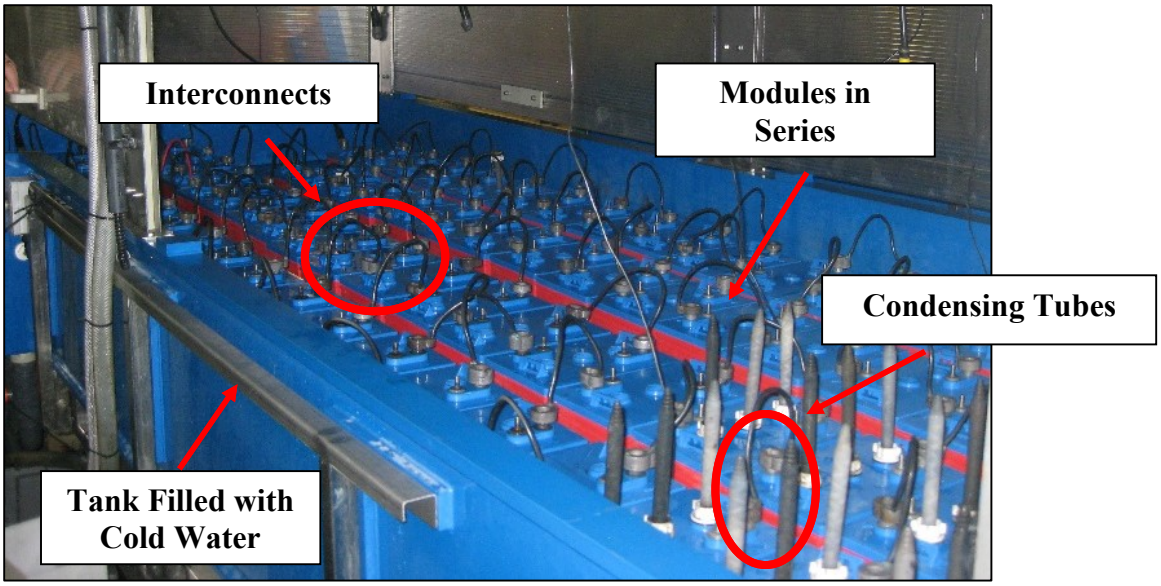

Figure 3 SBC Submerged Container Formation

This method works by immersing the batteries in tanks of cold water, or "water bath". This increases the heat rejection of the batteries due to the higher convection coefficient and heat capacity of the water, thus allowing for an increased formation rate [21]. While formation time can be reduced, it should be noted that additional energy input is required for this formation method when compared to the floor container formation method, due to the cooling and recirculation of water.

The circulated electrolyte formation method, shown in Figure 4, is the second technique used to avoid the temperature rise of the battery during the formation process. Lead bars are used to connect the cells in series.

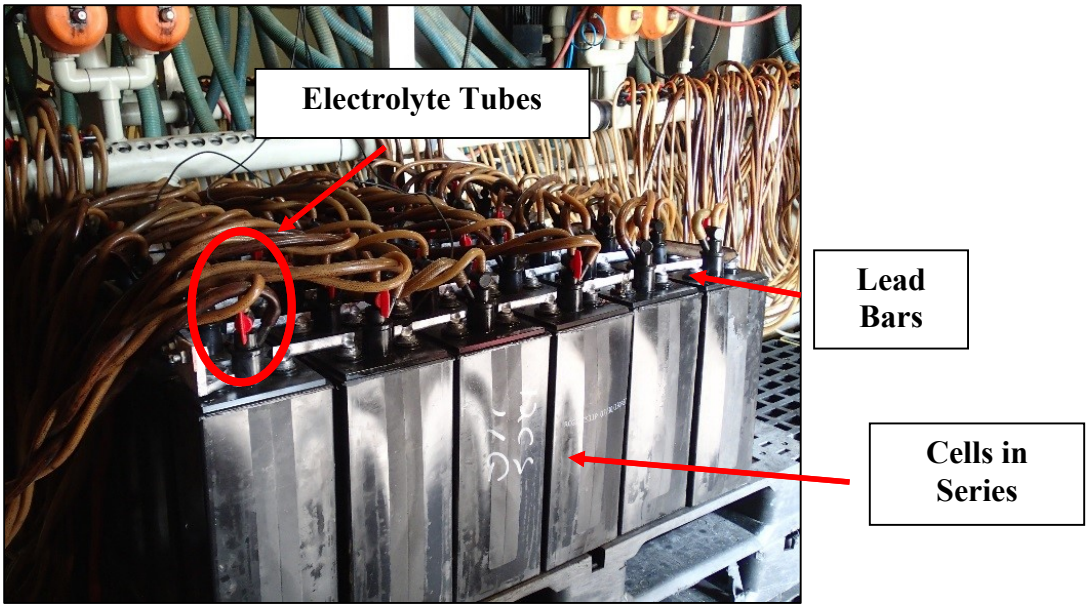

Figure 4 SBC Circulated Electrolyte Formation

As shown, this method works by connecting electrolyte tubes to fill ports on assembled cells, which remove the heated electrolyte from the top of the cell, and replaces it with cooled electrolyte as the cell is formed. Although allowing for even faster formation rates than the submerged contained method, this adds a significant level of complexity to the formation process, as one must ensure no electrolyte is lost in the system, while also requiring additional energy input to operate the hydraulic system [21]. One should note that a circulated electrolyte system typically employs at least two electrolyte tanks, one characterized by an electrolyte SG value of 1.10 used for battery formation, and one characterized by an electrolyte SG value of 1.28, which is used to replace the formation electrolyte before the batteries are sold [21].

Kumar *et al.* [28] reviewed the performance of the circulated electrolyte method by varying the conditions of formation, such as the specific gravity of the electrolyte, the formation algorithm, and the current density. Comparing their results to the floor container formation method, the authors determined that the average formation temperature of the battery is reduced by 10 °C when using the circulated electrolyte method. They also showed that as a result, the duration of the battery formation can be reduced by 25 % when compared to the conventional floor container formation method, without affecting the voltage profile of the battery. Thus, they concluded that the electrolyte circulation formation method produces batteries of similar quality as those formed using the container

method while reducing formation time, but at the expense of increasing the overall energy consumption.

Tank Formation Classification

Tank formation, the fourth formation method at SBC, is different in the sense that the positive and negative plates are formed before the battery is assembled, as depicted in the steps below [4].

1) Arrangement of plates in tank
2) Soaking of plates
3) Formation of plates
4) Washing and drying of plates
5) Cell assembly
6) Storage of dry-charged batteries, which require addition of electrolyte for operation.

Specifically at SBC, eight cured positive plates and nine cured negatives plates are arranged in cassettes (plates with same polarity assembled in parallel) which are then placed in large electrolytic tanks containing H_2SO_4 electrolyte with a SG ranging from 1.08 to 1.10. It should be noted that there are four cassettes in parallel per tank at SBC, as shown in Figure 5. This is an important characteristic, as unlike the three other aforementioned formation methods where the number of positive plates which are formed in parallel is a function of the cell type, there are 32 positive plates formed in parallel when using the tank formation method. In other words, to obtain the current received by each positive plate, the current provided by the tank formation charger must be divided by 32.

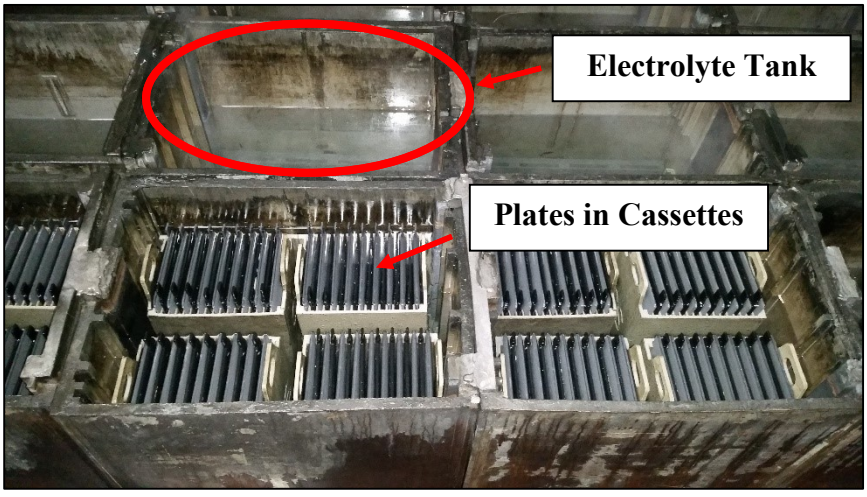

Figure 5 SBC Tank Formation

Once placed in the electrolyte tanks, the plates are then typically soaked for a predetermined period of time, with the amount of electrolyte calculated on the basis of two to three liters per kilogram of dry paste. The tank formation current usually varies between 0.7 and 2.5 mA per cm^2 of plate surface [4]. Unlike the conventional floor container formation method, the heat capacity of the tank is high, and the concentration of the H_2SO_4 solution is much lower. As such, only a small quantity of paste is sulfated, limiting the increase of temperature in the tank. Nevertheless, the formation time using this method ranges between 18 to 40 hours for starter battery plates (i.e., thin plates), and from 48 to 73 hours for traction battery plates (i.e., thick plates) [4]. The advantage of this method is in step 6, where the batteries are stored in dry-charged conditions (i.e., without electrolyte). Specifically, once the formation process has been completed, the plates are washed and dried, and the batteries assembled. This allows for an extended shelf battery life, as the aging process of the battery only starts once it has been filled with electrolyte [14].

There are certain criteria indicating the end of the formation process that are used in conjunction with the aforementioned desired formation levels. The most reliable criteria, although difficult to perform in practice, is to perform a chemical analysis on the positive and negative plates. Specifically, in order to achieve normal formation, the positive plates should be comprised of 88 to 92 % PbO_2, whereas the negative plates should be comprised of 92 to 94 % Pb [21]. The other criteria indicating the end of formation, as stated by Pavlov [21], include: a constant electrolyte concentration over a period of 2 hours, a constant rate of gas evolution over a period of 2 hours, the appearance of a metallic track upon the scratching of a negative plate, and a black to dark brown color for the PAM, hard and not subject to peeling. Due to the logistical difficulties of testing these criteria in a manufacturing environment, formation completion is typically based on the aforementioned formation levels.

2.3. Recent Developments

This section of the literature review will deal with the recent developments concerning LAB formation, and its joint operation with off-grid solar systems.

2.3.1. Formation of the Lead-acid Battery

Naidenov and Markov [29] studied the effects of applying ultrasonic waves during the formation process of LABs. To perform their test, the authors assembled 10 test cells comprised of one positive and two negative unformed plates, where each had a rated capacity of 9.5 Ah at a 10 hour discharge rate. The cells were of the flooded type with standard polyethylene pocket separators, and H_2SO_4 with a SG of 1.25 was used as the electrolyte. Half of the test cells were formed with no ultrasonic excitation, while the other half were formed by applying ultrasonic waves. The waves were produced by an ultrasonic bath with a capacity of 16 liters, a power consumption of 450 W, an 860 W ultrasonic peak power, and a frequency of 35 kHz. The cells were formed using the following algorithm. Firstly, currents of 0.478 A, 0.77 A, 1.1 A, and 2 A were individually applied for a duration of 20 minutes each. Secondly, formation was continued with a current of 4.31 A until the cell voltage reached 2.75 V. Finally, formation was conducted potentiostatically at 2.75 V until a capacity of 28.5 Ah was reached, a value corresponding to 1.5 times the theoretical capacity of the positive plate. Once formed, the cells were cycled with a charging current of 3 A up to a cell voltage of 2.62 V, followed by further charging at 2.50 V until an overcharge equivalent to 10 % of the rated capacity of the cell was reached. The cells were discharged with a current of 0.95 A, until a voltage of 1.70 V was reached. The authors showed that the cells formed without the application of ultrasonic waves needed more time to reach their preset capacity of 28.5 Ah than the cells subjected to ultrasonic waves. Specifically, formation time was 12 hours and 8 minutes for the former, and 8 hours and 35 minutes for the latter. During the cycling of the cells, it was shown that the capacity of the cells formed without application of ultrasonic waves declined below 80 % of their rated capacity after about 40 cycles, while 120 cycles were needed for the cells subjected to ultrasonic waves to reach this state. Thus, the authors showed that the application of ultrasonic waves during the formation of flooded cells results in a higher capacity and three times the cycle life, however it should be noted that 120 cycles is still relatively short for a deep discharge cell. These results were explained by the fact that ultrasonic excitation facilitates the crystallization processes in the positive plates and contributes to the release of the absorbed gas layer at the surface of the positive plates at the end of the formation process, leading to an increasing rate of the electrochemical reactions [29].

Diniz et al. [30] studied the effects of pulsed current formation on the positive plates of LABs. They conducted experiments by assembling batteries with one positive plate inside a polyethylene separator, located between two negative plates. H_2SO_4 with a SG of 1.14 was used as the electrolyte. 18 different pulsed formation algorithms with a total charge of 21.6 Ah were performed, varying in total formation time, pulse profile, and pulse length. It should be noted that no temperature control was attempted. As a benchmark, these results were compared to a formation algorithm using a constant-current of 1.0 A. The authors determined that pulsed current formation has a higher faradaic efficiency than constant-current formation for the conversion of the cured positive plate to PbO_2, due to better diffusion control of the H_2SO_4 electrolyte. It was also shown that pulsed formation yields a higher β-PbO_2/α-PbO_2 ratio than continuous formation. In theory, such a ratio would cause the batteries to display a better high rate discharge performance, at the expense of reduced cycle life. One should note that no batteries were cycled, and that only the effect on the positive plate of pulsed current formation was analyzed [30]. Thus, more research should be performed in order to gain a better understanding of the influence of pulsed current in the formation of LABs.

Adding carbon in the paste of the NAM of a LAB enhances its charge acceptance, yet the addition of too much carbon has been shown to produce detrimental changes in the electrical parameters of the negative plates, leading to reductions in plate strength, battery capacity, cold-cranking performance, and production throughput [31, 32]. Thus, as an effort to mitigate these disadvantages, Swogger *et al.* [32] tested the effects of adding a recently developed carbon nanotube derivative, called Molecular Rebar, with the goal of reducing long-term battery failures. This new material is provided as a pourable and aqueous fluid comprised of discrete surfactant-stabilized carbon nanotubes, and can be directly added to the active material of a battery. For their experiment, the authors formed batteries with and without the Molecular Rebar in the NAM, and compared battery performance based on their paste mixing profile, paste density, formation profile, reserve capacity, cold-cranking performance, and charge acceptance. After the curing process, a discrete surfactant-stabilized carbon nanotubes concentration of 0.16 % in the negative plate was observed. Automotive batteries (i.e., 12 V) with a rated capacity of 35 Ah at a 20 hour discharge rate were used for the basis of this experiment. They were comprised of

four positive and five negative plates, and were formed using a 7 A constant-current over 18 hours. Upon testing completion, it was determined that the batteries containing discrete surfactant-stabilized carbon nanotubes showed no detrimental changes to paste properties and formation profile when compared to the same batteries without this addition. Furthermore, the authors showed that when compared to the control battery, the addition of discrete surfactant-stabilized carbon nanotubes enhanced the reserve capacity of the battery by ~ 1 to 10 %, its cold-cranking performance by ~ 1 to 10 %, and its charge acceptance by ~ 200 % [32].

In an attempt to increase the specific energy of the LAB, Moncada *et al.* [33] tested battery performance using PbO_2 nanowires as the positive electrode. The authors obtained nanostructured electrodes by using template electrodeposition in polycarbonate membranes, and formed a battery by using commercial negative plates and separators. It should be noted that for all the tested batteries, the negative plates had more electro-active material than the positive electrode, thus ensuring the performance of the battery to be dependent on the positive plate. Interestingly, the conventional curing and formation processes of typical LAB plates are not required for nanostructured electrodes. Constant charge and discharge cycles at a 1 hour discharge rate were completed to a 90 % depth of discharge at room temperature, and in a H_2SO_4 electrolyte solution with a SG of 1.25. The authors determined that the nanostructured PbO_2 electrodes were able to deliver a discharge capacity of 190 mAh g^{-1} for over 1000 cycles, corresponding to an active material utilization ratio of 85 % [33]. On the other hand, a conventional LAB has a typical active material utilization ratio ranging from 45 % to 62 % [16, 34]. This improvement in performance was attributed to the large surface area of the nanostructured material, thus allowing a larger fraction of the positive active mass to react with the electrolyte when compared to a conventional plate [33].

Krivik *et al.* [35] studied the effects of three different additives with respect to the performance of the negative LAB electrodes during formation, and during partial state of charge operation. A total of six batteries were used for their experiments, with five being tested with different additives, and one for control purposes. Three different additives were pasted in the negative active masses of the electrodes, these being: powdered carbon, titanium dioxide, and silicone dioxide. Each negative electrode was paired with two

positive electrodes, two separators, and inserted into cells filled with H_2SO_4 electrolyte with a SG of 1.28. The batteries were subjected to 23 "formation cycles", one cycle consisting of a 0.2 A charging current for two hours, followed by a two hour resting period. Upon completing of the formation process, the six batteries were discharged at a constant-current of 0.7 A to a lower voltage limit of 1.6 V, and then charged at a constant-current of 0.7 A to an upper voltage limit of 2.45 V. The authors determined that the addition of carbon to the negative active mass of the battery results in an increase in the time of effective formation, as the carbon blocks pores in the active mass thus interfering with the electrolyte transport. Furthermore, they also determined that with respect to partial state-of-charge, the battery with silicone dioxide resulted in the lowest cycle life, with a total of 10,500 cycles. This value is significantly less than the control battery, which attained 42,000 cycles. Conversely, both additives of carbon and titanium dioxide resulted in a significant increase in cycle life, with both batteries attaining more than 90,000 cycles [35]. The authors thus showed that carbon and titanium dioxide improve the ability of the electrode to accept large charging currents, a result which is in agreement with Swogger *et al.* [32].

Fan *et al.* [20] studied the effects of different PbO_2 morphologies on the electrochemical performance of the positive active material of the LAB. Specifically, the authors chemically synthetized urchin-like and ball-like β-PbO_2 particles with sizes ranging between 0.5 and 1 μm, and flower-like α-PbO_2 particles with sizes ranging between 1 and 2 μm. They tested 2 V cells comprised of one positive electrode, and two conventional negative electrodes, submersed in a H_2SO_4 electrolyte solution with a SG of 1.25. Upon formation, the performance of the batteries with different β/α-PbO_2 ratios were tested using the following cycling algorithm. They were discharged with a constant-current corresponding to the 10 hour rate to a lower voltage limit of 1.8 V, and were charged with a constant-current corresponding to the 10 hour rate to an upper voltage limit of 2.4 V. The authors determined a 1:1 ratio of urchin-like β-PbO with flower-like α-PbO_2 to be the most promising, where a discharge capacity of 183 mAh g^{-1} was obtained at a 10 hour discharge rate after 100 cycles, corresponding to an active material utilization ratio of 82 %. Furthermore, the authors obtained a discharge capacity of 146.7 mAh g^{-1} at a 1 hour rate after 100 cycles, corresponding to an active material utilization ratio of 65 % [20]. As such,

these electrodes were determined to display better electrochemical performance than conventional LAB electrodes.

2.3.2. Operation of the Lead-acid Battery in Off-grid Solar Systems

The operating conditions of batteries used for off-grid solar systems are very different from conventional applications due to irregular cycling regimes, sporadic full battery charges, and a wide range of charging and discharging currents [36, 37]. Sauer *et al.* [38], who studied the performance of LABs in off-grid solar systems, have stated that while requirements for power density are small, with average discharging currents between I/50 and I/100 (50 hour and 100 hour discharging currents, respectively), the time available for battery charging is limited, as it is dependent on the number of sunshine hours per day, resulting in incomplete charges, and long periods of medium or low state of charge. To further illustrate this point, Wagner and Sauer [8] evaluated typical charging strategies for LABs in solar power applications, and found that the strategies presently used in the field have difficulties fully charging the batteries.

2.4. Summary

The major conclusions from this literature review are as follows. Conventional formation levels for the LAB range between 1.30 to 2.50 times the theoretical capacity of the cell [14, 21, 23-25]. However, these multipliers are dependent on the thickness of the plates, the phase composition of the cured paste, the size of the particles which constitute the individual phases, and the current and voltage algorithms of formation [21]. Furthermore, due to the differences in operating conditions between conventional and off-grid solar applications (i.e., strategies presently used in off-grid solar applications have difficulties fully charging the batteries [8]), battery performance may be less than expected by the off-grid client if conventional formation practices are applied [8, 26]. In other words, the manufacturing concept of strategically under-forming batteries, with the expectation that the client completes the formation process, is not viable for the off-grid solar market, as a LAB would likely never reach a fully formed state. As such, it is imperative that LABs intended for use in the off-grid solar market attain the optimal balance between capacity output and discharge formation efficiency. This will ensure lowest overall costs for LAB manufacturers, while still providing an optimized product for the client. The discharge

formation efficiency, or DFE, is defined as the ratio of initial discharge capacity output of a cell to its formation capacity, as shown in equation (5). DFE values are expected to range between 5 % and 20 %.

$$DFE = \frac{Initial\ Discharge\ Capacity\ (\text{Ah})}{Formation\ Capacity\ (\text{Ah})} \times 100\ \% \quad (5)$$

Concerning the recent developments in the formation process of LABs, promising work has been shown with respect to improving their performance in the context of conventional applications. For instance, the inclusion of carbon nanotubes in the NAM was shown to improve the performance of the LAB in [32], and the chemical synthesis of PbO_2 particles with different morphologies in the positive active material was also shown to improve the performance of the LAB in [20]. However, it should be noted that some of these recent developments are in fact disadvantages for LABs used in off-grid solar applications, such as using PbO_2 nanowires for the positive electrode of a LAB. While this increases the power density of the battery due to an increase in internal surface area of the PAM, it decreases its ability for a fast recharge, a necessary requirement for off-grid solar applications. This is due to higher voltages attained during the charging process, causing a reduction in bulk charge duration (i.e., highest current) [26, 33].

There are currently no studies published in the literature which specifically address the formation of LABs for off-grid solar systems. As such, the main objective of this thesis project can be stated as: What is the optimal *formation level and method* for the manufacturing of LABs intended for the off-grid solar storage market?

Chapter 3: Objectives and Phases

The main objective of this research project is to determine the optimal formation level and method for the manufacturing of the LAB intended for the off-grid solar storage market. To address this main objective, the research project was separated into two phases. The following will explain the scope and objective of these two phases, whereas the following chapter will describe the specifics of the methodology to address these objectives.

3.1. Phase 1: Lead-acid Battery Formation Optimization – Laboratory Study

The objective of this phase of the project was to perform an in-depth laboratory formation analysis of the LAB in order to determine the optimal formation level for off-grid solar applications, and to validate and refine the recommended formation levels presented in Table 1. An in-depth analysis of the LAB formation supported by experimental work is lacking in the literature, thus justifying the need for a control study. As such, the work for this phase of the project, which included the formation of LAB cells and their subsequent cycling, was conducted in the Renewable Energy Storage Laboratory (RESL) at Dalhousie University. A laboratory setting allowed for all research parameters to be controlled, thus ensuring ideal experimental conditions.

3.2. Phase 2: Lead-acid Battery Formation Optimization – Industrial Study

The objective of this phase of the project was twofold. First, to determine the optimal formation method for the LAB used in off-grid solar applications. Second, to determine the influence of said formation methods on the ideal formation level previously determined in phase 1 of this project. As different formation methods were required for this phase of the project, the cells were formed at SBC, and subsequently cycled at the RESL. The formation of the cells at SBC ensured typical marketable product (i.e., as received by a client), while subsequent cycling in a laboratory setting ensured all cells were subjected to the same testing parameters.

Chapter 4: Methodology

Formation levels are dependent on the thickness of the plates, the phase composition of the cured paste, the size of the particles which constitute the individual phases, and the current and voltage algorithms of formation [21]. As such, a singular LAB cell type, the ELG15, was selected for both phases of this project in order to establish a common basis for comparison. The ELG15 can be formed using RESL equipment, and all four formation methods at SBC. Table 2 highlights the characteristics of the cells which were used in this project. These LAB cells were assembled by SBC, and are typically sold as a 6 V module known as the S-480 battery. This flooded deep cycle LAB is part of SBC's *Renewable Energy* line. Furthermore, the rated capacity is based on a 3.8 hour discharge rate with an initial electrolyte SG of 1.265 [39], while the theoretical capacity was calculated based on the active material of the positive plates. The 3.8 hour rated capacity of the cell, 231 Ah, corresponds to a positive active material utilization of 32.5 %. It should be noted that the material utilization ratio is a function of discharge rate, where for example a 20 hour discharge rate would correspond to a positive active material utilization of 52.8 %. The data sheet for the S-480 battery is shown in Appendix D.

Table 2 ELG15 Cell Characteristics [39]

Cell Type	Flooded Lead-Acid
Number of Positive Plates	7
Number of Negative Plates	8
Plate Height	293 mm
Plate Width	143 mm
Positive Plate Thickness	4.32 mm
Negative Plate Thickness	3.05 mm
Dry Weight	12.3 kg
Rated Capacity at 3.8 hour rate	231 Ah
Theoretical Capacity (TC)	710 Ah

An Arbin BT-2000 power-cycler, located in the RESL, was used to form and cycle the cells in phase 1 of this project, and to cycle the cells in phase 2 of this project. This power-cycler is comprised of three channels, each rated for 0-20 V and +/- 100 A, and has 16 auxiliary T-type thermocouples and 16 auxiliary voltage ports. The SGs of the cells during formation and cycling were measured using the combination of a bulb hydrometer

(DURAC H-B 50860) and a digital density meter (Anton Paar DMA 35) by taking samples of electrolyte from the top of the cell through the fill port, and were corrected to a temperature of 20 °C. SG values obtained using this method are subjected to the effects of acid stratification. This effect was not taken into account due to the configuration of the cell, and the resulting difficulties in obtaining SG values at different height intervals. The experimental configuration used at the RESL to form and cycle cells is shown in Figure 6, while Figure 7 shows how the Anton Paar DMA 35 meter is used to measure electrolyte SG. It should be noted that the exhaust fans and condensing tubes were used to mitigate the chemical safety risks. An in-depth safety assessment for this project can be found in Appendix C.

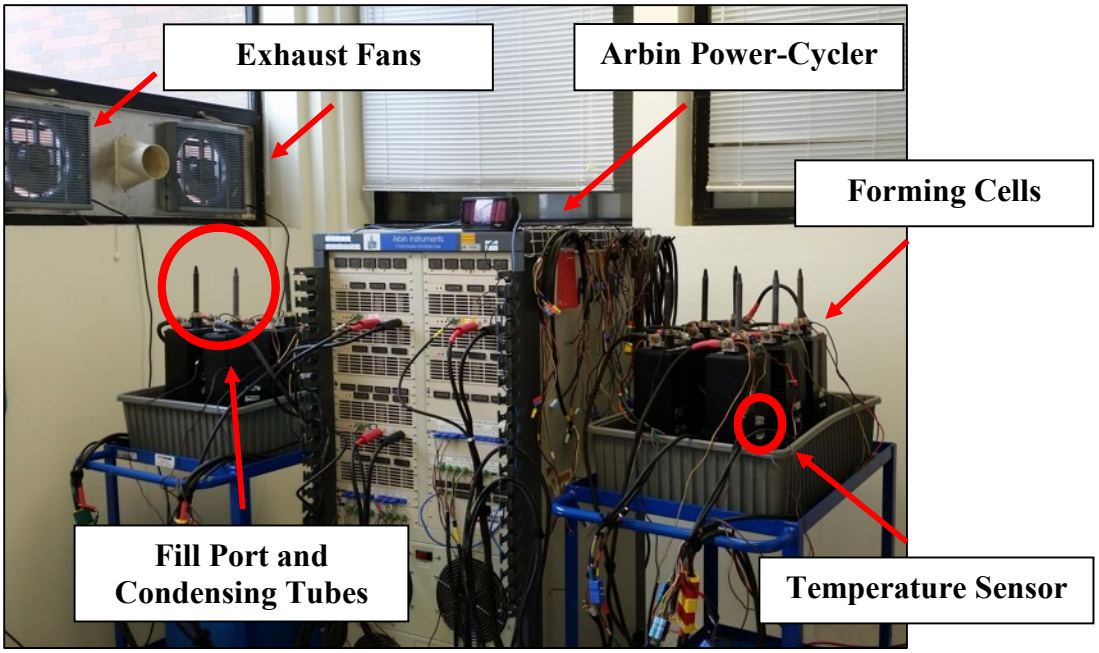

Figure 6 Experimental Configuration for Cell Formation and Performance Cycling (RESL)

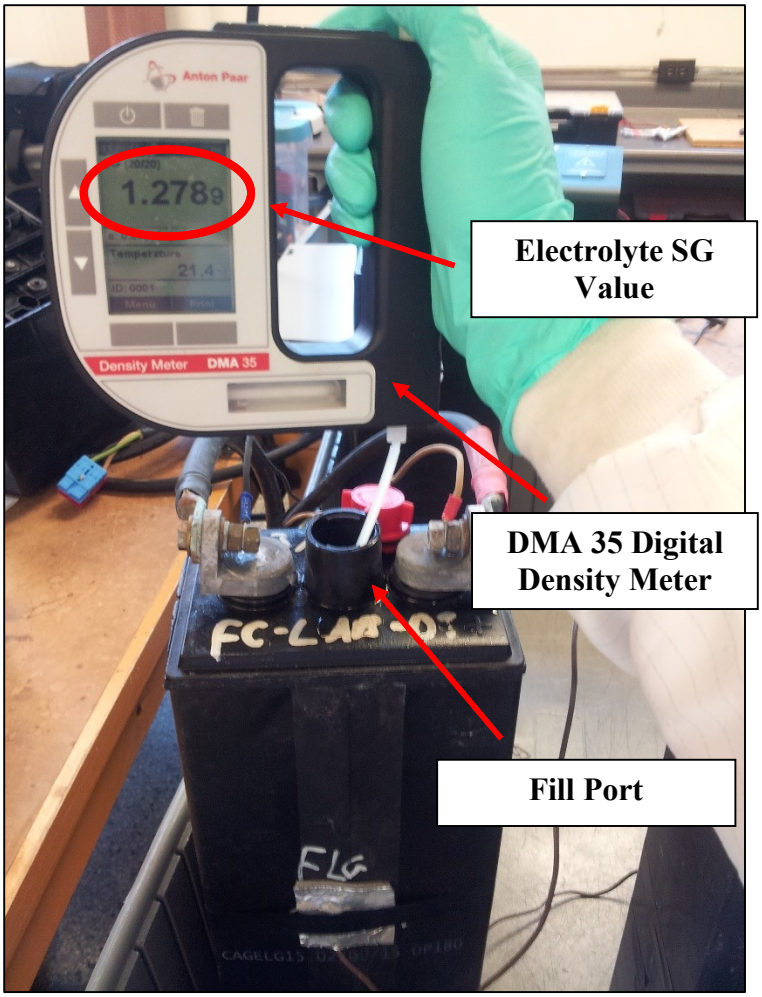

Figure 7 Electrolyte SG Measurement with DMA 35 Digital Density Meter

4.1. Phase 1: Lead-acid Battery Formation Optimization – Laboratory Study

The following will describe the specifics of the methodology for the first phase of this research project.

4.1.1. ELG15 Cell Formation

In order to study the impact of the formation algorithm on subsequent cell performance, two different formations were sequentially conducted for this phase of the project: (1) a formation with a constant-current algorithm, and (2) a formation with a multi-step current algorithm. For both formation algorithms, the one-shot container formation method was used as per the battery manufacturing standards at SBC, which avoids replacing the electrolyte once the formation has been completed [14]. Furthermore, the cells presented in Table 2 were provided to the RESL "green" for this phase of the project, which is to say the pasted and cured plates were assembled into cells, but electrolyte was not added, nor was formation current applied.

Constant-Current Formation (Group "a")

A constant-current formation algorithm is defined as applying a constant-current throughout the formation process "irrespective of electrolyte temperature and battery voltage" [21]. However, it was decided to maintain the temperature of the cells between 30 °C and 50 °C, the ideal formation temperature range as defined by Pavlov [21]. A formation current of 20 A, corresponding to a current density of 3.4 mA cm^{-2}, was chosen for this formation algorithm as it falls within the "normal range" of formation current densities as defined by Pavlov (i.e., 2 to 10 mA cm^{-2}) [21]. Prior to formation, the cells were soaked for one hour using H_2SO_4 electrolyte with an SG of 1.200. This concentration of electrolyte corresponds to the average of the recommended values, 1.15 to 1.23, for the container formation as defined by Pavlov [21], and is the standard used at SBC for the floor container formation method.

Using the constant-current formation algorithm, eight cells were formed in series, each to a different formation level, or coulombic value in Ah, in order to capture a wide range of formation levels. This was completed by sequentially removing cells from the series circuit once said cells had reached their desired formation level. A line diagram of this configuration is shown in Figure 8. The connections points labelled "Main Positive" and

"Main Negative" are connected to the Arbin power-cycler, while interconnects were used to connect the cells in series.

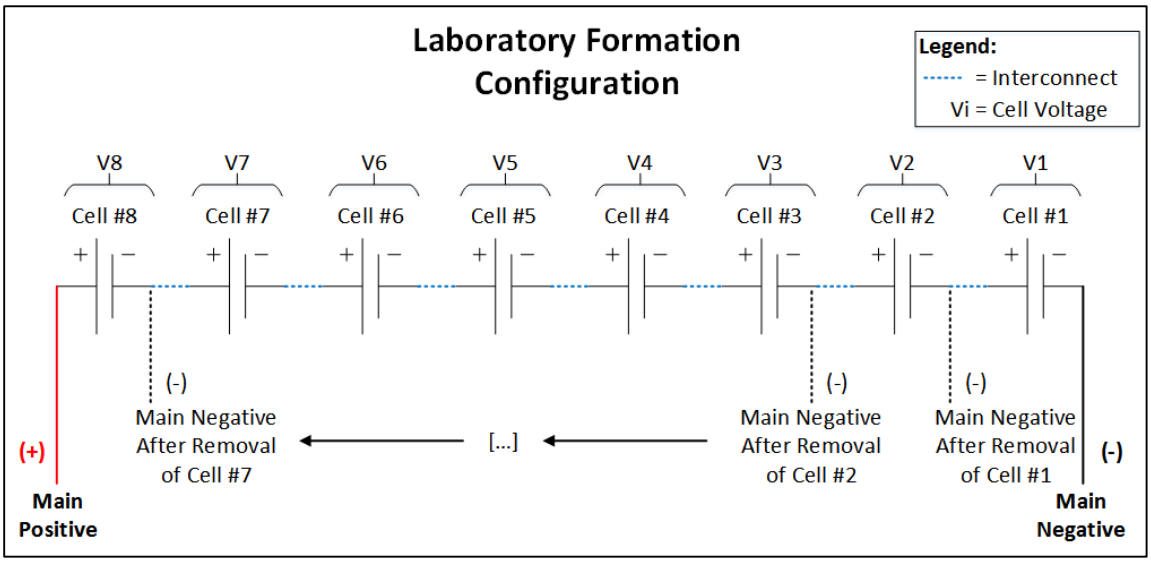

Figure 8 Laboratory Formation Configuration

The selected formation levels are shown in Table 3, along with their respective ratios of the calculated theoretical capacity. The cells are named based on their ratio of theoretical capacity, where the subscript "a" denotes the constant-current formation.

Table 3 Selected Formation Levels – Constant-Current Algorithm

Cell Name	Formation Input (Ah)	Ratio of Theoretical Capacity
$0.70TC_a$	500	0.70
$1.41TC_a$	1000	1.41
$1.88TC_a$	1333	1.88
$2.35TC_a$	1667	2.35
$2.82TC_a$	2000	2.82
$4.23TC_a$	3000	4.23
$5.63TC_a$	4000	5.63
$7.04TC_a$	5000	7.04

As shown in Table 3, a wide range of formation levels were covered in this phase of the project, with ratios of formation input to theoretical capacity of the plates ranging from 0.70 to 7.04. Formation input increments of 1000 Ah, with the exception of cells $0.70TC_a$, $1.88TC_a$, and $2.35TC_a$, were chosen in order to ensure a range of TC ratios extending beyond the ones recommended in literature. Cell $0.70TC_a$ was chosen as the extreme case for an under-formed cell, while cells $1.88TC_a$ and $2.35TC_a$ were chosen as they fall within

the formation range recommended by Pavlov [21] of 1.70 to 2.50 times the theoretical capacity of the cell.

Multi-Step Current Formation (Group "b")

A multi-step current formation algorithm is comprised of changes in formation current, typically used as a temperature control strategy [21]. The multi-step formation algorithm, shown in Table 4, was chosen as it allowed for a faster formation than the constant-current formation algorithm, while maintaining cell temperatures between 30 °C and 50 °C. Table 4 also highlights the corresponding current density values for the four current steps, where it can be noted that all of them are within the "normal range" of formation current densities as defined by Pavlov [21]. As was the case for the constant-current formation algorithm, the cells were soaked for one hour using H_2SO_4 electrolyte with an SG of 1.200 prior to formation.

Table 4 Multi-Step Current Formation Algorithm

Step #	Description	Current Density (mA cm^{-2})	Duration	Formation Capacity (Ah)
1	Charge at 10 A	1.7	2 hours	20
2	Charge at 20 A	3.4	22 hours	440
3	Charge at 30 A	5.1	24 hours	720
4	Charge at 40 A	6.8	Remainder of Formation	∫40 A dt

Using this formation algorithm, seven additional cells were formed in series to a different formation level as shown in Table 5, where the subscript "b" denotes the multi-step formation.

Table 5 Selected Formation Levels – Multi-Step Current Algorithm

Cell Name	Formation Input (Ah)	Ratio of Theoretical Capacity
$1.41TC_b$	1000	1.41
$1.88TC_b$	1333	1.88
$2.35TC_b$	1667	2.35
$2.82TC_b$	2000	2.82
$3.52TC_b$	2500	3.52
$4.23TC_b$	3000	4.23
$5.63TC_b$	4000	5.63

As shown in Table 5, the chosen formation levels are similar to the ones which were selected for the constant-current formation, with three exceptions. Based on the

performance results of the cells formed using the constant-current formation algorithm, cell $3.52TC_b$ was added to provide an additional cell in the range of interest, and formation inputs of 500 and 5000 Ah were removed as they were found to be significantly outside the optimal formation level.

It was hypothesized that the cells formed using the constant-current formation algorithm would provide better performance results when compared to the ones formed using the multi-step approach. This was based on the fact that a lower current would limit side reactions during formation, such as electrolysis, thus increasing the efficiency of formation.

Finally, it should be noted that cell voltage, outside cell temperature at mid-height, and cell SG values were recorded for both formation algorithms. While measuring the temperature of the electrolyte inside the cells would have provided a better representation of the formation profiles, equipment limitations made it unfeasible to do so. Cell voltage and temperature values were logged every 6 seconds using the auxiliary ports on the power-cycler, while the cell SG values were measured manually every 2 to 4 hours. Additionally, distilled water was added to the cells during formation when deemed necessary to ensure the plates remained submerged, while H_2SO_4 electrolyte with an SG of 1.265 was used to top-up the cells if required at the end of formation. This concentration of electrolyte was selected to top-up the cells as it is the standard used by SBC for off-grid solar cells.

4.1.2. ELG15 Cell Cycling

As stated in the literature review, the deep-discharge test is the most reliable method in determining the capacity of a LAB [6, 7]. Thus, a deep-cycling algorithm, shown in Table 6, was chosen to study the performance of the cells formed using the two aforementioned formation algorithms. The cells were individually deep-cycled 10 times, as it allowed for them to reach their maximum discharge capacity, thus demonstrating their attainable capacity if fully formed, and to determine the consistency of the discharge capacity results, thus ruling out any outliers. While outside the scope of this project, it is important to note that this deep-cycling algorithm was chosen following the completion of an in-depth iterative study, where it ensured ELG15 cells with electrolyte SG values of 1.265 formed using the floor container, submerged container, and circulated electrolyte

formation methods at SBC behaved as intended by the manufacturer, while also limiting the total amount of overcharge.

While the rated capacity of the cell presented in Table 2 is based on an initial SG of 1.265, the chosen discharging and charging rates for the deep-cycling algorithm presented below were based on the capacity data presented on the *Data Sheet for the S-480* battery using a reference electrolyte SG value of 1.280 [39], thus explaining the uneven discharging and charging ratios (i.e., 3.8 hour discharging rate instead of a 4 hour discharging rate). This was the only manufacturing data available at the time of the aforementioned iterative study, and by the time SBC released the capacity characteristics for the S-480 battery using a reference electrolyte SG value of 1.265, the deep-cycling algorithm had already been optimized. Electrolyte SG values are important to consider, as they affect the rated capacity of a battery. Specifically, batteries used in off-grid solar applications, and thus the ones used in this research project, are supplied with lower electrolyte SG values than those intended for conventional applications (i.e., 1.265 SG for solar vs. 1.280 SG for conventional), as lower SG values extend the cycle life of the battery, but at the expense of a slight decrease in available capacity [17]. Specifically, the 4 hour capacity rating of the S-480 battery (and by association the ELG15 cell) is 244 Ah based on an electrolyte SG of 1.280, and 232 Ah (5 % less) based on an electrolyte SG of 1.265.

The optimized deep-cycling algorithm is comprised of a 3.8 hour discharge rate at a constant-current (CC) to a voltage cutoff setpoint, and a three-step charging configuration: CC, constant-voltage (CV), and CC. The 3.8 hour discharge rate, and corresponding 3.8 hour rate for the first phase of charge, were selected in order to ensure cycles could be completed in a timely matter. Specifically, cycles were arranged so that a new one could be started every 16 hours (e.g., 08:30, 00:30, 16:30, 08:30, etc.), which allowed for SG measurements to be taken following the completion of each cycle. Furthermore, rest periods of 30 minutes were provided between the discharge/charge transitions, and additionally required that the cell be less than 28 °C before proceeding to the next step, as to limit the effect of cell temperature on battery performance.

Table 6 Deep-Cycling Algorithm – Phase 1

Step #	Step Name	Description
1	Rest – begin	30 seconds rest for OCV measurements
2	Discharge	CC of -60.93 A (3.8 Hour Rate) until cell reaches 1.75 V
3	Rest – transition	Rest 30 minutes and until cell temperature is < 28 °C
4	Charge phase 1	CC of 60.93 A until cell reaches a voltage of 2.50 V
5	Charge phase 2	CV at 2.50 V until 7.50 A is reached (2.1 % of 20 Hour Rate)
6	Charge phase 3	CC of 9.15 A for 4 hours (equivalent to 36.6 Ah)
7	Rest – end	Rest 30 minutes and until cell temperature is < 28 °C

The specific values shown in Table 6 were obtained using the *Rolls Battery Manual* [40], and the *Data Sheet for the S-480* [39]. Specifically, with respect to Step 2 it is indicated on the data sheet that the ideal cutoff voltage is 1.75 V for complete cell discharge.

With respect to Step 5 (Charge phase 2), a current cutoff of 7.50 A with a CV voltage of 2.50 V was selected. 7.50 A is equivalent to 2.1 % of the 20 hour capacity of the cell based on an SG of 1.265.

With respect to Step 6, the final CC step was comprised of an overcharge equivalent to 16 % of the rated capacity of the cell at the 3.8 hour rate (i.e., 37 Ah) based on an SG of 1.265. This overcharge value is between the typically recommended overcharge values of 5 and 30 % for the LAB [41]. One can also note that Wagner and Sauer [8], who used a deep-cycle algorithm to determine the full state-of-charge of LABs in different solar power systems, used an overcharge value of 12 % with respect to the rated capacity of the battery.

Internal Resistance Measurement

Finally, while not shown in Table 6, important substeps were embedded in Steps 2 (discharge) and 4 (charge) of the cycling algorithm consisting of current pulses of 10 seconds to -100 A (discharge) and +100 A (charge), respectively. These pulses, which occurred at the 5 Ah charge/discharge capacity point, and at every multiple of 50 Ah charge/discharge capacity points thereafter, were used to determine the DC internal resistance (IR) of the cell while cycling. With respect to the cells formed using the multi-step current algorithm, the pulse occurrence was changed to every multiple of 25 Ah charge/discharge capacity points in order to obtain additional IR data for these cells. It should be noted that current pulses only occurred during the CC steps of the cycling

algorithm, as this ensured the base current remained at +/- 60.93 A. During these current pulses, cell voltages were logged every second in order to provide a higher resolution of IR measurements.

The DC IR of a LAB battery is an important parameter in determining its power performance. As stated in the literature review, the power density requirements for a lead-acid battery used in off-grid solar applications are small, yet DC IR measurements can be correlated to capacity results and charge acceptance. Thus, this metric was included during the deep-cycling analysis of the cells in order to obtain additional performance information. The DC resistance is measured using Ohm's law, based on the relationship between the change in DC voltage resulting from a change in DC current, as shown in equation (6).

$$DC\ IR = (e_2 - e_1)/(i_2 - i_1) \quad (6)$$

where e_2 and i_2 are voltage and current values immediately before the end of the pulse, respectively, and e_1 and i_1 are voltage and current values immediately before the beginning of the pulse, respectively. Figure 9 shows an example of a discharging pulse profile, where the location of these variables are shown for clarity.

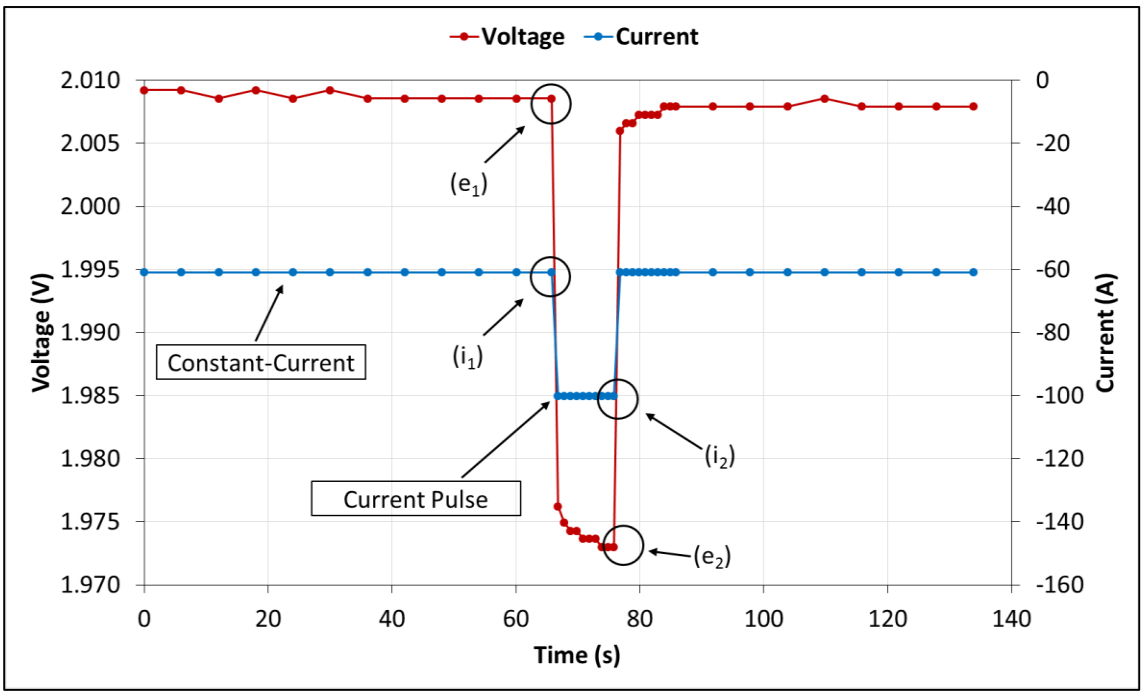

Figure 9 Example of Discharging Pulse Profile

The IR components of a battery can be modelled by an equivalent electric circuit, as shown in Figure 10. In the diagram, the current conducting elements, such as the tabs, grids,

active material, and electrolyte, are modelled with the series resistor, R_o (i.e., ohmic resistance), while the charge transfer reactions are modelled with the parallel resistor, R_{ct}. A charged electrode immersed in electrolyte will inherently feature an electrical double layer (EDL) at the interface. This phenomenon is explained in detail in [42]. The electrostatic charge and discharge of the EDL plays an important role in the charge/discharge mechanisms of the battery and is typically modelled as the parallel capacitor, C_{dl}. Diffusive mass transfer effects are usually included in the model as well, and are typically represented by the Warburg impedance, Z_W, which is a constant-phase-element [42]. While the electrical response of the ohmic resistance is instantaneous, both the EDL and the diffusion effects have significant time constants in their electrical responses to stimuli. Time constants for the EDL, while current dependent, are typically on the order of seconds, while time constants for diffusion are typically on the order of minutes to hours [43].

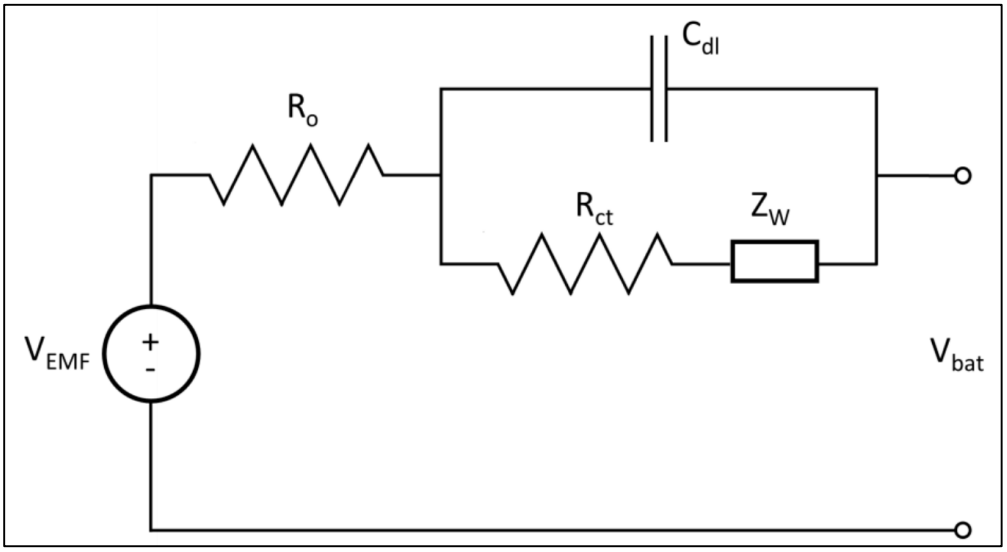

Figure 10 Simple Equivalent Electric Circuit for a Battery

With respect to the aforementioned ohmic resistance of the LAB (R_o in Figure 10), its three major components (i.e., the electrode, the electrolyte, and the separators) have the greatest influence. Wagner [44] states that in order to achieve ideal battery performance and to reduce the effect of inhomogeneous current distribution across the plates, the overall resistance of the electrode must be minimized. This parameter can be controlled by the grid structure and material of the plates, and by the composition of the active material [44, 45]. The resistivity of the electrolyte, influenced by its concentration and temperature, plays a

significant role regarding the IR of a LAB and consequently on its power capability [17]. Pavlov [17] has shown that electrolyte SG values ranging between 1.100 and 1.275 have the lowest resistivity (i.e., 1.7 Ω cm to 1.3 Ω cm, respectively, for an electrolyte temperature of 25 °C), where being outside this range (i.e., electrolyte SG < 1.100 or electrolyte SG > 1.275) results in a substantial increase. Furthermore, he has shown that the resistivity of the electrolyte has an inverse relationship with temperature, with electrolyte temperatures higher than 40 °C offering the lowest resistivity, and temperatures below 0 °C resulting in a reduction in available power and energy for a LAB [17]. Finally, the resistance of the separator is a function of its porosity and tortuosity factor (i.e., the ratio of the mean path length the ion will travel, to the actual thickness of the membrane) [15]. Thus, one is able to reduce the electrical resistance of the separator by increasing its porosity and by decreasing the tortuosity factor.

Based on this information, pulse magnitudes of -39 A for discharging, and +39 A for charging were chosen for this algorithm as they corresponded to the difference between the regular cycling current of +/- 60.93 A and the +/- 100 A current limits of the Arbin power-cycler. Furthermore, Kirchev *et al.* [46] found that the EDL pulse response of a LAB electrode was able to approach equilibrium with a pulse duration of 5 seconds when alternating between a 10-hour rate current and a resting state. Thus, a pulse duration of 10 seconds was chosen with the intent of providing enough time for the capacitive pulse responses to stabilize, without greatly affecting the state-of-charge of the battery during the respective charging and discharging pulses. Since diffusive mass transfer processes are much slower than ohmic and EDL processes, diffusion effects were not taken into consideration.

Finally, it should be noted that during deep-cycling operation, cell voltages, outside cell temperature at mid-height, cell IR values, and cell electrolyte SG values were measured. Cell voltage and temperature values were logged every 6 seconds using the auxiliary ports on the power-cycler, cell IR values were measured during Steps 4 and 6 of the algorithm using the aforementioned current pulses, and cell electrolyte SG values were measured before the start of each deep-cycle (i.e., before each discharge).

4.1.3. Determining the Optimal Formation Level

As stated in the literature review, the operating conditions of batteries in off-grid solar systems are very different than those of conventional applications, as strategies presently used in off-grid solar applications have difficulties fully charging the batteries. Thus, it is apparent that a charging algorithm such as the one presented in Table 6 would not be available in an off-grid solar setting. With this in mind, and as a significant research contribution to the field of LABs, the following methodology was developed (and used) to determine the optimal LAB formation level by optimizing the balance between the initial discharge capacity and DFE (i.e., initial discharge capacity output of a cell divided by its formation capacity) values of these cells.

1) Deep-cycling performance analyses of the cells were independently completed for both formation algorithms.
2) Upon completion of Step 1, a regression analysis was performed with respect to the initial discharge capacity outputs of the cells as a function of their formation input. Again, this was completed for both formation algorithms independently. This allowed for a broader representation of potential formation levels, which were previously limited to eight levels for the constant-current formation method, and seven levels for the multi-step current formation method. It should be noted that if multiple cells were formed using the same formation input level, one would obtain small differences in initial discharge capacity results due to a variance in cell OCV, cell electrolyte SG, cell IR, and cell mass. Nevertheless, the assumption that cells behave as defined by a regression model constrained between experimental data was deemed acceptable.
3) Initial discharge capacity values, and corresponding DFE values for a broad range of formation input levels were then normalized over their respective maximum values. It should be noted that the range of formation input levels were maintained between the lowest and highest formation levels of each formation algorithm, respectively. An example of normalized initial discharge capacity and DFE values is shown in Figure 11.

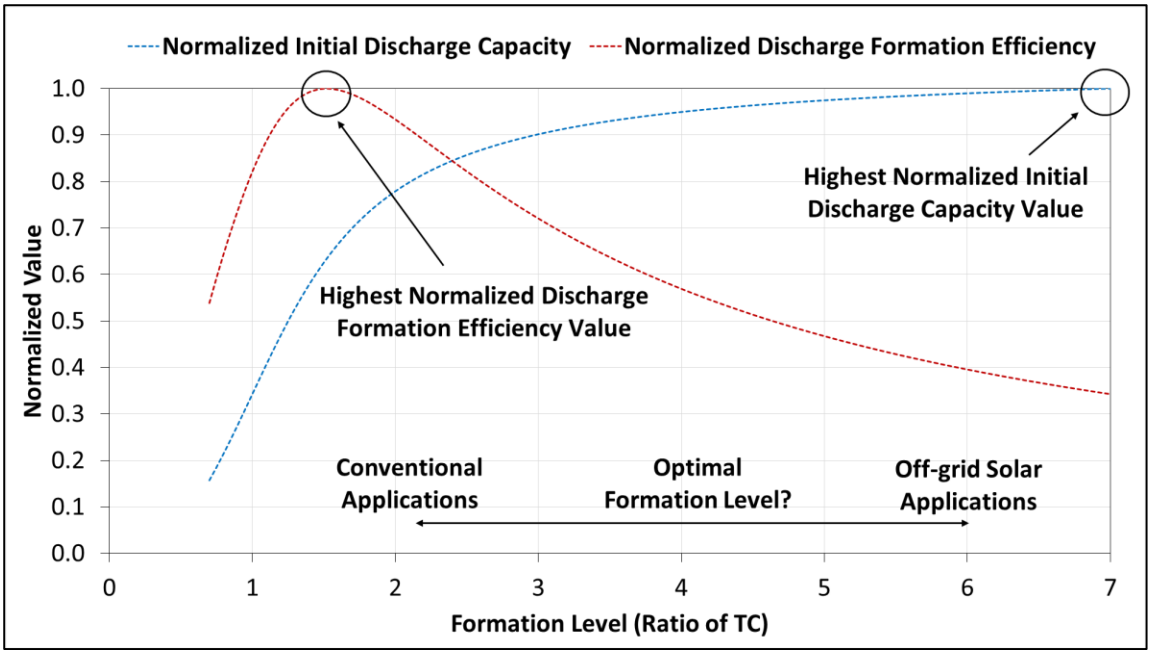

Figure 11 Example of Normalized Initial Discharge Capacity and Discharge Formation Efficiency Values

As shown in Figure 11, the formation levels corresponding to the highest initial discharge capacity and DFE values are not in agreement. Specifically in this example, a formation level of 7.00TC should be used in order to maximize the initial discharge capacity, while a formation level of 1.50TC should be used in order to maximize the DFE. Thus, the optimal formation level is determined by applying appropriate weighting factors to these two curves, as explained in Step 4.

4) By applying weighting ratios to the normalized initial discharge capacity and DFE values, the optimal formation level for both formation algorithms was then determined by evaluating the sum of these two values, with the highest resulting in the optimal formation level. In other words, if a LAB manufacturer were to attribute more importance to the initial discharge capacity of the cell than to its DFE (i.e., as is the case for off-grid solar applications), it would select a weighting ratio higher than 50 % in favor of the former. As an example, a weighting ratio of 70 % attributed to the initial discharge capacity of the cell would result in a weighting ratio of 30 % attributed to the importance of its DFE (i.e., 100 % = [Importance of Initial Discharge Capacity] % + [Importance of DFE] %). Figure 12 shows the results of applying a 70 % / 30 % weighting ratio to the normalized initial discharge

capacity and DFE curves shown in Figure 11, respectively. The figure also shows the corresponding sum of the weighted normalized values.

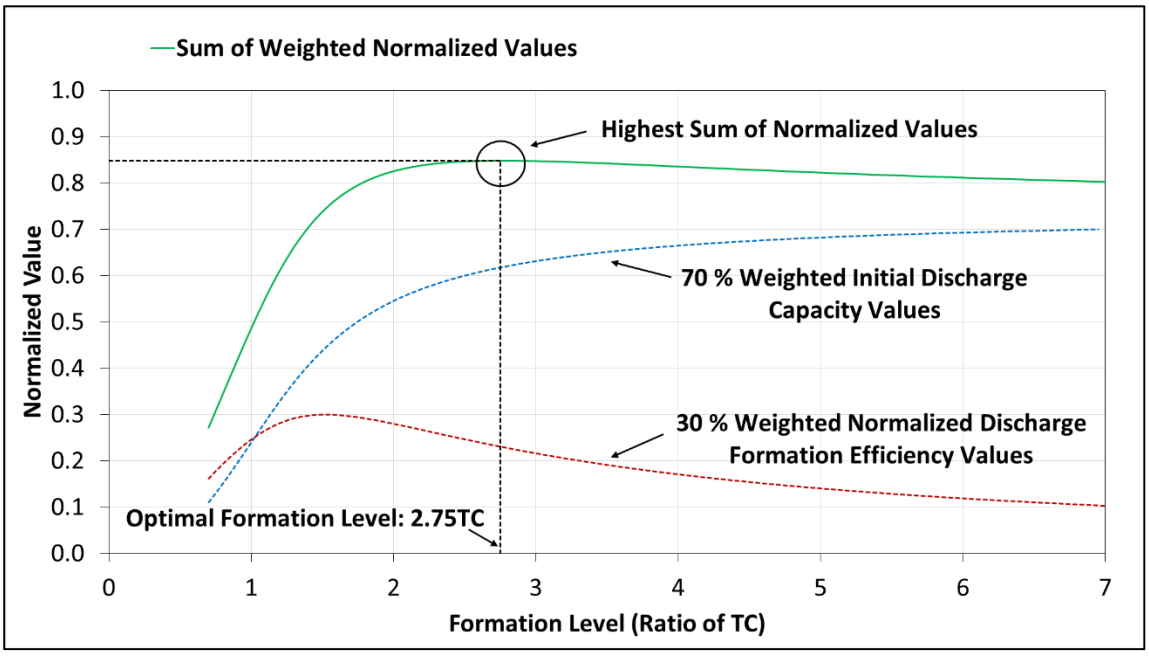

Figure 12 Weighted Normalized Initial Discharge Capacity and Discharge Formation Efficiency Values

The effects of the 70 % / 30 % weighting ratios on the normalized initial discharge capacity and DFE values are clearly shown in Figure 12. Thus by evaluating the sum of these two values, it was determined that the highest value coincides with an optimal formation level of 2.75TC.

4.2. Phase 2: Lead-acid Battery Formation Optimization – Industrial Study

The goal of this phase of the project was to identify the optimal LAB formation method for the off-grid solar PV market between four methods:

- the floor container formation method,
- the submerged container formation method,
- the circulated electrolyte formation method, and
- the tank formation method.

Furthermore, it sought to determine the influence of these methods on the ideal formation level determined in phase 1 of this project.

Unlike the power-cycler which was used to form cells in phase 1 of this project, the formation chargers at SBC, with the exception of the submerged container and circulated electrolyte chargers, are not equipped with data logging features. As such, a portable external monitoring system, the *measurement unit*, was designed to measure the DC and AC formation characteristics for each of the four formation chargers. Figure 13 shows a line diagram of the measurement unit, while Figure 14 and Figure 15 show the measurement unit as installed at SBC. A complete summary of this monitoring system can be found in Appendix A. As the scope of this project for this section is limited to the formation characteristics at SBC, only the DC formation characteristics of current and voltage will be presented.

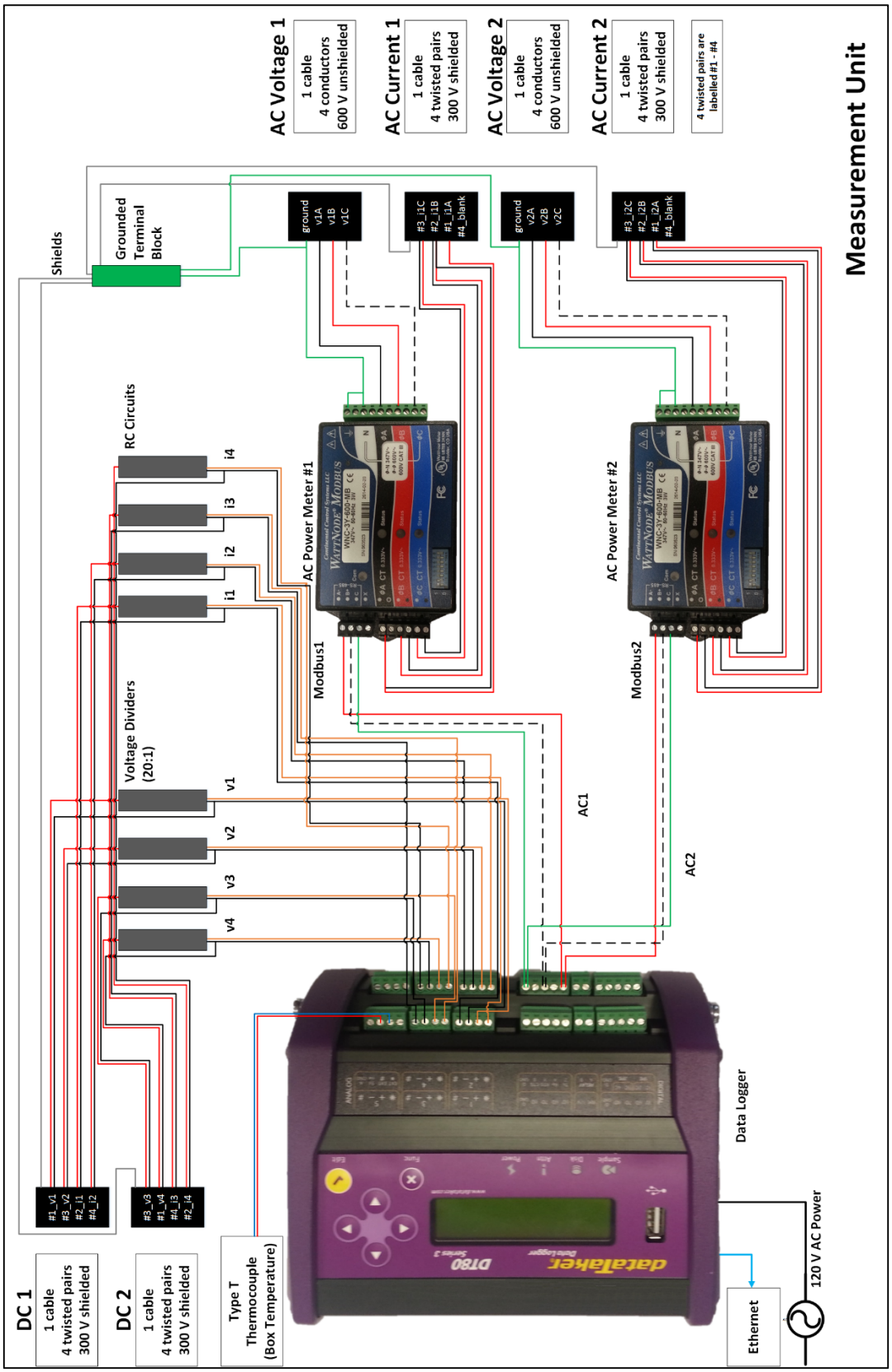

Figure 13 Line Diagram of Measurement Unit

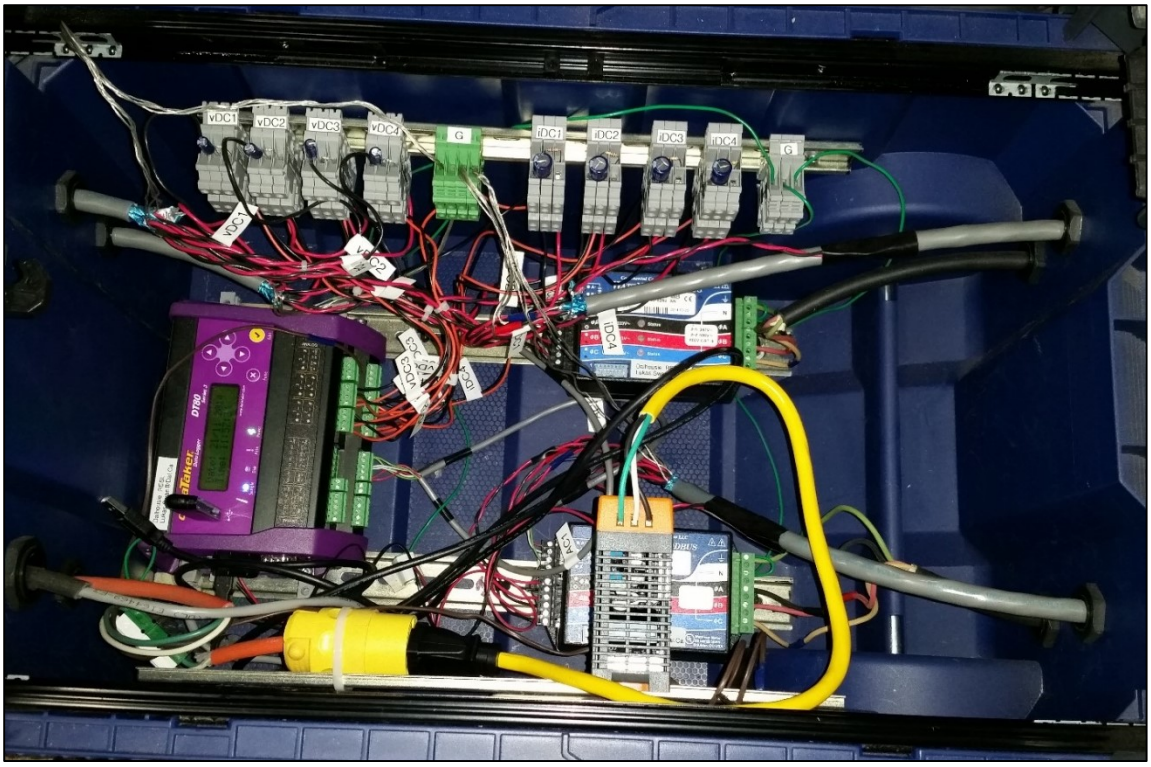

Figure 14 As-Built Measurement Unit

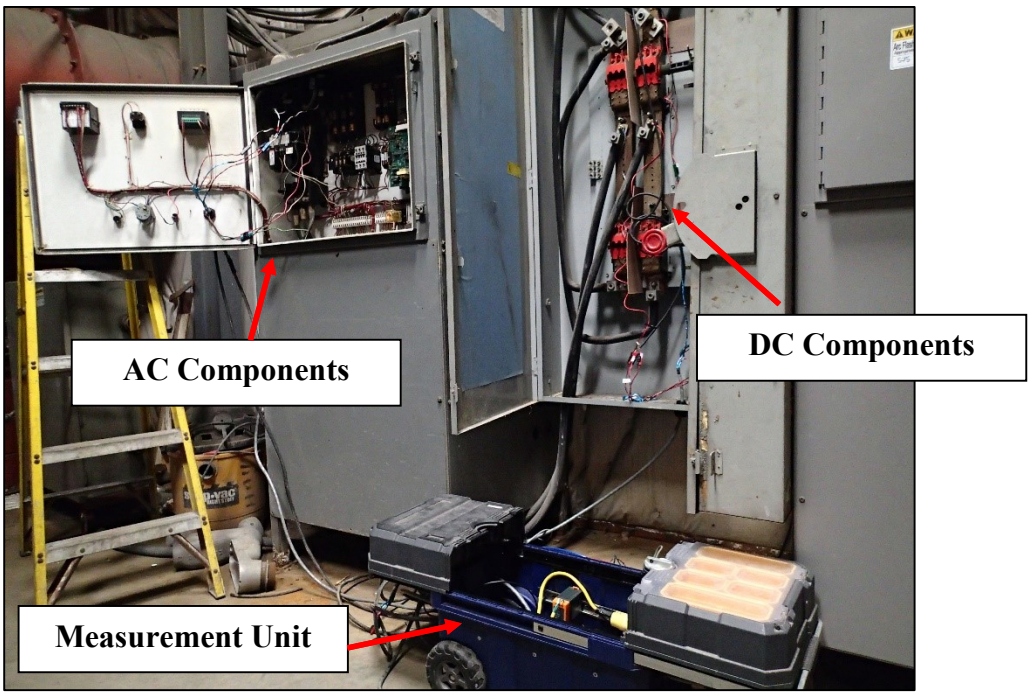

Figure 15 Measurement Unit and SBC Tank Formation Charger

DC values were measured using current shunts and voltage taps, and recorded using a dataTaker DT80 data logger. Current shunts, which have a known resistance, are used to

measure current in a circuit by measuring the voltage drop across them, which is in turn proportional to the current flowing through it. Low-pass filtered voltage dividers (20:1 ratio, 0.14 Hz cutoff) were used between the DC voltage measurements and the data logger, due to the data logger voltage limit of +/- 30 V [47], and resistor-capacitor (RC) circuits were used as low-pass filters (0.72 Hz cutoff) to provide smoother DC current values to the data logger. The shunts and voltage taps were located directly inside the enclosure of each respective formation charger, whereas the voltage dividers, the RC circuits, and the data logger were located within the enclosure of the measurement unit.

The design of the measurement unit also included a grounded terminal block used to protect the equipment, a T-type thermocouple to measure the temperature of the unit, Ethernet capability to communicate with the data logger, 12 V AC to power the data logger, and shielded cables to avoid noise interference from other cables, thus providing more accurate readings.

Table 7 shows the DC output ratings of the four formation chargers, and the current shunts which were used to measure their respective formation current. It is important to note that while the submerged container formation charger is comprised of eight different circuits, only four were monitored due to equipment limitations. Thus, it was ensured that the ELG15 cells were formed using one of these four circuits.

Table 7 Formation Chargers DC Output Ratings

	DC Output Characteristics			
Formation Method	Current (A)	Voltage (V)	# of Circuits	Current Shunt Rating (mV/A)
Floor Container	0 – 100	12 – 280	1	50/100
Submerged Container	0 – 80	0 – 375	8	50/100
Circulated Electrolyte	0 – 300	0 – 150	2	50/500
Tank	0 – 600	0 – 200	1	50/500

4.2.1. ELG15 Cell Formation

Ideally, cells would have been formed using the range of formation levels presented in section 4.1.1 for each of the four formation methods, as this would have provided the greatest amount of information regarding the influence of these different methods. Although due to production constraints at SBC, it was decided to obtain three different formation levels for each method: under-formed (UF) cells, normal-formed (NF) cells, and over-formed (OF) cells, resulting in a total of 12 different variations. NF cells were defined

as cells formed using the standard SBC algorithm for each of the respective formation methods, whereas UF and OF cells corresponded to 80 % and 120 %, respectively, of the NF cells with respect to the formation input in Ah (see Table 12). It was ensured that a minimum of four cells were formed for each formation level and method, which allowed for three cells to be cycled simultaneously (i.e., a module) on one channel using a series configuration, thus mimicking the S-480 battery. Cycling one cell at a time was determined to be unpractical due to time constraints and channel limitations. Furthermore, it should be noted that the formation using the four different methods were completed separately, as to ensure cells from each method could be cycled as soon as possible following the completion of their respective formation process. This was done in order to avoid significant shelf time for the cells, which might otherwise have negatively affected the performance results.

Table 8 – Table 11, show the formation algorithms which were used to form the ELG15 cells using the floor container method, the submerged container method, the circulated electrolyte method, and the tank formation method, respectively. It is important to remember that the following formation currents are applied over seven positive plates in parallel (i.e., ELG15 cell), with the exception of the tank formation method, where the formation current is applied over 32 positives plates in parallel due to the characteristics of this formation method (see section 2.2.3).

Table 8 SBC Floor Container Formation Algorithm

Step #	Description	Duration
1	Electrolyte Filling	Completed Manually
2	Soaking (1.200 SG Electrolyte)	1 hour
3	Charge at 20 A	24 hours (i.e., 480 Ah)
4	Charge at 30 A	24 hours (i.e., 720 Ah)
5	Charge at 40 A	Remainder of Formation

As shown in Table 8, the SBC floor container formation algorithm is very similar to the multi-step current formation algorithm that was used in phase 1 of this project (see Table 4), the main difference being the exclusion of the 10 A charging step.

Table 9 SBC Submerged Container Formation Algorithm

Step #	Description	Duration
1	Electrolyte Filling	Completed Manually
2	Soaking (1.200 SG Electrolyte)	30 minutes
3	Charge at 22 A	3 hours (i.e., 66 Ah)
4	Begin while loop (steps #4-6)	Remainder of Formation
5	Charge at 75 A	Until cell temperature > 53 °C, then go to Step 6
6	Charge at 55 A	Until cell temperature > 58 °C or < 50 °C, then go to Step 7
7	Charge at 40 A	Until cell temperature < 54 °C, then go to Step 5

As shown in Table 9, the main formation current for the submerged container formation method is dependent on the temperature of the cells in the water tank, with the while loop ensuring that the cell temperatures do not exceed 58 °C. As per the design of the water bath, the measurement of temperature was limited to the internal temperature above the plates of one cell per circuit. It should also be noted that the overall current values are higher than the ones presented for the floor container algorithm, thus resulting in a shortened formation period.

Table 10 SBC Circulated Electrolyte Formation Algorithm

Step #	Description	Duration
1	Electrolyte Filling	10 minutes
2	Soaking (1.250 SG Electrolyte)	30 minutes
3	Charge at 28.0 A	1 hour (i.e., 28 Ah)
4	Charge at 70.0 A	16 hours (i.e., 1120 Ah)
5	Charge at 46.7 A	1 hour (i.e., 47 Ah)
6	Charge at 70.0 A	6.7 hours for UF Cells (i.e., 469 Ah), 14 hours for NF and OF Cells (i.e., 980 Ah)
7	Rest	5 minutes
8	Discharge at 37.3 A	4 hours (i.e., 149 Ah)
9	Rest	5 minutes
10	Charge at 70.0 A	Remainder of Formation

As shown in Table 10, the duration of Step 6 was reduced for the UF cells formed using the circulated electrolyte formation method. This was completed in order to attain the desired UF formation input, which would otherwise have been exceeded with a complete 14 hour charge at 70.0 A. This formation algorithm uses a discharge current (Step 8), which as stated by Pavlov [21], is used to uncover unformed portions of $PbSO_4$, which are then formed in the next charging step. As such, this increases the overall amount of

formed $PbSO_4$, and has been shown to increase the initial discharge capacity of a LAB [13, 21]. The rest periods are used to lower the cell temperatures.

Table 11 SBC Tank Formation Algorithm

Step #	Description	Duration
1	Charge at 100 A (Reversed Direction) (equivalent to 21.9 A per ELG15 cell)	1 hour (i.e., 22 Ah/cell)
2	Rest	30 minutes
3	Charge at 288 A (Regular Direction) (equivalent to 63.0 A per ELG15 cell)	Remainder of Formation

As shown in Table 11, two current directions are used in this formation algorithm. The charge at 100 A in the reversed direction is used to ensure the adhesion of the plates to the contact bar at the bottom of the tank. Additionally, this causes lead to be deposited irregularly on the smooth metal surface of the positive grids, causing an increase in the formation efficiency due to a reduction in the formation of plate-like $PbSO_4$ crystals [21]. It is important to note that Step 1 of this formation algorithm does not count towards to the total Ah formation input, while the 30 minutes rest period is used to cool the electrolyte in the tank. The SG of the electrolyte for this formation method was 1.100.

Table 12 shows the formation levels which were used for all four formation methods using the ELG15 cell as a basis, and their corresponding formation times. It should be noted that the formation levels for the under-formed and over-formed cells with respect to the submerged container formation method are equivalent to 82 % and 119 % of the normal-formed level, respectively, due to the inability of this formation charger to be stopped at precise Ah input values. The formation times are based on the presented formation algorithms, and do not include the electrolyte filling step for the first three formation methods. Furthermore, as the main formation current for the submerged container formation method is dependent on the temperature of the cells, an average current of 65 A was selected for this calculation. This selection was based on the average of the currents used in Steps 5 (i.e., 75 A) and 6 (i.e., 55 A), as time spent in Step 7 (i.e., 40 A) is relatively rare.

Table 12 SBC Formation Levels and Formation Times (ELG15 Cell Basis)

	Under-formed		Normal-formed		Over-formed	
Formation Method	Formation Input (Ah)	Time (hrs)	Formation Input (Ah)	Time (hrs)	Formation Input (Ah)	Time (hrs)
Floor Container Formation	1982 (2.79TC)	68.6	2478 (3.49TC)	81.0	2974 (4.19TC)	93.4
Submerged Container Formation	1704 (2.40TC)	28.7	2089 (2.94TC)	34.6	2492 (3.51TC)	40.8
Circulated Electrolyte Formation	2049 (2.89TC)	34.9	2560 (3.61TC)	42.2	3072 (4.33TC)	49.5
Tank Formation	1223 (1.72TC)	20.9	1534 (2.16TC)	25.9	1846 (2.60TC)	30.8

As shown in Table 12, the three different formation levels (UF, NF, and OF) for the submerged container formation method are lower than the levels used for the floor container and circulated electrolyte formation methods. This is an important characteristic, as these three formation methods were shown to be relatively similar in the literature review (see section 2.2.3), differing only in their cooling methods and respective formation currents. The tank formation method has significantly lower formation levels than the other three formation levels. While this formation process is different than the other three formation levels, these low formation levels are nonetheless expected to result in lesser performance characteristics. The tank formation method also requires the least amount of overall formation time, because it has the lowest TC ratios when compared to the other three formation methods.

Figure 16 provides a visual comparison of the differences between the formation levels and times of the four different formation methods used at SBC.

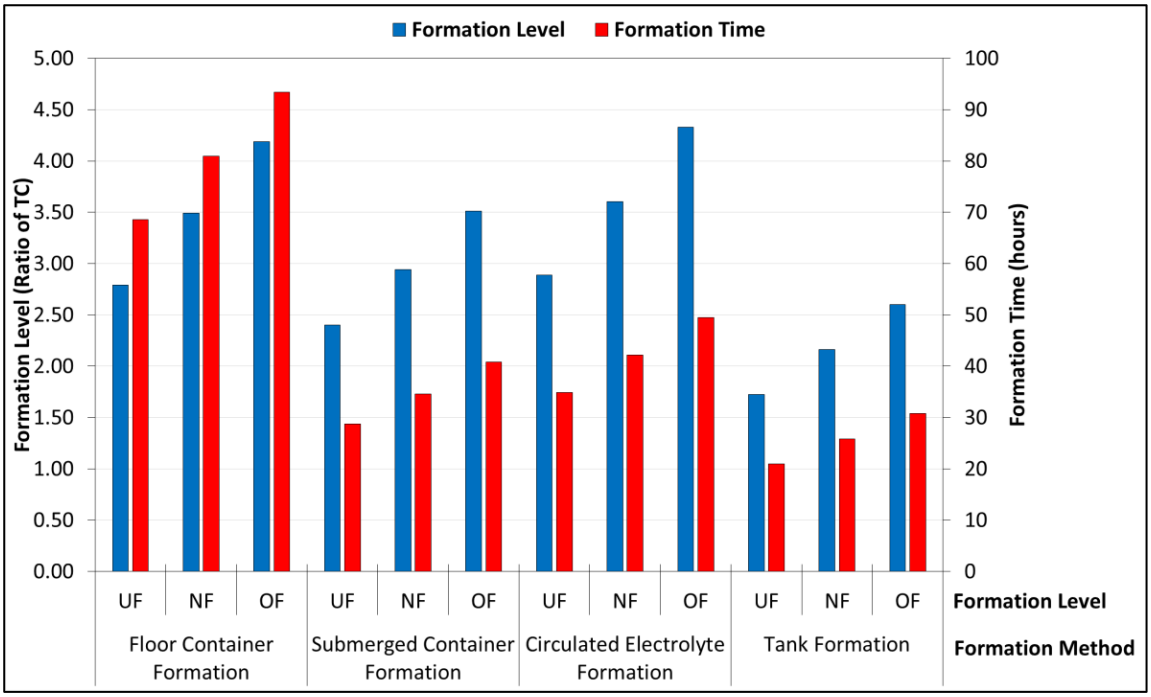

Figure 16 Comparison of Formation Levels and Times at SBC

As shown in Figure 16, significantly more formation time is required with respect to the floor container formation method due to its smaller formation currents. Specifically with respect to NF cells, an additional 92 % of formation time is required for the floor container formation method when compared to the circulated electrolyte formation method.

Based on this information, it was hypothesized that the cells formed using either the floor container formation method or the circulated electrolyte formation method would provide the best performance results when comparing the methods used at SBC. Similarly to the constant-current formation method used in phase 1 of this project, the floor container formation method uses relatively small currents, which in turn increases the efficiency of formation by limiting side reactions. On the other hand, the circulated electrolyte formation method makes use of a discharge current, which as stated above, increases the overall amount of formed $PbSO_4$ and can lead to an increase in capacity.

4.2.2. ELG15 Cell Cycling

As stated above, three cells with the same formation level were deep-cycled 10 times in a series configuration in order to represent the S-480 battery. The deep-cycling algorithm used to study the performance of the cells formed using the four aforementioned formation methods is shown in Table 13. This cycling algorithm has identical discharging and

charging rates as the one used in phase 1 of this research project (Table 6), albeit with small modifications to account for the three cells in series. The same discharging and charging rates allowed for a comparison basis between the cells formed at SBC (phase 2) and the cells formed at the RESL (phase 1), thus demonstrating the influence of the different formation methods on the ideal formation level as determined in phase 1 of this project. Individual cell voltage limits, instead of module voltage limits, were used in order to reduce the impact of a misaligned cell on the performance of the module, thus allowing for a more accurate representation of the ideal performance of the S-480 battery.

Table 13 Deep-Cycling Algorithm – Phase 2

Step #	Step Name	Description
1	Rest – begin	30 seconds rest for OCV measurements
2	Discharge	CC of -60.93 A (3.8 Hour Rate) until each cell reaches 1.75 V, with an 1.60 V per cell limit triggering the end of discharge
3	Rest – transition	Rest 30 minutes and until cell temperatures are < 28 °C
4	Charge phase 1	CC of 60.93 A until each cell reaches a voltage of 2.50 V
5	Charge phase 2	CV at the channel voltage attained in Step 4 until 7.50 A is reached (2.1 % of the 20 Hour Rate)
6	Charge phase 3	CC of 9.15 A for 4 hours (equivalent to 36.6 Ah)
7	Rest – end	Rest 30 minutes and until cell temperatures are < 28 °C

Again, while not shown in Table 13, important substeps were embedded in Steps 2 (discharge) and 4 (charge) of the cycling algorithm consisting of current pulses of 10 seconds to -100 A (discharge) and +100 A (charge), respectively. These pulses, which occurred at the 5 Ah charge/discharge capacity point, and at every multiple of 25 Ah charge/discharge capacity points thereafter, were used to determine the DC internal resistance (IR) of the cell while cycling.

4.2.3. Determining the Optimal Formation Method

The methodology used to determine the optimal formation method was similar to the one presented in determining the optimal formation level for phase 1 of this research project, as cells which are targeted for off-grid solar applications cannot be under-formed. Although in this case, a regression model was not applied to the different formation methods, as only three different respective formation levels were obtained. As such, all 12 different formation variations were compared simultaneously, where the optimal formation method was determined using the following methodology:

1) Deep-cycling performance analyses of the modules were independently completed for each formation method.
2) Using the 12 different formation variations, initial discharge capacity values and corresponding DFE values were then normalized over their respective maximum values.
3) Weighting ratios were then applied to the normalized initial discharge capacity and DFE values. The optimal formation method and level was then determined by evaluating the sum of these two values, with the highest resulting in the optimal formation method and level.

Chapter 5: Results and Discussions – Phase 1 (Laboratory Study)

The following will present and discuss the results for the first phase of this research project. The results of the constant-current and multi-step current formation algorithms are first presented independently (i.e., sections 5.1 and 5.2, respectively), followed by a comparison of these results in section 5.3.

As described in Chapter 4, the goal of studying two independent formation algorithms was to determine the optimal formation level for LABs in off-grid solar applications, and to study the impact of the formation algorithm on subsequent cell performance. A summary of the formation algorithms and levels studied for phase 1 of this research project is shown in Figure 17.

An uncertainty analysis, pertaining to the principal sources of measurement uncertainty for both phases of this research project, is presented in Appendix B.

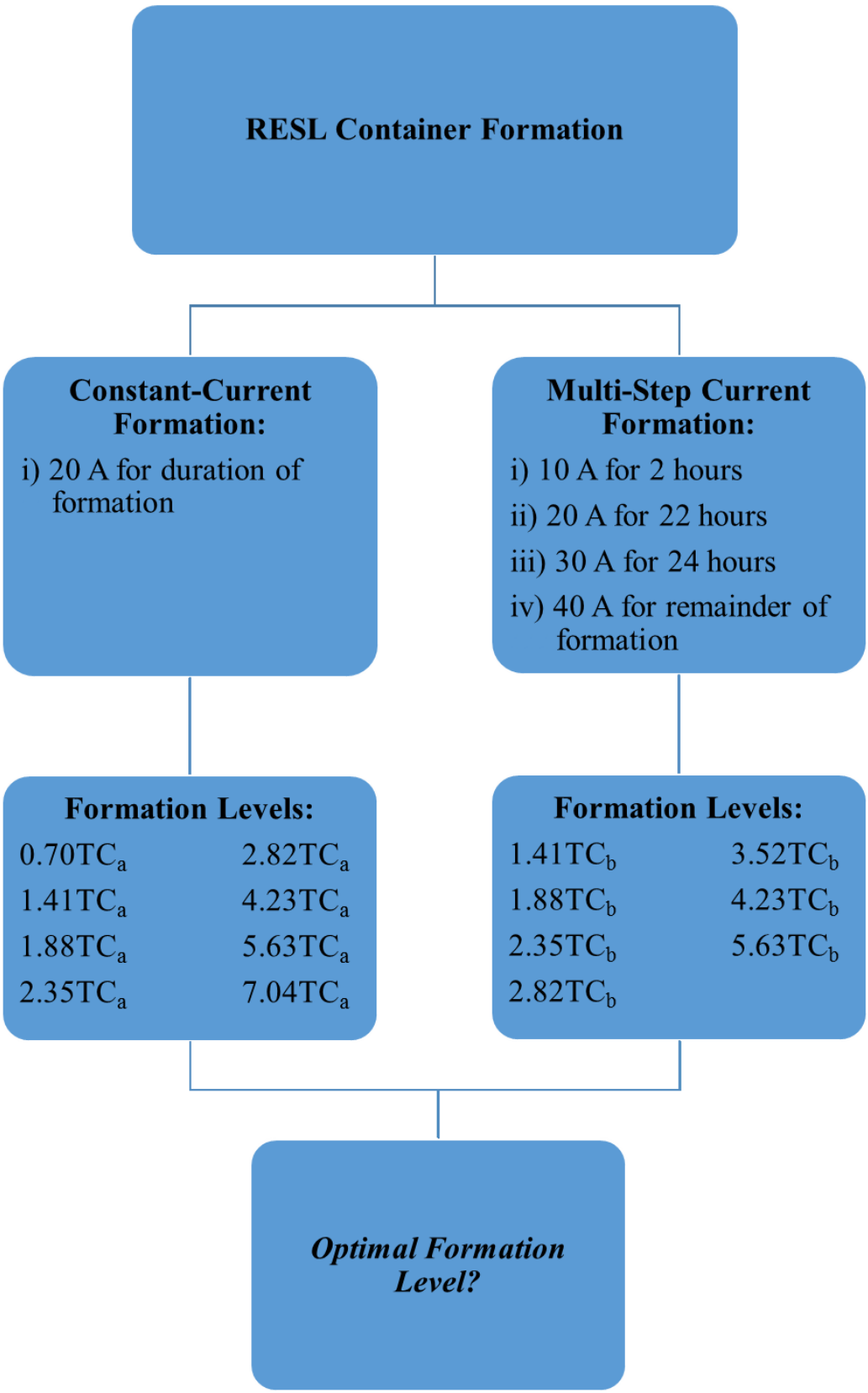

Figure 17 Phase 1 Summary – Formation Algorithms and Levels

5.1. Constant-Current Formation Algorithm Results

Cell Formation

Figure 18 shows the constant-current formation profile with respect to the current and temperature of the eight cells which were highlighted in Table 3 as a function of formation time. It should be noted that as the cells were formed in series, once a cell had reached its pre-determined formation level, the current was stopped and the cell was disconnected, before restarting the current to continue forming the remaining cells. While not shown in Figure 18, this step change in current was repeated eight times, explaining the corresponding drop in temperature for the disconnected cells.

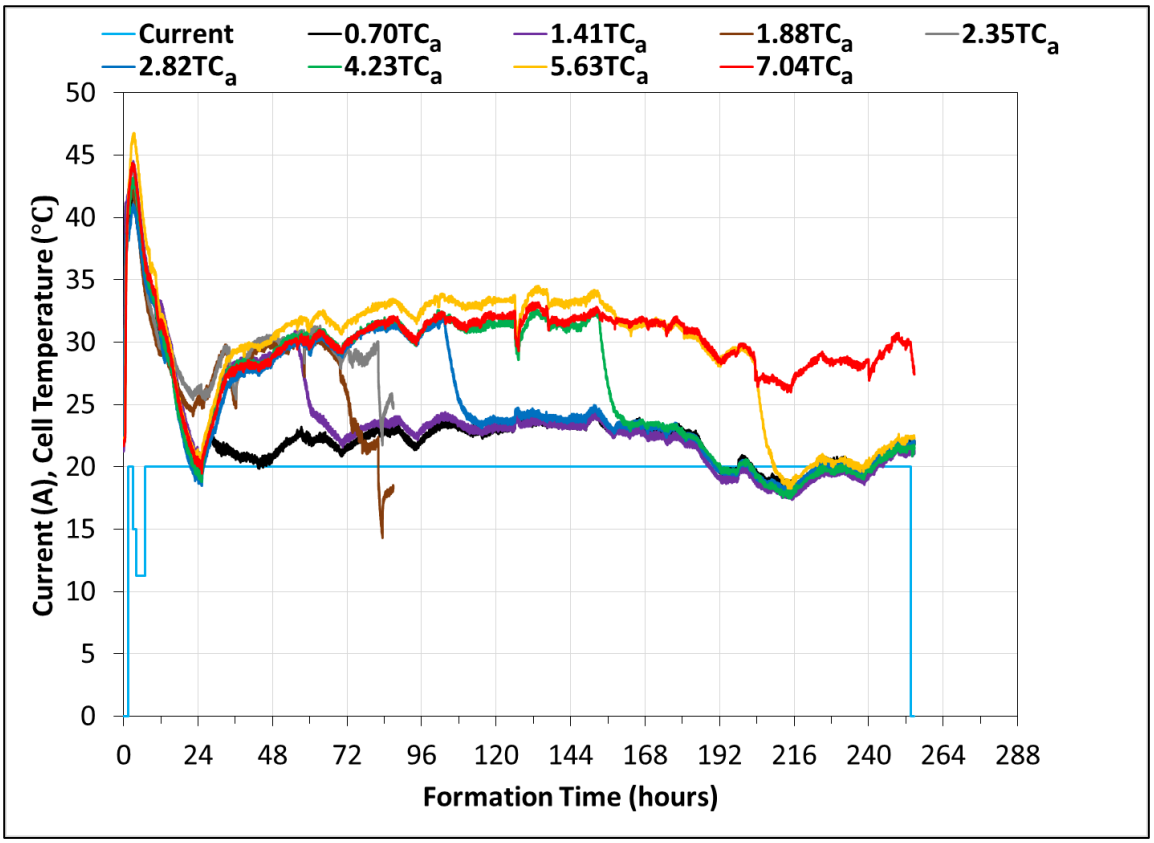

Figure 18 Formation Profile – Current and Temperature (Constant-Current Algorithm)

As shown in Figure 18, there was a substantial increase in temperature to nearly 50 °C for all eight cells during the soaking period. As stated in section 2.2.1, this was because the reactions between PbO, basic lead sulfates, and H_2SO_4 are exothermic [21]. It was because of this steep increase in temperature that the formation current was first decreased from 20

A to 15 A for 1 hour, and then from 15 A to 11.25 A for 3 hours. These reduction in current values were used to maintain the cell temperature below 50 °C. While the reactions between PbO, basic lead sulfates, and H_2SO_4 are exothermic, the formation of Pb and PbO_2 are endothermic [21], which explained the decrease in temperature around the 25 hour formation mark. One should note that the sudden drop in temperature for cells $1.88TC_a$ and $2.35TC_a$ shortly after the 80 hour mark was due to a drop in temperature in the laboratory. As only the final formation stage of cell $2.35TC_a$ was affected, this did not have any substantial effects on subsequent cycling. It is important to remember that the cell temperatures shown in Figure 18 represent the temperatures on the outside of the cells at mid-height. It was measured from a separate investigation that cell electrolyte temperatures are on average 4 °C higher than the outside cell temperatures during formation. Thus, it can be stated that as was the case for the outside cell temperatures, cell electrolyte temperatures also did not exceed 50 °C.

Figure 19 shows the individual cell SG values (solid lines) and voltages (dashed lines) as a function of formation time.

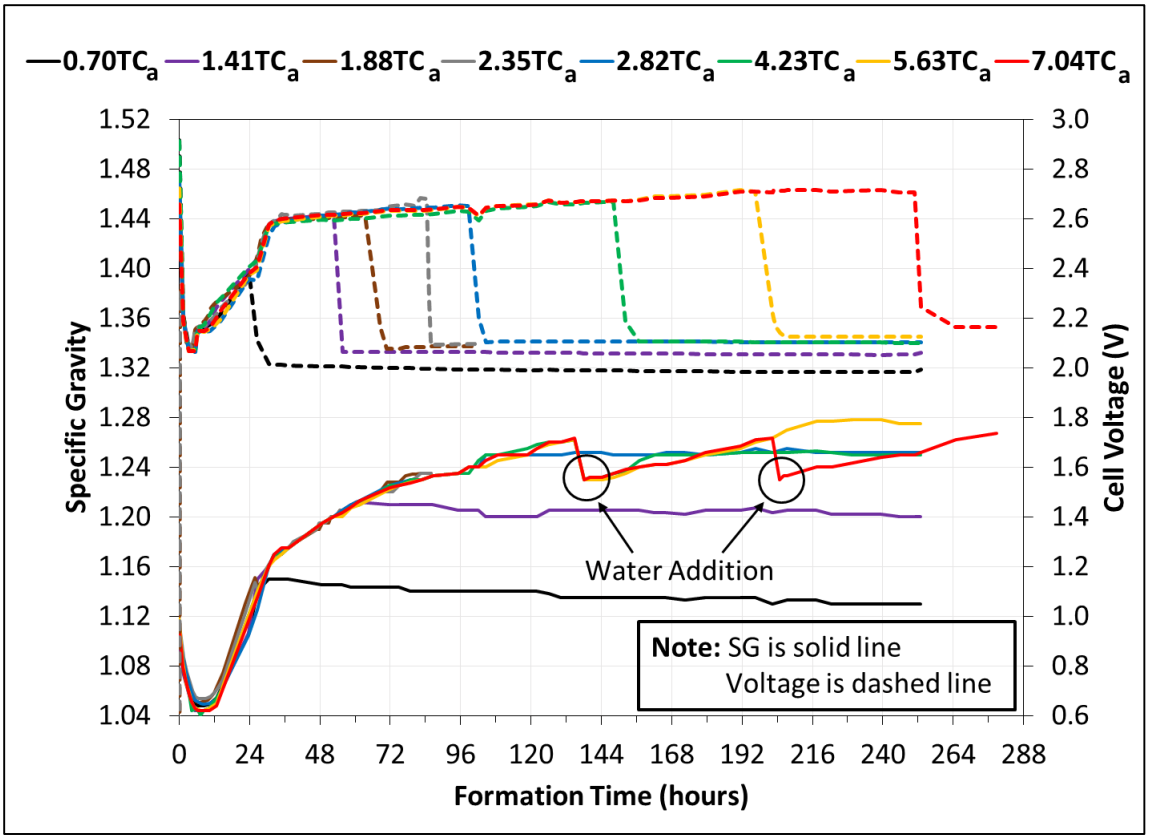

Figure 19 **Formation Profile – Cell SG Values and Voltages (Constant-Current Algorithm)**

As shown in Figure 19, there was an initial reduction in both cell SG and voltage, followed by an increase in both sets of values shortly after the 10 hour formation mark. These results are consistent with the first and second formation stages, respectively. As was stated in the literature review, the first stage is explained by the fact that the reactions of sulfation dominate, lowering the cell SGs and increasing the cell temperatures (see Figure 18), while the cell voltages are reduced due to the low equilibrium potential of the electrodes [21]. During the second stage of formation, H_2SO_4 is released from the plates, which causes an increase in SG, while the cell voltages increase due to the electrochemical reactions of oxidation and reduction of $PbSO_4$ [21]. The sudden drops in SG values for cells $4.23TC_a$, $5.63TC_a$, and $7.04TC_a$ at a formation time of 140 hours, and cell $7.04TC_a$ at a formation time of 205 hours, was because 500 mL of distilled water was added to each of these cells in order to ensure the plates remained submerged during formation.

Based on Figure 19, one can also determine when the individual cells were disconnected from the power-cycler, as made evident by the sudden drop in voltage values.

Furthermore, it is apparent that the final SG and OCV values have a clear positive correlation to total formation capacity.

Table 14 shows for each of the eight formed cells: the amount of distilled water that was added during formation, the amount of 1.265 electrolyte that was added at the end of formation for top-up (with corresponding percentage of initial electrolyte volume), and the final SG and OCV values. It should be noted that the SG and voltage values were taken before the first step of the cycling algorithm for each cell. Furthermore, the level of electrolyte for cell $5.63TC_a$ fell below the top of the plates near the end of its formation process. This is an important consideration, as this may have affected the deep-cycling performance of the cell, as will be discussed below.

Table 14 Formed Cell Status (Constant-Current Algorithm)

Cell Name	Water Added During Formation (mL)	Electrolyte Added After Formation (mL), (% of Initial Electrolyte Volume)	Final SG (Corrected to 20 °C)	Final OCV
$0.70TC_a$	0	310 (8.84 %)	1.134	2.00
$1.41TC_a$	0	430 (10.9 %)	1.207	2.06
$1.88TC_a$	0	560 (14.6 %)	1.232	2.09
$2.35TC_a$	0	550 (18.3 %)	1.246	2.10
$2.82TC_a$	0	710 (13.0 %)	1.253	2.11
$4.23TC_a$	500	540 (13.0 %)	1.249	2.10
$5.63TC_a$	500	900 (21.2 %)	1.267	2.12
$7.04TC_a$	1000	770 (20.2 %)	1.264	2.11

As shown in Table 14, there is a positive correlation between the formation level, and the amount of water added during formation and/or the amount of electrolyte needed for top-up. Thus based on this information, it was hypothesized that some of the additional formation capacity for cells $4.23TC_a$, $5.63TC_a$, and $7.04TC_a$ was simply used for the electrolysis of water.

Figure 20 shows a clear correlation between the final SG and OCV values of the eight cells as a function of their respective formation input in Ah and ratio of the theoretical capacity. This is to be expected, as there is a positive correlation between the formation level, the amount of H_2SO_4 released from the plates, and the electromotive potential of the positive and negative electrodes.

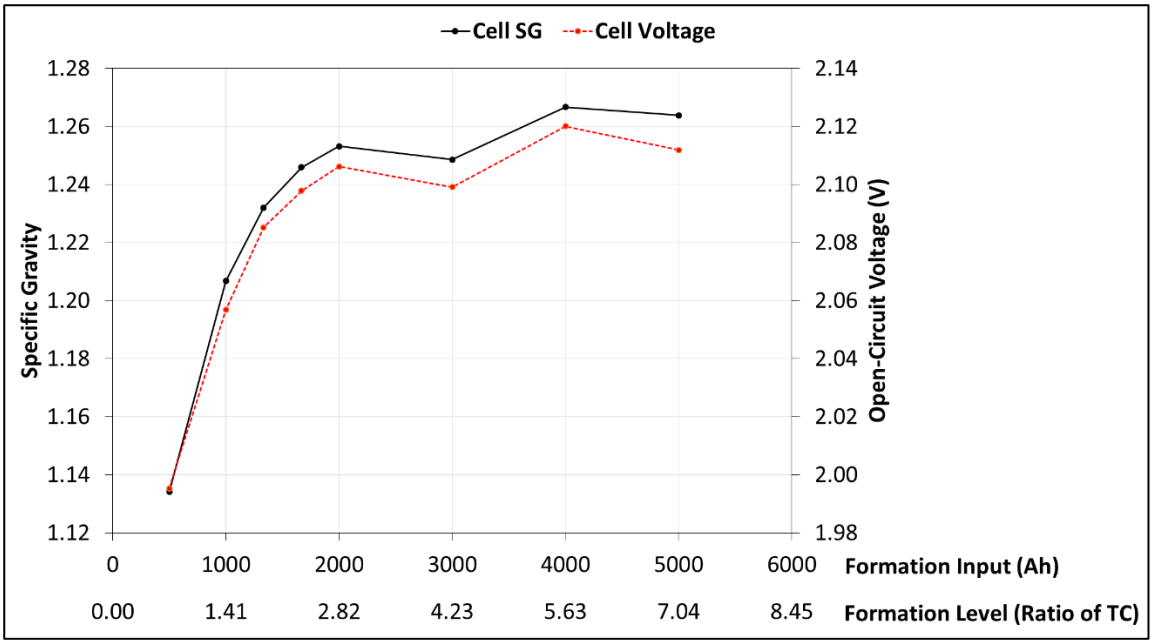

Figure 20 Final SG and OCV Values of Formed Cells (Constant-Current Algorithm)

As shown in Figure 20, cell 4.23TC_a, although having received additional formation input, has a lower final cell SG and OCV values than cell 2.82TC_a. This is because distilled water was added to this cell late in its formation process, resulting in lower cell SG and OCV values.

Deep-Cycling Characteristics

As outlined in section 4.1.3, the first step in determining the optimal formation level was comprised of completing a deep-cycling performance analysis of the cells.

As part of the performance analysis, each cell was cycled 10 times using the deep-cycling algorithm presented in Table 6. As an example, Figure 21 shows the voltage, current, temperatures, and Ah depletion as a function of cycle time for the 10^{th} cycle of cell 2.82TC_a. One should note that the discharging process of the cell results in the negative count of Ah depletion, while the charging process of the cell results in the positive count of Ah depletion.

(a)

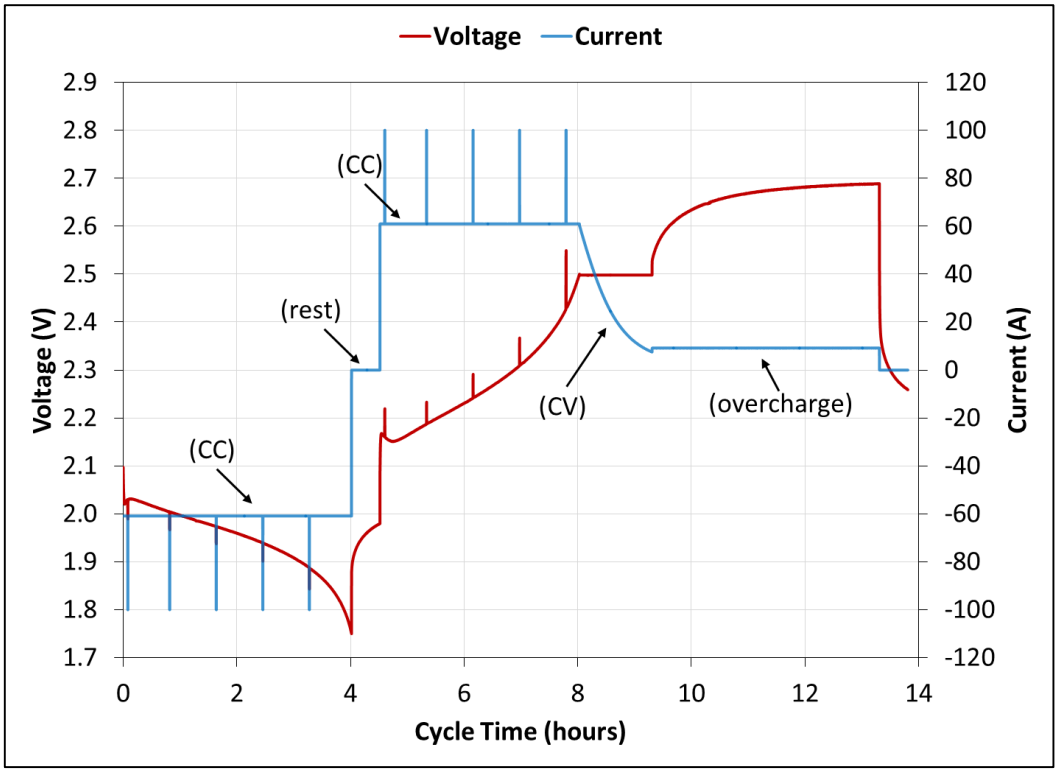

(b)

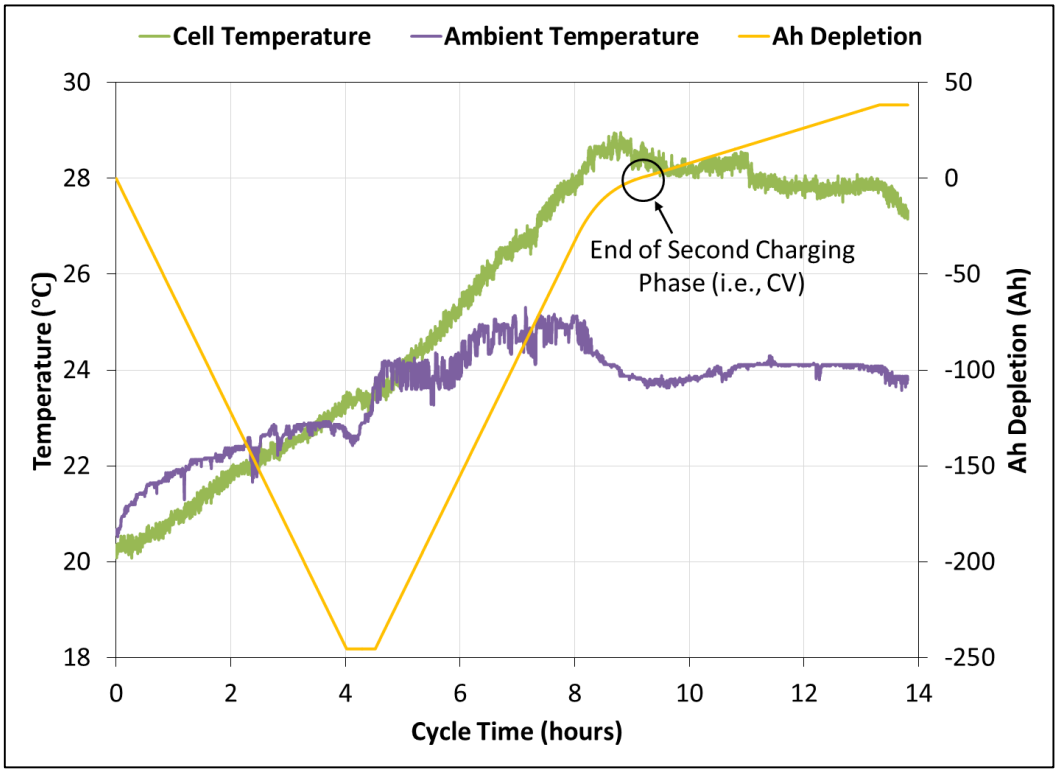

Figure 21 **Cycle 10 Profile of Cell 2.82TC$_a$ as a Function of Cycle Time (Constant-Current Algorithm) – (a) Voltage and Current, (b) Temperature, Ah Depletion**

Figure 21 shows that as planned, the cell initially underwent a –60.93 A discharge for approximatively 4 hours, while the cell voltage decreased to 1.75 V. During the 30 minute rest period, the OCV relaxed upwards to 1.98 V. The charging phase then commenced, with an initial charging current of 60.93 A while the voltage increased to 2.50 V. The current was then reduced as this voltage was maintained, until the cutoff current of 7.50 A was reached as defined in the cycling schedule. A CC of 9.15 A was then maintained for 4 hours, during which the voltage rose to 2.69 V. Figure 21 also highlights the current pulses to -100 A during discharge, and to +100 A during charge. The ambient temperature increased by approximatively 5 °C for the first eight hours of cycling (i.e., 20 °C to 25 °C), and then reached a steady state value of 24°C for the remainder of the cycle. With respect to the cell, its temperature increased by approximatively 9 °C during the first nine hours of cycling, a result of energy losses due to the ohmic resistance of the cell.

It should be noted that the first two charging phases (see Table 6) accounted for 100 % of the depleted Ah, confirming the effectiveness of the chosen cycling algorithm. The characteristic of Ah depletion is further explored in Figure 22, where the voltage and current are plotted as a function of Ah depletion for the 10^{th} cycle of cell $2.82TC_a$. With respect to the CV portion of the charging process, it is interesting to note that the current has an exponential decay relationship while plotted against time (see Figure 21), and a linear relationship while plotted against Ah depletion (see Figure 22). The final Ah depletion value for this cell was determined to be 39 Ah (i.e., 284 Ah charge – 245 Ah discharge = 39 Ah), corresponding to an overcharge value of 15.9 % (i.e., [[284 Ah / 245 Ah] – 1 × 100 = 15.9 %]).

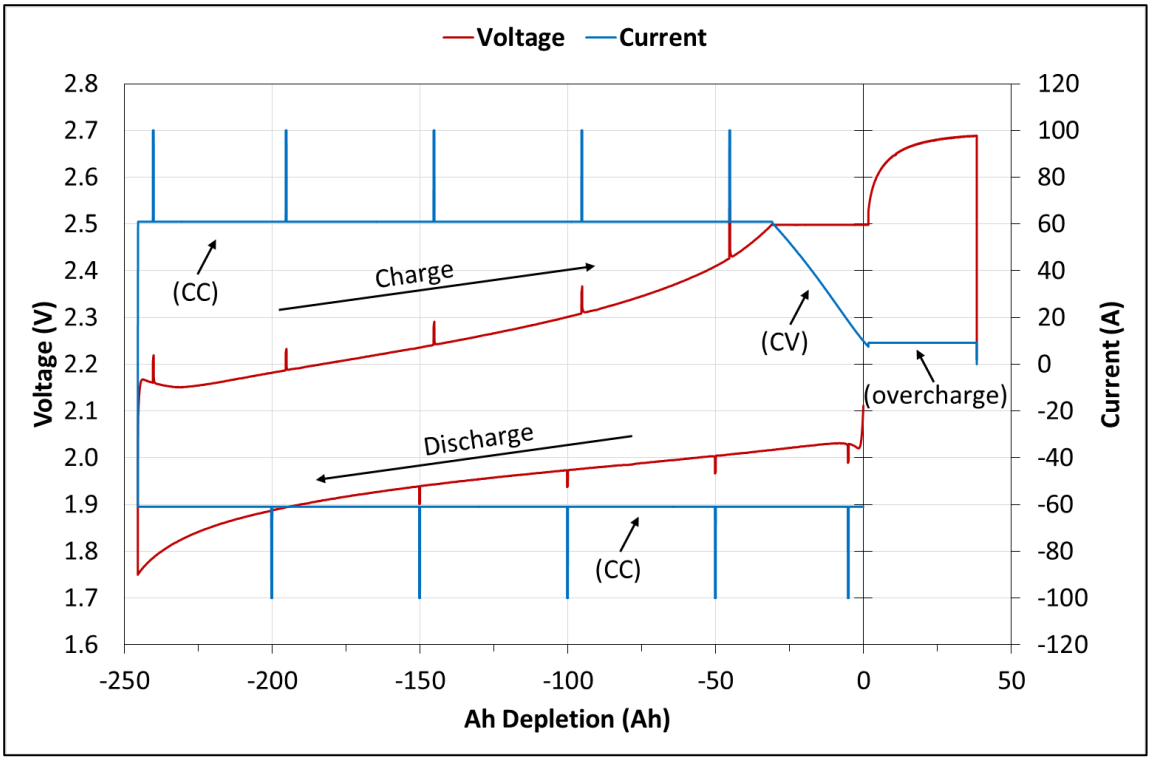

Figure 22 **Cycle 10 Ah Depletion Profile of Cell 2.82TC$_a$ (Constant-Current Algorithm)**

Discharge Capacity Characteristics

Figure 23 shows the measured discharge capacities of the cells for all 10 cycles. The discharge capacities were corrected based on a reference temperature of 25 °C using equation (7), as defined by the International Electrotechnical Commission [48].

$$C_{25\,°C} = C/[1 + \lambda(\theta - 25\,°C)] \quad (7)$$

where $C_{25\,°C}$ is the corrected capacity at 25 °C, C is the measured discharge capacity, λ is a factor based on the discharge rate, which in this case is equal to 0.006 due to the usage of a discharge current slower than the 3 hour rate, and θ is the cell temperature immediately prior to discharge.

As an example, the average coulombic efficiency of cell 2.82TC$_a$ was calculated to be 86.8 % over a span of 10 cycles. This value is in agreement with the other seven cells. The coulombic efficiency of a cell is defined as the ratio of its Ah discharge capacity over its Ah charge capacity. The charge capacity is always greater than the discharge capacity for a proper cycling algorithm in order to account for side reactions and cell inefficiencies. Thus, coulombic efficiency values are always below 100 %.

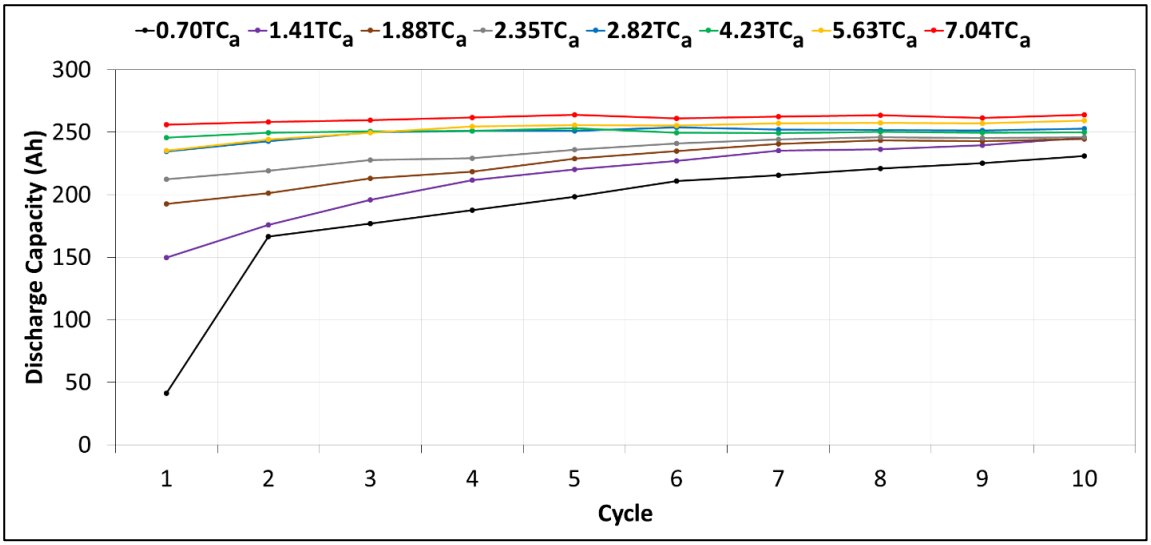

Figure 23 Cell Discharge Capacities (Constant-Current Algorithm)

As shown in Figure 23, cells formed using capacity input levels ≤ 2.35TC show noticeable capacity reductions when compared to the other cells, indicating that they were not fully formed. Specifically, the discharge capacities of cells $0.70TC_a$ and $1.41TC_a$ increased significantly with each cycle, thus confirming that these two cells were still forming. Similarly for the remaining cells, with the exception of cell $7.04TC_a$ which is fully formed, a slight increase in respective discharge capacities is also noticed, with all eight cells settling at a final capacity of approximatively 250 Ah, 8.2 % higher than the rated capacity of the cell. Furthermore, one should note that cells $2.82TC_a$ and $5.63TC_a$ have the same initial discharge capacity values. As cell $5.63TC_a$ has an additional 100 % of formation capacity input when compared to cell $2.82TC_a$, this cell could thus be considered as an outlier and could be explained by the fact that a portion of the plates were exposed during the formation process.

Finally, it should be noted that while cells $4.23TC_a$, $5.63TC_a$, and $7.04TC_a$ offer slightly higher discharge capacities than cell $2.82TC_a$ over a span of ten cycles, the difference is relatively insignificant when compared to the additional formation capacity that is required. These three cells are compared with cell $2.82TC_a$ in Table 15.

Table 15 Comparing Cells 2.82TC$_a$, 4.23TC$_a$, 5.63TC$_a$, and 7.04TC$_a$

Cell Comparison	Cycle	Discharge Capacity Difference (Ah)	% of Rated Capacity	Additional Formation Capacity Required (%)
4.23TC$_a$ vs. 2.82TC$_a$	1	11.3	4.9 %	50 %
	2	6.7	2.9 %	
	4	0.0	0.0 %	
	Avg. (1-10)	0.8	0.3 %	
5.63TC$_a$ vs. 2.82TC$_a$	1	0.8	0.3 %	100 %
	2	1.5	0.7 %	
	4	3.5	1.5 %	
	Avg. (1-10)	3.5	1.5 %	
7.04TC$_a$ vs. 2.82TC$_a$	1	21.6	9.3 %	150 %
	2	15.3	6.6 %	
	4	10.6	4.6 %	
	Avg. (1-10)	12.1	5.2 %	

As shown in Table 15, while a techno-economic analysis has not been completed in this regard due to it being outside of the scope of this research project, it is clear that the gain in discharge capacity for cells 4.23TC$_a$, 5.63TC$_a$, and 7.04TC$_a$ is not worth the additional formation capacity when compared to cell 2.82TC$_a$. For instance, over an average of 10 cycles, cell 4.23TC$_a$ offers an additional 0.8 Ah of discharge capacity (i.e., 0.3 % of the rated capacity) when compared to cell 2.82TC$_a$ but required an additional 1000 Ah of formation capacity (equivalent to 50 % more). Thus, it can be stated that of the cells formed using the constant-current formation algorithm, the formation level of 2.82 times the theoretical capacity of the cell is the highest practical ratio, or formation threshold, as the majority of the additional formation capacity for cells 4.23TC$_a$, 5.63TC$_a$, and 7.04TC$_a$ is simply used for the electrolysis of water. This is confirmed by the fact that the addition of water was required for the cells formed with capacity input levels ≥ 4.23TC, as was shown in Table 14.

Specific Gravity Characteristics

Figure 24 shows the electrolyte SG values of the eight cells which were measured before the start of each deep-cycle.

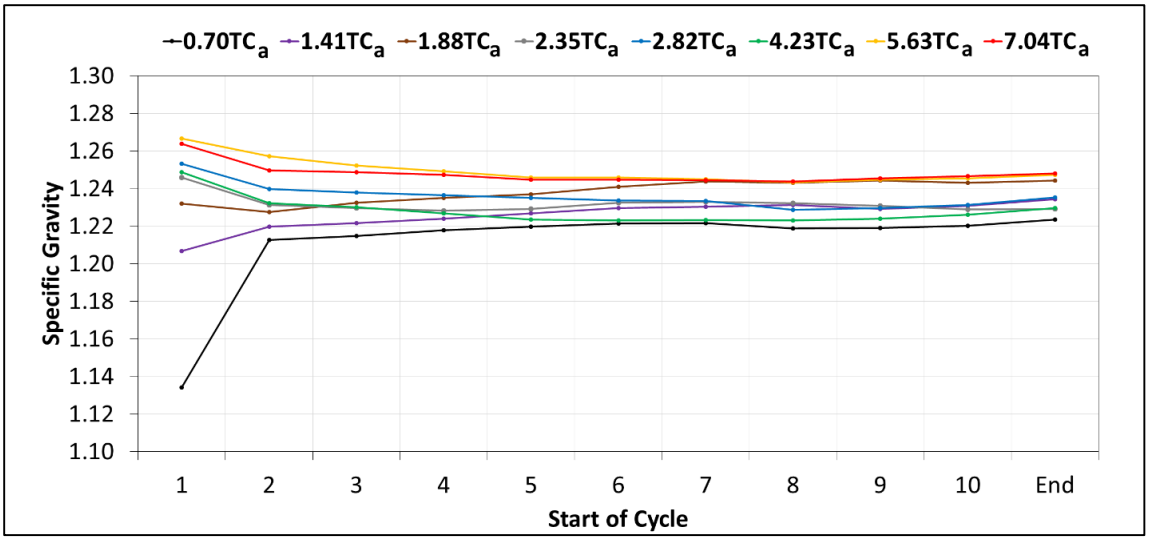

Figure 24 Cell Electrolyte SG Values (Constant-Current Algorithm)

As shown in Figure 24, cells $0.70TC_a$ and $1.41TC_a$ are the only two cells where an increase in electrolyte SG is observed over a span of 10 cycles, whereas the SG concentration of the other cells (with the exception of cell $1.88TC_a$) decrease slightly over the span of their first 6 cycles, where steady-state values are then obtained. This is an interesting characteristic, as it coincides with the discharge capacity results presented in Figure 23, where cells $0.70TC_a$ and $1.41TC_a$ were shown to be relatively under-formed with respect to the other six cells. Thus, it can be confirmed that as cells continue their formation process, additional H_2SO_4 is released from the plates, which causes an increase in SG.

The initial reduction in electrolyte SG for the other six cells following the first cycle is a result of non-mixed electrolyte in these respective cells. Specifically, the addition of 1.265 electrolyte at the end of formation for top-up (see Table 14) resulted in a misrepresentation of the actual electrolyte SG values of these cells. Thus, as a result of the participation of the electrolyte in the cycling operation of a LAB (i.e., resulting in the mixing of electrolyte), the electrolyte concentration for these cells decreased after their first cycle.

The electrolyte SG characteristics of cell $1.88TC_a$ are explained by these two aforementioned factors. Specifically, the high initial reading of electrolyte concentration was influenced by the addition of 1.265 electrolyte, and the increase in SG between cycles 2 and 7 was due to the cell continuing its formation process.

It is interesting to note that although cell 5.63TC_a was shown to be an outlier in Figure 23 due to its relatively poor performance, this does not translate to low electrolyte concentration values. Thus in other words, relatively high SG values do not guarantee optimal battery performance. This is further demonstrated in Figure 25, where cell discharge capacity and SG values after the completion of 10 cycles are compared to cell 7.04TC_a (i.e., a fully formed cell). These values are compared on a percent difference basis.

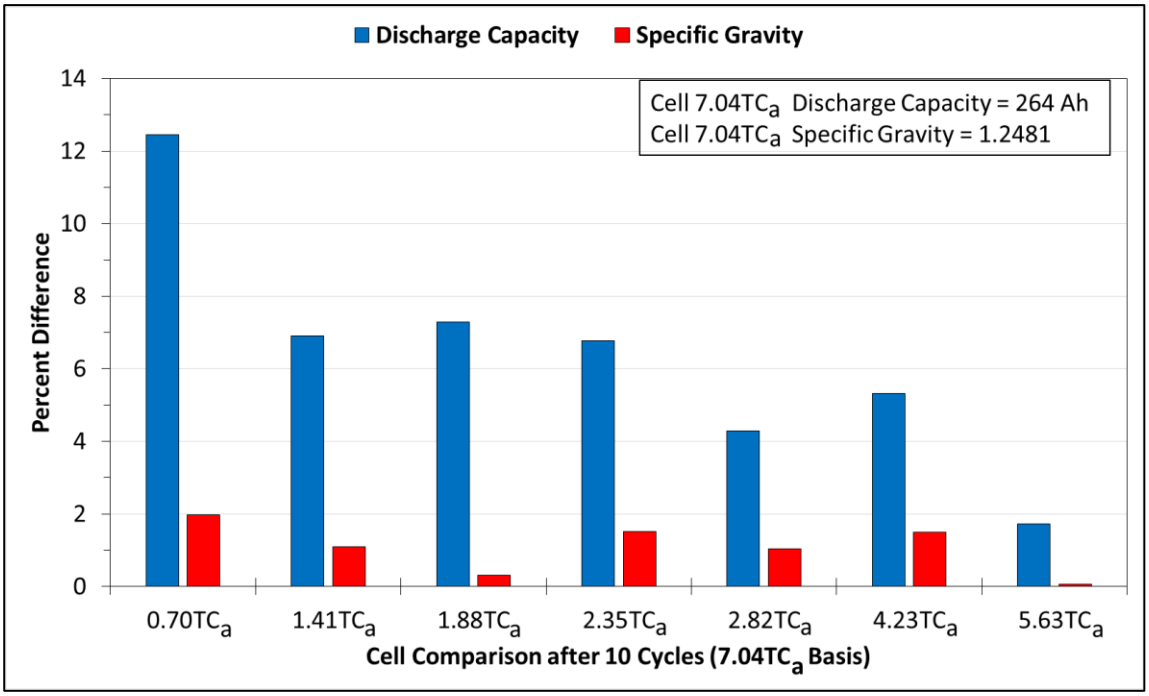

Figure 25 Discharge Capacity and Specific Gravity Comparison after 10 Cycles, 7.04TC_a Cell Basis

As shown in Figure 25, there is no relationship between the percent difference values of SG and discharge capacity for these cells when compared to cell 7.04TC_a. For instance, after the completion of 10 cycles, cell 0.70TC_a has a discharge capacity difference of 12 % (i.e., large difference) when compared to cell 7.04TC_a, and a specific gravity difference of 2 % (i.e., small difference) when compared to cell 7.04TC_a. Thus, electrolyte SG values are not a reliable indicator of available discharge capacity for a LAB.

Figure 25 also supports the argument that cells targeted for the off-grid solar market cannot be under-formed, as even after undergoing 10 deep-cycles making use of a 16 % overcharge, cells formed using capacity input levels $\leq$ 2.35TC still show discharge capacity differences exceeding 5 % when compared to cell 7.04TC_a. Compounding this effect to the

fact that strategies presently used in off-grid solar applications have difficulties fully charging the batteries, cells which have been under-formed for this market would likely never attain a fully formed state.

Figure 26 shows the electrolyte SG profile for the 10th deep-cycle of cells 0.70TC_a, 1.41TC_a, 2.82TC_a, 4.23TC_a, 5.63TC_a, and 7.04TC_a. This profile was obtained by taking SG measurements every half hour for the duration of the 10th deep-cycle. Unfortunately, SG values were not taken for cells 1.88TC_a and 2.35TC_a during their 10th cycle. While these six cells were cycled individually, the six SG profiles are superimposed as a function of cycle time due to their similar characteristics.

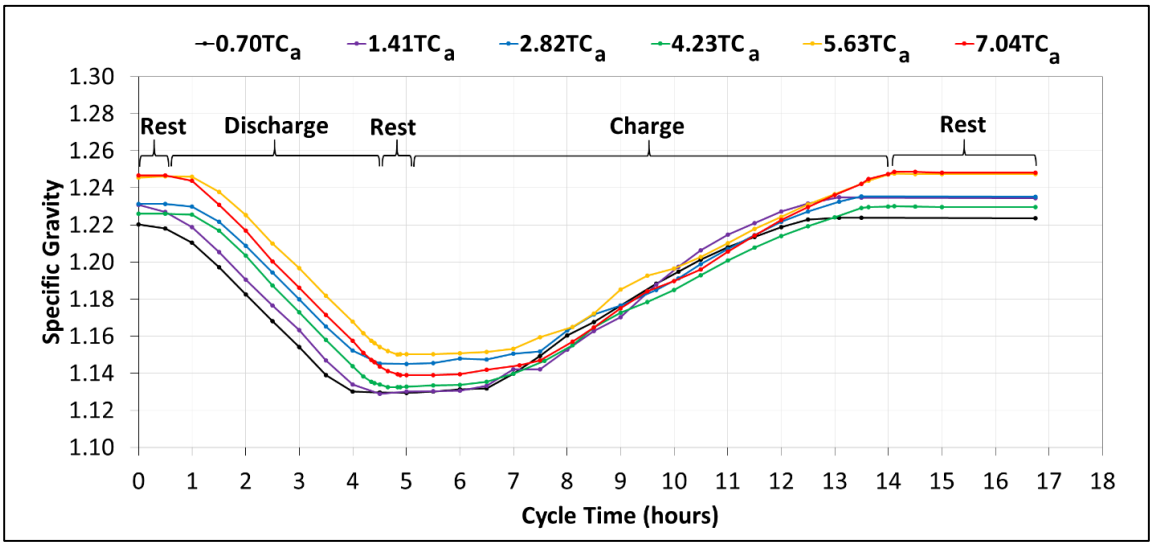

Figure 26 Electrolyte SG Profile – Cycle 10 (Constant-Current Algorithm)

As shown in Figure 26, all six cells regardless of initial formation capacity have similar SG profiles, albeit the cells with lower formation levels have lower overall electrolyte SG values than the cells with higher formation levels. Cell electrolyte SG decreases as expected during the discharging process of the cycling algorithm (see Table 6 and Figure 21). Furthermore, there was only a 30 minute rest period between the discharge phase and the subsequent charging phase for all six cells, thus it is shown that electrolyte SG values remained relatively constant during the first phase of the charging process, and only started increasing at the ~7 hour mark of the total cycling time, corresponding to the CV phase of the charging process (see Table 6 – Step 5). However, it is believed that the SG values did increase at the start of the charging process, yet as the electrolyte samples were limited to being taken from the top of the cell, the increase in electrolyte SG was not noticeable until

the gassing process became more pronounced (i.e., CV phase of the charging process). Finally, the total change in electrolyte SG values for all six cells was approximatively 0.10 (e.g., cell $0.70TC_a$ has a maximum electrolyte SG value of 1.22 and a minimum value of 1.13, for a delta of 0.09, whereas cell $7.04TC_a$ has a maximum electrolyte SG value of 1.25 and a minimum value of 1.14, for a delta of 0.11). These values are in agreement with the range of typical electrolyte SG values for a LAB during deep-cycling operation as was presented in the literature review.

Internal Resistance Characteristics

Figure 27 shows the IR values for cycles 1, 2, 4, 6, and 10 of discharging and charging pulses using 10 seconds voltage intervals as a function of cycle number and discharge/charge Ah. As the charging current pulses only occurred during the first phase of the charging process (CC phase only, see Table 6 – Step 4), IR values obtained at a charging capacity of 200 Ah correspond to approximatively 73 % of the total Ah input received by these cells during their respective charging processes. Furthermore, these charging IR values are dependent on the status of the previous discharge. Specifically, as each cell had previously attained a different discharge capacity value, the Ah depletion values corresponding to the Ah Charge values listed in Figure 27 are different for each cell. Nonetheless, one should note that from the perspective of a fully discharged state, the cells are all on the same basis.

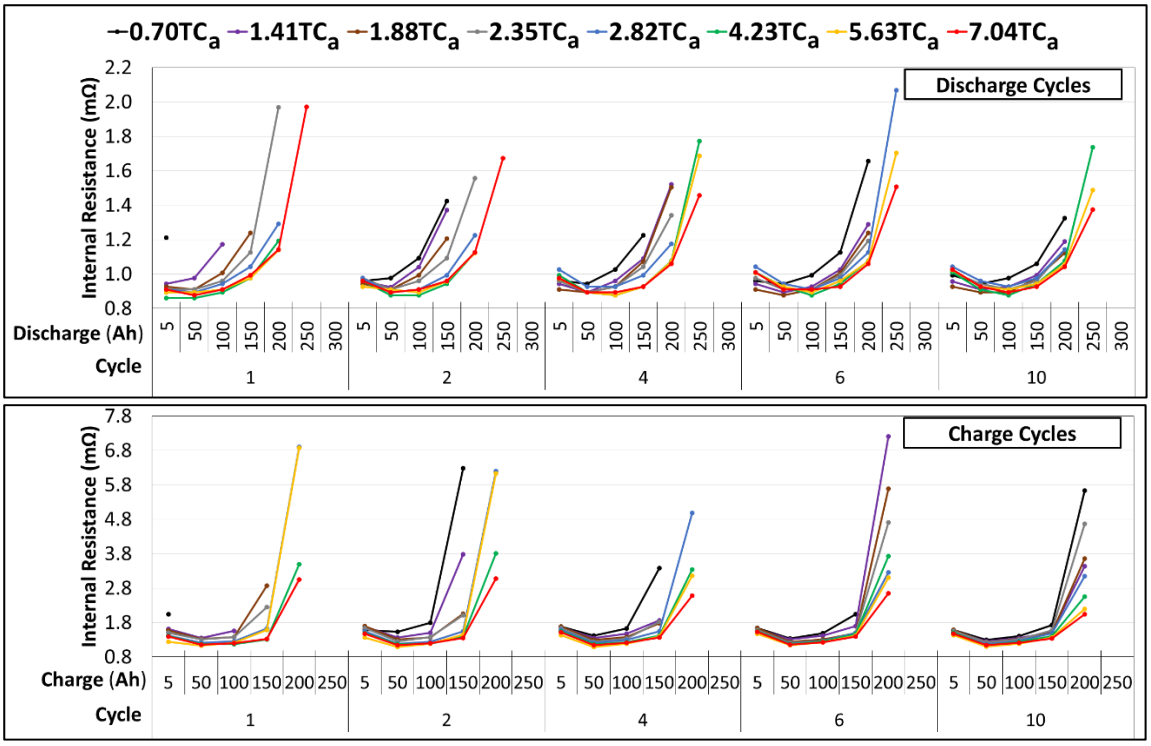

Figure 27 Discharge and Charge IR with 10 Second Voltage Intervals (Cycles 1, 2, 4, 6, and 10) (Constant-Current Algorithm)

As shown in Figure 27, it is clear that the higher the formation level, the lower the IR when respective discharging capacities are compared. The cell IR values of the different formation levels start converging after 4 cycles, which coincides with the convergence of total capacities as shown in Figure 23. In other words, as the cells continue their formation process due to their respective deep-cycling operation, increasing amounts of PbO (~ 10^{12} Ω cm [49]) and $PbSO_4$ (~ 0.3 × 10^{10} Ω cm [50]) are formed into PbO_2 (~ 10^{-5} to 1.2 × 10^{-6} Ω cm [49]) for the positive plates, and Pb (~ 20.6 × 10^{-6} Ω cm [51]) for the negative plates, which both have ohmic resistances lower than PbO and $PbSO_4$, thus reducing the overall IR of the respective cells.

The shape of the discharging IR curves shown in Figure 27 can be explained as follows. The first two values of IR, at 5 and 50 Ah, are higher than the IR values measured at a discharge capacity of 100 Ah, with the exceptions of the cells which have not yet finished forming. This is due to the oxygen layer which forms on the positive plate of the cell during the overcharge of the charging phase. It has been stated by Shukla *et al.* [52] that this oxygen layer acts as a barrier during the discharge of the cell, which limits its performance.

The cells which are achieving rated capacity will at this point experience their lowest measured IR values at a discharge capacity of 100 Ah. The IR for these cells then increases significantly until the end of discharge due to a reduction in available active material due to the conversion of Pb and PbO_2 to $PbSO_4$, and a reduction in electrolyte SG (see Figure 28 for an example).

The IR during discharge is a direct representation of the available power in the cell. In other words, the higher the IR, the lower the available power from the cells, which in turns adversely affects its energy efficiency and potential to supply larger loads.

The IR charging trend is relatively similar to the discharging trend discussed above albeit with higher magnitudes of IR values (e.g., 0.94 mΩ discharging vs. 1.3 mΩ charging, equivalent to a discharging/charging ratio of 72 %, for cycle 1 of cell $2.82TC_a$ at the 100 Ah value). Specifically, the higher formation levels correspond to lower values of IR when respective charging capacities are compared, and cell IR values once again start converging during charge after 4 cycles. Furthermore, the higher the IR during the CC bulk charge (see Table 6 – Step 4), the higher the cell voltage. This results in a premature shift to the absorption phase of the charging algorithm (see Table 6 – Step 5), which increases total charging time. As such, for cells that are under-formed, the voltage setpoint indicating the end of the bulk charge should be increased, as this would overcome said IR limitations and allow for faster formation completion of these cells.

The shape of the charging IR curves shown in Figure 27 can be explained as follows. The first IR value (i.e., 5 Ah) is shown to be higher than the next two IR values for all eight cells, which is due to the presence of $PbSO_4$ on the positive and negative plates. The measured IR values then reach their lowest point during charging at a capacity of 50 Ah due to the dissolution of the unstable $PbSO_4$ crystal structure. IR values are then increasing until charge completion due to the increasingly limited reaction rate as the bulk of the electrode materials become fully converted to their charged state. This corresponds to a significance increase in the charge transfer resistance (see R_{ct} in Figure 10), which will neglect the decrease in ohmic resistance (see R_o in Figure 10) associated with the conversion of PbO and $PbSO_4$, to PbO_2 and Pb. The progressive appearance of H_2 bubbles which block the active material, will also contribute to an increase in IR towards the end of charge [53].

Comparing SG, IR, and Temperature Characteristics

An example of the influence of electrolyte SG and cell temperature on IR as a function of Ah depletion is shown in Figure 28 for cycle 10 of cell 2.82TC$_a$. It should be noted that the cell temperature has been divided by 10 for presentation purposes.

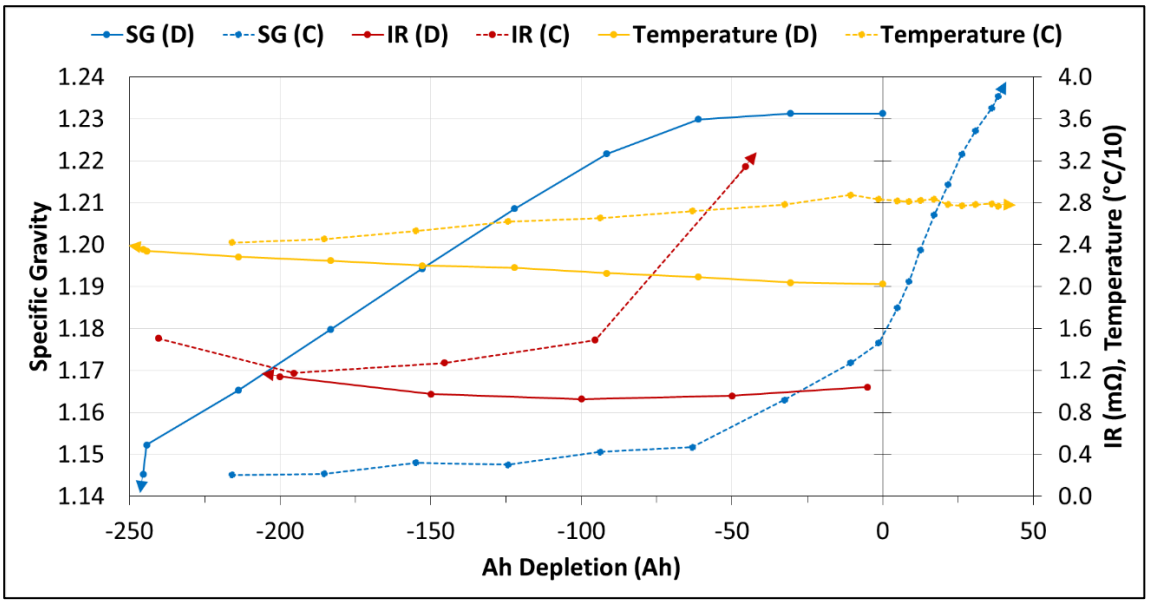

Figure 28 SG, IR, and Temperature as a Function of Ah Depletion where D = Discharge and C = Charge (Cell 2.82TC$_a$, Cycle 10) (Constant-Current Algorithm)

As shown in Figure 28, the SG of the cell decreases linearly during discharge, yet does not start increasing significantly during charge until an Ah depletion value of -50 Ah, corresponding to the CV phase of the charging process (see Table 6 – Step 5). However, it is important to remember that as the electrolyte samples were limited to being taken from the top of the cell, the increase in electrolyte SG was not noticeable until the gassing process became more pronounced (i.e., CV phase of the charging process). Thus, it difficult to determine the influence of electrolyte SG on the rise in IR which occurs between amp-hour depletion values of -100 Ah and -50 Ah. Additionally, one should note that the cell temperature increases by about 4 °C during discharge, and by a further 4 °C during charge.

Optimal Formation Level

As the next step in the methodology used to determine the optimal formation level (see section 4.1.3), a regression model was applied to the initial discharge capacity outputs of the cells as a function of their formation level, as shown in Figure 29. Also shown in the

figure are the corresponding values of DFE (i.e., initial discharge capacity output of a cell divided by its formation capacity) for the different cells.

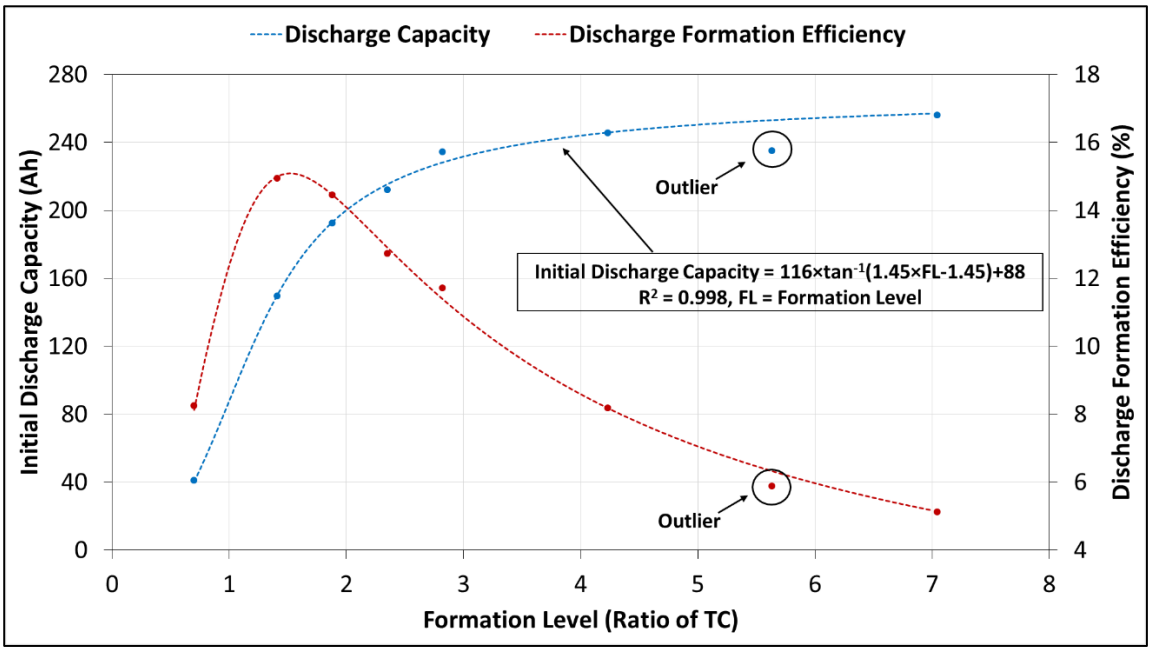

Figure 29 Initial Discharge Capacity and Discharge Formation Efficiency as a Function of Formation Level (Constant-Current Algorithm)

As shown in Figure 29, the model best representing the initial discharge capacity data has an inverse tangent relationship with an R^2 of 0.998. It is important to note that initial discharge capacity results are asymptotic, with maximum values at approximatively 260 Ah. In other words, the capacity gains by increasing the formation input value past 7.00TC would be insignificant as the majority of the additional formation capacity would simply be used for the electrolysis of water. Using this regression model, normalized capacity and DFE values were calculated for different ratios of theoretical formation input values ranging from 0.70TC to 7.00TC, using increments of 0.05TC.

Weighting ratios, in 5 % increments, were then applied to the normalized initial discharge capacity values and normalized DFE values. Figure 30 shows the resulting optimal formation levels, corresponding to the highest sum of weighted normalized values, as a function of the weight attributed to the normalized initial discharge capacity.

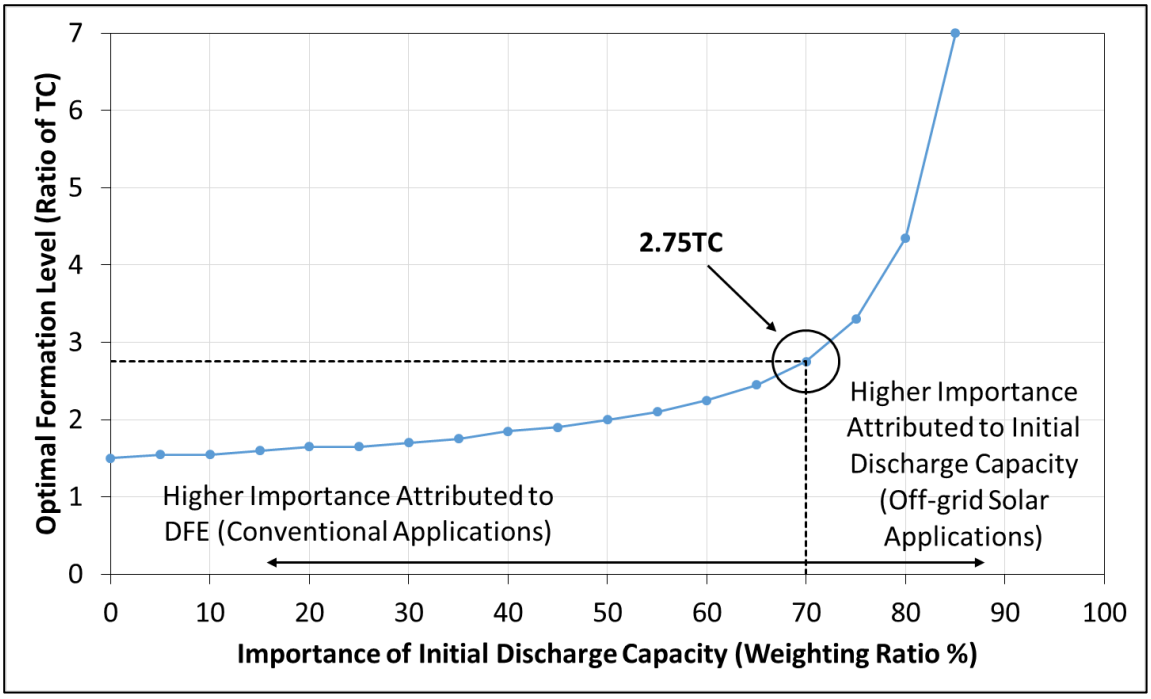

Figure 30 Optimal Formation Levels for the Constant-Current Formation Algorithm as a Function of Weighting Ratio

As shown in Figure 30, the optimal formation level increases as more importance is attributed to the initial discharge capacity. A maximum formation level of 7.00TC (i.e., highest formation level obtained using the constant-current formation algorithm) is obtained when a weight of 85 % is attributed to the initial discharge capacity.

The level of importance (or weight) attributed to initial discharge capacity and DFE values will vary for different LAB manufacturers due to different objectives in operational strategy. Again, if a LAB manufacturer were to attribute more importance to the initial discharge capacity of the cell than to its DFE, it would select a weighting ratio higher than 50 % in favor of the former. For the purpose of this research project focused on off-grid solar applications, a recommended weighting of 70 % / 30 % was attributed to the initial discharge capacity and DFE values, respectively, as this ensured more importance was attributed to the performance of the cell, a necessary requirement for off-grid solar applications. Using this weighting ratio, the optimal formation input level for the constant-current formation method was determined to be 2.75TC (i.e., 1953 Ah). Based on the regression model presented in Figure 29, a cell formed using a formation input of 2.75TC is estimated to obtain an initial discharge capacity output of 227 Ah. This value is in

agreement with the rated capacity of the cell (i.e., < 2 % difference), thus ensuring client satisfaction, while providing a DFE of 12 % for the LAB manufacturer. This DFE value is above the calculated average of 9.4 % for formation input values ranging from 0.70TC to 7.00TC.

5.2. Multi-Step Current Formation Algorithm Results

Cell Formation

Figure 31 shows the multi-step current formation profile with respect to the current and temperature of the seven cells which were highlighted in Table 5, as a function of formation time. Similarly to the constant-current formation, these cells were also formed in series. Thus once a cell had reached its pre-determined formation level, the current was stopped and the cell was disconnected, before restarting the current to continue forming the remaining cells. Again, this explains the corresponding drop in temperature for the disconnected cells.

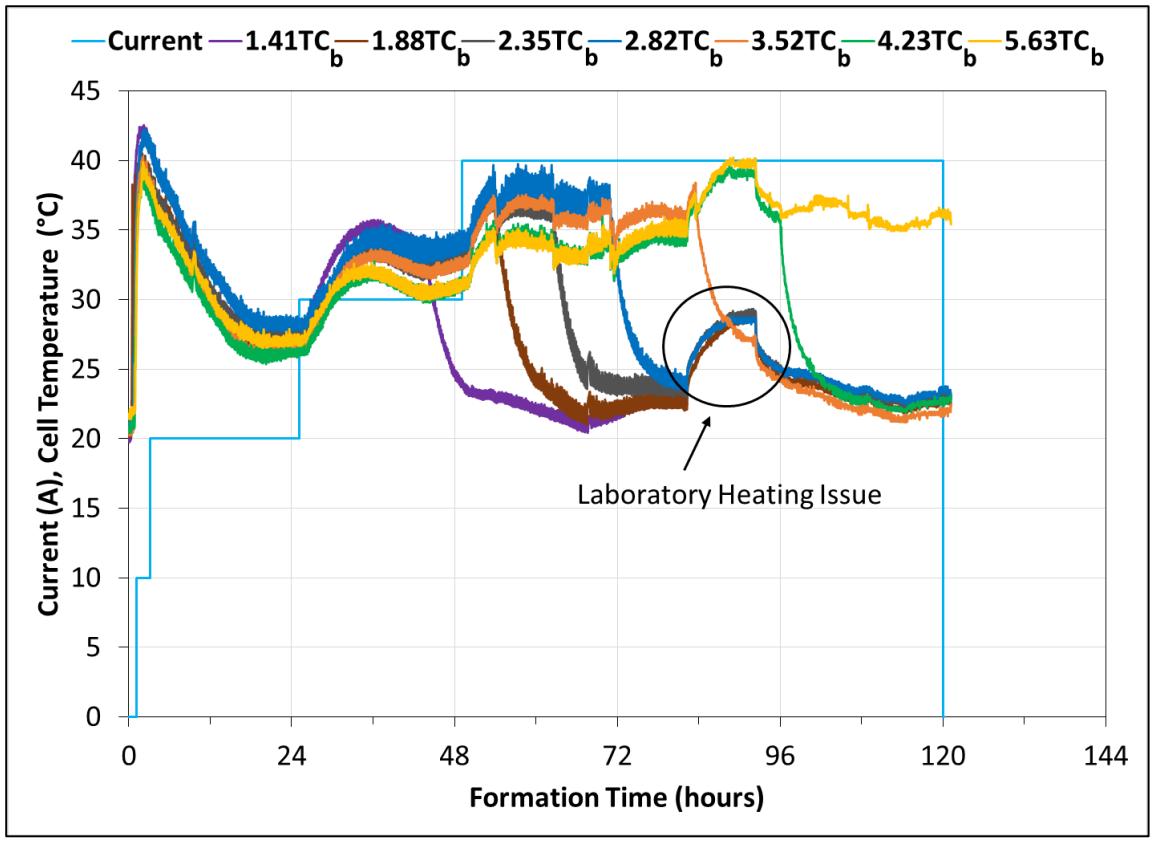

Figure 31 Formation Profile – Current and Temperature (Multi-Step Current Algorithm)

As shown in Figure 31, there was a substantial increase in temperature to nearly 45 °C for all seven cells during the soaking period as expected due to the chemical reactions of the LAB. Unlike the constant-current formation presented above, there was no need to modify the formation current as cell temperatures remained between the desired range of 30 °C

and 50 °C, due to the incremental current steps. It is important to note that cell temperatures increased when the formation current was increased from 20 A to 30 A, and again from 30 A to 40 A, due to the acceleration of the chemical and electrochemical reactions of formation. The increase in cell temperatures between formation times 84 and 96 hours was due to laboratory heating issues. Again, it is important to remember that the cell temperatures shown in Figure 31 represent the temperatures on the outside of the cells at mid-height. By considering the cell electrolyte temperatures to be 4 °C higher on average than the outside cell temperatures, it can be stated that the cell electrolyte temperatures also did not exceed 50 °C.

Figure 32 shows the individual cell SG values (solid lines) and voltages (dashed lines) as a function of formation time.

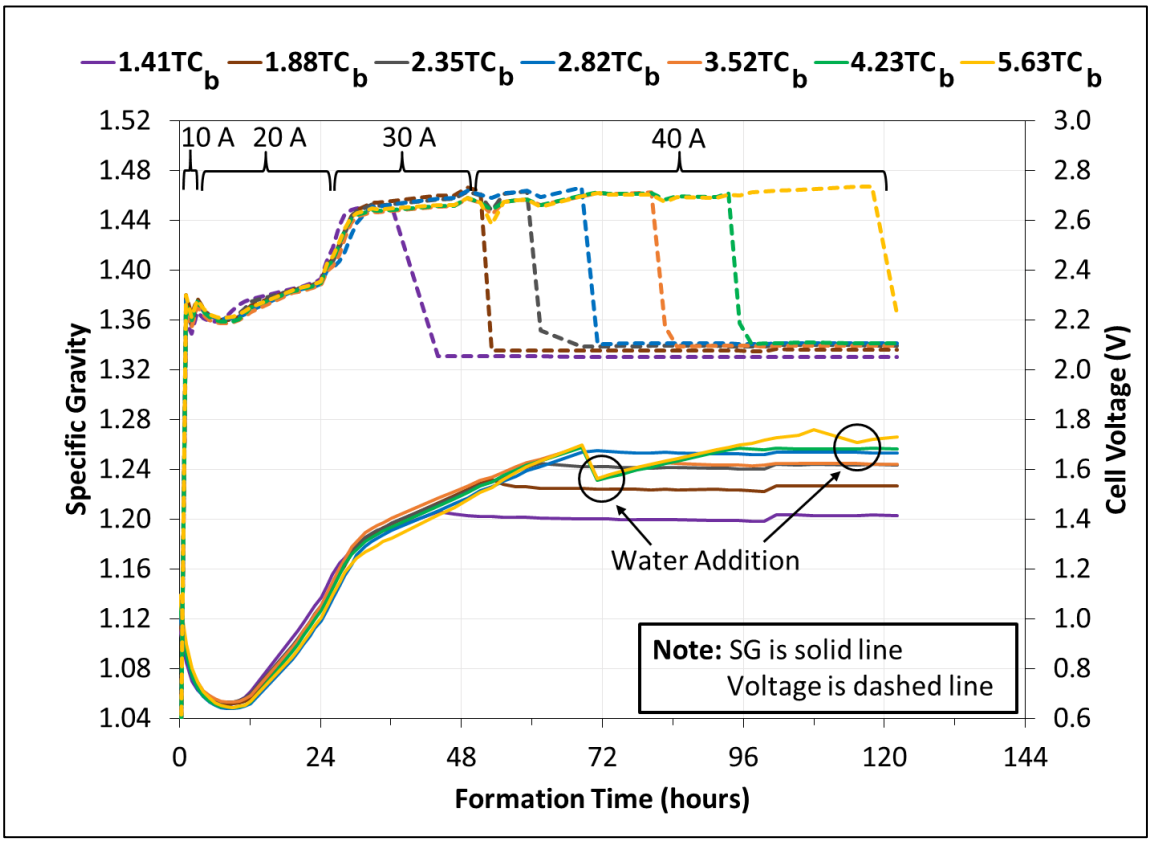

Figure 32 Formation Profile – Cell SG Values and Voltages (Multi-Step Current Algorithm)

As shown in Figure 32, there was an initial reduction in both cell SG and voltage, followed by an increase in both sets of values shortly after the 12 hour formation mark (i.e., 220 Ah). These results are consistent with the constant-current formation profile shown in Figure 19,

and the first and second stages of formation. The maximum voltages reached by these cells were higher than the corresponding maximum voltages reached by the cells formed using the constant-current formation algorithm, the impact of which will be discussed in section 5.3. The sudden drops in SG values for cells, $3.52TC_b$, $4.23TC_b$, and 5.63TC at a formation time of 69 hours was because 500 mL of distilled water was added to these cells in order to ensure the plates remained submerged during formation. A further 250 mL of distilled water was added to $5.63TC_b$ at a formation time of 108 hours. As was the case for the constant-current formation, the final SG and OCV values have a clear positive correlation to total formation capacity.

Table 16 shows for each of the seven formed cells: the amount of distilled water that was added during formation, the amount of 1.265 electrolyte that was added at the end of formation for top-up (with corresponding percentage of initial electrolyte volume), and the final SG and OCV values. It should be noted that the SG and voltage values were taken before the first step of the cycling algorithm for each cell.

Table 16 Formed Cell Status (Multi-Step Current Algorithm)

Cell Name	Water Added During Formation (mL)	Electrolyte Added After Formation (mL), (% of Initial Electrolyte Volume)	Final SG (Corrected to 20 °C)	Final OCV
$1.41TC_b$	0	490 (12.7 %)	1.202	2.05
$1.88TC_b$	0	590 (15.4 %)	1.226	2.08
$2.35TC_b$	0	920 (24.1 %)	1.241	2.09
$2.82TC_b$	0	840 (22.0 %)	1.249	2.09
$3.52TC_b$	500	570 (15.0 %)	1.242	2.09
$4.23TC_b$	500	680 (17.8 %)	1.248	2.08
$5.63TC_b$	750	700 (18.0 %)	1.257	2.10

As shown in Table 16, a greater amount of electrolyte was required to top-up the cells formed using the multi-step current formation algorithm than was required for the cells formed using the constant-current formation algorithm. Thus, it can be confirmed that water electrolysis was heightened for the multi-step formation algorithm when compared to the constant-current formation algorithm.

Figure 33 shows a clear correlation between the final SG and OCV values of the seven cells as a function of their respective formation input in Ah and ratio of the theoretical capacity.

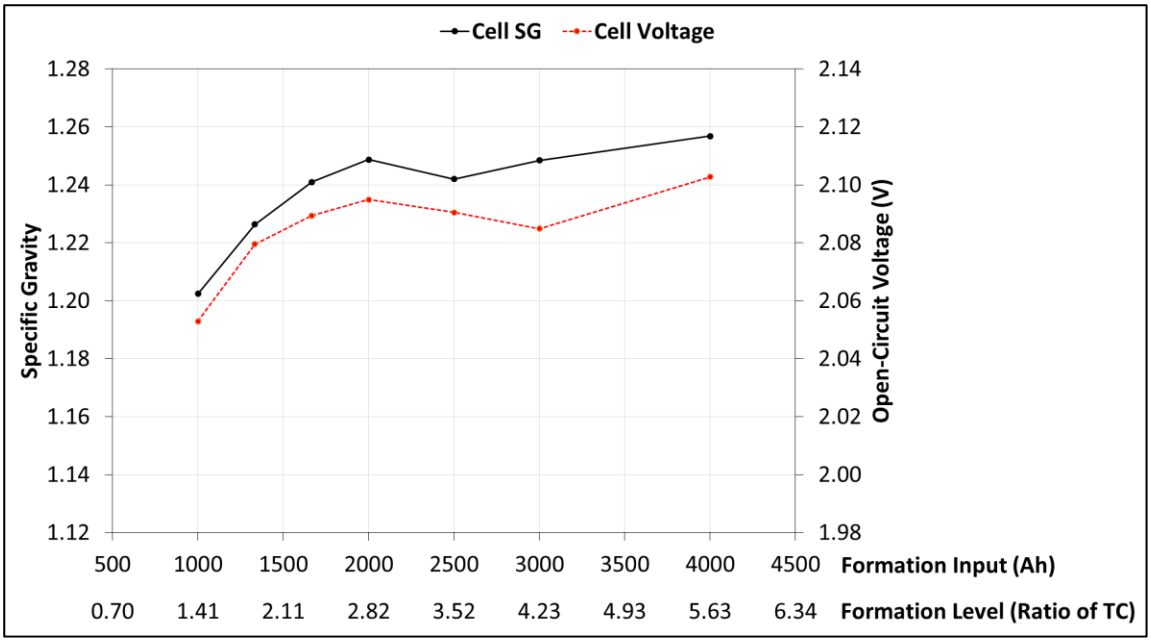

Figure 33 Final SG and OCV Values of Formed Cells (Multi-Step Current Algorithm)

As shown in Figure 33, cells $3.52TC_b$ and $4.23TC_b$, although having received additional formation inputs, have lower final cell SG and OCV values than cell $2.82TC_b$. This is because distilled water was added to these two cells late in their respective formation process, resulting in lower cell SG and OCV values. By comparing Figure 33 to Figure 20, it can be noted that cell SG and OCV values tend to be higher for the constant-current formation algorithm than the values obtained using the multi-step current formation algorithm. This is explained by the fact that the higher overall current in the multi-step current algorithm heightened the side reactions during formation, thus reducing the efficiency of formation.

Deep-Cycling Characteristics

The following will be based on the methodology used to determine the optimal formation level, as outlined in section 4.1.3, where the first step comprised of completing a deep-cycling performance analysis of the cells. It should be noted there are a lot of similarities between the cycling results of the cells formed using the multi-step current algorithm when compared to the cycling results of the cells formed using the constant-current algorithm. Thus in these instances, discussion will be kept short, as a detailed comparison of these results is presented in section 5.3.

As was the case for the cells formed using the constant-current formation, the seven cells formed using the multi-step current formation algorithm were also deep-cycled 10 times using the algorithm presented in Table 6. In order to obtain additional IR data for these cells, the IR measurements were taken at every multiple of 25 Ah charge/discharge capacity points, instead of every multiple of 50 Ah as per the performance analysis of the cells formed using the constant-current formation algorithm. As an example, Figure 34 shows the voltage, current, temperatures, and Ah depletion as a function of cycle time for the 10^{th} cycle of cell $2.82TC_b$, where the results are shown to be consistent with the cycle 10 profile of cell $2.82TC_a$ (see Figure 21).

(a)

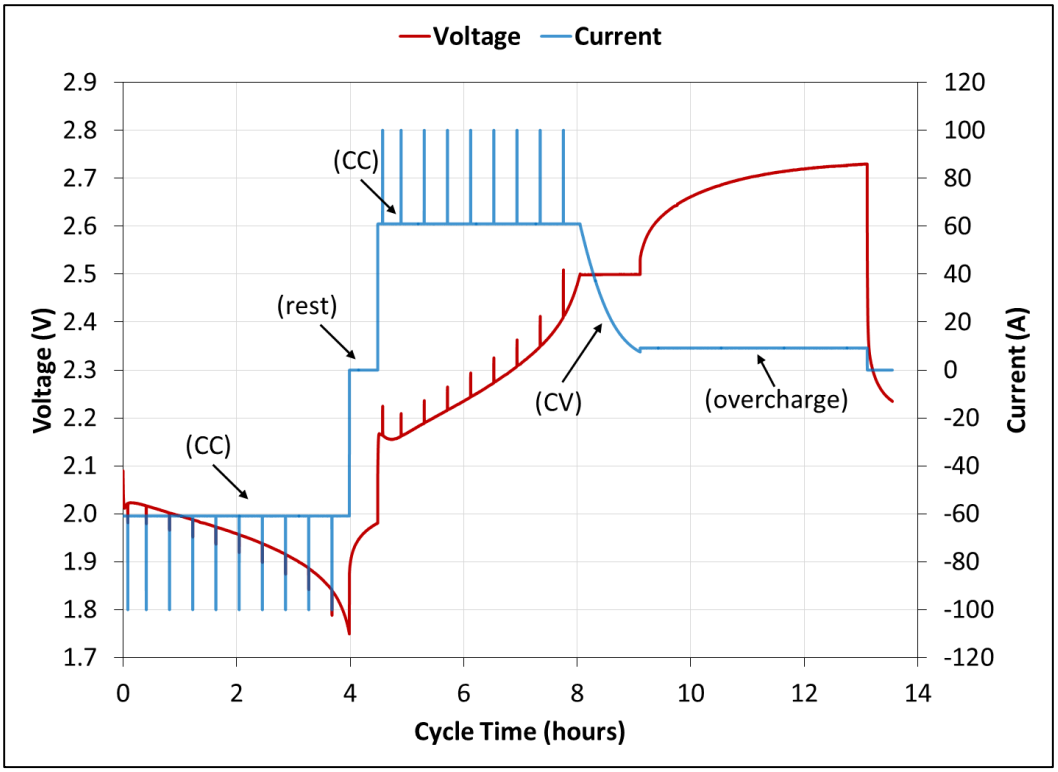

(b)

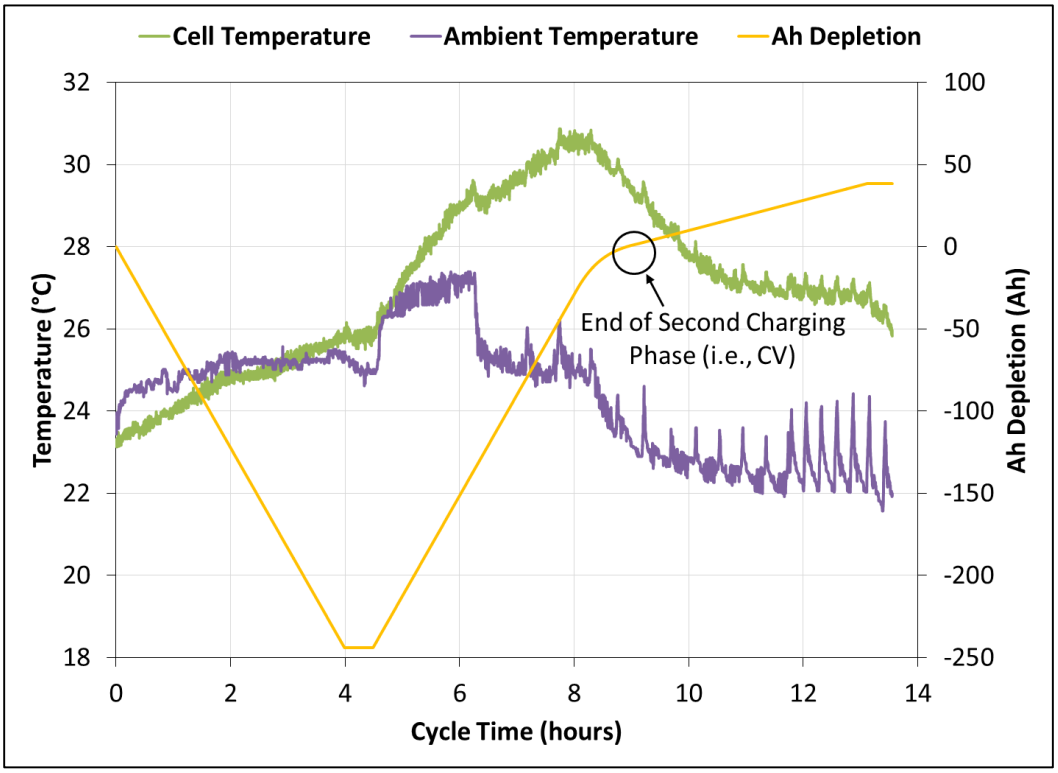

Figure 34 **Cycle 10 Profile of Cell 2.82TC$_b$ as a Function of Cycle Time (Multi-Step Current Algorithm) – (a) Voltage and Current, (b) Temperature, Ah Depletion**

Discharge Capacity Characteristics

Figure 35 shows the measured discharge capacities of the cells for all 10 cycles. The average coulombic efficiency of cell $2.82TC_b$ was calculated to be 86.4 % over a span of 10 cycles. This value is in agreement with the average coulombic efficiency of cell $2.82TC_a$, which had a coulombic efficiency of 86.8 % over a span of 10 cycles, and with the other six cells formed using the multi-step current algorithm.

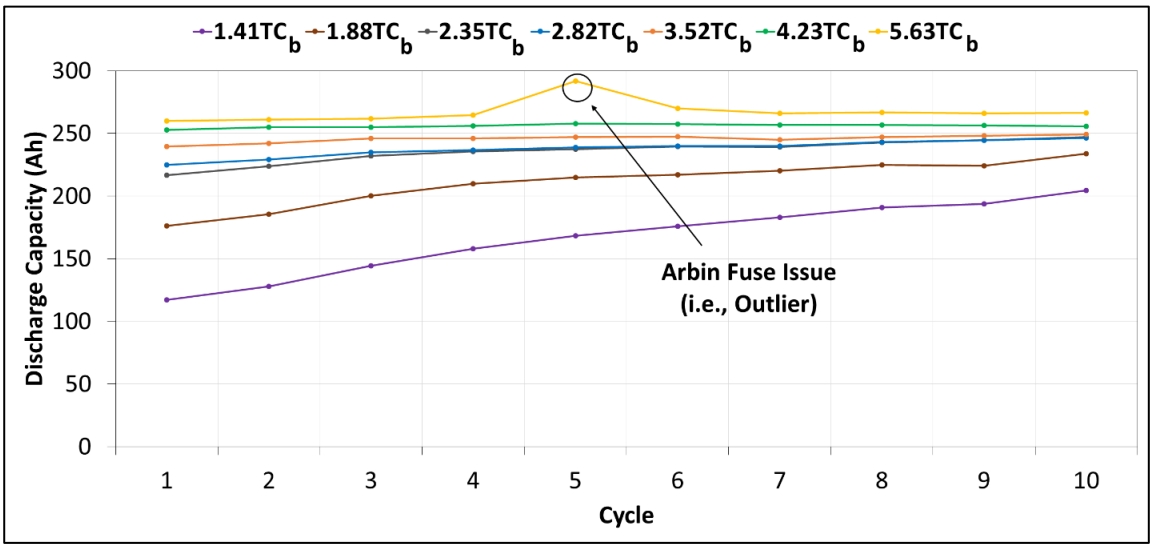

Figure 35 Cell Discharge Capacities (Multi-Step Current Algorithm)

As shown in Figure 35, the discharge capacities of cells $1.41TC_b$ and $1.88TC_b$ increased significantly with each cycle, thus confirming that these two cells were still forming. Similarly for the remaining cells, with the exception of cells $3.52TC_b$ and $4.23TC_b$, a slight increase in respective discharge capacities is also noticed. All cells, with the exception of cells $1.41TC_b$ and $1.88TC_b$, settled at a final capacity of approximatively 250 Ah, 8.2 % higher than the rated capacity of the cell. It should be noted that cell $3.52TC_b$ had an atypical discharge capacity value for its 5^{th} cycle. This discrepancy came as a result of a fuse failing within the Arbin power-cycler while discharging the cell, causing a reduction in discharging current by 33 %, which in turn increased the discharge capacity of the cell. The fuse was replaced for the subsequent cycles, as shown by the drop in discharge capacity for cycle 6 to a value near the ones obtained for cycles 1-4.

It should be noted that unlike the discharge capacity results of the cells formed using the constant-current formation algorithm, and with the exception of cells $2.35TC_b$ and $2.82TC_b$, there was a clear distinction between the discharge capacity results of the cells

formed using the multi-step current algorithm. Thus, there is no clear indication that a formation level of 2.82 times the theoretical capacity of the cell is the highest practical ratio for this formation algorithm, as was the case for the cells formed using the constant-current algorithm. In other words, these results support the case of lower formation efficiency for the multi-step formation algorithm when compared to the constant-current formation algorithm.

Specific Gravity Characteristics

Figure 36 shows the electrolyte SG values of the seven cells which were measured before the start of each deep-cycle.

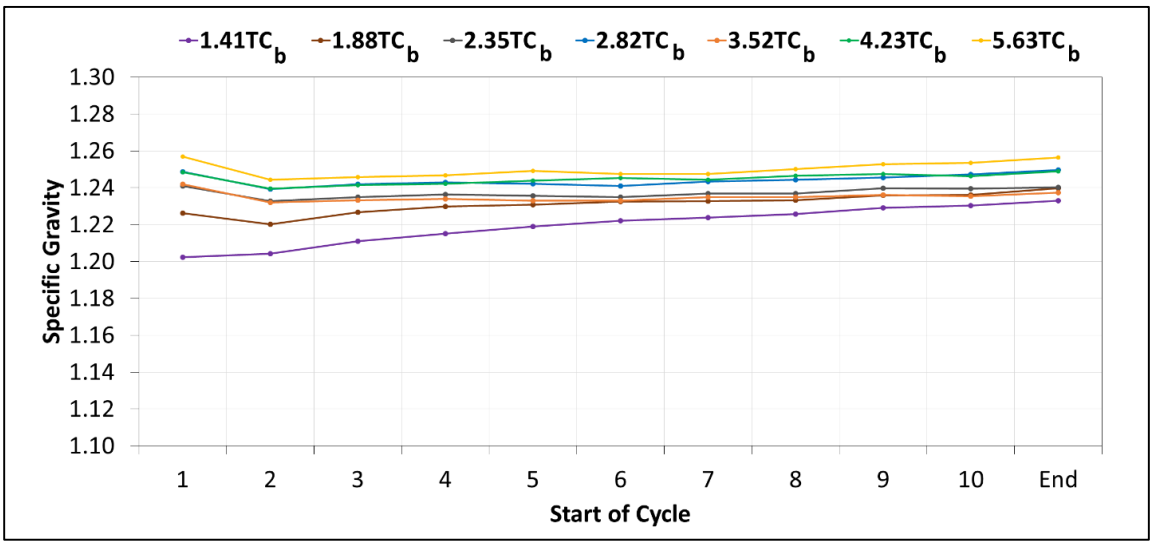

Figure 36 Cell Electrolyte SG Values (Multi-Step Current Algorithm)

As shown in Figure 36, cell 1.41TC_b is the only cell where an increase in electrolyte SG is observed over a span of 10 cycles, whereas the SG concentration of the other cells (with the exception of cell 1.88TC_b) decrease slightly over the span of their first 6 cycles, where steady-state values are then obtained. This coincides with the discharge capacity results presented in Figure 35, where cell 1.41TC_b was shown to be relatively under-formed with respect to the other six cells. Thus, it is again confirmed that additional H_2SO_4 is released from the plates as the formation process is continued. These results are in agreement with the cells formed using the constant-current formation algorithm.

Figure 37 shows the electrolyte SG profile for the 10^{th} deep-cycle of the seven cells formed using the multi-step current formation algorithm.

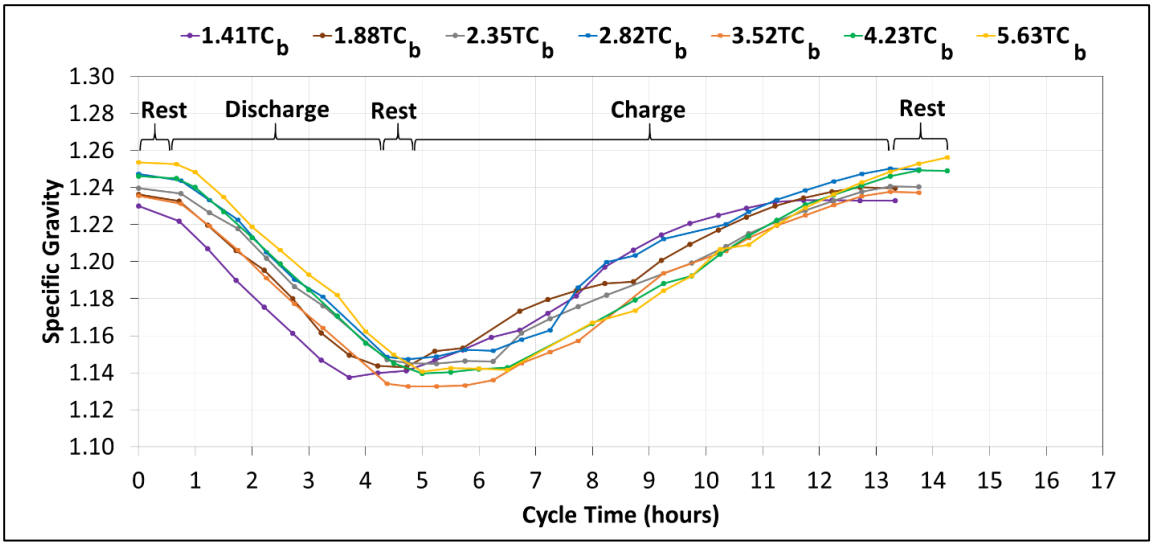

Figure 37 Electrolyte SG Profile – Cycle 10 (Multi-Step Current Algorithm)

As shown in Figure 37, the SG profile of the cells formed using the multi-step current algorithm is in agreement with the SG profile of the cells formed using constant-current formation algorithm.

Internal Resistance Characteristics

Figure 38 shows the IR values for cycles 1, 2, 4, 6, and 10 of discharging and charging pulses using 10 seconds voltage intervals as a function of cycle number and discharge/charge Ah. As the charging current pulses only occurred during the first phase of the charging process (CC phase only, see Table 6 – Step 4), IR values obtained at a charging capacity of 200 Ah correspond to approximatively 75 % of the total Ah input received by these cells during their respective charging processes.

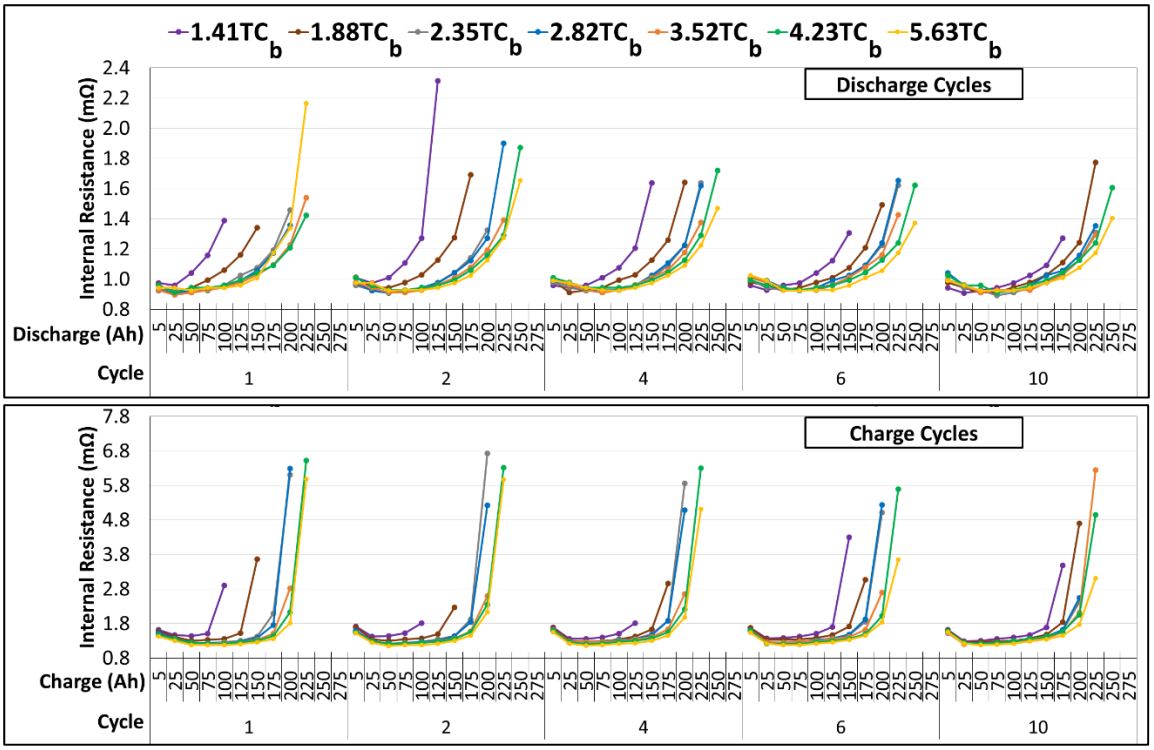

Figure 38 Discharge and Charge IR with 10 Second Voltage Intervals (Cycles 1, 2, 4, 6, and 10) (Multi-Step Current Algorithm)

As shown in Figure 38, it is clear that as was the case for the constant-current formation, the higher the formation level, the lower the IR when respective discharging and charging capacities are compared. The cell IR values of the different formation levels, with the exception of cells $1.41TC_b$ and $1.88TC_b$, start converging after 4 cycles, which coincides with the convergence of total capacities as shown in Figure 35. These results, and the shape of the IR curves shown in Figure 38, are in agreement with the cells formed using the constant-current formation algorithm.

Optimal Formation Level

As the next step in the methodology used to determine the optimal formation level (see section 4.1.3), a regression model was applied to the initial discharge capacity outputs of the cells as a function of their formation level, as shown in Figure 39. Also shown in the figure are the corresponding values of DFE (i.e., initial discharge capacity output of a cell divided by its formation capacity) for the different cells.

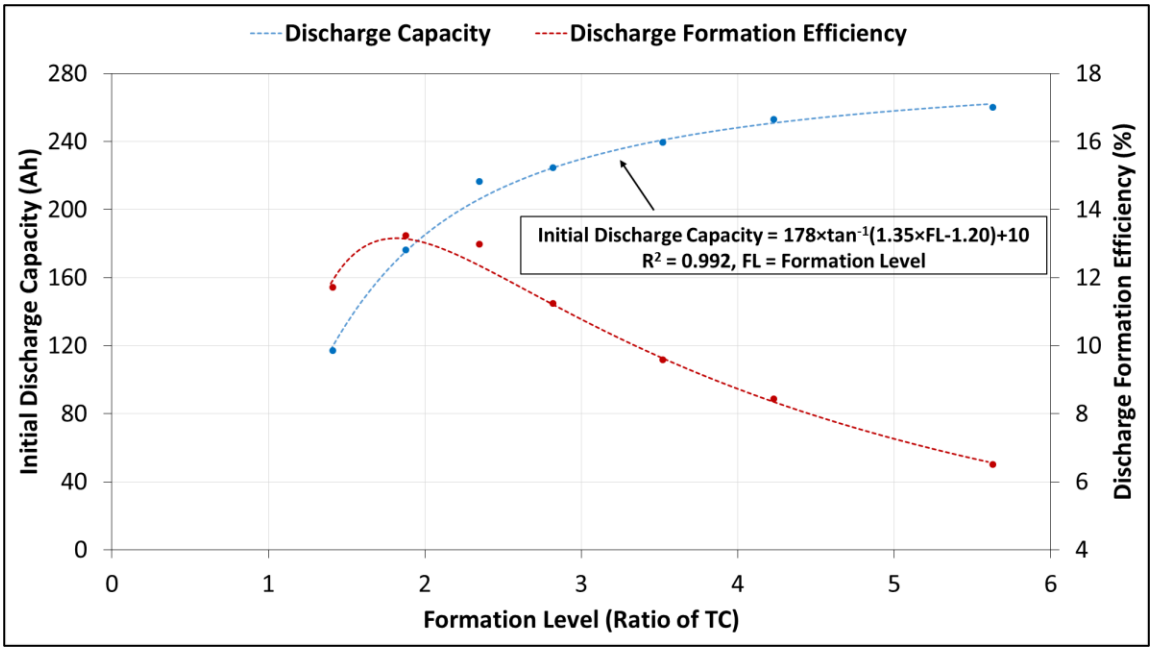

Figure 39 Initial Discharge Capacity and Discharge Formation Efficiency as a Function Formation Level (Multi-Step Current Algorithm)

As shown in Figure 39, the model best representing the initial discharge capacity data has an inverse tangent relationship with an R^2 of 0.992. Using this regression model, normalized capacity and DFE values were calculated for different ratios of theoretical formation input values ranging from 1.40TC to 5.60TC, using increments of 0.05TC.

Weighting ratios, in 5 % increments, were then applied to the normalized initial discharge capacity values and normalized DFE values. Figure 40 shows the resulting optimal formation levels, corresponding to the highest sum of weighted normalized values, as a function of the weight attributed to the normalized initial discharge capacity. Also shown in the figure is the curve representing the optimal formation levels for the constant-current algorithm, which was shown in Figure 30.

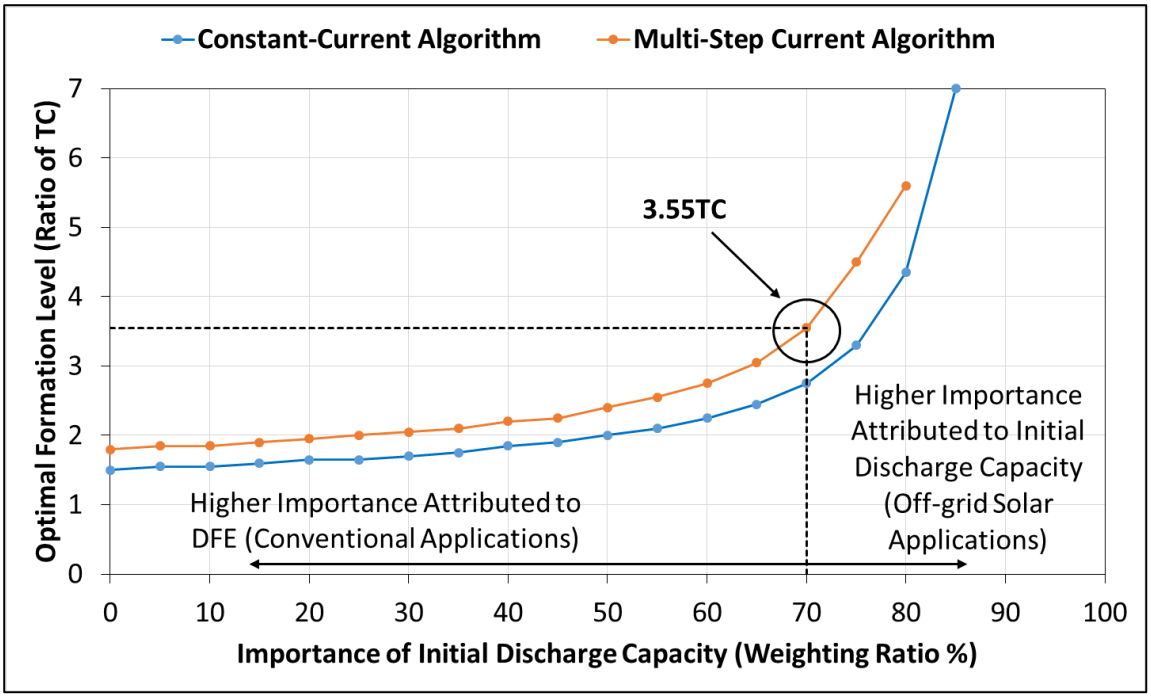

Figure 40 Optimal Formation Levels for the Constant-Current and Multi-Step Current Formation Algorithms as a Function of Weighting Ratio

As shown in Figure 40, the optimal formation level increases as more importance is attributed to the initial discharge capacity for both algorithms. With respect to the multi-step current formation algorithm, a maximum formation level of 5.60TC (i.e., highest formation level obtained using the multi-step current formation algorithm) is obtained when a weight of 80 % is attributed to the initial discharge capacity. Figure 40 also shows that for normalized capacity weighting ratios ≤ 80 %, the corresponding optimal formation level is lower for the constant-current algorithm when compared to the multi-step current algorithm. Thus, these results also support the case of lower formation efficiency for the multi-step formation algorithm when compared to the constant-current formation algorithm.

By applying the aforementioned recommended weighting ratio of 70 % / 30 % to the initial discharge capacity and DFE values, respectively, the optimal formation input level for the multi-step current formation method was determined to be 3.55TC (i.e., 2521 Ah). Based on the regression model presented in Figure 39, a cell formed using a formation input of 3.55TC is estimated to obtain an initial discharge capacity output of 241 Ah. The

rated capacity of the cell would be achieved, thus ensuring client satisfaction, while providing a DFE of 9.6 % for the LAB manufacturer.

5.3. Impact of Formation Algorithms and Optimal Formation Level

In order to fully understand the impact of the two different formation algorithms on the performance of the cells, and subsequently to finalize the determination of the optimal formation level, the differences in formation and performance characteristics between the two algorithms are examined below. Specifically with respect to the formation characteristics, the differences in curing and soaking conditions will be explored, along with the important formation parameters as listed out in section 2.2.1 of formation current, formation temperature, formation voltage, and the H_2SO_4 formation concentration, which make up the formation profile. With respect to the performance characteristics, differences in discharge capacity values, SG values, and IR values during deep-cycling operation will be discussed.

Curing Conditions

With respect to the curing conditions, the plates which made up the ELG15 cells, and subsequently formed using the constant-current and multi-step current formation algorithms were from the same batch. Thus, the H_2SO_4/LO ratio in the paste and the curing conditions were identical for both formation algorithms. It was assumed based on the curing conditions at SBC that the PAM was comprised of a 3BS/4BS crystal structure, and that the NAM was comprised of a 3BS crystal structure due to the addition of the lignosulfonate expander.

Soaking Conditions

As stated in section 4.1.1, both formation algorithms used the same soaking conditions. Cells were soaked for one hour using H_2SO_4 electrolyte with an SG of 1.200 prior to formation. This is important because the outcomes of the soaking procedure are impacted by the concentration of the electrolyte, the duration of the soaking period, and the crystal structure of the cured paste. Thus, as all three of these conditions were the same (i.e., 1.200 SG, 1 hour soaking period, a 3BS/4BS crystal structure for the PAM, and a 3BS crystal structure for the NAM), it was assumed that the sulfation of the cured material to $PbSO_4$ proceeded at the same rate for both formation algorithms during their respective soaking period.

Formation Profile

As expected, there were differences in the formation profile of the cells formed using the constant-current algorithm when compared to the cells formed using the multi-step current algorithm. This was a result of the differences in formation current densities. Specifically, as stated in section 4.1.1, the current density used for the constant-current formation algorithm was 3.4 mA cm^{-2}, whereas the current density used for the multi-step current formation algorithm varied between 1.7 and 6.8 mA cm^{-2}. Although all current density values fell within the "normal range" of formation currents, it is clear that the larger formation currents used during the multi-step current formation algorithm had a direct impact on the cell characteristics, as a result of the heightened chemical and electrochemical reactions.

With respect to the characteristic of formation temperature, outside cell temperatures (and corresponding electrolyte temperatures) for both formation algorithms were relatively similar, and remained lower than 50 °C throughout their respective formation process. Thus it can be stated that all cells were formed with an appropriate ratio of β/α-PbO_2.

By comparing cell formation voltages (i.e., Figure 19 vs. Figure 32), it was determined that the multi-step current formation algorithm induced higher cell voltages than the constant-current formation algorithm. This is shown in Figure 41, which compares the maximum formation voltages of the cells formed using both formation algorithms. Cell $0.70TC_a$ was excluded from this analysis.

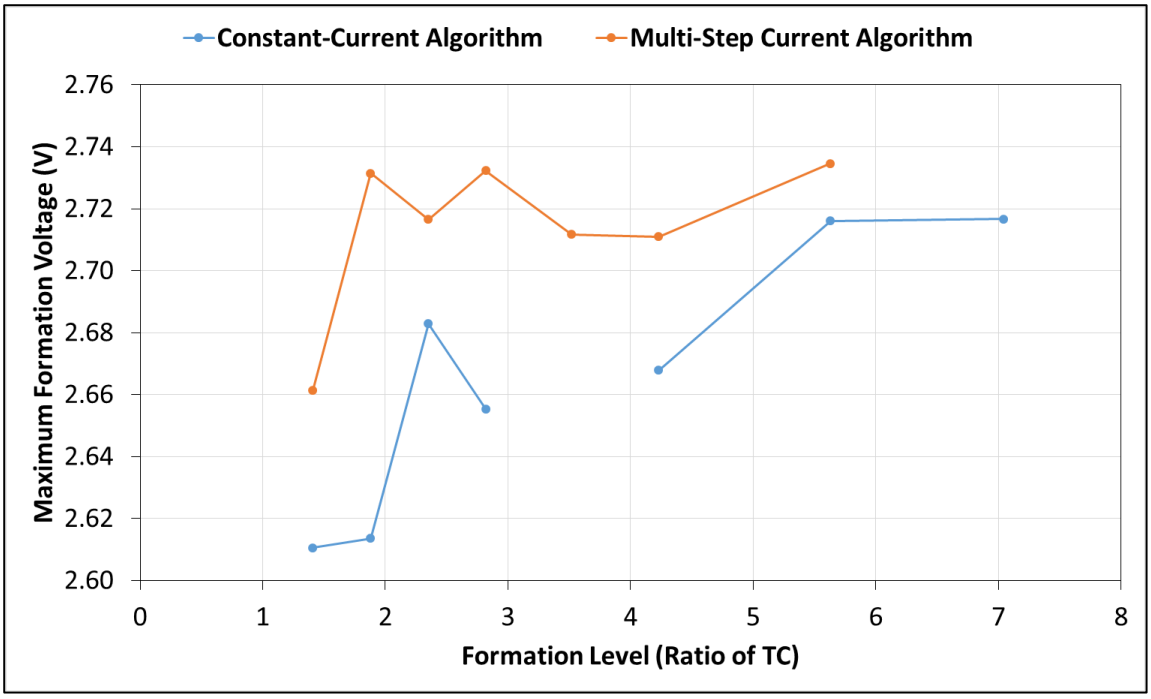

Figure 41 Maximum Formation Voltages – Phase 1

As shown in Figure 41, maximum formation voltages were higher for the cells formed using the multi-step current algorithm. This characteristic was more apparent for the cells corresponding to formation levels of 1.41TC and 1.88TC, with maximum voltage differences of 0.05 V and 0.12 V, respectively. Higher voltages for these two cells formed using the multi-step current algorithm would have heightened the effect of water electrolysis, in turn reducing their respective formation efficiencies. It should be noted that the maximum formation voltage values shown in Figure 41, with the exception of cells $1.41TC_a$ and $1.88TC_a$, exceeded the generally accepted voltage formation limits of 2.60 to 2.65 V per cell.

The formation characteristic of SG is a difficult parameter to compare between the two different formation algorithms due to the differences in cell electrolyte volumes, and the differences in timing with respect to the addition of distilled water. Nevertheless, by comparing the two SG formation profiles (i.e., Figure 19 vs. Figure 32), it can be stated that cells reached their respective maximum SG values in less time when formed using the multi-step current formation algorithm than when formed using the constant-current formation algorithm. This is because the multi-step current formation algorithm accelerates

the reactions of formation (i.e., due to higher formation currents), thus heightening the release of H_2SO_4 from the plates during the second stage of formation.

The final cell SG and OCV values following formation completion were shown to be higher for the constant-current formation algorithm than the values obtained using the multi-step current formation algorithm. This is because the lower overall current in the constant-formation method limited the chemical reactions during formation, thus resulting in a marginally higher formation efficiency. This is in agreement with the fact that less electrolyte was required to top-up of these cells at the end of their formation process when compared to the cells formed using the multi-step current formation algorithm.

Discharge Capacity Characteristics

Figure 42 shows a comparison of the discharge capacities of the cells formed using the constant-current and multi-step current algorithms for all 10 cycles. The capacity value for cycle 5 of cell $5.63TC_b$ was removed due to it being an outlier, and only the cells in common between the two different algorithms were included.

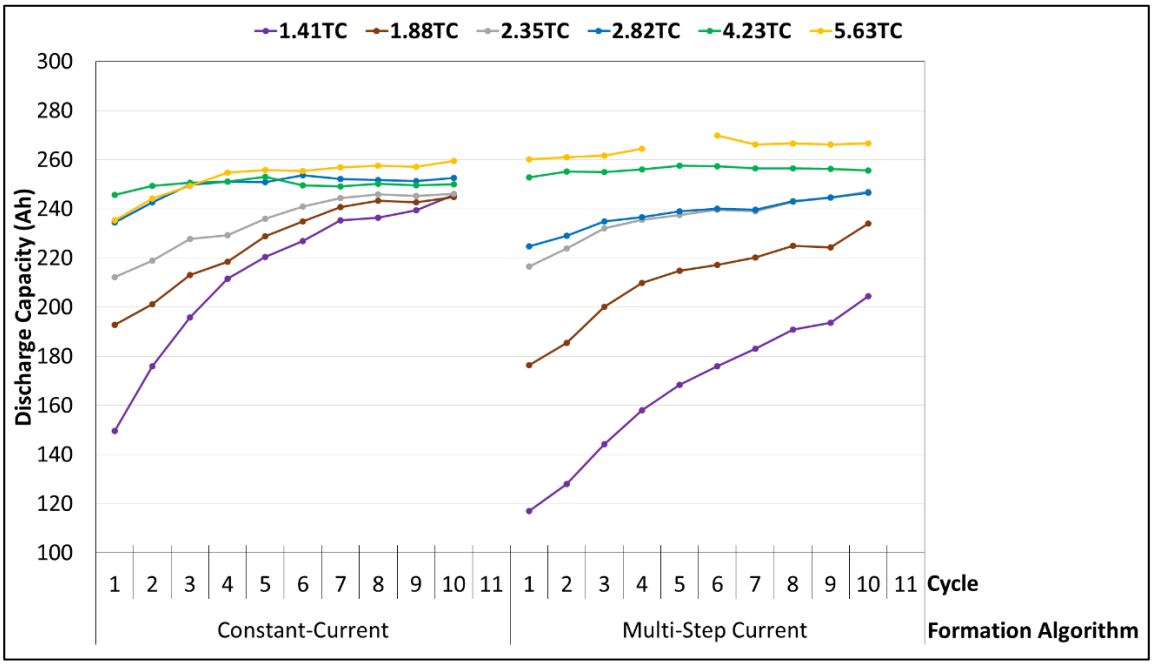

Figure 42 Comparison of Capacity Results – RESL Formation Algorithms

As shown in Figure 42, there are differences between the two formation algorithms when comparing the discharge capacity values through 10 cycles. Specifically, it should be noted that the two cells which received the lowest formation input (i.e., cells 1.41TC and 1.88TC)

performed significantly better when formed using the constant-current formation algorithm than when formed using the multi-step formation algorithm. While these two cells eventually converged with the remaining four cells for the constant-current formation algorithm, the same cannot be said for the multi-step current formation algorithm, with results showing that these cells take much longer to finish their respective formation process. Conversely, when comparing cells 2.35TC, 2.82TC, 4.23TC, and 5.63TC, which received higher formation inputs, the discharge capacity results between the two different formation algorithms are relatively similar (i.e., < 5 % difference). Thus, it is observed that the formation algorithm does impact the performance of cells formed using capacity input levels ≤ 1.88TC. This is explained by the fact that the **higher formation currents used in the multi-step current algorithm reduces the overall formation efficiency of the cells, a factor which is more evident at relatively low formation input values.** Although only one cell per formation level was cycled for each respective formation algorithm, the agreement in discharge capacities for cells having been formed using input levels ≥ 2.35TC provides an acceptable level of confidence with respect to these results.

In order to further compare the performance results of the two different formation algorithms, Figure 43 shows a comparison of the initial discharge capacity and DFE results for the constant-current and multi-step formation algorithms. The optimal formation level is identified by purple star for the constant-current formation algorithm (i.e., 2.75TC), and by a green star for the multi-step formation algorithm (i.e., 3.55TC).

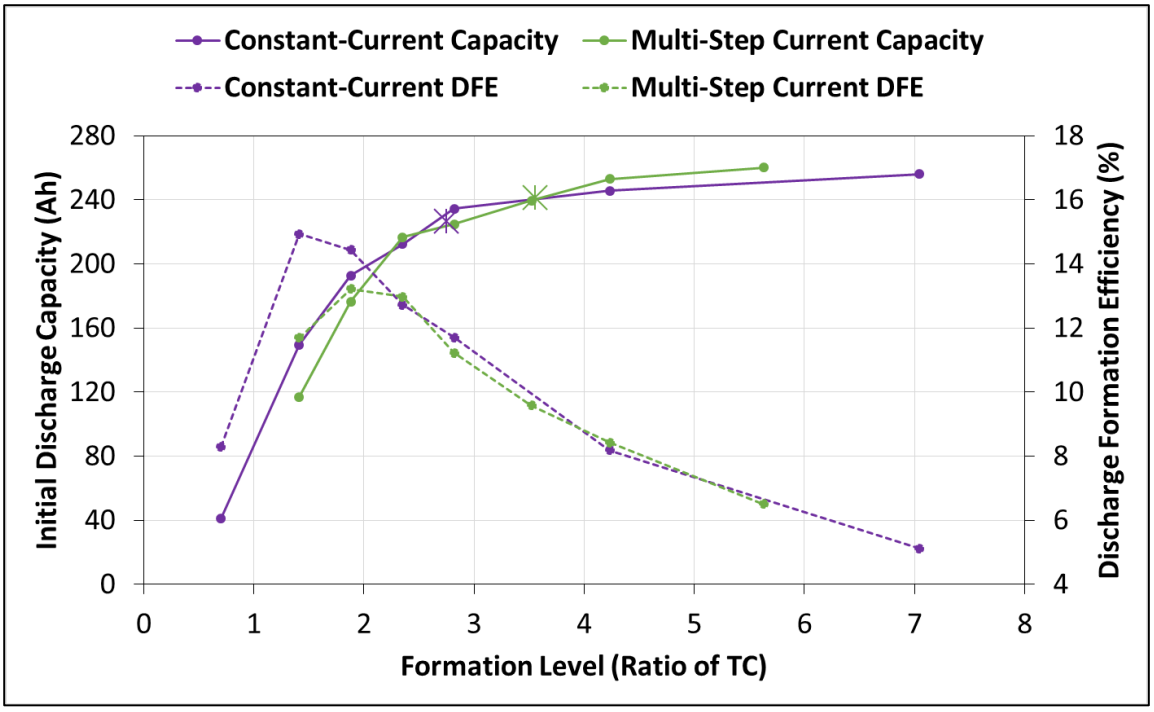

Figure 43 Comparison of Initial Discharge Capacity and Discharge Formation Efficiency Results as a Function Formation Level

As shown in Figure 43, comparable capacity and efficiency results were obtained between the two different formation algorithms when comparing capacity input levels ≥ 2.35TC. These results were alluded to in Figure 42. Thus, while the formation algorithm does impact the performance of cells formed using capacity input levels ≤ 1.88TC, the hypothesis that cells formed using the constant-current formation algorithm would provide better performance results than the ones formed using the multi-step approach cannot be confirmed for all formation input levels. Furthermore, it should be noted that while the optimal formation input level for the multi-step current formation algorithm required an additional 29 % of formation input capacity when compared to the constant-current formation algorithm (i.e., 2521 Ah vs. 1953), it required only 58 % of the total formation time (i.e., 58 hours vs. 100 hours). Thus based on these results, it can be stated that **the multi-step current formation algorithm is advantageous over the constant-current formation algorithm on the basis of a shortened formation duration, by achieving similar performance for a well formed cell.**

Specific Gravity Characteristics

By comparing the electrolyte SG values at the start of each cycle for the cells formed using the constant-current (see Figure 24) and multi-step current (see Figure 36) formation algorithms, there were no significant differences beyond the already mentioned characteristic of higher finalized resting SG values for the cells formed using the constant-current formation algorithm.

With respect to the cycle 10 SG profiles of the cells formed using the two different formation algorithms, no significant differences were noted.

Internal Resistance Characteristics

By comparing the discharge and charge IR values of the cells formed using the constant-current (see Figure 27) and multi-step current (see Figure 38) formation algorithms, there is a distinction for the cells having been formed with capacity input levels < 2.35TC (i.e., $1.41TC_a$ vs $1.41TC_b$, and $1.88TC_a$ vs $1.88TC_b$). Specifically, for both discharging and charging pulses, the aforementioned cells formed using the multi-step current formation algorithm have slightly higher IR values than the ones formed using the constant-current formation algorithm. Thus, these results are in agreement with the deep-cycling discharge capacity results, where cells having received relatively low formation inputs when formed using the multi-step current formation algorithm remain at a lower formation level than cells formed using the constant-current formation algorithm, throughout a minimum of 10 deep-discharge cycles.

Optimal Formation Level

Based on the performance results of the cells formed using the constant-current and multi-step current formation algorithms, it has been determined that the optimal formation level for this cell when using a 70 % (initial discharge capacity) / 30 % (DFE) weighting ratio that is appropriate for off-grid solar applications, is between 2.75 and 3.55 times its theoretical capacity. This range is higher than the values recommended by other researchers in Table 1, of 1.30 to 2.50 times the theoretical capacity of the cell. A graphical comparison is shown in Figure 44.

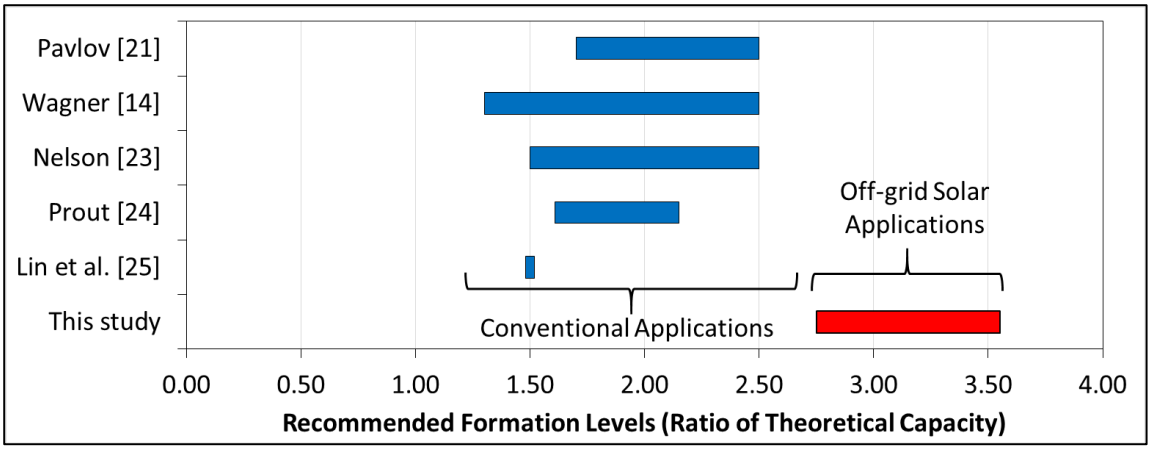

Figure 44 Comparison of Recommended Formation Levels

As shown in Figure 44, this new recommended formation range extends beyond the range recommended by the aforementioned authors. This was not unexpected, as while unsupported by published experimental work (with the exception of Lin *et al.*), one can assume that these recommendations are based on cells targeted for conventional applications. In other words, if one were to form batteries using the formation levels as recommended in literature, the cells would be under-formed, and would likely never attain a fully formed state when implemented in off-grid solar applications. It is worth noting that if a weighting ratio of 30 % / 70 % were instead applied to the initial discharge capacity and DFE values, respectively, of the constant-current and multi-step current algorithm results (i.e., weighting ratio appropriate for conventional applications), a recommended formation range of 1.70 to 2.05 times the theoretical capacity of the cell would be obtained, which is in agreement with the values recommended in literature.

With this in mind, one is reminded that these multipliers are dependent on the thickness of the plates, the phase composition of the cured paste, the size of the particles which constitute the individual phases, and the current and voltage algorithms of formation. Thus, the results of the four different formation methods employed at SBC are presented in Chapter 6 as a mean to study their impact on the ideal formation range.

Chapter 6: Results and Discussions – Phase 2 (Industrial Study)

The following will present and discuss the results for the second phase of this research project. The results of the floor container, submerged container, circulated electrolyte, and tank formation methods are first presented independently (i.e., sections 6.1, 6.2, 6.3, and 6.4, respectively), followed by a comparison of these results in section 6.5.

As described in Chapter 4, the goal of this phase of the project was identify the optimal LAB formation method for the off-grid solar PV market, and to determine the influence of these four methods on the ideal formation level determined in phase 1 of this project. A summary of the formation methods and levels studied for phase 2 of this research project is shown in Figure 45.

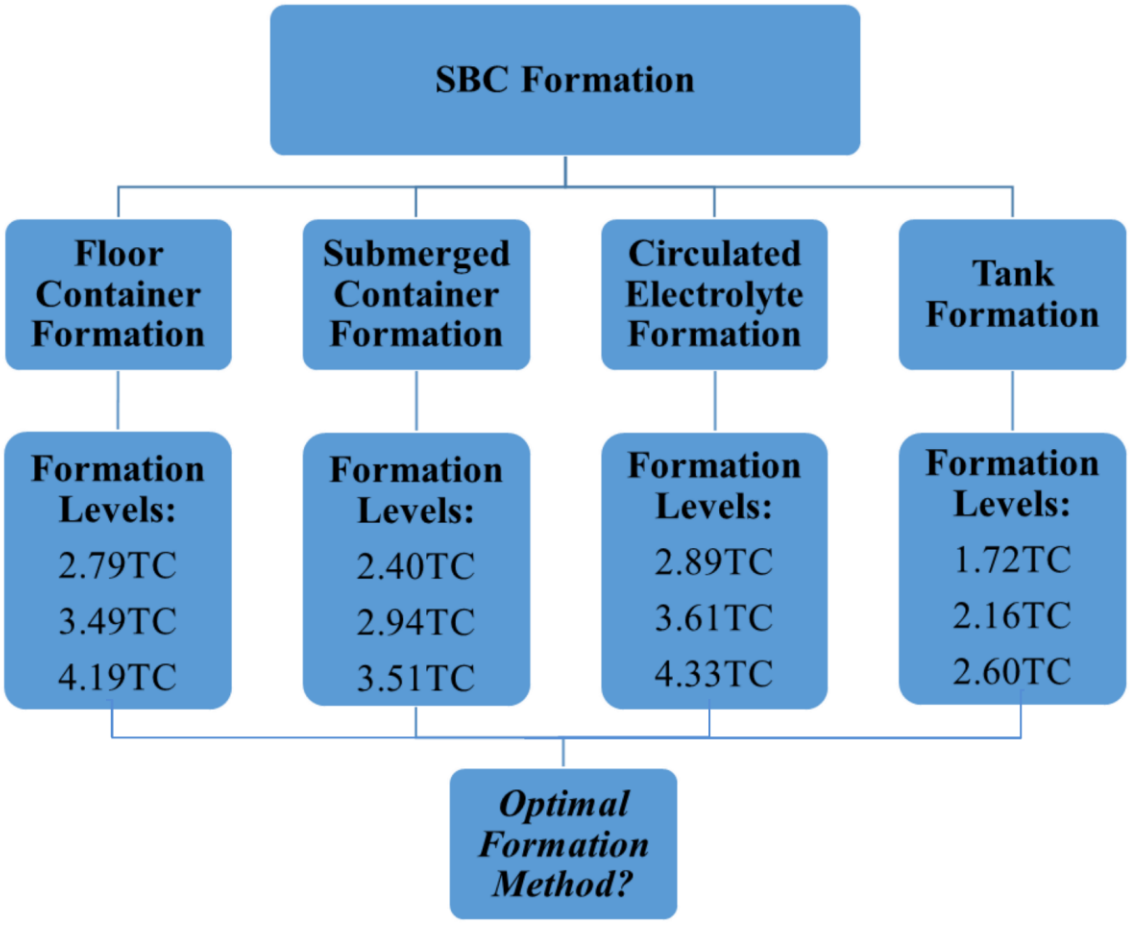

Figure 45 Phase 2 Summary – Formation Methods and Levels

6.1. Floor Container Formation Method

Cell Formation

A total of 30 ELG15 cells were formed in series using the floor container formation method at SBC, which allowed for 10 cells to be formed at each formation level (i.e., UF, NF, and OF). Figure 46 shows the formation profile with respect to the pack voltage, formation current, and formation capacity of these cells as a function of formation time, which was obtained using the measurement unit. For this formation method, the measurement unit was configured to log formation data every 6 seconds, obtained by taking the average of six 1 second readings. As the cells were formed in series, once the UF and NF cells had reached their respective pre-determined formation level, the current was stopped and the cells were disconnected, before re-starting the current to continue forming the remaining cells. This is shown in the figure by a reduction in current and voltage values to zero at formation times of 62 hours (i.e., 1982 Ah), 74 hours (i.e., 2478 Ah), and 86 hours (i.e., 2974 Ah), corresponding to the removal of the UF, NF, and OF cells, respectively.

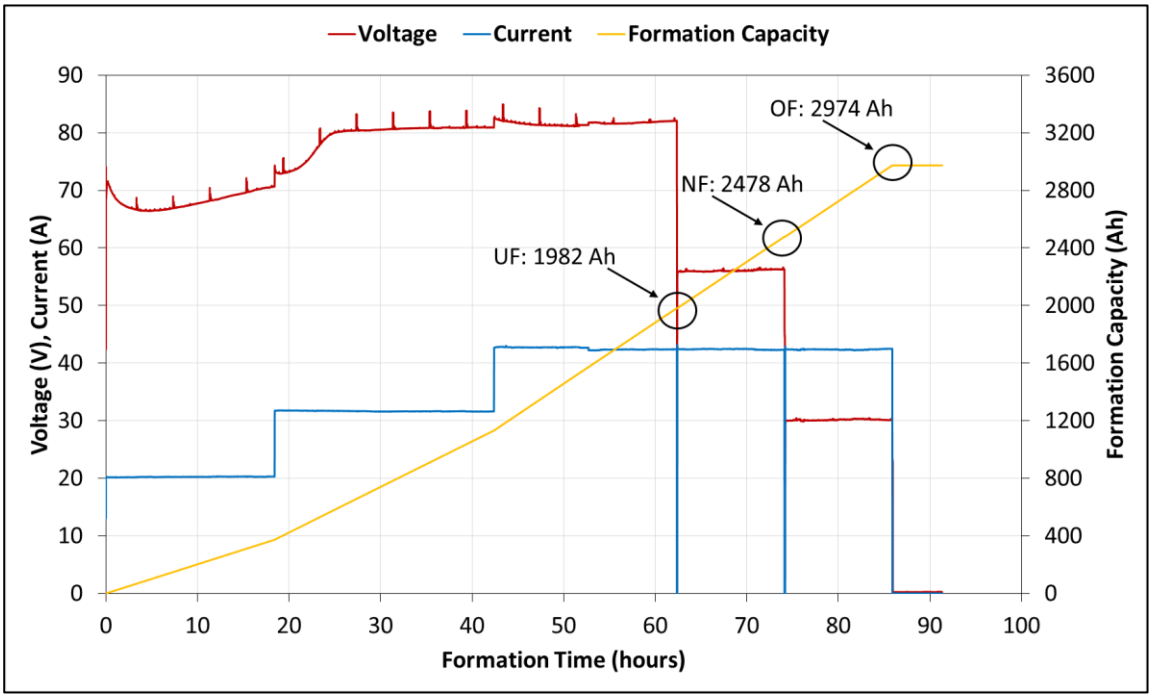

Figure 46 **Formation Profile – Voltage, Current, and Formation Capacity (Floor Container Formation Method)**

As shown in Figure 46, the formation current was slightly higher than what was shown in Table 8, corresponding to shorter formation times for the three different formation levels. This was because the current output for the floor container formation charger is controlled by a manually operated dial, rendering precise current output difficult. For each instance of increase in current, there was a small increase in pack cell voltage due to the increase in chemical and electrochemical formation reactions.

The pack cell voltage, as was the case for the voltage results of the cells formed in phase 1, decreased at the start of formation, and then started increasing shortly after the 5 hour mark, equivalent to a formation capacity of 100 Ah. These results are consistent with the first and second stages of formation.

The addition of distilled water was not necessary during the formation of these cells, although electrolyte with an SG value of 1.265 was used to top-up the cells at the end of formation when deemed necessary. This addition of electrolyte was completed as per the standard operating procedures at SBC, therefore the volume of electrolyte added to each cell was not measured.

Table 17 shows the as-received characteristics of the 30 cells formed using the floor container formation method, along with their respective minimum, maximum, average, and relative standard deviation (RSD) values (i.e., RSD = [standard deviation / average] × 100 %). These measurements were taken one day after formation completion.

Table 17 Floor Container ELG15 Cells – As-Received Characteristics

Cell /	UF (2.79TC)			NF (3.49TC)			OF (4.19TC)		
Statistics	*OCV (V)*	*Mass (kg)*	*SG*	*OCV (V)*	*Mass (kg)*	*SG*	*OCV (V)*	*Mass (kg)*	*SG*
1	2.107	17.9	1.2526	2.121	17.7	1.2679	2.138	17.9	1.2734
2	2.107	18.1	1.2520	2.124	18.1	1.2674	2.133	17.9	1.2732
3	2.107	17.9	1.2534	2.124	18.1	1.2681	2.136	18.3	1.2715
4	2.105	17.8	1.2502	2.121	17.7	1.2671	2.134	18.1	1.2717
5	2.105	18.0	1.2509	2.123	17.9	1.2682	2.135	17.7	1.2739
6	2.106	17.8	1.2522	2.124	17.9	1.2681	2.133	18.1	1.2720
7	2.094	17.6	1.2480	2.124	17.7	1.2688	2.135	17.6	1.2734
8	2.106	18.1	1.2513	2.124	18.0	1.2682	2.134	17.6	1.2744
9	2.105	18.8	1.2501	2.123	17.8	1.2685	2.136	17.7	1.2733
10	2.106	18.0	1.2517	2.121	17.5	1.2671	2.135	17.8	1.2730
Minimum	2.094	17.6	1.2480	2.121	17.5	1.2671	2.133	17.6	1.2715
Maximum	2.107	18.8	1.2534	2.124	18.1	1.2688	2.138	18.3	1.2744
Average	2.105	18.0	1.2512	2.123	17.8	1.2679	2.135	17.9	1.2730
RSD	0.184%	1.78%	0.123%	0.0645%	1.10%	0.0451%	0.0714%	1.32%	0.0748%

As shown in Table 17, there is little variation for the as-received characteristics of OCV and SG when respective formation levels are compared. The same cannot be said regarding the as-received characteristic of mass, which indicates differences in the amount of active material and/or electrolyte for these cells (i.e., manufacturing differences). Furthermore, there is a positive correlation between formation level, and the as-received values of OCV and SG. This correlation will be explored in section 6.5. These results are in agreement with the results obtained in phase 1 of this research project.

Deep-Cycling Characteristics

As part of the performance analysis, three cells with the same formation level were deep-cycled in a series configuration in order to represent the S-480 battery. These cells were cycled 10 times using the deep-cycling algorithm presented in Table 13. As an example, Figure 47 shows the voltage, current, temperatures, and Ah depletion as a function of cycle time for the 10^{th} cycle of the three UF cells. UF_1, UF_2, and UF_3 designate the 1^{st}, 2^{nd}, and 3^{rd} UF cells, respectively.

(a)

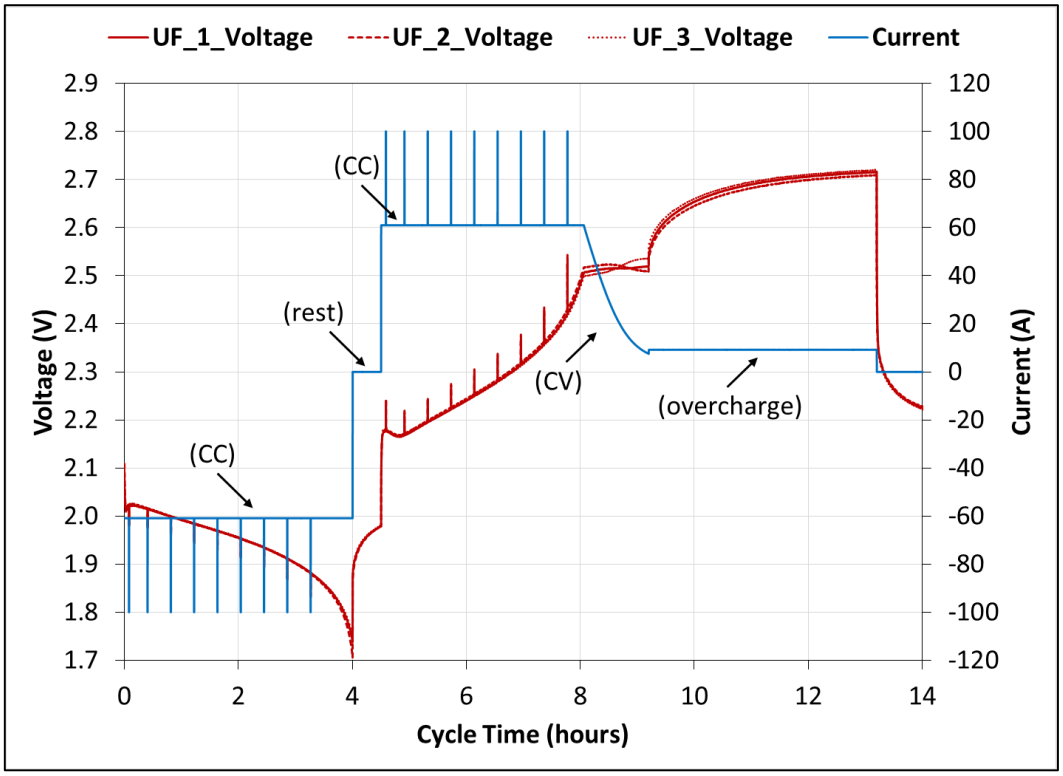

(b)

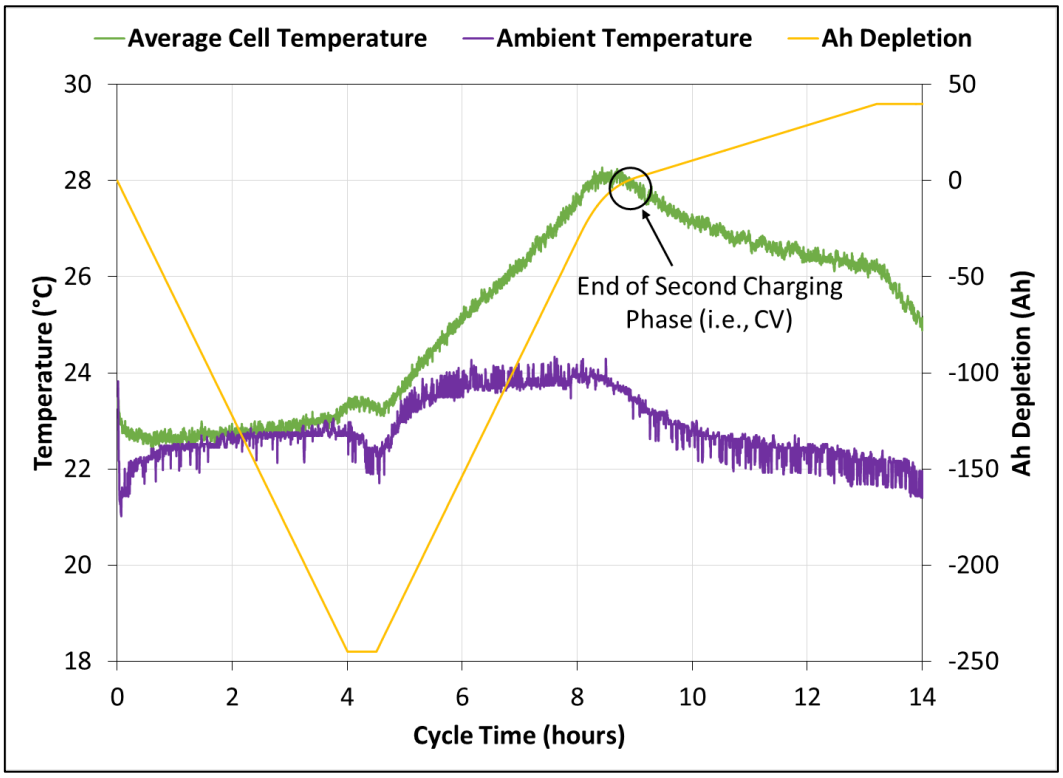

Figure 47 **Cycle 10 Profile of UF Cells as a Function of Cycle Time (2.79TC, Floor Container Formation Method) – (a) Voltage and Current, (b) Temperature, Ah Depletion**

Figure 47 shows that as planned, the cells initially underwent a -60.93 A discharge for approximatively 4 hours, while each of the three cell voltages decreased to 1.75 V. During the 30 minute rest period, the cell OCVs relaxed to 1.98 V. The charging phase then commenced, with an initial charging current of 60.93 A while the voltage of each cell increased to 2.50 V. The current was then reduced as this voltage was maintained, until the cutoff current of 7.50 A was reached as defined in the cycling schedule. A CC of 9.15 A was then maintained for 4 hours, during which the voltage rose to 2.72 V per cell. Thus as shown, the voltages of the three cells behaved in a similar fashion.

The ambient temperature increased by approximatively 2 °C for the first eight hours of cycling (i.e., 22 °C to 24 °C), and then declined to a temperature of 21 °C before climbing back to 24 °C at the end of the cycle period. With respect to the temperature average of the three cells, their temperature increased by approximatively 5 °C during the first nine hours of cycling, a result of energy losses due to the ohmic resistance of the cells.

It should be noted that as was the case for the cells formed in phase 1, the first two charging phases (see Table 13) also accounted for 100 % of the depleted Ah, confirming the effectiveness of the chosen cycling algorithm. The final Ah depletion value for these cells was determined to be 40 Ah, corresponding to an overcharge value of 16.2 %.

Discharge Capacity Characteristics

Figure 48 shows the measured discharge capacity, charge capacity, and coulombic efficiency of the three cells cycled in series for the UF, NF, and OF formation levels. The charge capacity should be read as the sum of the blue (discharge) and red (charge) columns for each respective cycle. The discharge capacities were corrected based on a reference temperature of 25 °C using equation (7).

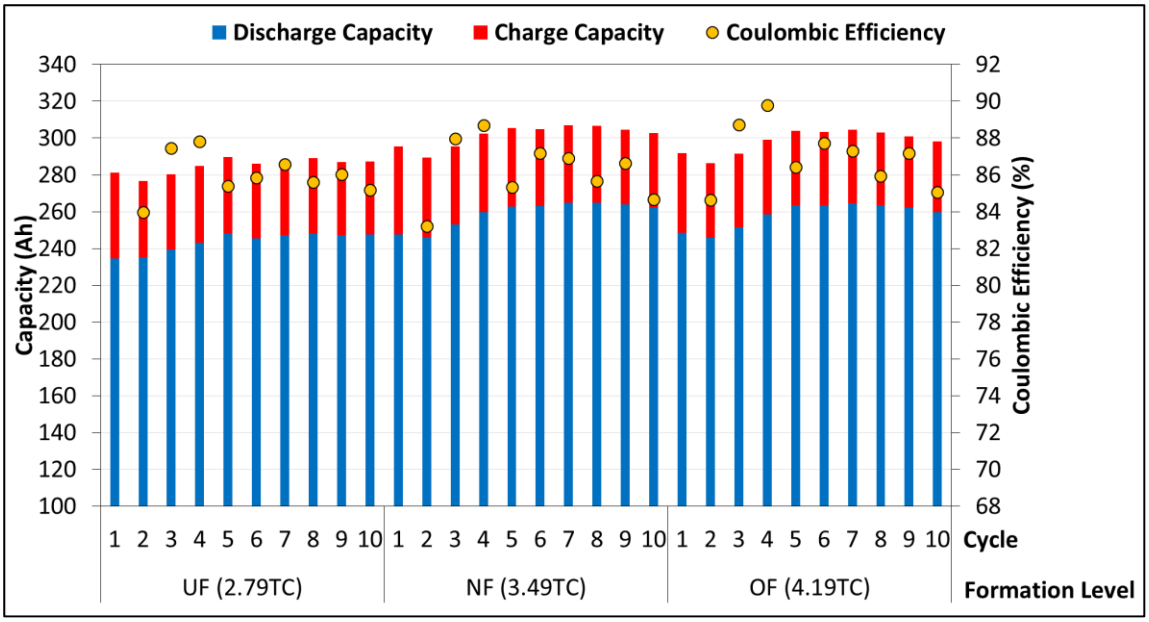

Figure 48 Module Discharge Capacity and Coulombic Efficiency Values (Floor Container Formation Method)

As shown in Figure 48, discharge capacity results between the three different formation levels were similar. Specifically for cycles 6-10, average discharge capacity results were determined to be 247 Ah, 264 Ah, and 263 Ah, for the UF, NF, and OF modules, respectively, while the average coulombic efficiency values were determined to be 85.8 %, 86.2 %, and 86.6 %, for the UF, NF, and OF modules, respectively. All three modules appear to be continuing their formation process, as shown by an increase in discharge capacities between cycles 1 and 5. Finally, for all 10 cycles, all three modules met the rated capacity output of 231 Ah.

Figure 49 provides a discharge capacity comparison of the three modules. For example, the first column is the difference in discharge capacity for the first cycle between the NF module (248 Ah) and the UF module (235 Ah), resulting in 13 Ah, while the corresponding equivalent percent difference is represented by the second column (5 %).

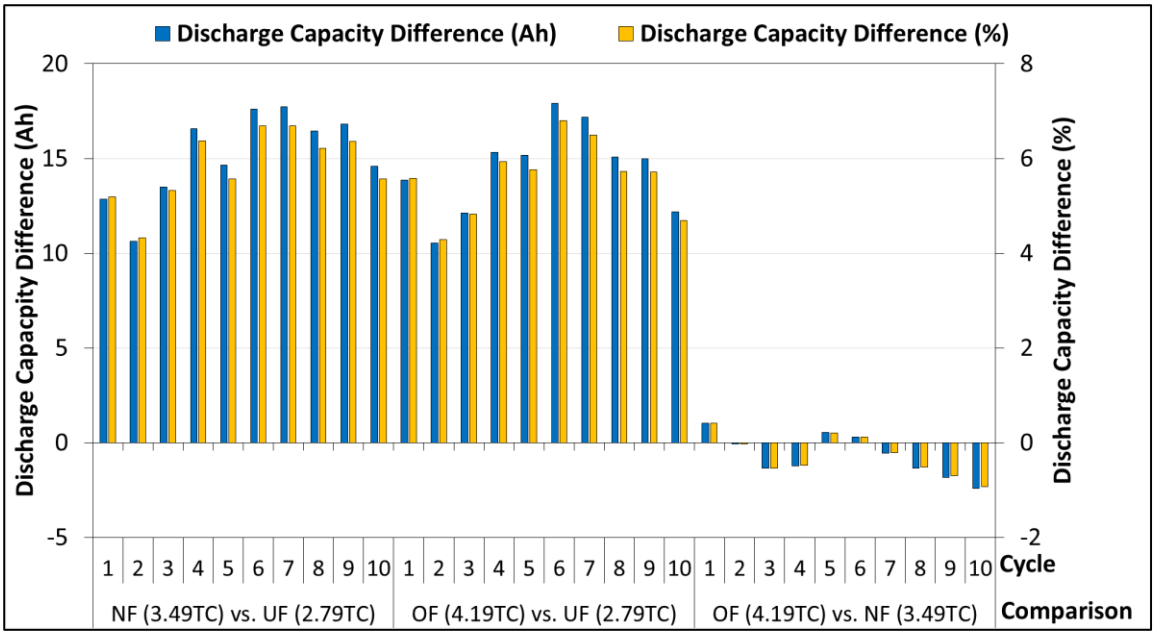

Figure 49 Module Discharge Capacity Comparison (Floor Container Formation Method)

As shown in Figure 49, both the NF and OF modules offer slightly better (i.e., ~ 5+ %) discharge capacity performance characteristics when compared to the UF module. It is interesting to note that following the completion of six deep-cycles, discharge capacity differences are shown to be decreasing when comparing the NF and UF modules, and the OF and UF modules. This is due to the continued formation process of the UF module, a process which occurs faster for the UF module than it does for both the NF and OF modules. The comparison of the OF and NF modules show only small differences in discharge capacity (i.e., < 1 %), thus it can be stated that the OF formation level with respect to the floor container formation method at SBC offers no discharge capacity advantages over the NF formation level.

Specific Gravity Characteristics

Figure 50 shows the average electrolyte SG values of the three modules which were measured before the start of each deep-cycle.

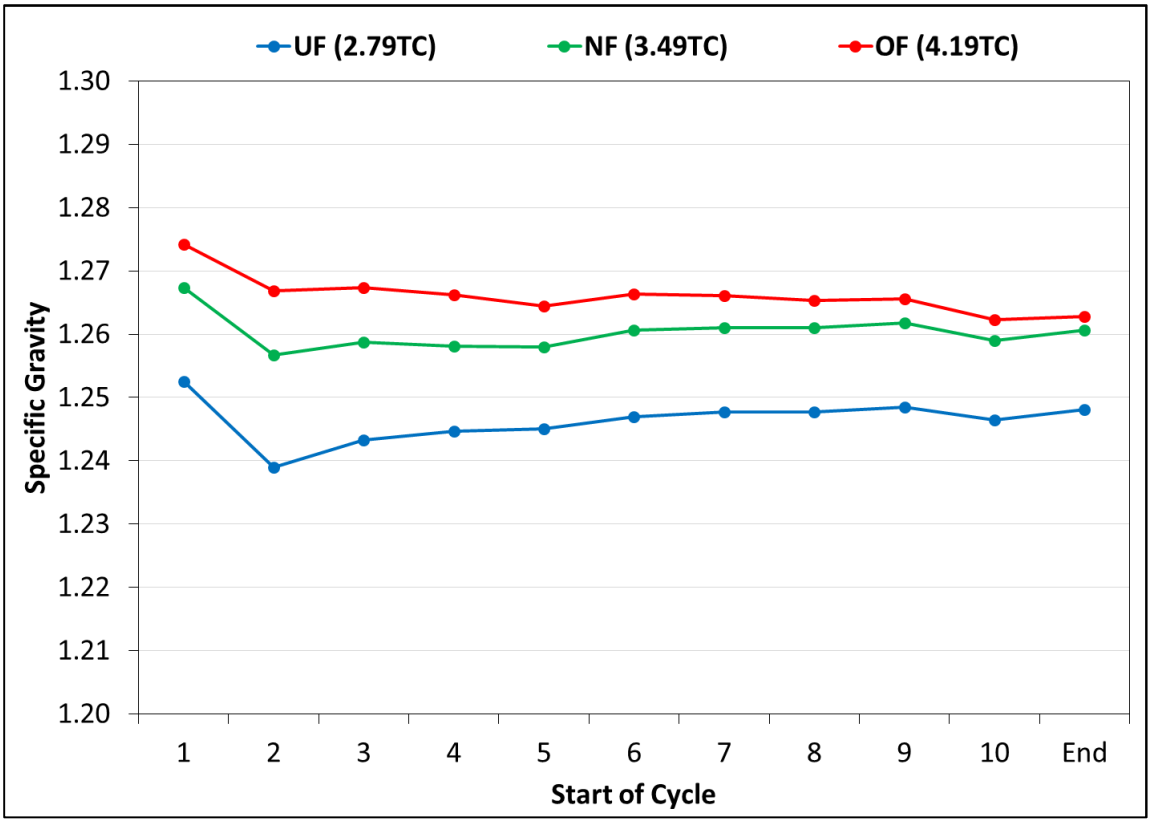

Figure 50 Module Electrolyte SG Values (Floor Container Formation Method)

As shown in Figure 50, there was an initial reduction in electrolyte SG for all three modules. This was a result of non-mixed electrolyte in the cells following the addition of 1.265 electrolyte for top-up. It is clear in Figure 50 that the electrolyte SG values for the UF cells are the lowest, which is in agreement with the discharge capacity results presented in Figure 48, where the UF cells were shown to have the lowest discharge capacity results. There is an increase in SG values for the UF cells between cycles 2 and 6. This again corresponds with the discharge capacity results presented in Figure 48, where discharge capacity values for the UF cells were shown to increase between cycles 1 and 5. The electrolyte SG values are relatively similar between the NF and OF cells, supporting their similarities with respect to the results of discharge capacity.

Internal Resistance Characteristics

Figure 51 shows the IR values of the three modules for cycles 1, 2, 4, 6, and 10 of the discharging and charging pulses using 10 seconds voltage intervals as a function of cycle number and discharge/charge Ah. The IR results are presented as the average of the three

respective cells for each formation level. As the charging current pulses only occurred during the first phase of the charging process (see Table 13– Step 4), IR values obtained at a charging capacity of 200 Ah correspond to approximatively 68 % of the total Ah input received by these cells during their respective charging processes.

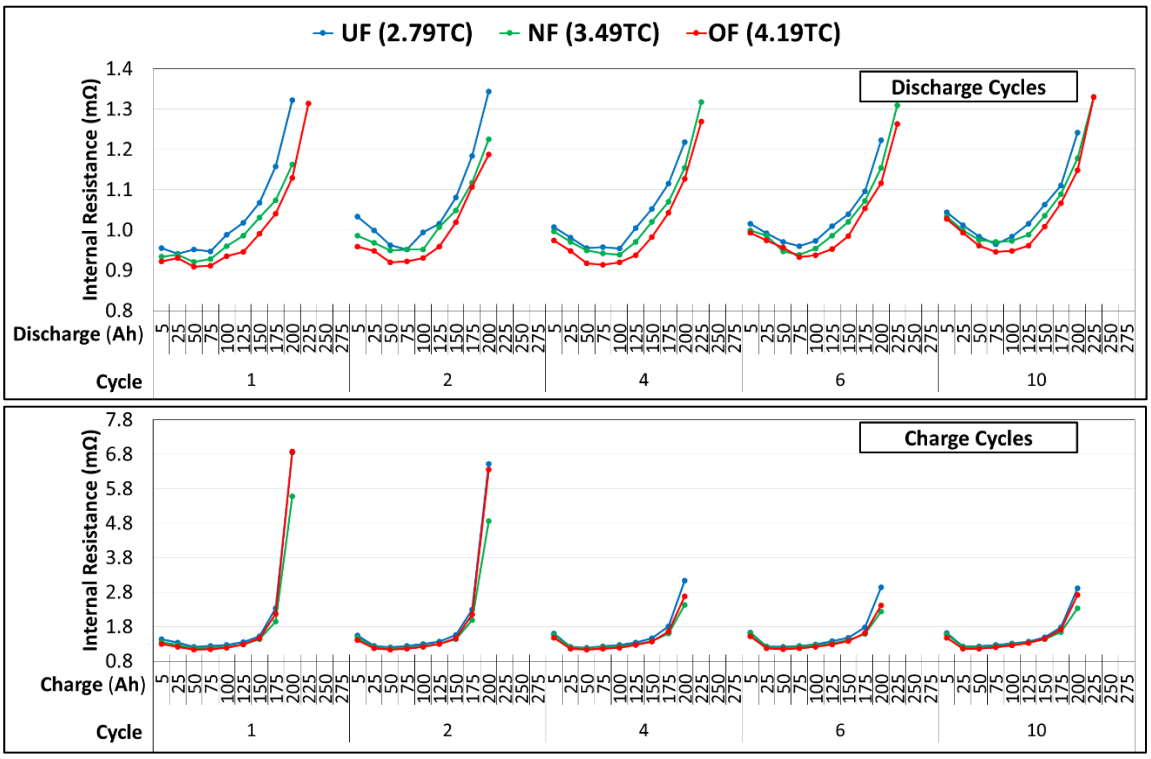

Figure 51 Discharge and Charge IR with 10 Second Voltage Intervals (Cycles 1, 2, 4, 6, and 10) (Floor Container Formation Method)

As shown in Figure 51, the higher the formation level, the lower the IR when respective discharging capacities are compared. Furthermore, overall IR values for the respective modules are shown to decrease with cycling iterations, due to the continued formation of the cells.

The IR charging trend is similar to the discharging trend albeit with higher magnitudes of IR values (e.g., 0.96 mΩ discharging vs. 1.2 mΩ charging, equivalent to a discharging/charging ratio of 80 %, for cycle 1 of the NF cells at the 100 Ah value). The higher formation levels correspond to lower values of IR when respective charging capacities are compared, and the charge IR values also decrease with cycling iterations, due to the continued formation of the cells.

These results are in agreement with the IR results presented in phase 1, and the shape of the IR curves shown in Figure 51 follow the same relationships as were explained for the IR results of the constant-current formation algorithm (see section 5.1).

Module Voltage Alignment

It is worth remembering that relatively higher electrolyte SG values and lower IR values are typically indicators of a better performing battery with respect to discharge capacity. Thus based on these results, one would have expected the OF cells to better by discharge capacity both the UF and NF cells, but as shown in Figure 49, this was not the case. This discrepancy may have been caused by an OF cell reaching a voltage of 1.60 V (i.e., a misaligned cell) before the other two cells in series reached voltages of 1.75 V, thus prematurely triggering the end of the discharge process as per the deep-cycling algorithm (see Table 13 – Step 2). Thus in order to study their voltage alignment, Figure 52 shows the individual discharge voltages of the nine cells as a function of their first discharge capacity, while Figure 53 shows the final discharge voltages of these same cells as a function of cycle number. The first discharge characteristics are important, as they define the performance basis of a LAB in off-grid solar applications.

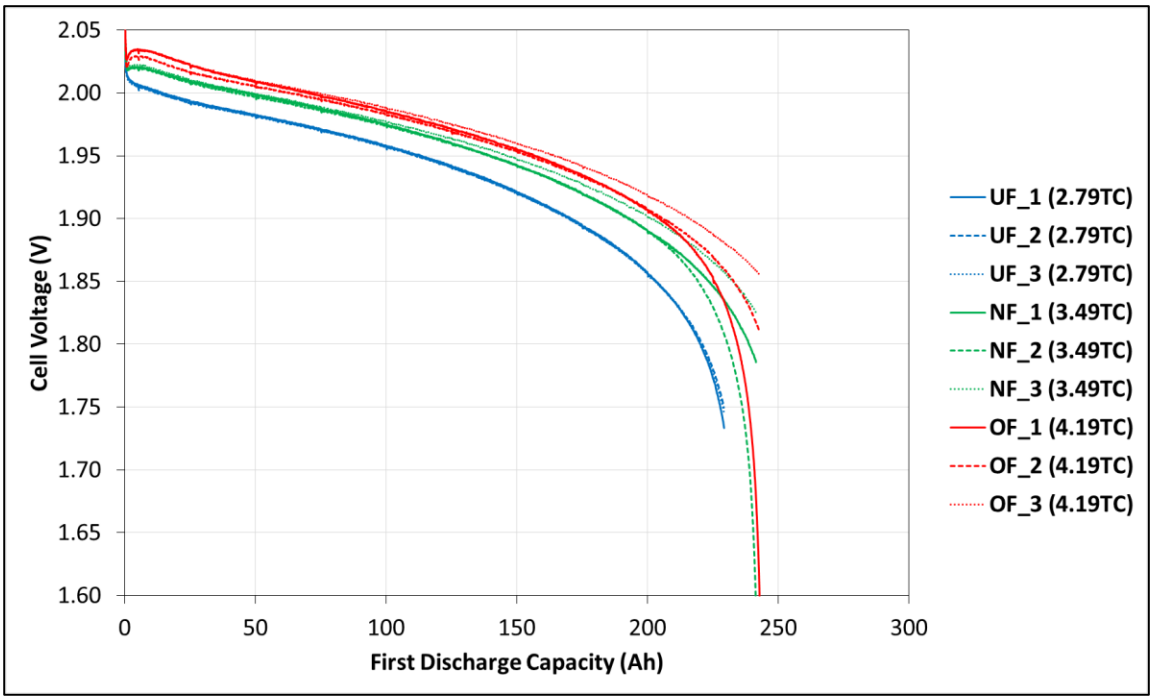

Figure 52 Cell Voltages as a Function of First Discharge Capacity (Floor Container Formation Method)

As shown in Figure 52, it is apparent that the cell voltages for respective formation levels have a positive correlation to total formation capacity. Furthermore, there was very tight cell voltage agreement between the three UF cells, with all of them reaching 1.75 V. Cells NF_2 and OF_1 each reached voltages of 1.60 V before the other two cells in their respective modules reached 1.75 V. Thus as constrained by the deep-cycling algorithm, this event triggered the end of the discharging process. In other words, as shown by the curves of the two other cells for each respective module (i.e., cells NF_1 and NF_3, and cells OF_2 and OF_3), additional discharge capacity might have been obtained for the NF and OF modules with the removal of cells NF_2 and OF_1, respectively. Specifically, it is estimated that an additional 5 Ah might have been obtained for the NF module, while an additional 11 Ah might have been obtained for the OF module.

Figure 53 highlights the individual cell voltages of the three different modules at the end of each deep-discharge cycle. In this figure, three individual cell voltages above 1.60 V for a respective module would indicate ideal cell voltage alignment.

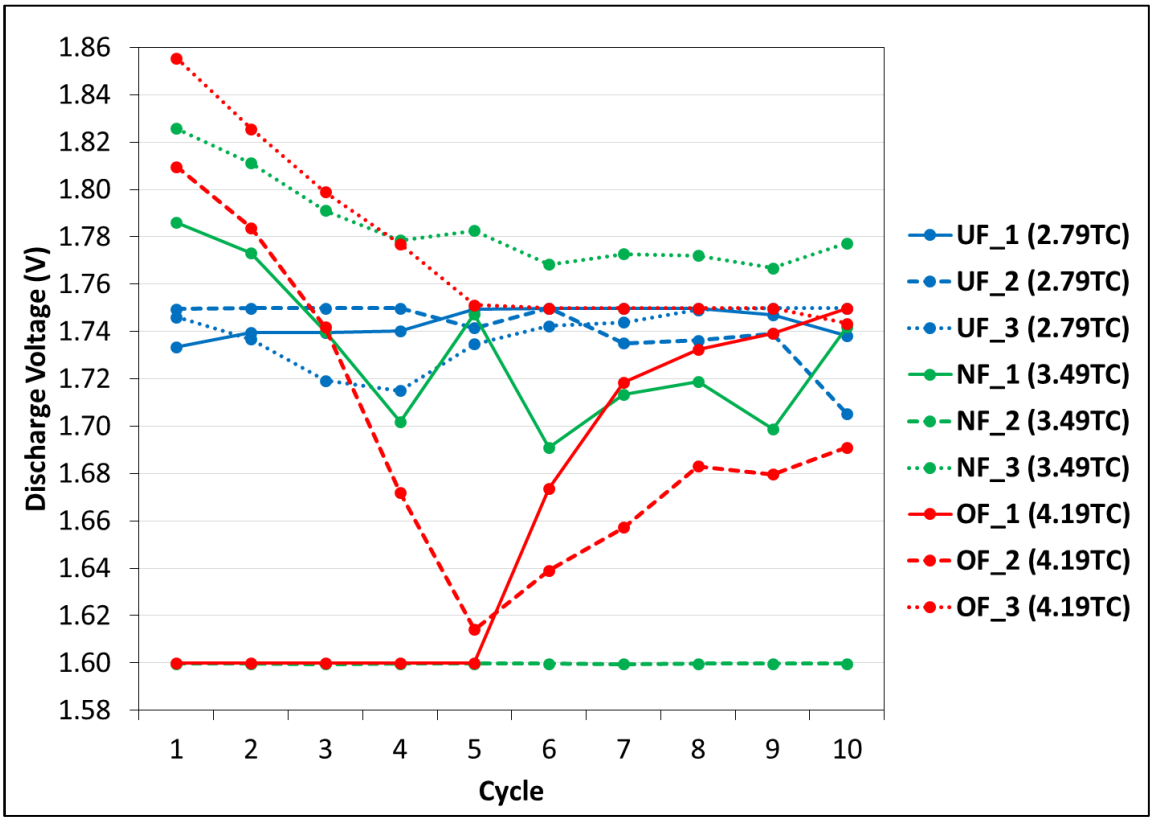

Figure 53 Discharge Voltages as a Function Cycle Number (Floor Container Formation Method)

As shown in Figure 53, ideal cell voltage alignment was maintained for the UF module over a span of 10 cycles, as individual cell voltages remained above 1.60 V. With respect to the NF module, cell NF_2 triggered the end of the discharging process for all 10 deep-cycles due to it continuously reaching a voltage of 1.60 V. With respect to the OF module, it is interesting to note that cell OF_1 remained misaligned for cycles 1-5, yet corrected itself for the remaining 5 cycles. Thus, although ideal cell voltage alignment was obtained for the OF module for cycles 6-10, it still offered no advantages with respect to discharge capacity when compared to the NF module, as was shown in Figure 49. Thus based on these results, it cannot be concluded that cell OF_1 (i.e., the misaligned OF cell) was the reason for the similar discharge capacity performances between the NF and OF modules. Instead, this discrepancy may simply be explained by manufacturing differences at SBC as alluded to in Table 17 with respect to the as-received characteristic of mass, or by the concept of formation threshold, where cells formed at a level higher than 3.49TC on the floor container formation method do not correlate into a better performing battery with respect to its discharge capacity.

6.2. Submerged Container Formation Method

Cell Formation

A total of 12 ELG15 cells were formed in series using the submerged container formation method at SBC for this phase of the project, which allowed for four cells to be formed at each formation level (i.e., UF, NF, and OF). However, it should be noted that within this string of 12 ELG15 cells, additional ELG15 cells were formed simultaneously (in series) in order to meet the physical constraints of the water bath, and to ensure optimal formation temperature.

Figure 54 shows the formation profile with respect to the pack voltage, formation capacity (divided by 10 for presentation purposes), formation current, and temperature of these cells as a function of formation time. This data was obtained using the built-in monitoring feature of the submerged container formation charger, due to scheduling conflicts at SBC which made it impossible to re-locate the measurement unit in time for this formation. The built-in monitoring feature of the submerged container formation charger used a different data logging interval based on the formation current. Specifically, a logging time interval of 5 minutes was used for the formation current of 22 A, while a logging time interval of 1 minute was used for the remainder of the formation. The cell temperature was limited to one ELG15 cell due to the design of the water bath. Again, as the cells were formed in series, once the UF and NF cells had reached their respective pre-determined formation level, the current was stopped and the cells were disconnected, before re-starting the current to continue forming the remaining cells. Thus in Figure 54, the reduction in current to 0 A at formation times of ~ 28 hours (i.e., 1704 Ah), ~ 34 hours (i.e., 2089 Ah), and ~ 39 hours (i.e., 2492 Ah) corresponds to the removal of the UF, NF, and OF cells, respectively. The reduction in current to 0 A at formation times of ~ 19 hours (i.e., 1154 Ah), and ~ 22 hours (i.e., 1352 Ah) were due to the removal of one ELG15 cell, and four ELG15 cells, respectively, as part of the requirements for a different research project. Finally, the reduction in current to 0 A at a formation time of ~ 29 hours (i.e., 1806 Ah) was due to the replacement of a faulty connection between the batteries in the water bath.

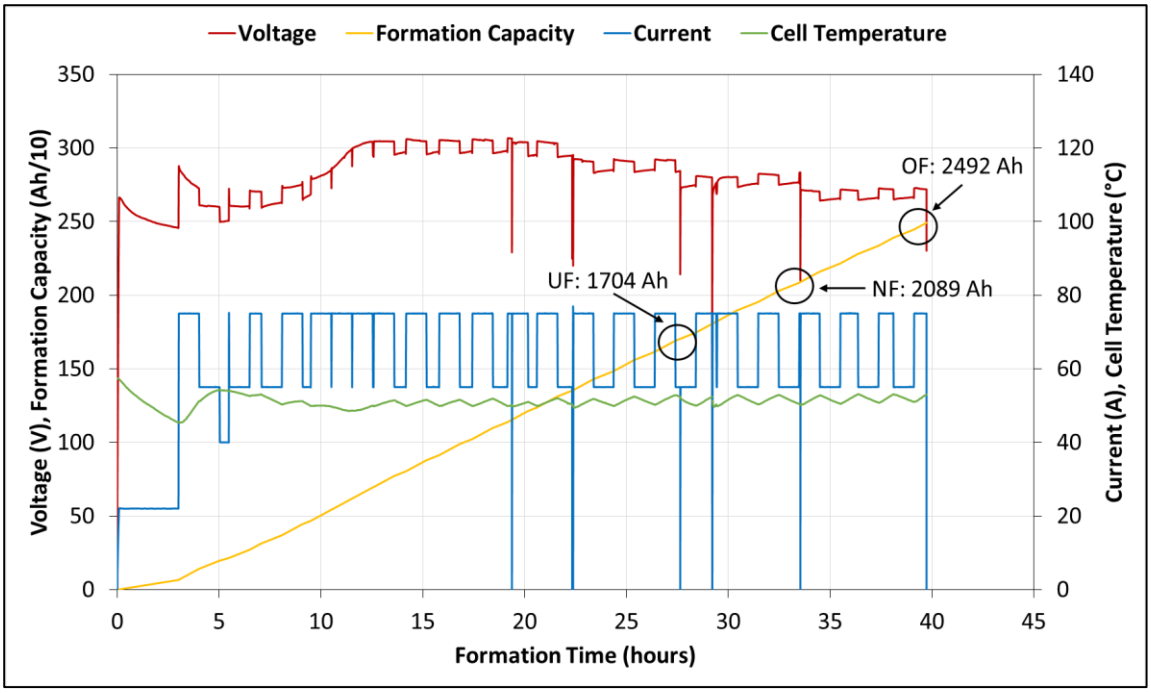

Figure 54 Formation Profile – Voltage, Formation Capacity, Current, and Cell Temperature (Submerged Container Formation Method)

As shown in Figure 54, the formation current behaved as was shown in Table 9. Specifically, after the completion of Step 3 (i.e., formation current of 22 A for 3 hours), the formation current varied between 55 A and 75 A for the majority of the formation, as dictated by the temperature of the cell. As expected, a limited amount of time, 26 minutes, was spent at a formation current of 40 A. The average current for this formation was calculated to be 65 A.

The pack cell voltage, as was the case for the voltage results of the floor container formation method, decreased at the start of formation, and then started increasing shortly after the 7 hour mark (i.e., ~ 322 Ah). These results are consistent with the first and second stages of formation.

The addition of distilled water was not necessary during the formation of these cells, although electrolyte with an SG value of 1.265 was used to top-up the cells at the end of formation. This addition of electrolyte was completed as per the standard operating procedures at SBC, therefore the volume of electrolyte added to each cell was not measured.

Table 18 shows the as-received characteristics of the 12 cells formed using the submerged container formation method, along with their respective minimum, maximum,

average, and RSD values. These measurements were taken one day after formation completion.

Table 18 Submerged Container ELG15 Cells – As-Received Characteristics

Cell /	UF (2.40TC)			NF (2.94TC)			OF (3.51TC)		
Statistics	*OCV (V)*	*Mass (kg)*	*SG*	*OCV (V)*	*Mass (kg)*	*SG*	*OCV (V)*	*Mass (kg)*	*SG*
1	2.090	17.2	1.2351	2.101	17.2	1.2473	2.116	17.5	1.2620
2	2.088	17.6	1.2349	2.108	17.6	1.2524	2.119	17.4	1.2631
3	2.084	17.6	1.2301	2.100	17.3	1.2462	2.117	17.3	1.2625
4	2.088	17.5	1.2339	2.105	17.3	1.2492	2.122	18.2	1.2661
Minimum	2.084	17.2	1.2301	2.100	17.2	1.2462	2.116	17.3	1.2620
Maximum	2.090	17.6	1.2351	2.108	17.6	1.2524	2.122	18.2	1.2661
Average	2.088	17.5	1.2335	2.104	17.4	1.2488	2.119	17.6	1.2634
RSD	0.121%	1.08%	0.189%	0.176%	1.00%	0.217%	0.125%	2.32%	0.146%

As shown in Table 18, there is little variation for the as-received characteristics of OCV and SG when respective formation levels are compared. The same cannot be said regarding the as-received characteristic of mass, which indicates differences in the amount of active material and/or electrolyte for these cells (i.e., manufacturing differences). Furthermore, there is a positive correlation between formation level, and the as-received values of OCV and SG. These results are in agreement with the as-received characteristics of the cells formed using the floor container formation method.

Deep-Cycling Characteristics

As part of the performance analysis, three cells with the same formation level were deep-cycled in a series configuration in order to represent the S-480 battery. These cells were cycled 10 times using the deep-cycling algorithm presented in Table 13, and exhibited the same characteristics as the cells formed using the floor container formation method. The reader is referred to Figure 47 for an example of the deep-cycling profile.

Discharge Capacity Characteristics

Figure 55 shows the measured discharge capacity, charge capacity, and coulombic efficiency of the three cells cycled in series for the UF, NF, and OF formation levels.

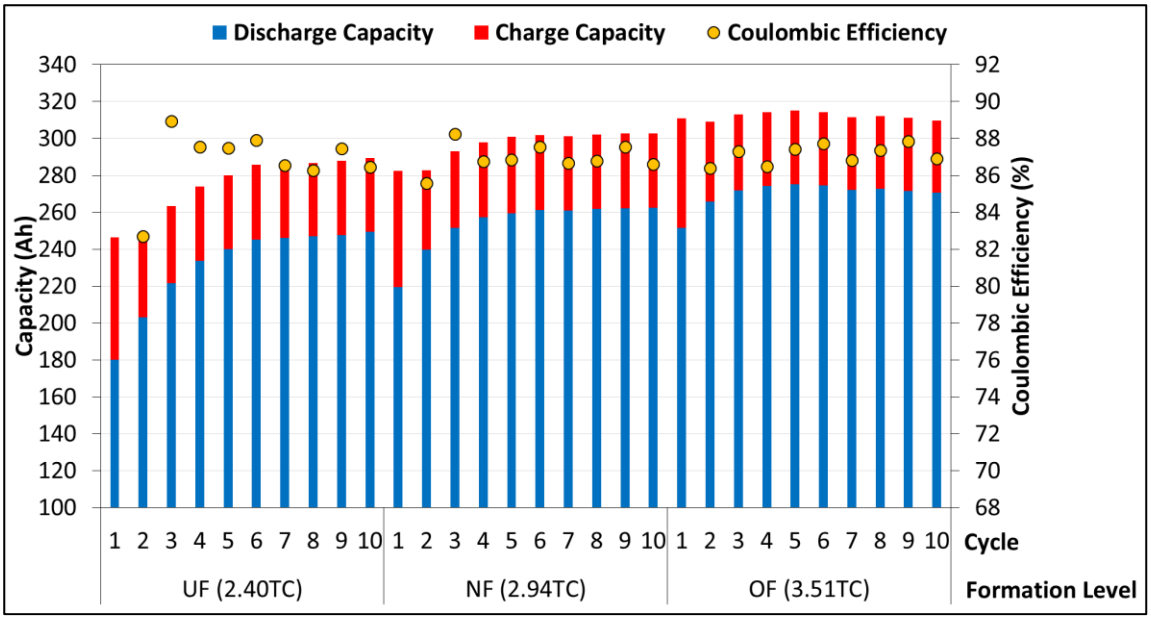

Figure 55 Module Discharge Capacity and Coulombic Efficiency Values (Submerged Container Formation Method)

As shown in Figure 55, there were significant differences between the discharge capacity results of the three different formation levels. Specifically for cycles 6-10 cycles, average discharge capacity results were determined to be 247 Ah, 262 Ah, and 272 Ah, for the UF, NF, and OF modules, respectively, while the average coulombic efficiency values were determined to be 86.9 %, 87.0 %, and 87.3 %, for the UF, NF, and OF modules, respectively. Only the OF cells met the rated capacity output of 231 Ah for all 10 cycles. While the UF and NF modules eventually reached rated capacity due to the continuation of their respective formation process, this process took four deep-cycles for the UF module, and one deep-cycle for the NF module. Again, it is worth noting that strong charging algorithms, such as the one used to deep-cycle these cells, are simply not available in off-grid solar systems. Thus, cells formed using the submerged container method at SBC with formation levels $\leq$ 2.94TC would likely never attain a fully formed state when implemented in off-grid solar applications.

The differences in discharge capacity results are further illustrated in Figure 56, which provides a discharge capacity comparison of the three modules.

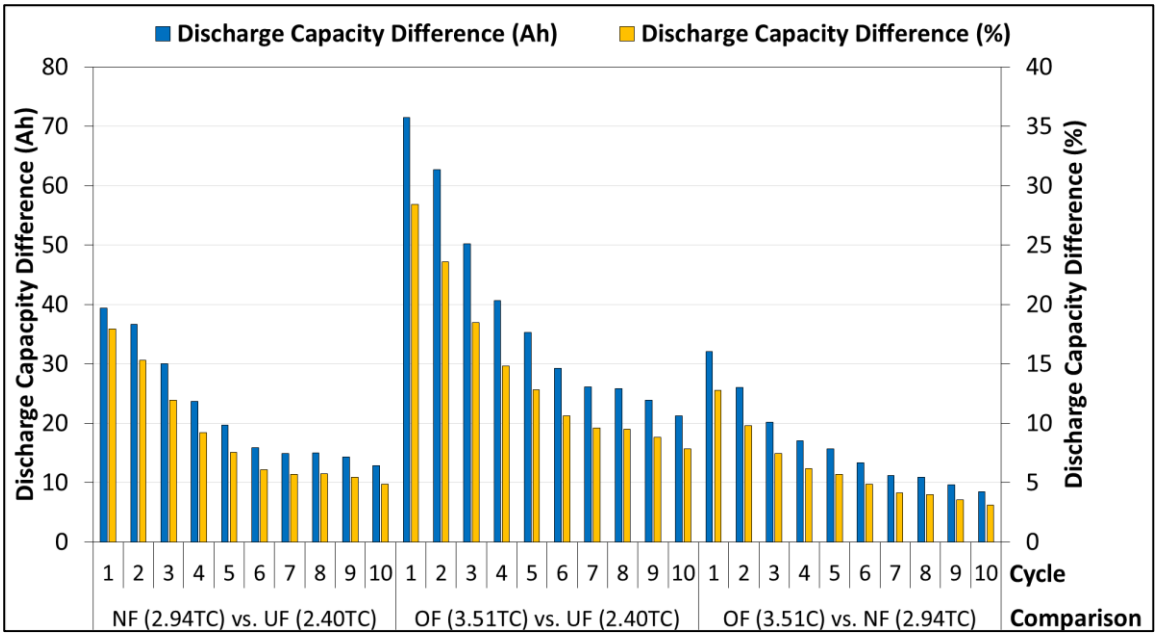

Figure 56 Module Discharge Capacity Comparison (Submerged Container Formation Method)

As shown in Figure 56, both the NF and OF modules offer discharge capacity advantages when compared to the UF module. Furthermore, unlike the comparison of the OF and NF modules for the floor container formation method where only small differences in discharge capacities were observed (i.e., < 1 %, see Figure 49), the average difference over a span of 10 cycles for these two modules with respect to the submerged container formation method is equivalent to 6 %. Thus with respect to the submerged container formation method, the OF formation level does offer advantages over the NF formation level, explained by the relatively low formation capacity of the latter, as alluded to in Table 12. Finally, all three discharge capacity differences are shown to be decreasing with deep-cycling iterations due to the continued formation process of the UF and NF modules.

Specific Gravity Characteristics

Figure 57 shows the average electrolyte SG values of the three modules which were measured before the start of each deep-cycle.

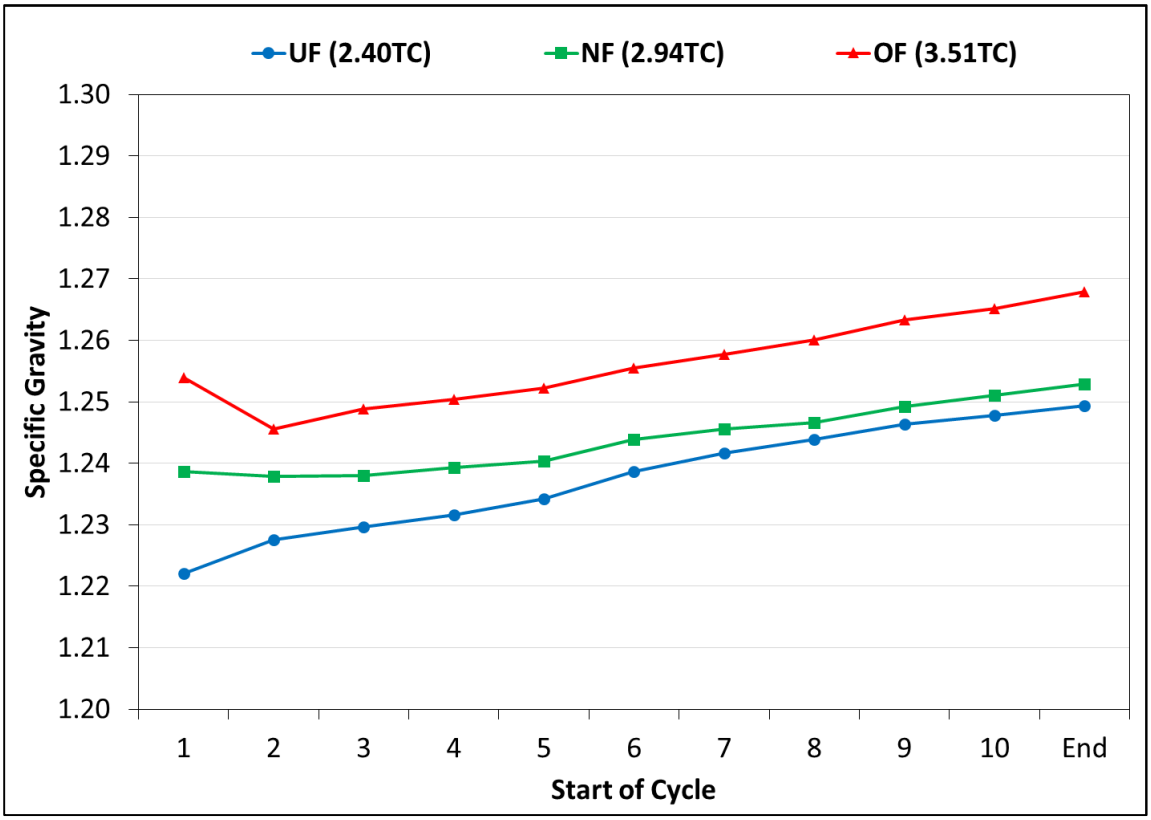

Figure 57 Module Electrolyte SG Values (Submerged Container Formation Method)

As shown in Figure 57, with the exception of the first cycle for the OF module, it is clear that there was an increase in electrolyte SG values for all three modules throughout the 10 deep-cycles. These SG characteristics are different than the ones which were obtained for the cells formed using the floor container formation method (see Figure 50), where SG values were shown to remain relatively constant. This difference is explained by the fact that the respective formation levels at SBC (i.e., UF, NF, and OF) are lower for the submerged container formation method when compared to the floor container formation method. Thus as the cells formed using the submerged container formation method continued their formation process (see Figure 55), a feature which was less prominent for the cells formed using the floor container formation method, additional H_2SO_4 was released from the plates, causing an increase in SG. It is hypothesized that electrolyte SG values

would have eventually reached steady-state values as the cells attained their fully formed state. The completion of additional deep-cycles, not possible due to the time constraints of this research project, would have been required to further study the electrolyte SG values of these cells.

Figure 58 shows the electrolyte SG profile for the 10th deep-cycle of one cell per module (i.e., cells UF_2, NF_1, and OF_1). This profile was obtained by taking SG measurements every half hour for the duration of the 10th deep-cycle. While these three cells were cycled individually in series as part of their respective modules, the three SG profiles are superimposed as a function of cycle time due to their similar characteristics.

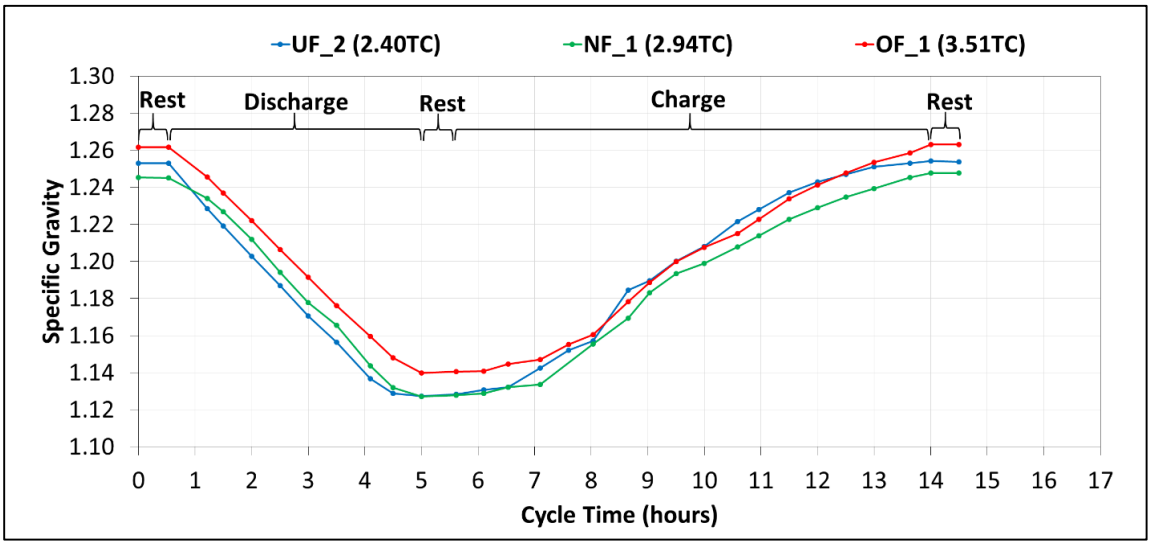

Figure 58 Electrolyte SG Profile – Cycle 10 (Submerged Container Formation Method)

As shown in Figure 58, all three cells regardless of initial formation capacity had similar SG profiles. Cell electrolyte SG values decreased during the first 4 hours of cycling, corresponding to the discharging process of the cycling algorithm (see Table 13). There was only a 30 minute rest period between the discharging phase and the subsequent charging phase for all three cells, thus it is shown that electrolyte SG values remained relatively constant during the first phase of the charging process, and only started increasing at the ~7 hour mark of the total cycling time, corresponding to the CV phase of the charging process. However, as was the case for the SG profile of the cells formed in phase 1 of this research project, is it believed that the SG values did increase at the start of the charging process, yet as the electrolyte samples were limited to being taken from the

top of the cell, the increase in electrolyte SG was not noticeable until the gassing process became more pronounced (i.e., CV phase of the charging process).

An interesting characteristic can be observed regarding cell UF_2. During the charging process, the electrolyte SG of cell UF_2 was shown to increase at a faster rate than both cells NF_1 and OF_1, only to settle at a value between the other two cells. This discrepancy can be explained by the difficulty in obtaining electrolyte SG values during the charging process due to the gassing of electrolyte.

Finally, as was the case for the SG profile of the cells formed in phase 1 of this research project, the total change in electrolyte SG values for these three cells was also calculated to be approximatively 0.10.

Internal Resistance Characteristics

Figure 59 shows the IR values of the three modules for cycles 1, 2, 4, 6, and 10 of the discharging and charging pulses using 10 seconds voltage intervals as a function of cycle number and discharge/charge Ah. The IR results are presented as the average of the three respective cells for each formation level. As the charging current pulses only occurred during the first phase of the charging process (see Table 13 – Step 4), IR values obtained at a charging capacity of 200 Ah correspond to approximatively 68 % of the total Ah input received by these cells during their respective charging processes.

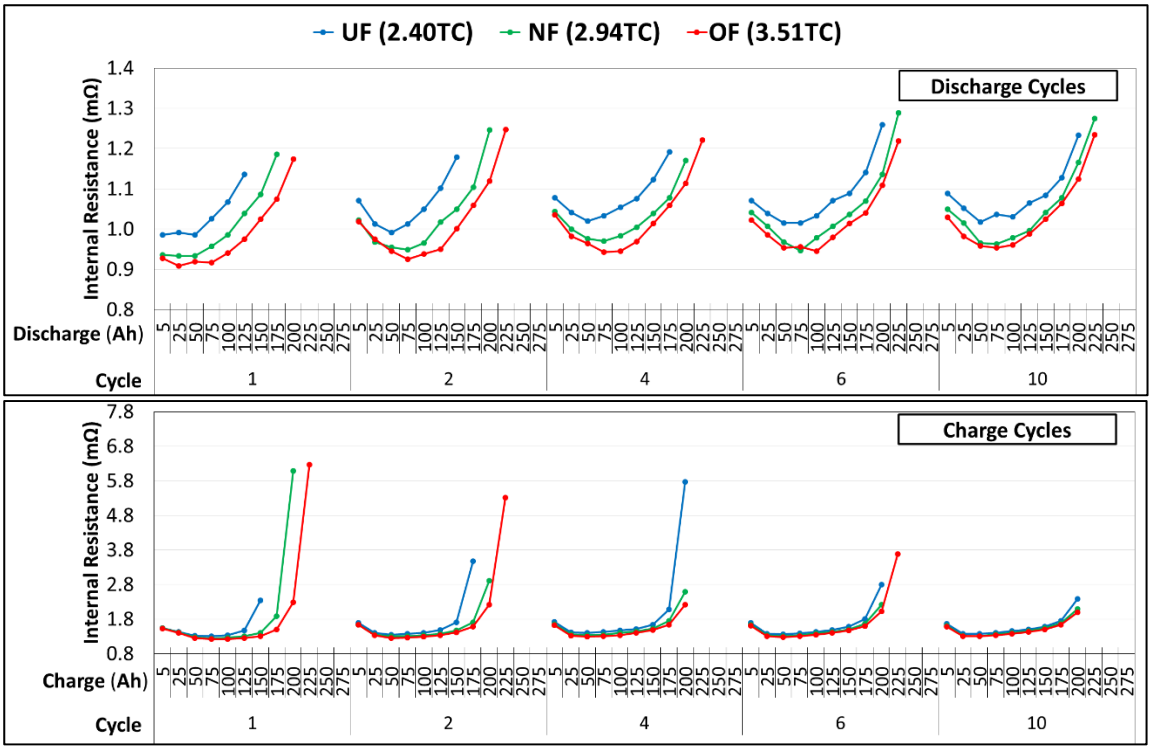

Figure 59 Discharge and Charge IR with 10 Second Voltage Intervals (Cycles 1, 2, 4, 6, and 10) (Submerged Container Formation Method)

As shown in Figure 59, the higher the formation level, the lower the IR when respective discharging and charging capacities are compared. Furthermore, overall IR values for the respective modules are shown to decrease with cycling iterations, due to the continued formation of the cells. These results are in agreement with the IR characteristics of the cells formed using the floor container formation method, and the shape of the IR curves shown in Figure 59 follow the same relationships as were explained for the IR results of the constant-current formation algorithm (see section 5.1).

Module Voltage Alignment

The three modules performed as expected with respect to discharge capacity, with the OF module achieving the better performance, followed by the NF module, and finally by the UF module. Nevertheless, the concept of a misaligned cell introduced in section 6.1 is still worth exploring. Thus, Figure 60 shows the individual discharge voltages of the nine cells as a function of their first discharge capacity, while Figure 61 shows the final discharge voltages of these same cells as a function of cycle number.

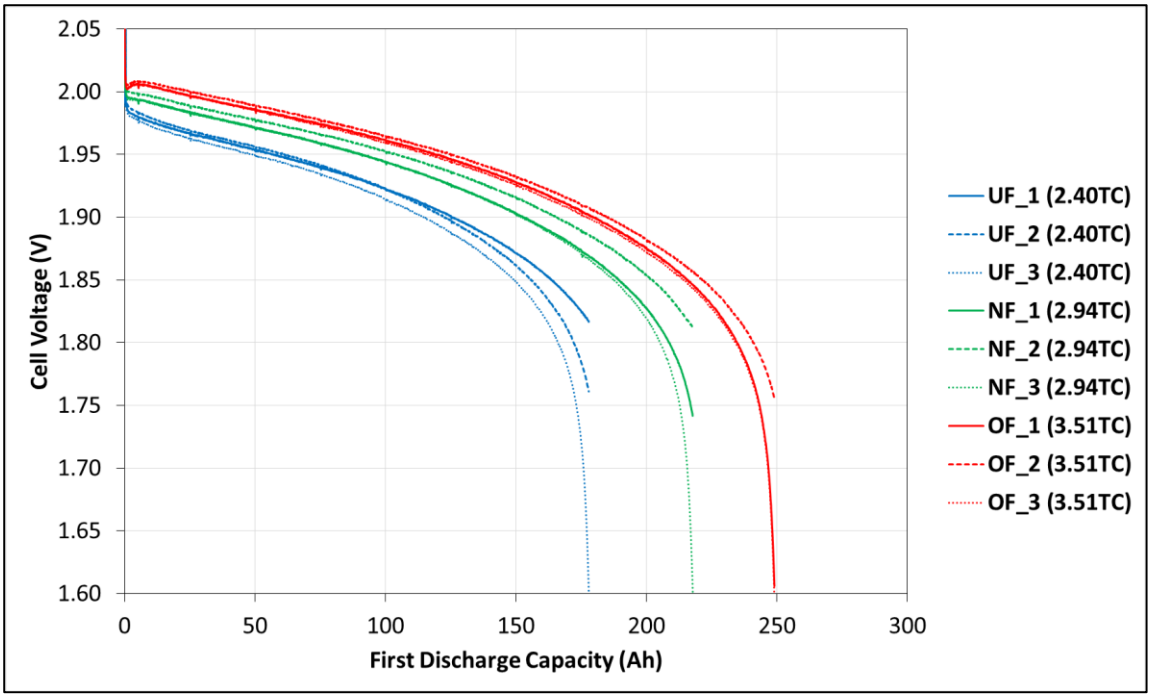

Figure 60 Cell Voltages as a Function of First Discharge Capacity (Submerged Container Formation Method)

As shown in Figure 60, it is apparent that the cell voltages of the respective formation levels have a positive correlation to total formation capacity. Furthermore, one cell per module (i.e., UF_3, NF_3, and OF_3) reached a voltage of 1.60 V before the other two cells in their respective modules reached 1.75 V, triggering the end of the discharging process. Thus, it is possible that without their respective misaligned cells, the UF and NF modules may have achieved higher discharge capacity results. This concept is less feasible for the OF module, as cell OF_2 was very close in attaining a discharge voltage of 1.75 V (i.e., final discharge voltage of 1.756 V).

Figure 61 highlights the individual cell voltages of the three different modules at the end of each deep-discharge cycle. In this figure, three individual cell voltages above 1.60 V for a respective module would indicate ideal cell voltage alignment.

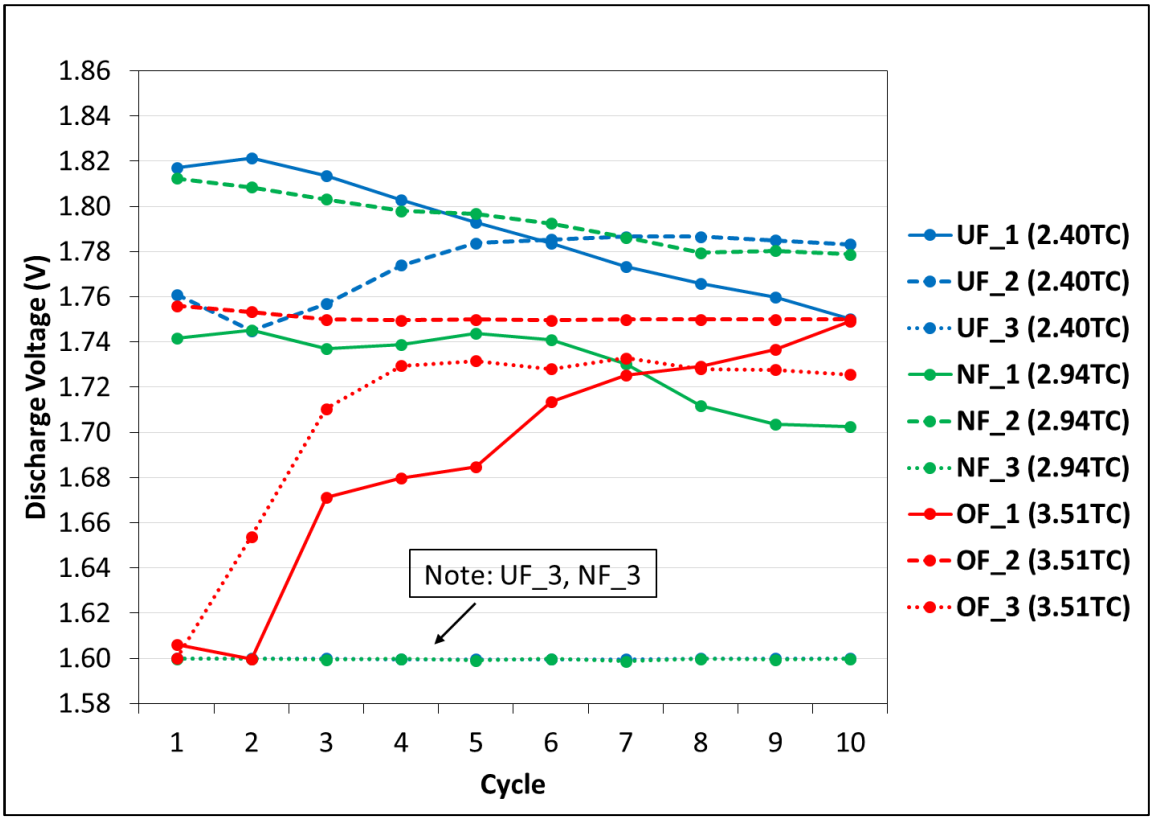

Figure 61 Discharge Voltages as a Function Cycle Number (Submerged Container Formation Method)

As shown in Figure 61, the OF module obtained ideal cell voltage alignment after the completion of two deep-cycles. With respect to the UF and NF modules, cells UF_3 and NF_3, respectively, triggered the end of the discharging process for all 10 of their deep-cycles.

Although misaligned cells were identified for the UF and NF modules over a span of 10 cycles, UF_3, and NF_3, respectively, it is not believed that their removal would have resulted in substantial capacity gains for these two respective modules. Specifically, based on the first discharge capacity characteristics of these two modules as shown in Figure 55, the UF and NF cells would have required additional discharge capacities of 51 Ah (i.e., an additional 50 minutes of discharge time), and 12 Ah (i.e., an additional 12 minutes of discharge time), respectively, in order to attain rated capacity on their first discharge. However, based on the cell voltage curves of cells UF_2 and NF_1, only a limited amount of additional discharge capacity (~ 5 Ah) would have been obtained before these two cells triggered the end of the discharging process for their respective module. This is because

the elapsed time for a cell to reach 1.60 V from a voltage of 1.75 V using this discharge rate was calculated to be approximatively 5.3 minutes. Thus based on these results, it cannot be concluded that cells UF_3 and NF_3 were the reasons for the poor capacity performances of their respective modules. Instead, the reduced performance in capacity for the UF and NF modules can be explained by their relatively low formation levels when compared to the other formation methods used at SBC, as alluded to in Table 12.

6.3. Circulated Electrolyte Formation Method

Cell Formation

As shown in Table 10, two different formation algorithms had to be employed to obtain the desired formation levels for the circulated electrolyte formation method. As such, the two circuits on the circulated electrolyte formation charger were used simultaneously to form the required ELG15 cells. Specifically, four ELG15 cells were formed in series on circuit #1 to the UF level, while an additional eight ELG15 cells were formed in series on circuit #2, resulting in four NF cells and four OF cells. It should be noted that within the string of four ELG15 cells on circuit #1, an additional four ELG15 cells were formed simultaneously (in series) as part of the requirements for a different research project.

Figure 62 shows the formation profile of the eight cells formed on circuit #1 (i.e., UF cells) and the formation profile of the eight cells formed on circuit #2 (i.e., NF and OF cells). Both formation profiles are represented by their respective pack voltage, formation capacity (divided by 100 for presentation purposes), and formation current as a function of formation time. The data for both formation profiles was obtained simultaneously using the measurement unit with a data logging rate of 1 second, in order to obtain higher resolution data with respect to the formation profiles. It is important to note that the circulated electrolyte formation charger at SBC has a slow response rate. In other words, a change in current as dictated by the formation algorithm resulted in a brief reduction in current until it reached its desired target, thus explaining the unwarranted drop in current at formation times of 1 hour, 17 hours, and 18 hours for the cells formed on circuits #1 and #2.

(a)

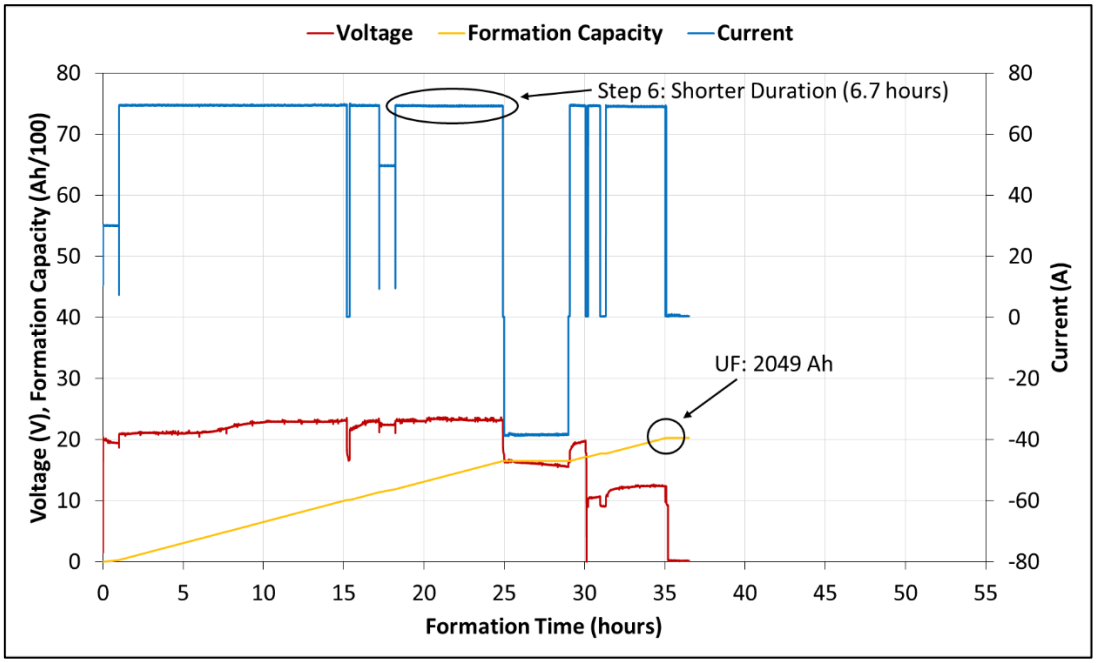

(b)

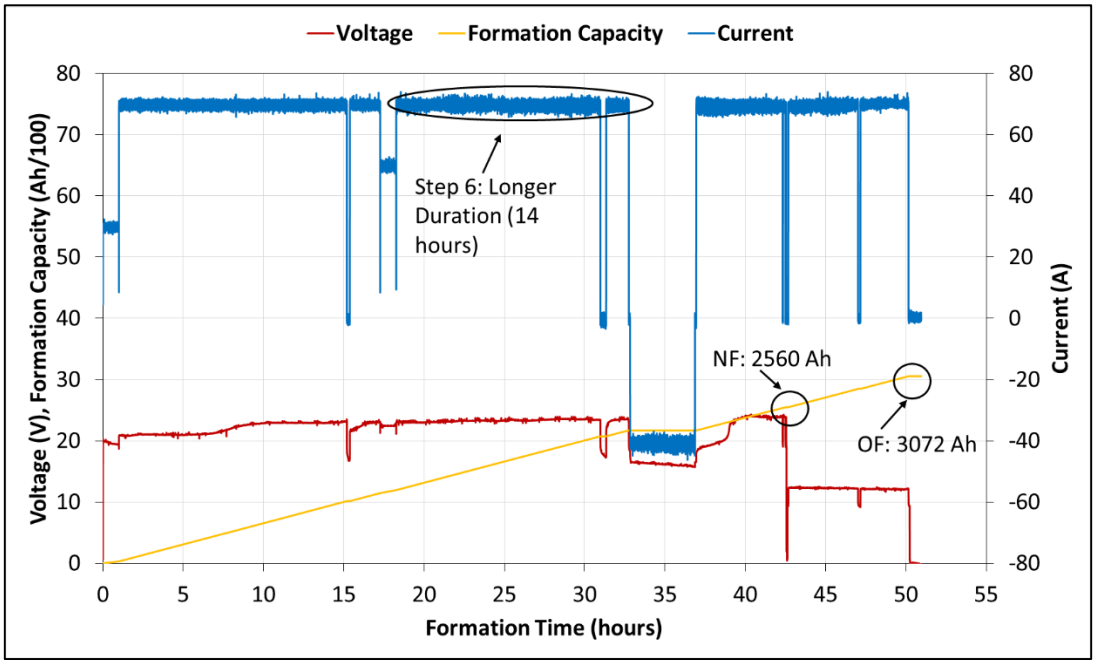

Figure 62 Formation Profile – Voltage, Formation Capacity, and Current (Circulated Electrolyte Formation Method) – a) Circuit # 1 (UF Cells), b) Circuit #2 (NF and OF Cells)

As shown in Figure 62, the formation current behaved as was shown in Table 10 for both algorithms. The formation profile of the NF and OF cells is of lower quality (i.e., noise on the current signal) than the formation profile of the UF cells, which was determined to be caused by the rectifier of circuit #2.

There were three current interruptions during the formation of the UF cells. Firstly, at a formation time of 15 hours (i.e., 1008 Ah), the current was reduced to 0 A for a span of 10 minutes due to the sudden failure of the circulated electrolyte pumping system. Secondly, at a formation time of 30 hours (i.e., 1743 Ah), the current was stopped and the first set of four ELG15 cells were disconnected, before re-starting the current to continue forming the UF cells. Again, these initial four cells were formed as part of the requirements for a different research project. And thirdly, at a formation time of 31 hours (i.e., 1813 Ah), the current was again reduced to 0 A for a span of 20 minutes due to low levels of electrolyte in the storage tanks.

In addition to the same current interruptions experienced on circuit #1, circuit #2 experienced two additional current interruptions due to the additional formation time. Firstly, at a formation time of 43 hours (i.e., 2653 Ah), the current was stopped and the four NF ELG15 cells were disconnected, before re-starting the current to continue forming the OF cells. And secondly, at a formation time of 47 hours (i.e., 2933 Ah), the current was again reduced to 0 A for a span of 10 minutes due to low levels of electrolyte in the storage tanks.

For both formation profiles, the pack cell voltage decreased at the start of formation, and then started increasing shortly after the 6 hour mark (i.e., ~ 376 Ah). These results are consistent with the first and second stages of formation.

The addition of distilled water was not necessary during the formation of these cells. As the circulated electrolyte formation method allows for the electrolyte of the LABs to be changed automatically, the algorithm was preset to balance the electrolyte of the cells to a SG value 1.265 at the end of the formation process (although it should be noted that this procedure is not exact). Therefore, the volume of additional electrolyte added to each cell was not measured.

Table 19 shows the as-received characteristics of the 12 cells formed using the circulated electrolyte formation method, along with their respective minimum, maximum, average, and RSD values. These measurements were taken three days after formation completion.

Table 19 Circulated Electrolyte ELG15 Cells – As-Received Characteristics

Cell /	UF (2.89TC)			NF (3.61TC)			OF (4.33TC)		
Statistics	*OCV (V)*	*Mass (kg)*	*SG*	*OCV (V)*	*Mass (kg)*	*SG*	*OCV (V)*	*Mass (kg)*	*SG*
1	2.115	18.1	1.2697	2.111	18.0	1.2670	2.108	17.8	1.2646
2	2.116	18.1	1.2697	2.112	18.0	1.2677	2.108	17.8	1.2644
3	2.114	18.0	1.2682	2.109	18.6	1.2657	2.106	17.9	1.2644
4	2.113	18.4	1.2695	2.111	18.7	1.2673	2.108	17.8	1.2643
Minimum	2.113	18.0	1.2682	2.109	18.0	1.2657	2.106	17.8	1.2643
Maximum	2.116	18.4	1.2697	2.112	18.7	1.2677	2.108	17.9	1.2646
Average	2.115	18.2	1.2693	2.111	18.3	1.2669	2.108	17.8	1.2644
RSD	0.061%	0.95%	0.057%	0.060%	2.06%	0.068%	0.047%	0.28%	0.010%

As shown in Table 19, unlike the as-received characteristics of the cells formed using the floor container and submerged container formation methods, there is no positive correlation between the formation levels and the as-received values of OCV and SG. Specifically, it is interesting to note that it is the UF cells that have the highest values with regards to OCV and SG values. This will be explored in more details below. Furthermore, there is variation regarding the as-received characteristic of mass, which indicates differences in the amount of active material and/or electrolyte for these cells (i.e., manufacturing differences).

Deep-Cycling Characteristics

As part of the performance analysis, three cells with the same formation level were deep-cycled in a series configuration in order to represent the S-480 battery. These cells were cycled 10 times using the deep-cycling algorithm presented in Table 13, and exhibited the same characteristics as the cells formed using the floor container formation method. The reader is referred to Figure 47 for an example of the deep-cycling profile.

Discharge Capacity Characteristics

Figure 63 shows the measured discharge capacity, charge capacity, and coulombic efficiency of the three cells cycled in series for the UF, NF, and OF formation levels.

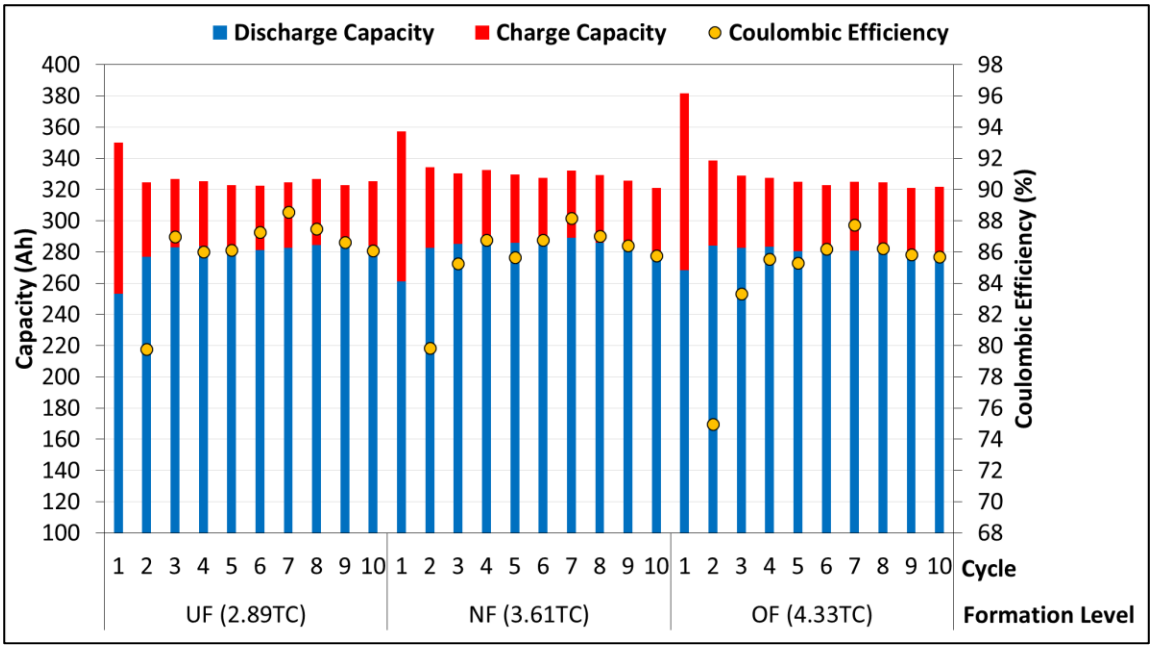

Figure 63 Module Discharge Capacity and Coulombic Efficiency Values (Circulated Electrolyte Formation Method)

As shown in Figure 63, discharge capacity results between the three different formation levels were similar. Specifically for cycles 6-10, average discharge capacity results were determined to be 283 Ah, 285 Ah, and 280 Ah, for the UF, NF, and OF modules, respectively, while the average coulombic efficiency values were determined to be 87.2 %, 86.8 %, and 86.3 %, for the UF, NF, and OF modules, respectively. Furthermore, unlike the cells formed using the floor container or submerged container formation methods, it should be noted that with the exception of the first cycle, none of these three modules appear to be continuing their formation process. This can be explained by the fact that all three modules attained a fully formed state during their respective formation process. Finally, for all 10 cycles, all three modules met the rated capacity output of 231 Ah.

The similarities in discharge capacity results are further illustrated in Figure 64, which provides a discharge capacity comparison of the three modules.

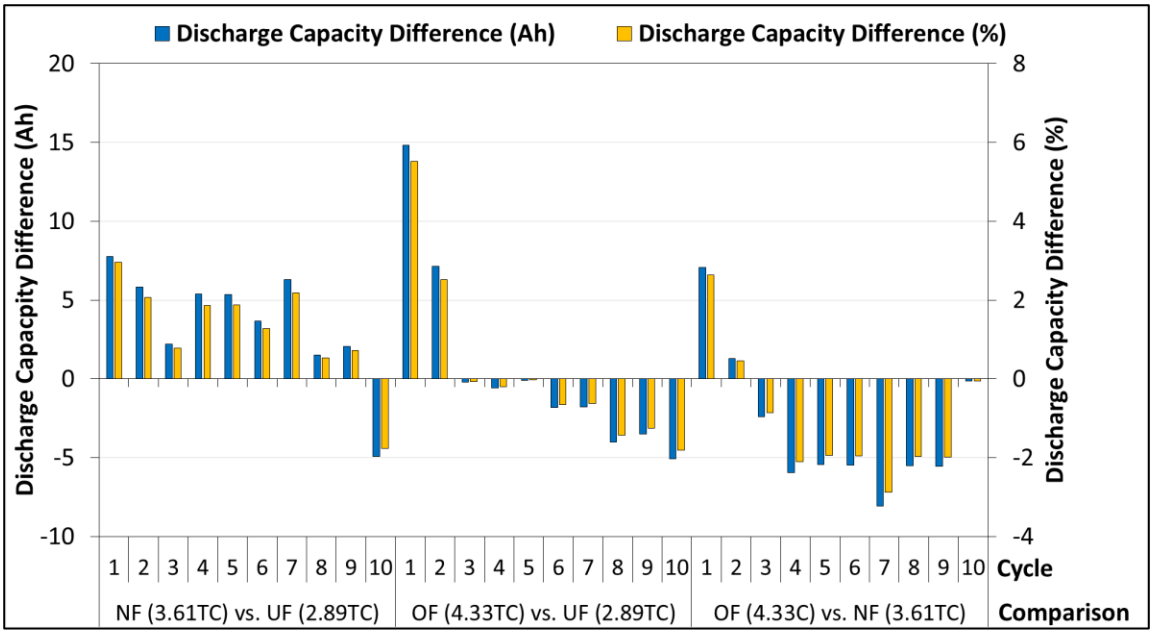

Figure 64 Module Discharge Capacity Comparison (Circulated Electrolyte Formation Method)

As shown in Figure 64, it is apparent that the NF or OF cells do not offer significant advantages with respect to discharge capacity when compared to the UF cells, with discharge capacity differences of ~ 2 % between the NF and UF modules, and the OF and UF modules. Again, this is explained by the fact that all three modules attained a fully formed state during their respective formation process.

Specific Gravity Characteristics

Figure 65 shows the average electrolyte SG values of the three modules which were measured before the start of each deep-cycle.

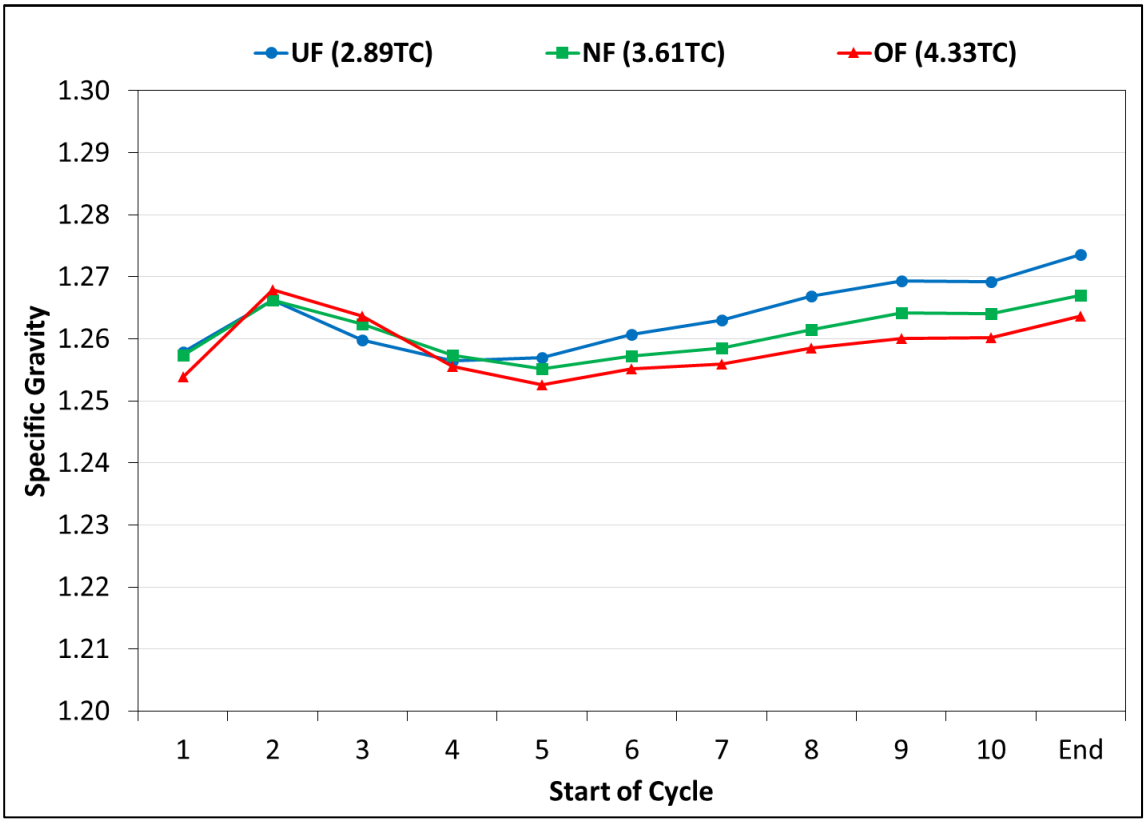

Figure 65 Module Electrolyte SG Values (Circulated Electrolyte Formation Method)

As shown in Figure 65, there was an increase in electrolyte SG values for all three modules following their first deep-cycle, coinciding with the initial increase in capacity results as shown in Figure 63. Following this increase, there was a decrease in electrolyte SG values for all three modules between cycles 2 and 5, which can be explained by the correction of the electrolyte to SG values of 1.265 at the end of the formation process. It is difficult to justify the subsequent increase in electrolyte SG values between cycles 5 and 10, as this did not translate to a continuous increase in module performance with respect to discharge capacity. As such, these results are not in agreement with the SG results of the floor container formation method or the submerged container formation method, where it was shown that increases in discharge capacity corresponded to an increase in in SG values. Thus with respect to the circulated electrolyte formation method, it can be stated that although the modules are fully formed, additional H_2SO_4 is nonetheless released from the plates during deep-cycling operation. It is hypothesized that electrolyte SG values would have eventually reached steady-state values. The completion of additional deep-cycles, not

possible due to the time constraints of this research project, would have been required to further study the electrolyte SG values of these cells.

Furthermore, it is interesting to note that while the electrolyte SG values are relatively similar between all 9 cells, the UF cells (followed by the NF cells) had the highest overall values following the completion of the 4th deep-cycle. Thus, while it is possible that the higher electrolyte SG values for the UF cells were influenced by a reduction in Step 6 of the formation algorithm when compared to the NF and OF cells (see Table 10 and Figure 62), this does not explain why the electrolyte SG values of the NF cells were determined to be higher than the electrolyte SG values of the OF cells. Instead, this discrepancy may be explained by the fact that the electrolyte which was used to balance the UF cells at end of formation had a higher H_2SO_4 concentration than the electrolyte which was used to balance the NF and OF cells. This in turn resulted in higher SG values for the UF cells. This concept is supported by the as-received characteristics of the cells (see Table 19), where the UF cells are shown to have the highest electrolyte SG values.

Figure 66 shows the electrolyte SG profile for the 10th deep-cycle of one cell per module (i.e., cells UF_2, NF_2, and OF_2).

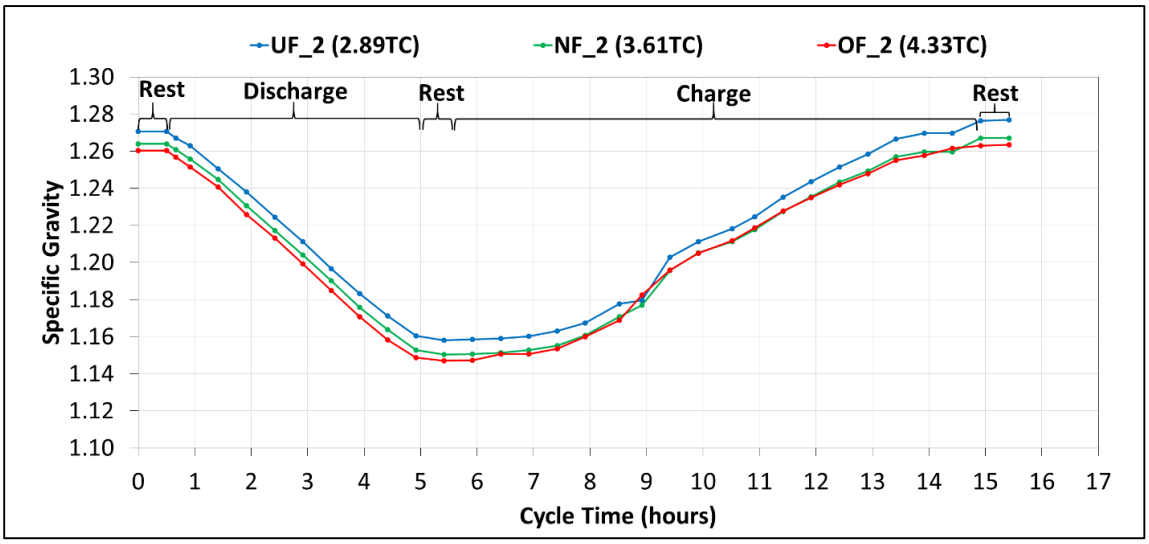

Figure 66 Electrolyte SG Profile – Cycle 10 (Circulated Electrolyte Formation Method)

As shown in Figure 66, the circulated electrolyte SG profile is in agreement with the SG profile of the cells formed using the submerged container formation method, with the

exception of higher SG values for the UF cell when compared to the NF or OF cells, as was discussed above.

Internal Resistance Characteristics

Figure 67 shows the IR values of the three modules for cycles 1, 2, 4, 6, and 10 of the discharging and charging pulses using 10 seconds voltage intervals as a function of cycle number and discharge/charge Ah. The IR results are presented as the average of the three respective cells for each formation level. As the charging current pulses only occurred during the first phase of the charging process (see Table 13 – Step 4), IR values obtained at a charging capacity of 200 Ah correspond to approximatively 61 % of the total Ah input received by these cells during their respective charging processes.

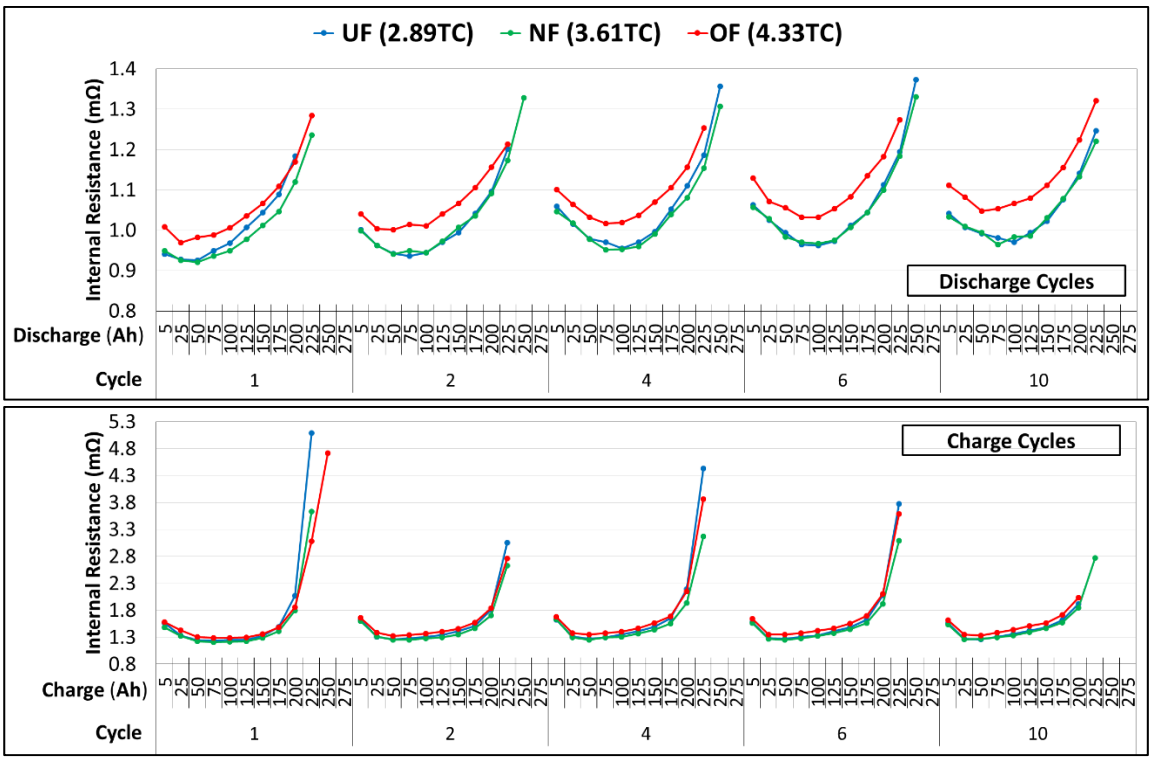

Figure 67 Discharge and Charge IR with 10 Second Voltage Intervals (Cycles 1, 2, 4, 6, and 10) (Circulated Electrolyte Formation Method)

As shown in Figure 67, these results are not in agreement with the IR results of the floor container and submerged container formation methods. Specifically, the OF cells, even though they received the highest amount of formation capacity relatively to the other two modules, had the highest IR values for both discharging (distinctively) and charging

capacities throughout the 10 deep-cycles. It is believed that these results were influenced by the aforementioned discrepancies in electrolyte SG values.

Furthermore, the overall IR values for the respective modules did not decrease with cycling iterations, which is in agreement with the capacity results shown in Figure 63, as these cells were not shown to be continuing their formation process. Finally, the shape of the IR curves shown in Figure 67 follow the same relationships as were explained for the IR results of the constant-current formation algorithm (see section 5.1).

Module Voltage Alignment

While the OF module achieved slightly better performance characteristics with respect to its discharge capacity when compared to the other two modules, it did not behave as expected with respect to its SG and IR values. Thus, the concept of a misaligned cell introduced in section 6.1 is explored below. Figure 68 shows the individual discharge voltages of the nine cells as a function of their first discharge capacity, while Figure 69 shows the final discharge voltages of these same cells as a function of cycle number.

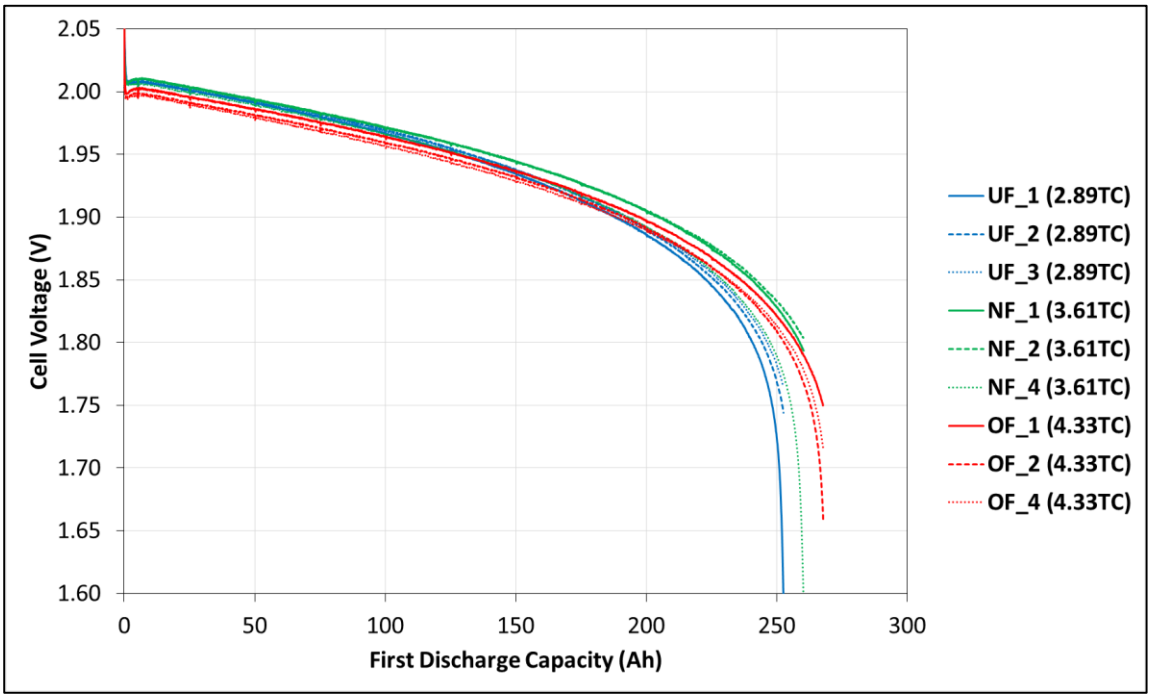

Figure 68 Cell Voltages as a Function of First Discharge Capacity (Circulated Electrolyte Formation Method)

As shown in Figure 68, unlike the results of the floor container and submerged container formation methods, there is no clear distinction between the cell voltage values of the three

different modules during their first discharge. In fact, it is interesting to note that for the first 150 Ah of discharge capacity, it is the OF cells which had the lowest cell voltage values. Thus while the OF module obtained a higher discharge capacity value on its first discharge when compared to the other two modules, it can be stated that based on individual cell voltages, there is relatively no difference between these three formation levels when formed using the circulated electrolyte formation method. Again, this can be explained by the fact that all three modules attained a fully formed state during their respective formation process.

Furthermore, cells UF_1 and NF_4 reached voltages of 1.60 V before the other two cells in their respective modules reached 1.75 V, triggering the end of the discharging process. Thus, it is possible that without their respective misaligned cells, the UF and NF modules may have achieved higher discharge capacity results. Specifically it is estimated that an additional 5 Ah might have been obtained for the UF module, while an additional 8 Ah might have been obtained for the NF module.

Figure 69 highlights the individual cell voltages of the three different modules at the end of each deep-discharge cycle. In this figure, three individual cell voltages above 1.60 V for a respective module would indicate ideal cell voltage alignment.

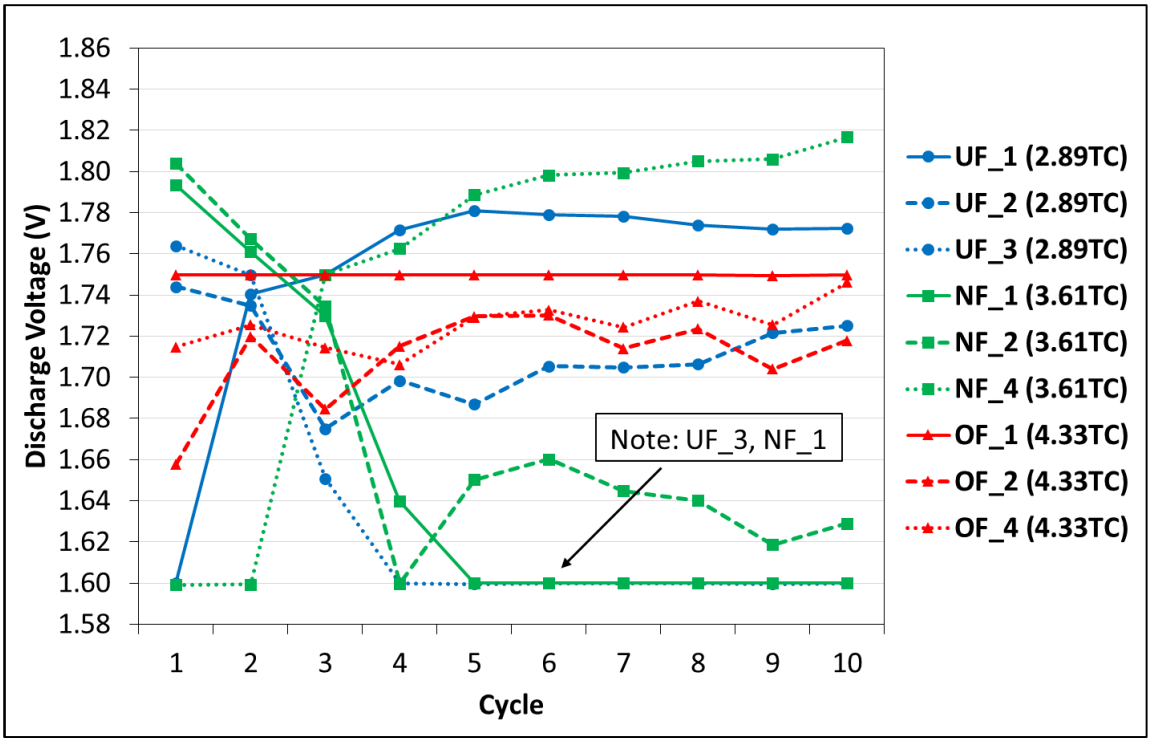

Figure 69 Discharge Voltages as a Function Cycle Number (Circulated Electrolyte Formation Method)

As shown in Figure 61, ideal cell voltage alignment was maintained for the OF module over a span of 10 cycles, as individual cell voltages remained above 1.60 V. With respect to the UF module, cell UF_1 triggered the end of the discharging process for the first deep-cycle, while cell UF_3 triggered the end of the discharging process for deep-cycles 4 – 10. With respect to the NF module, cell NF_3 triggered the end of the discharging process for deep-cycles 1 – 2, cell NF_2 triggered the end of the discharging process for the 4th deep-cycle, and cell NF_1 triggered the end of the discharging process for deep-cycles 5 – 10. These results exhibit the same characteristics as the floor container and submerged container formation methods, where it was shown that the OF modules were able to attain ideal cell voltage alignment.

Although misaligned cells were identified for the UF and NF modules over a span of 10 cycles, none were identified for the OF module. In other words, a potential misaligned cell in the OF module does not explain the discrepancies with regards to its SG and IR characteristics when compared to the UF and NF modules. Instead, as was stated above, the resulting discrepancies of SG may have been influenced by the electrolyte SG balancing

at the end for the formation process at SBC, while the resulting discrepancies of IR may have been influenced by these same SG values.

6.4. Tank Formation Method

Cell Formation

A total of 60 individual tanks, each comprised of four cassettes with eight positive plates, were formed in series using the tank formation method at SBC for this phase of the project. In order to ensure the proper amount of plates were formed at each desired formation level, six tanks (i.e., 24 cassettes) were formed at both the UF and NF levels, while the remaining 48 tanks (i.e., 192 cassettes) were formed at the OF level. With respect to this research project, this resulted in the assembly of 24 UF ELG15 cells, 10 NF ELG15 cells, and 10 OF ELG15 cells.

Figure 70 shows the formation profile with respect to the overall tank voltage, formation current, and formation capacity of these plate as a function of formation time. One should note that the measured formation current values, and corresponding capacity values were scaled to represent the formation profile of an ELG15 cell, thus providing a comparison basis between the four formation methods. The measurement unit was used to log formation data every 6 seconds, obtained by taking the average of six 1 second readings. Similarly to the other formation methods, as the 60 individual tanks were formed in series, once the six UF and NF tanks had reached their respective pre-determined formation level, the current was stopped and the respective cassettes were removed, before re-starting the current to continue forming the remaining plates. Thus as shown in Figure 70, the reduction in current to 0 A at formation times of ~ 22 hours (i.e., 1223 Ah per ELG15 cell), ~ 28 hours (i.e., 1534 Ah per ELG15 cell), and ~ 34 hours (i.e., 1846 Ah per ELG15 cell), corresponded to the removal of the UF, NF, and OF cassettes, respectively.

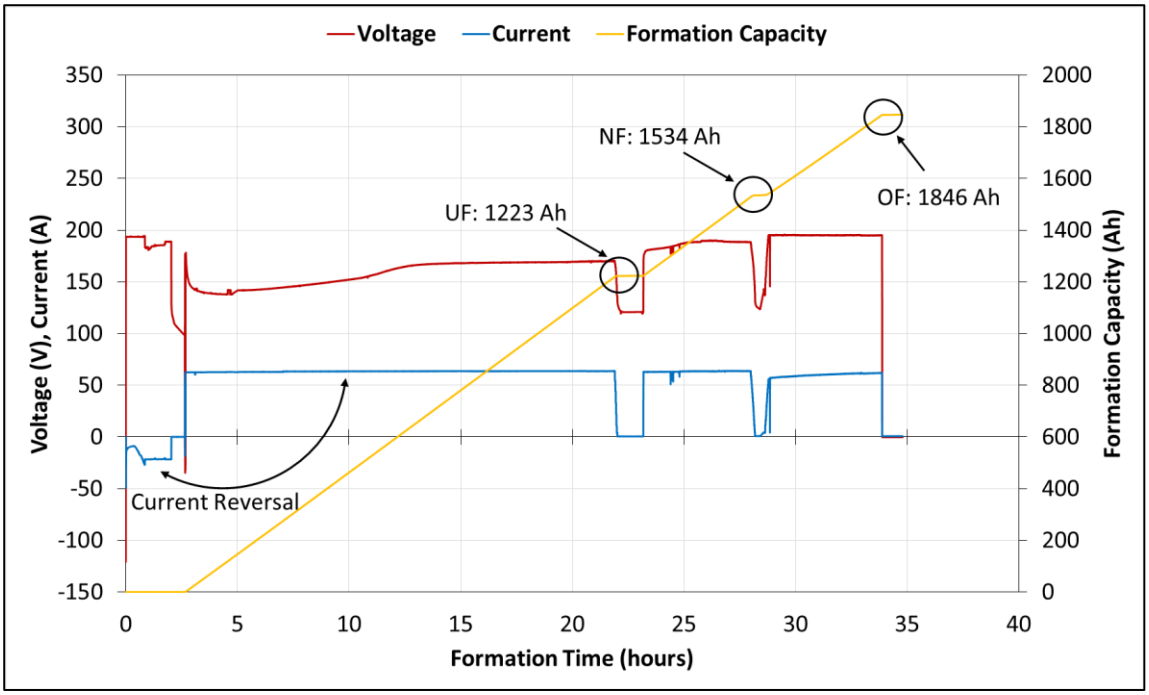

Figure 70 Formation Profile – Voltage, Current, and Formation Capacity (Tank Formation Method)

As shown in Figure 70, the formation current behaved as was shown in Table 11. Specifically, after the completion of Step 2 (i.e., rest for 30 minutes), the formation current was reversed and maintained itself at a value of 63.0 A for the formation of the UF and NF plates. Due to the limitations of the formation charger, it was unable to maintain this CC value once the NF plates were removed, instead maintaining a formation current of 60.0 A for the remainder of the formation period.

The overall tank voltage decreased at the start of formation (i.e., 3 hour mark), and then started increasing shortly after the 5 hour mark (i.e., 155 Ah). These results are consistent with the first and second stages of formation. However, unlike the other three formation methods, where the removal of ELG15 cells resulted in a drop in pack voltage, the individual tanks maintain a positive charge of approximatively 2.1 V following the removal of their respective cassettes. This explains the lack of any significant voltage drop following the removal of the respective cassettes once a desired formation level had been reached.

The addition of distilled water was not necessary during the formation of these cells, as the plates were formed using an abundance of electrolyte. Furthermore as stated in

section 2.2.3, cells formed using this formation method are provided in a dry-charged state (i.e., without electrolyte), thus no electrolyte was added to the cells following their assembly at SBC.

Figure 71 shows an example of the positive and negative plates formed using the tank formation method at the three different formation levels following their respective drying process.

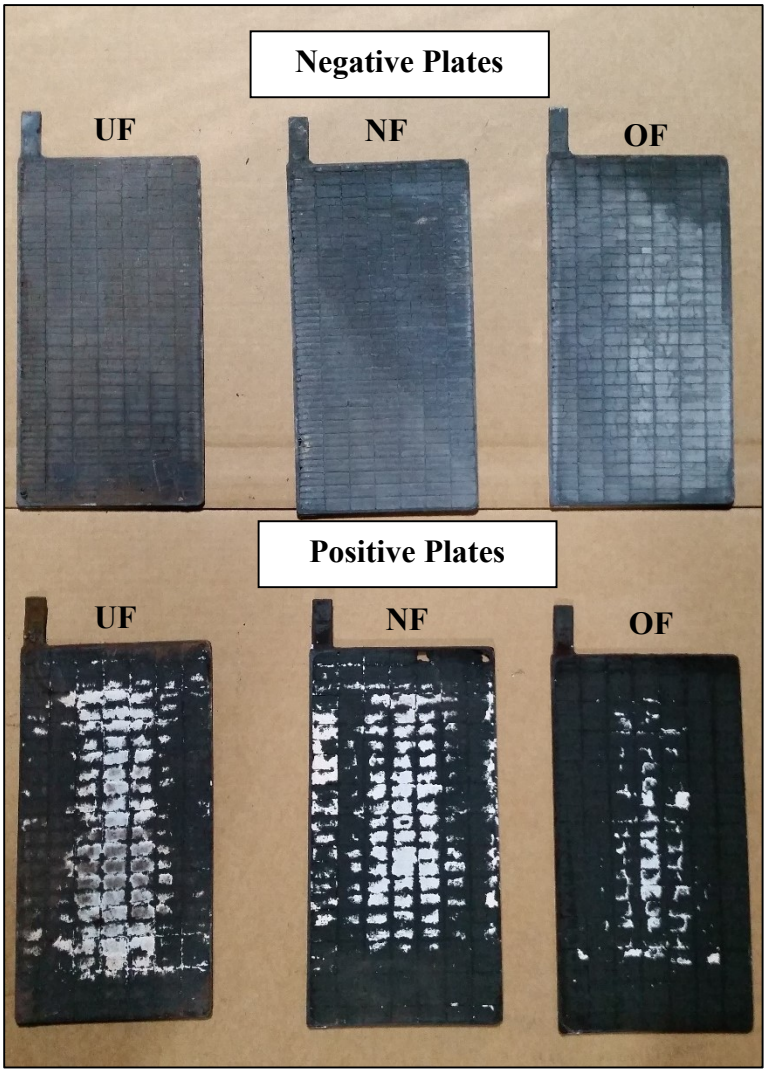

Figure 71 Tank Formation Plates

As shown in Figure 71, there is a positive correlation between the formation level of the positive plates, and the amount of unformed $PbSO_4$, as shown by the amount of remaining white material on the plates. It is clear based on this figure that the conversion ratio to PbO_2 from inactive material is higher for the OF plates when compared to the UF and NF plates.

Table 20 shows the as-received characteristics of mass for the 44 cells formed using the tank formation method, along with the respective minimum, maximum, average, and RSD values. The measurements of mass were taken two months after formation completion without the addition of electrolyte.

Table 20 Tank Formation ELG15 Cells – As-Received Characteristics

Cell /	UF (1.72TC)			NF (2.16TC)			OF (2.60TC)		
Statistics	*OCV (V)*	*Mass (kg)*	*SG*	*OCV (V)*	*Mass (kg)*	*SG*	*OCV (V)*	*Mass (kg)*	*SG*
1	-	12.3	-	-	12.4	-	-	12.3	-
2	-	12.3	-	-	12.4	-	-	12.3	-
3	-	12.3	-	-	12.4	-	-	12.4	-
4	-	12.3	-	-	12.4	-	-	12.4	-
5	-	12.4	-	-	12.6	-	-	12.7	-
6	-	12.5	-	-	12.1	-	-	12.6	-
7	-	12.4	-	-	12.0	-	-	12.6	-
8	-	12.1	-	-	12.2	-	-	12.6	-
9	-	12.4	-	-	12.0	-	-	12.7	-
10	-	12.6	-	-	12.5	-	-	12.5	-
11	-	12.3	-	-	-	-	-	-	-
12	-	12.3	-	-	-	-	-	-	-
13	-	12.6	-	-	-	-	-	-	-
14	-	12.6	-	-	-	-	-	-	-
15	-	12.6	-	-	-	-	-	-	-
16	-	12.6	-	-	-	-	-	-	-
17	-	12.4	-	-	-	-	-	-	-
18	-	12.6	-	-	-	-	-	-	-
19	-	12.4	-	-	-	-	-	-	-
20	-	12.2	-	-	-	-	-	-	-
21	-	12.2	-	-	-	-	-	-	-
22	-	12.6	-	-	-	-	-	-	-
23	-	12.6	-	-	-	-	-	-	-
24	-	12.3	-	-	-	-	-	-	-
Minimum	-	12.1	-	-	12.0	-	-	12.3	-
Maximum	-	12.6	-	-	12.6	-	-	12.7	-
Average	-	12.4	-	-	12.3	-	-	12.5	-
RSD	-	1.26%	-	-	1.71%	-	-	1.22%	-

As shown in Table 20, there are differences regarding the as-received characteristic of mass when respective formation levels are compared, which indicates differences in the amount of active material (i.e., manufacturing differences).

Cell Activation

Prior to the performance cycling of the cells formed using the tank formation method, the cells were activated using the power-cycler as per the requirements outlined in the *Rolls Battery Manual* [40]. Specifically, 1.265 electrolyte was added to the chosen UF, NF, and

OF cells, which had previously been connected in series to represent the three S-480 modules. Following the addition of electrolyte, a soaking period of 90 minutes ensued to allow the electrolyte to saturate into the plates and separators. The three modules were then charged using a current of 17.8 A, corresponding to 5 % of the 20 hour rated capacity of the S-480 battery, until each cell attained SG values of 1.265 +/- 0.005. Finally, once the target SG values were reached, the activation current was maintained for an additional hour. Figure 72 shows the average activation profile of the UF, NF, and OF modules, with respect to cell SG and voltage values as a function of activation time. The relaxation in cell voltage is indicative of the completion of the activation process, and thus a stop in current.

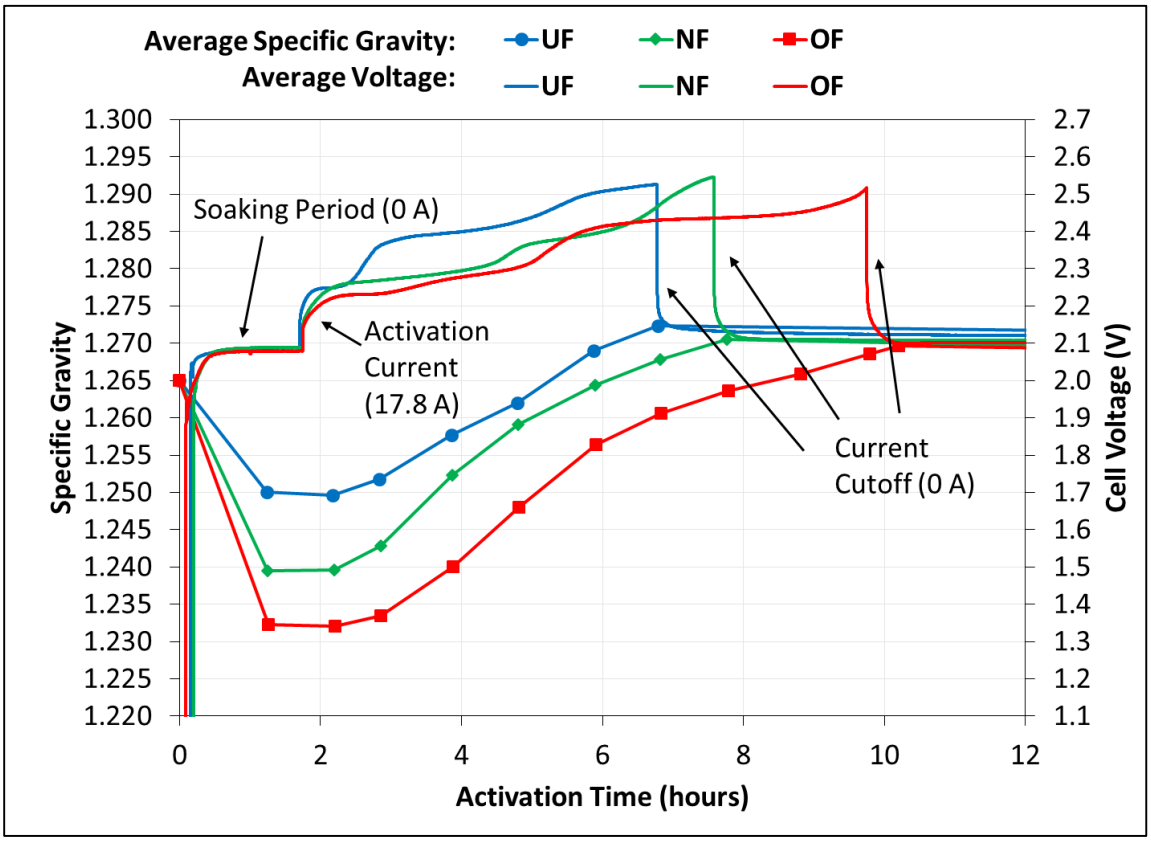

Figure 72 Tank Modules Activation

As shown in Figure 72, total activation times of 7 hours, 8 hours, and 10 hours were required for the UF, NF, and OF modules, respectively. These results are indicative of the fact that more electrolyte was able to saturate into the plates and separators of the OF module when compared to the other two modules. This is supported by the fact that during the 90 minutes soaking period, the SG values of the OF cells were the lowest. These results

were expected, as the OF plates had a higher conversion ratio of active material than the plates of the UF and NF modules, thus allowing them to absorb a higher volume of H_2SO_4.

Deep-Cycling Characteristics

As part of the performance analysis, three cells with the same formation level were then deep-cycled in a series configuration in order to represent the S-480 battery. These cells were cycled 10 times using the deep-cycling algorithm presented in Table 13, and exhibited the same characteristics as the cells formed using the floor container formation method. The reader is referred to Figure 47 for an example of the deep-cycling profile.

Discharge Capacity Characteristics

Figure 73 shows the measured discharge capacity, charge capacity, and coulombic efficiency of the three cells cycled in series for the UF, NF, and OF formation levels.

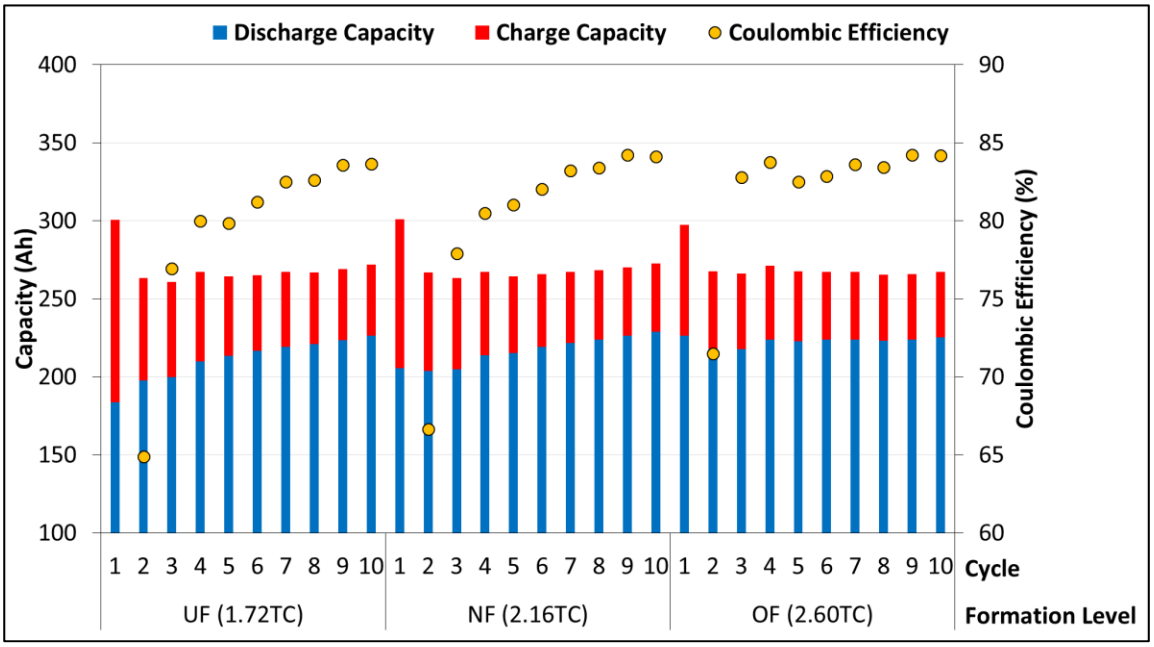

Figure 73 Module Discharge Capacity and Coulombic Efficiency Values (Tank Formation Method)

As shown in Figure 73, the discharge capacity and coulombic efficiency results of the tank formation method were lower than the results obtained using the other three formation methods at SBC. Specifically for cycles 6-10, average discharge capacity results were determined to be 221 Ah, 224 Ah, and 224 Ah, for the UF, NF, and OF modules, respectively, while the average coulombic efficiency values were determined to be 82.7 %,

83.4 %, and 83.7 %, for the UF, NF, and OF modules, respectively. The lower coulombic efficiency values are directly correlated to the lower discharge capacity results, as the deep-cycling algorithm was consistent between all four formation methods. Unlike the OF module, the UF and NF modules appear to be continuing their formation process, as shown by their respective increase in discharge capacity values between cycles 1 and 10. None of the modules met the rated capacity output of 231 Ah over the span of this performance analysis. Thus, cells formed using the tank formation method at SBC with formation levels ≤ 2.60TC would likely never attain a fully formed state when implemented in off-grid solar applications.

The differences in discharge capacity results are further illustrated in Figure 74, which provides a discharge capacity comparison of the three modules.

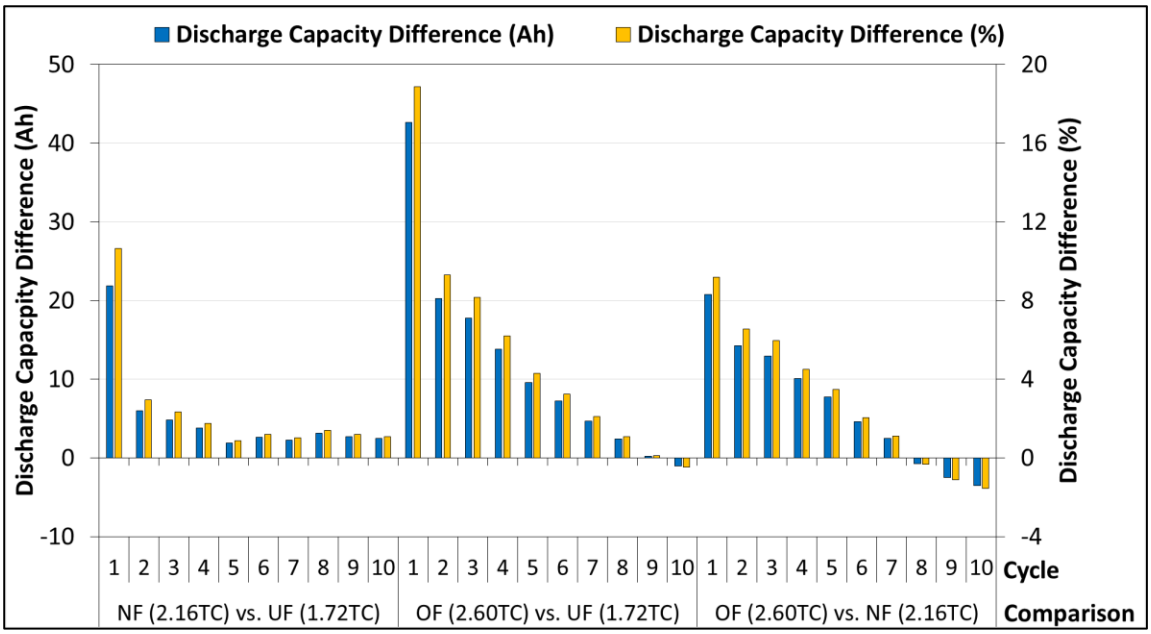

Figure 74 Module Discharge Capacity Comparison (Tank Formation Method)

As shown in Figure 74, with the exception of the first cycle, discharge capacity differences between the NF and UF modules are small (i.e., < 2 %). Conversely, the OF module offers discharge capacity advantages when compared to both the UF and NF modules. Finally, all three discharge capacity differences are shown to be decreasing with deep-cycling iterations due to the continued formation process of UF and NF modules.

Specific Gravity Characteristics

Figure 75 shows the average electrolyte SG values of the three modules which were measured before the start of each deep-cycle.

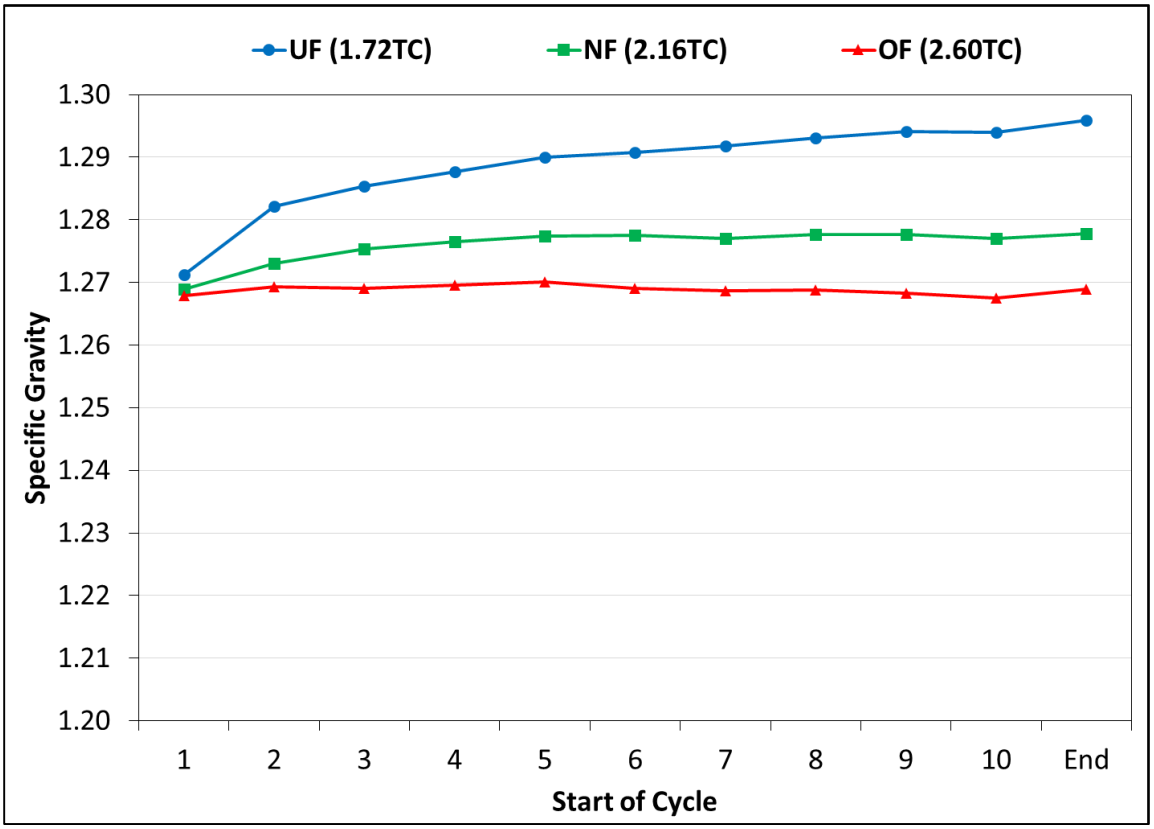

Figure 75 Module Electrolyte SG Values (Tank Formation Method)

As shown in Figure 75, there was an increase in electrolyte SG values for the UF module throughout 10 deep-cycles and for the NF module throughout five deep-cycles, while SG values for the OF module remained relatively constant. Unlike the SG results of the other three formation methods, there was no initial decrease in electrolyte SG values for any of the modules. This was due to the SG stabilization effect of the aforementioned activation process. The increase in electrolyte SG values for the UF cells throughout the 10 deep-cycles coincides with the increase in capacity results as shown in Figure 73. The same cannot be said with respect to the NF cells, where discharge capacity results were shown to increase for the duration of the performance analysis, while electrolyte SG values reached a steady-state after five deep-cycles. Thus by cycle 6, the maximum amount of H_2SO_4 had been released from the plates of the NF cells. It is hypothesized that the

electrolyte SG values for the UF module, like those of the NF and OF modules, would have eventually reached steady-state values.

Furthermore, as was observed regarding the SG results of the circulated electrolyte formation method, the UF cells (followed by the NF cells) had the highest overall values for the duration of the performance analysis. This is explained by the fact that all cells formed using the tank formation method were activated using the same concentration of electrolyte (i.e., 1.265 SG). Thus due to the lower formation capacity inputs of the UF and NF cells when compared to the OF cells, higher amounts of H_2SO_4 were released from the plates of the UF and NF cells as they continued forming, which caused respective increases in their electrolyte SG values.

Figure 76 shows the electrolyte SG profile for the 10th deep-cycle of one cell per module (i.e., cells UF_3, NF_2, and OF_2).

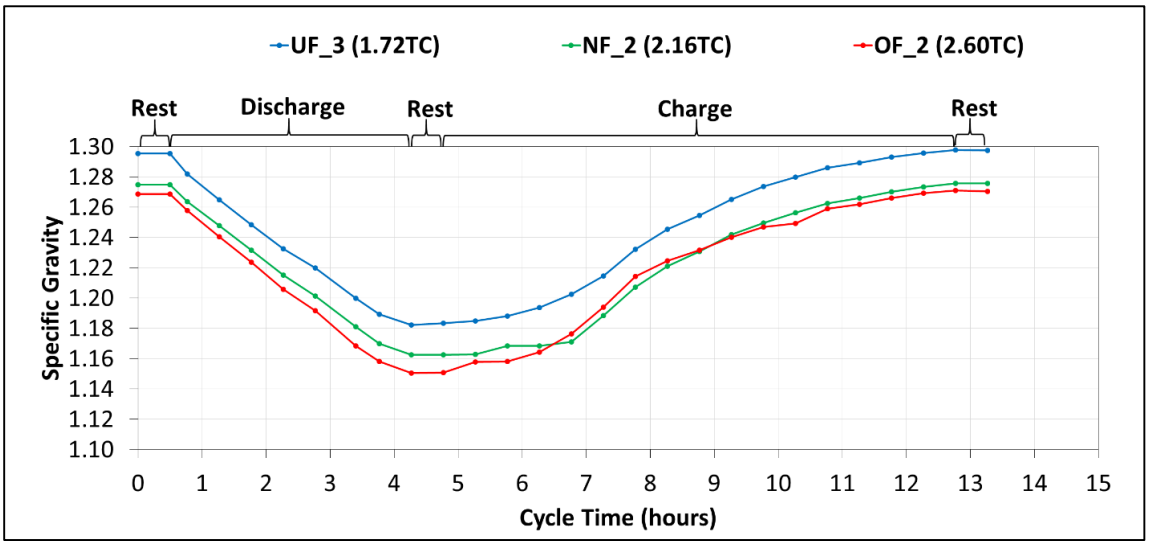

Figure 76 Electrolyte SG Profile – Cycle 10 (Tank Formation Method)

As shown in Figure 76, the circulated electrolyte SG profile is in agreement with the SG profile of the cells formed using the submerged container formation method, with the exception of higher SG values for the UF cell when compared to the NF or OF cells, as was discussed above.

Internal Resistance Characteristics

Figure 77 shows the IR values of the three modules for cycles 1, 2, 4, 6, and 10 of the discharging and charging pulses using 10 seconds voltage intervals as a function of cycle number and discharge/charge Ah. The IR results are presented as the average of the three respective cells for each formation level. As the charging current pulses only occurred during the first phase of the charging process (see Table 13 – Step 4), IR values obtained at a charging capacity of 200 Ah correspond to approximatively 74 % of the total Ah input received by these cells during their respective charging processes.

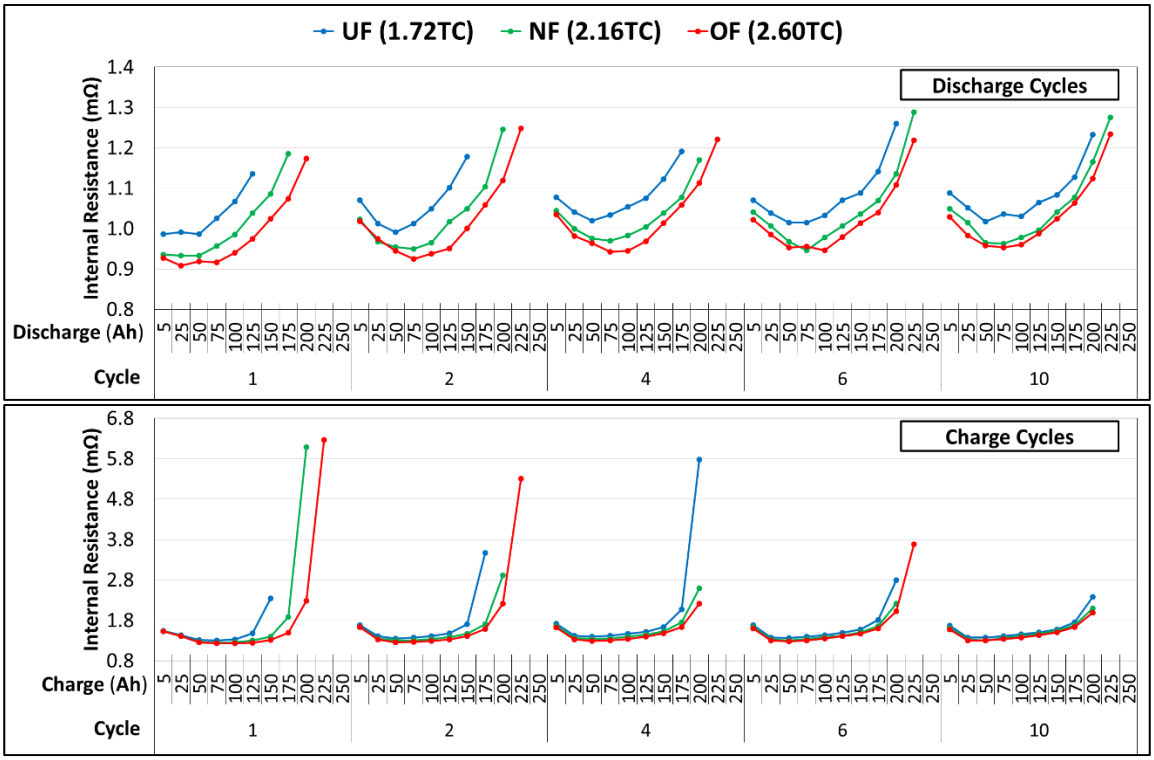

Figure 77 Discharge and Charge IR with 10 Second Voltage Intervals (Cycles 1, 2, 4, 6, and 10) (Submerged Container Formation Method)

As shown in Figure 77, the higher the formation level, the lower the IR when respective discharging and charging capacities are compared. Furthermore, overall IR values for the respective modules are shown to decrease with cycling iterations, due to the continued formation of the cells. These results are in agreement with the IR characteristics of the cells formed using the floor container formation method, and the shape of the IR curves shown in Figure 77 follow the same relationships as were explained for the IR results of the constant-current formation algorithm (see section 5.1).

Module Voltage Alignment

In order to provide additional information regarding the performance characteristic of the cells formed using the tank formation method, the concept of a misaligned cell introduced in section 6.1 is explored below. Figure 78 shows the individual discharge voltages of the nine cells as a function of their first discharge capacity, while Figure 79 shows the final discharge voltages of these same cells as a function of cycle number.

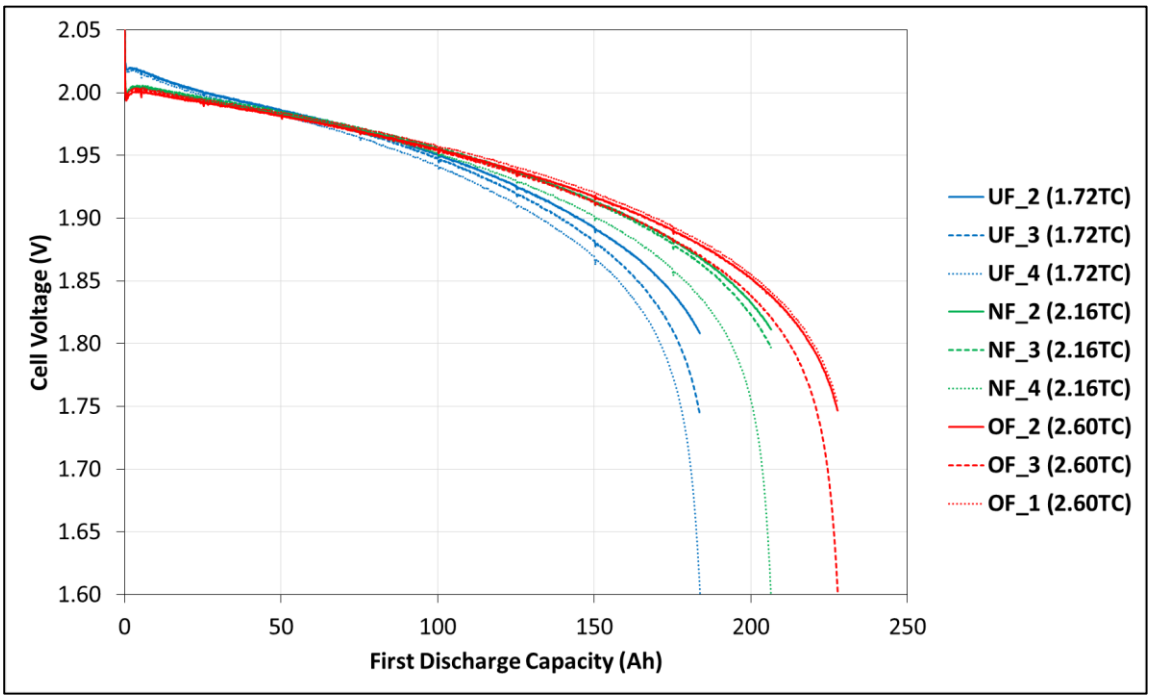

Figure 78 Cell Voltages as a Function of First Discharge Capacity (Tank Formation Method)

As shown in Figure 78, the UF cells had the highest voltage values for the first 50 Ah of discharge capacity. Following the first 100 Ah of discharge capacity, the distinction between the three modules becomes more apparent, with the OF cells maintaining higher voltage values, followed by the NF cells, and then finally by the UF cells.

Furthermore, cells UF_4, NF_4, and OF_3 reached voltages of 1.60 V before the other two cells in their respective modules reached 1.75 V, triggering the end of the discharging process. Thus, it is possible that without their respective misaligned cells, the UF and NF modules may have achieved higher discharge capacity results. Specifically it is estimated that an additional 5 Ah might have been obtained for the UF module, while an additional 8 Ah might have been obtained for the NF module. The same cannot be said for the OF

module, as cell OF_1 was very close to attaining a discharge voltage of 1.75 V (i.e., final discharge voltage of 1.752 V).

Figure 79 highlights the individual cell voltages of the three different modules at the end of each deep-discharge cycle. In this figure, three individual cell voltages above 1.60 V for a respective module would indicate ideal cell voltage alignment.

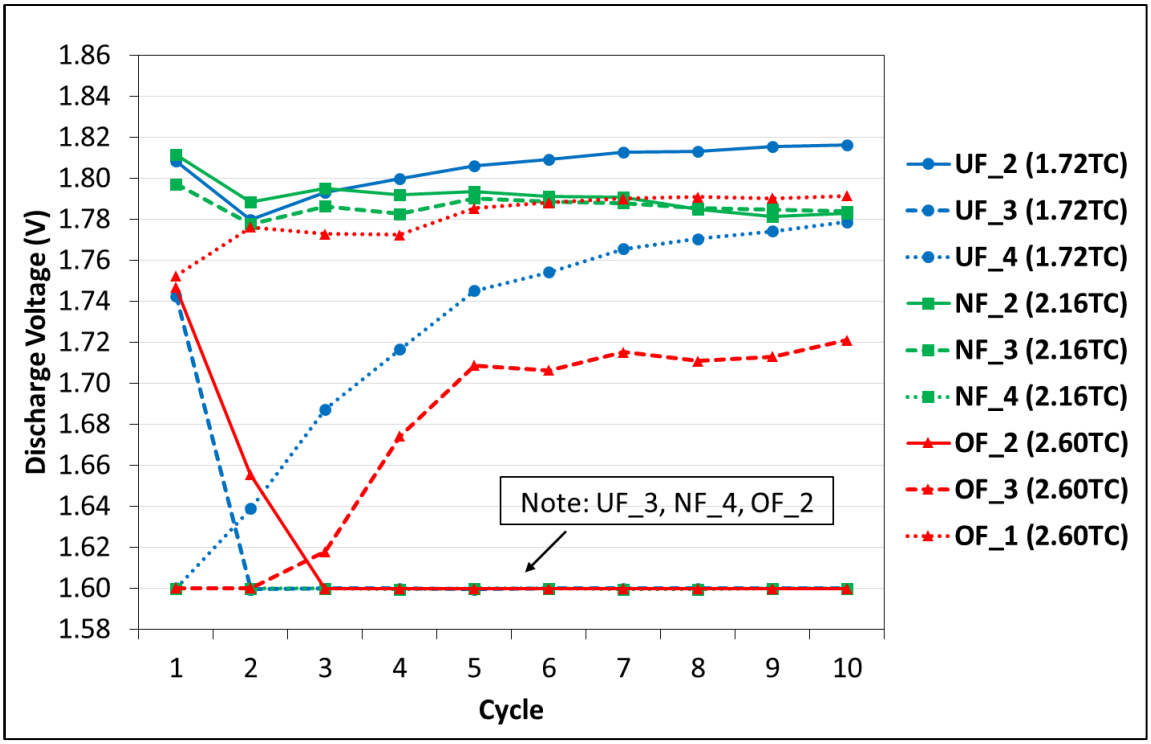

Figure 79 Discharge Voltages as a Function Cycle Number (Tank Formation Method)

As shown in Figure 79, no module formed using the tank formation method was able to maintain ideal cell voltage alignment. With respect to the UF module, cell UF_4 triggered the end of the discharging process for the first deep-cycle, while cell UF_3 triggered the end of the discharging process for deep-cycles 2 – 10. With respect to the NF module, cell NF_4 triggered the end of the discharging process for all 10 cycles. Finally, with respect to the OF module, cell OF_3 triggered the end of the discharging process for deep-cycles 1 – 2, while cell OF_2 triggered the end of the discharging process for deep-cycles 3 – 10. These results are not in agreement with the module voltage alignment results of the other three formation methods, where it was shown that the OF modules were able to attain ideal cell voltage alignment. Thus, it can be stated that of the four formation methods studied, the cells formed using the tank formation method had the worse characteristics with respect

to voltage alignment. This can be explained by the relatively low formation levels of the tank formation method when compared to the other three formation methods, as was alluded to in Table 12.

6.5. Impact of Formation Methods and Optimal Formation Method

In order to fully understand the impact of the four different formation methods on the performance of the cells, and subsequently to finalize the determination of the optimal formation method, the differences in formation and performance characteristics between the four methods are examined below. Specifically with respect to the formation characteristics, the differences in curing and soaking conditions will be explored, along with the important formation parameters as listed out in section 2.2.1 of formation current, formation temperature, formation voltage, and the H_2SO_4 formation concentration, which make up the formation profile. With respect to the performance characteristics, differences in discharge capacity values, SG values, IR values, and module voltage alignment during deep-cycling operation will be discussed.

Curing Conditions

Unlike the cells which were obtained for phase 1 of this research project, the plates which made up the ELG15 cells for phase 2 of this research project were not from the same batch. Nevertheless, it is appropriate to assume relatively identical H_2SO_4/LO ratios and curing conditions for all four formation methods, as there is no variance in the preparation of the positive and negative plates, respectively, between these four formation methods at SBC. Thus, following the curing process of the plates at SBC, it can be stated that the PAM was comprised of a 3BS/4BS crystal structure, and that the NAM was comprised of a 3BS crystal structure due to the addition of the lignosulfonate expander.

Soaking Conditions

Unlike the cells formed using the two different formation algorithms in phase 1 of this research project, the soaking conditions employed for the four formation methods at SBC were different, as summarized in Table 21.

Table 21 SBC Soaking Conditions

Formation Method	SG of Soaking H_2SO_4 Electrolyte	Soaking Period
Floor Container Formation	1.200	1 hour
Submerged Container Formation	1.200	0.5 hour
Circulated Electrolyte Formation	1.250	0.5 hour
Tank Formation	1.100	0 hour

As shown in Table 21, identical soaking electrolyte SG values were used for the floor container and submerged container formation methods, albeit the soaking period was twice as long for the former. A higher electrolyte SG value was used for the circulated electrolyte formation method due to its ability to maintain relatively constant SG values during formation. It should be noted that Kumar *et al.* [28], who studied the performance of cells formed using the circulated electrolyte method, found relatively no differences in discharge capacity between cells formed using 1.150 SG electrolyte and cells formed using 1.245 SG electrolyte. Thus, with respect to the cells formed using the circulated electrolyte formation method, no advantages were expected concerning the characteristic of discharge capacity due to a higher soaking electrolyte SG when compared to the floor container and submerged container formation methods. Furthermore, it was stated in the literature review that when plates are subjected to a soaking electrolyte SG value of 1.200, most of the reactions of sulfation occur within the first 0.5 hour. Thus for all three of these aforementioned formation methods, similar conversion ratios of cured material to $PbSO_4$ would have occurred. The shortened soaking periods for the submerged container and circulated electrolyte formation methods are a result of the inherent characteristics of these two methods to maintain lower formation temperatures, thus avoiding the need for an extended cool-down period following the addition of the electrolyte.

With respect to the tank formation method, the plates were submerged in electrolyte with an SG of 1.100 with relatively no soaking time due to the immediate charging phase in reversed polarization (see Table 11 – Step 1). However, even though no material is formed during this step, the sulfation of the cured material would still have occurred, albeit at a lower conversion rate than the other three formation methods due to the lower concentration of H_2SO_4.

Finally, as stated in the literature review, a high H_2SO_4 concentration during the formation process, as was the case for the floor container, submerged container, and circulated electrolyte formation methods, results in a higher β/α-PbO_2 ratio at the end of the formation process, than if a lower H_2SO_4 concentration were to be used, as was the case for the tank formation method. Thus, as an increase in the β/α-PbO_2 ratio results in higher overall discharge capacity values, at the expense of reduced cycle life, it would be expected that if a cell were to be formed at the same formation level using all four formation methods,

the one formed using the tank formation method would have the lowest discharge capacity values.

Formation Profile

Figure 80 compares the current density values and total formation times of the four different formation methods. These calculations made use of the formation algorithms presented in section 4.2.1, and a formation current of 65 A (i.e., 11 mA cm^{-2}) was used for Steps 5-7 of the submerged container formation method. Current density values were separated into three different categories: 1 – 4 mA cm^{-2} (i.e., low), 4 – 8 mA cm^{-2} (i.e., medium), and 8 – 12 mA cm^{-2} (i.e., high).

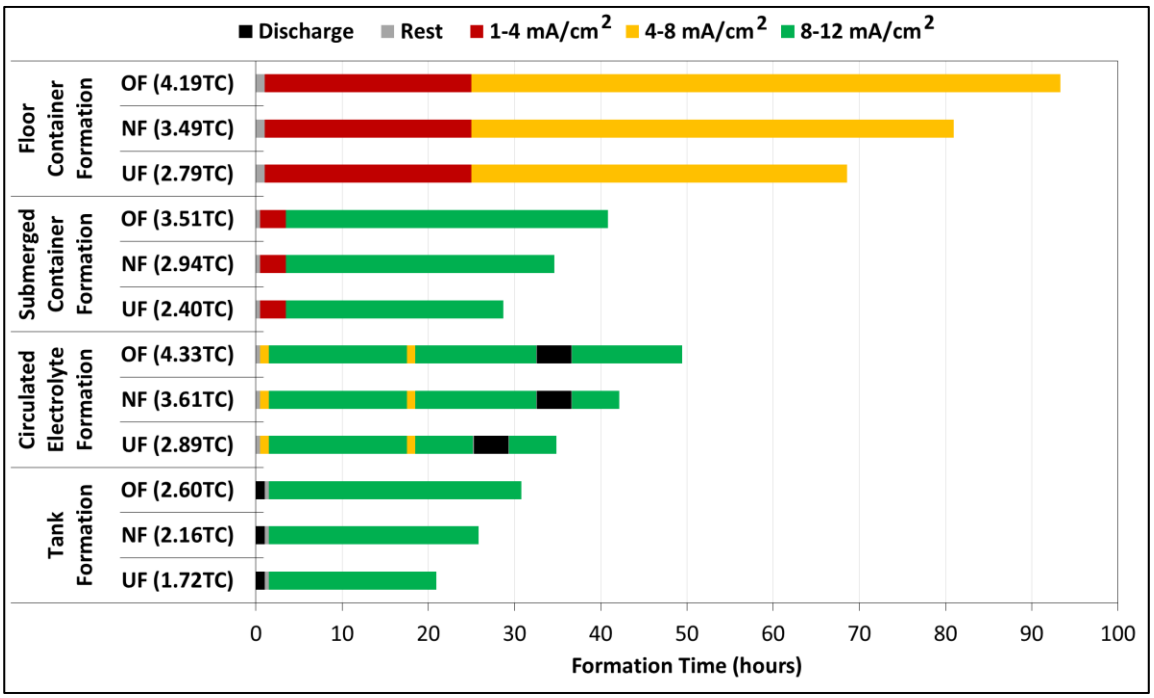

Figure 80 Current Density and Formation Time Comparison of Formation Methods at SBC

As shown in Figure 80, there were significant differences between the floor container formation method and the other three formation methods. Specifically, current density values for the floor container formation method did not exceed the medium range due to temperature limitations, which resulted in extended formation times when compared to the other three formation methods.

With respect to the other three formation methods, current density values were in agreement, with the majority of the formation process being completed in the high range.

This was enabled by the cell cooling characteristics of the submerged container and circulated electrolyte formation methods, and the high heat capacity of the electrolytic tanks with respect to the tank formation method. Of the four different formation methods, only the circulated electrolyte formation method made use of a discharging current once active material had been formed. Formation times differed due to the variance in the standard formation levels used at SBC for each respective formation method. These are clearly differentiated in Figure 16 (reproduced from section 4.2.1).

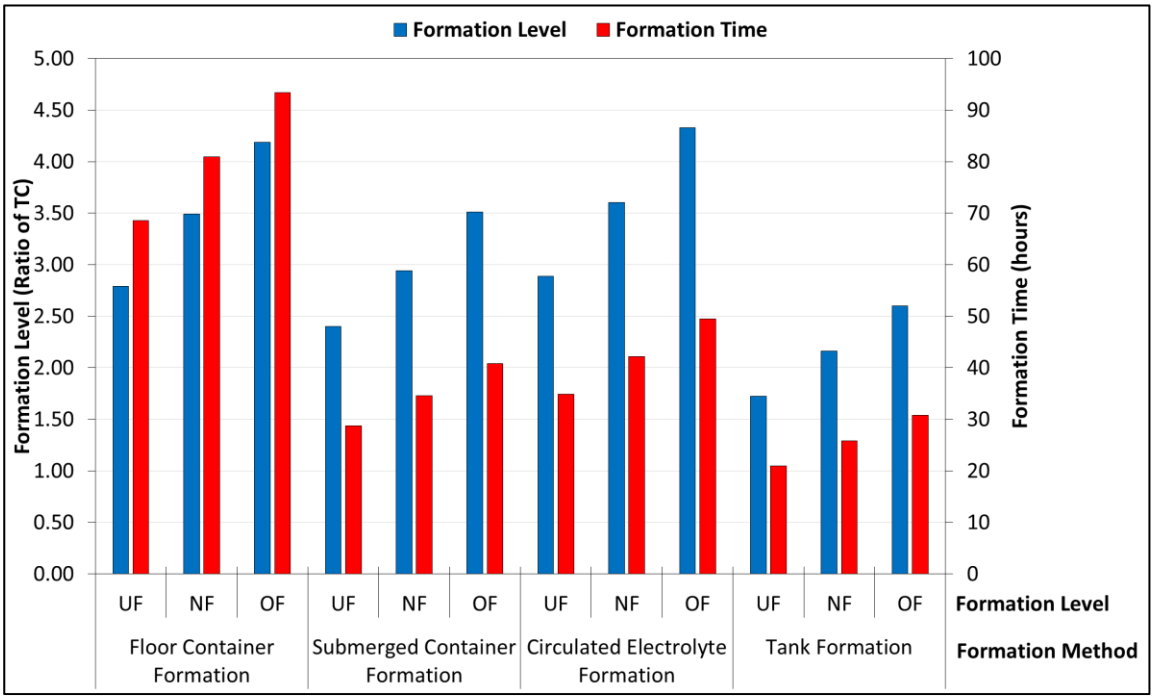

Figure 16 Comparison of Formation Levels and Times at SBC

Thus if formation levels were in agreement, one would expect similar performance characteristics between cells formed using the submerged container formation method and cells formed using the circulated electrolyte formation method, due to their similarities in formation current density values, curing conditions, and soaking conditions.

With respect to the formation characteristic of cell temperature, this was only monitored using the submerged container formation method, as was shown in Figure 54. Specifically, the average temperature of the one cell which was monitored was calculated to be 51.1 °C. Thus as this value is just above the recommended formation temperature range of 30 °C to 50 °C, it can be confirmed that the current density profile with respect to the submerged container formation method is appropriate, and should not be increased.

The transition between the first and second stages of formation is indicated by an increase in electrolyte SG and voltage values. Thus, as SG values were not recorded throughout the formations at SBC, the formation characteristic of voltage was instead used to identify this transition. Specifically, the duration of the first stage of formation was determined to be 5 hours, 7 hours, 6 hours, and 5 hours, for the floor container, submerged container, circulated electrolyte, and tank formation methods, respectively. One should note that the soaking periods, as were shown in Table 21, are not included in these calculations. Thus, it can be stated that the different formation methods did not have a great impact on the formation characteristics of voltage, and corresponding formation stages.

The averages of the final cell SG and OCV values following their respective formation process are compared in Figure 81. The SG and OCV of the cells cycled in phase 1 of this research project (i.e., constant-current and multi-step current formation algorithms) are included for comparison purposes, while the results of the cells formed using the tank formation method were excluded due to their being received in dry-charged conditions.

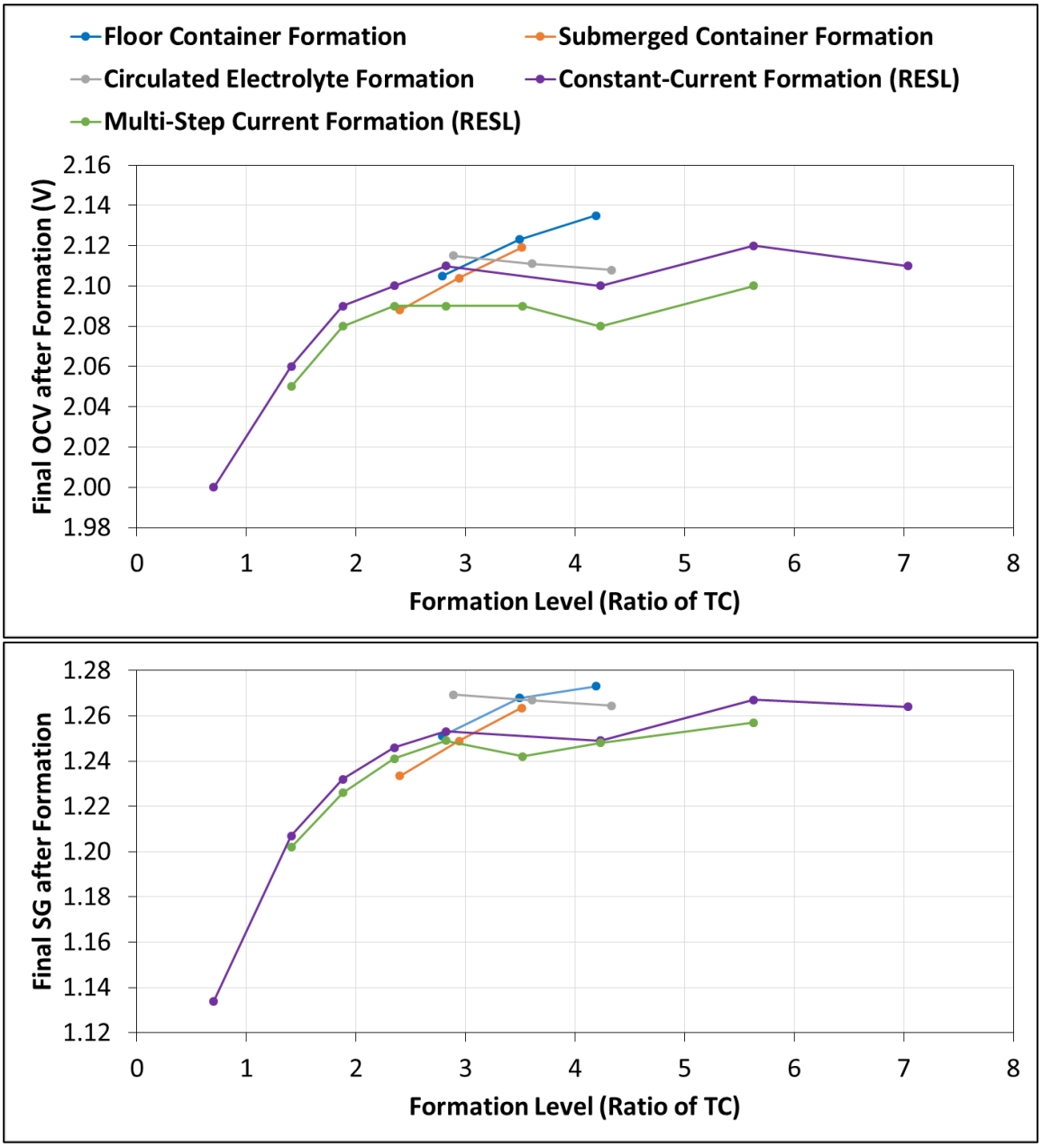

Figure 81 Comparison of Final OCV and SG Results – Phases 1 and 2

As shown in Figure 81, with the exception of the circulated electrolyte formation results, there is a direct correlation between the final OCV and SG values to formation level. Again, the dip in OCV and SG values for cells $4.23TC_a$ and $4.23TC_b$ was because distilled water was added to these cells late in their respective formation process. With respect to the final OCV and SG results of the cells formed using the circulated electrolyte formation method, this discrepancy can be explained by the fact that the electrolyte which was used to balance the UF cells at the end of formation had a higher H_2SO_4 concentration than the electrolyte

which was used to balance the NF and OF cells. This in turn resulted in higher OCV and SG values for the UF cells.

Discharge Capacity Characteristics

As shown above, deep-cycling performance analyses of the 12 modules were independently completed for each of the four formation methods. Figure 82 shows a comparison of the discharge capacity results for the 12 different modules over a span of 10 cycles.

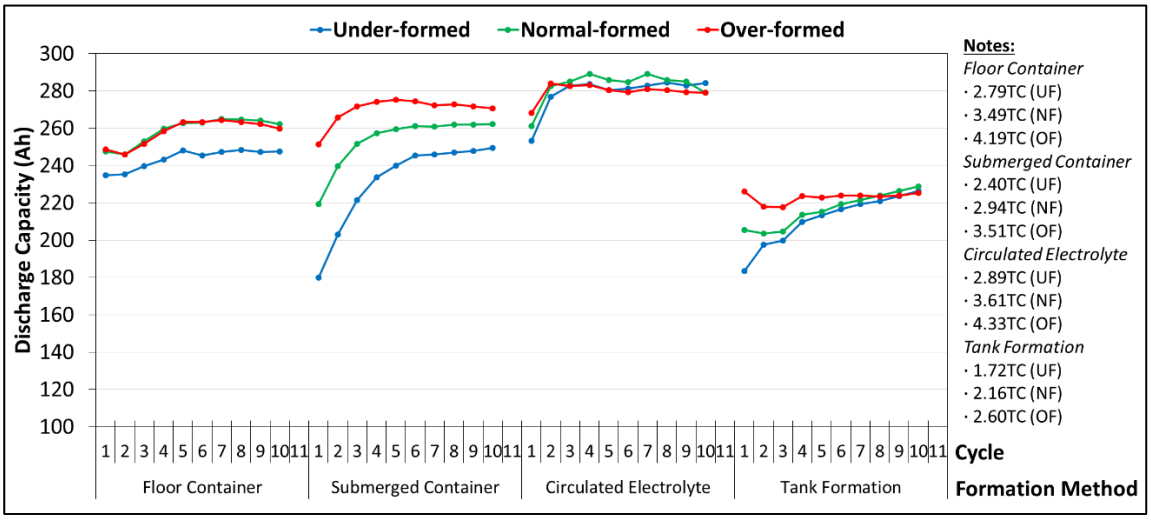

Figure 82 Comparison of Discharge Capacity Results – SBC Formation Methods

As shown in Figure 82, there were obvious differences between the discharge capacity results of the modules obtained using the four different formation methods employed at SBC. Specifically, as was hypothesized in section 4.2.1, the modules obtained using the circulated electrolyte formation method had the better performance results, and the modules obtained using the tank formation method had the worst performance results. Additionally, the majority of the modules, and especially the ones obtained using the submerged container and tank formation methods, were shown to continue to some extent their formation process as a result of deep-cycling operation.

Furthermore as shown in Figure 82, there was a clear differentiation between the discharge capacity results of the three different formation levels for the cells formed using the submerged container formation method. While there were differences in capacity results between the formation levels of the other three formation methods, this characteristic was not as evident. Thus, is can be stated that once a cell has reached a certain

formation level, or formation threshold, additional formation input does not correlate into a better performing battery with respect to its discharge capacity. Figure 82 shows that this is the case when cells are formed at a level higher than 3.49TC when using the floor container formation method, and when cells are formed at a level higher than 2.89TC when using the circulated electrolyte formation method. Results pertaining to the tank formation method are less evident due to the significantly better performance of the OF module when compared to the NF module. The concept of the formation threshold was also apparent for the cells formed using the constant-current formation algorithm, where it was shown that additional formation input exceeding a formation level of 2.82 times the theoretical capacity of the cell did not correlate to an increase in discharge capacity performance.

Although the cells formed corresponded to the UF, NF, and OF levels for all four formation methods as per their respective formation algorithm, these three formation levels are not identical for all methods as was stated in section 4.2.1, and further illustrated in Figure 16. Thus as an effort to compare the four different formation methods on the same basis, initial discharge capacity results, and corresponding DFE values (i.e., initial discharge capacity output of a cell divided by its formation capacity), are shown in Figure 83 as a function of formation level. The results pertaining to phase 1 of this research project (i.e., constant-current and multi-step current formation algorithms) are included for comparison purposes. With respect to the cells formed using the constant-current formation algorithm, the discharge capacity results of cells $0.70TC_a$ and $5.63TC_a$ were excluded from this analysis due to the former being insignificant, and the latter being an outlier.

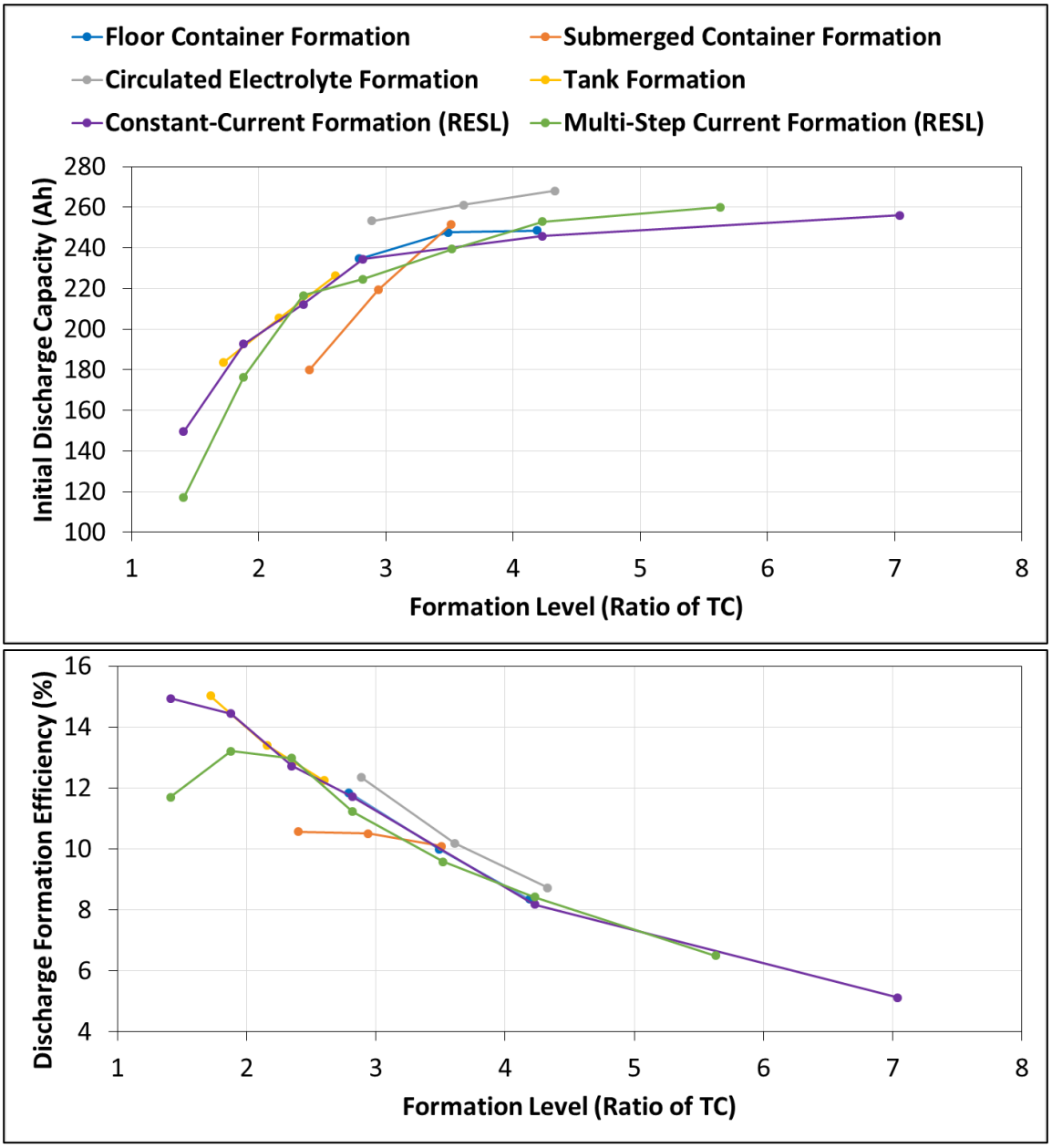

Figure 83 Initial Discharge Capacity Results – Phases 1 and 2

As shown in Figure 83, the modules obtained using the circulated electrolyte formation method outperformed all other formation methods, including the cells formed in phase 1 of this research project. It is hypothesized that this came as a result of the discharge current within the formation algorithm of the circulated electrolyte formation method, due to it being the main difference when comparing the formation characteristics of all four formation methods. Other advantages worth considering with respect to the circulated electrolyte formation method include its ability to maintain relatively constant electrolyte

temperature and SG values. Furthermore, the initial discharge capacity results of the modules formed using the floor container and the tank formation methods are in agreement with the results of the constant-current and multi-step current formation algorithms when respective formation levels are compared. Thus, it cannot be stated that cells formed using the tank formation method result in poor performance characteristics, even with the differences in soaking conditions, as the tank formation levels are simply lower than the other three formation methods used at SBC. Finally, it is interesting to note that the UF module obtained using the submerged container formation method (i.e., 2.89TC) performed relatively poorly (i.e., ~ 22 % difference) when compared to the cells which received similar amounts of formation capacity input (i.e., cells $2.82TC_a$ and $2.82TC_b$ of phase 1). This is explained by the fact that the higher formation currents used in the submerged container formation algorithm when compared to the algorithms used in phase 1 of this research project results in a lower formation efficiency for the former. As was the case for the multi-step current formation algorithm, this reduction in efficiency is more evident at relatively low formation input values. Thus, based on the results of the submerged container and circulated electrolyte formation methods, it is observed that the formation method does impact the performance of LABs. This was to be expected, as the differences in formation algorithms and cell formation temperatures caused by these formation methods affect the crystal structure of the positive and negative plates of the battery.

With respect to the DFE values, the lower the formation capacity input, with the exception of cell $1.41TC_b$, the higher the DFE. This general trend was expected, due to the slow conversion process of $PbSO_4$ in the second stage of the LAB formation. With this in mind, it is interesting to note the relatively constant DFE values for the modules formed using the submerged container formation method. Specifically, there was only a small difference in DFE values between the UF (i.e., 10.6 %) and OF (i.e., 10.1 %) modules. Thus, based on these results and their corresponding initial discharge capacity results, it is recommended that formation levels higher than 3.51TC be formed and cycled using the submerged container formation method. Finally, the average DFE value for the 12 modules formed at SBC was calculated to be 11 %.

In order to provide additional information regarding the performance characteristics of the cells and modules presented in Figure 83, the UF module formed using the circulated electrolyte formation method (i.e., 2.89TC) was used as the basis to calculate respective percent differences in initial discharge capacity and total formation time (including respective soaking times) for the other cells and modules, the results of which are shown in Figure 84. Values greater than 0 for both the *% Difference in Discharge Capacity* and *% Difference in Formation Time* criteria represents an improvement relative to the UF circulated electrolyte module.

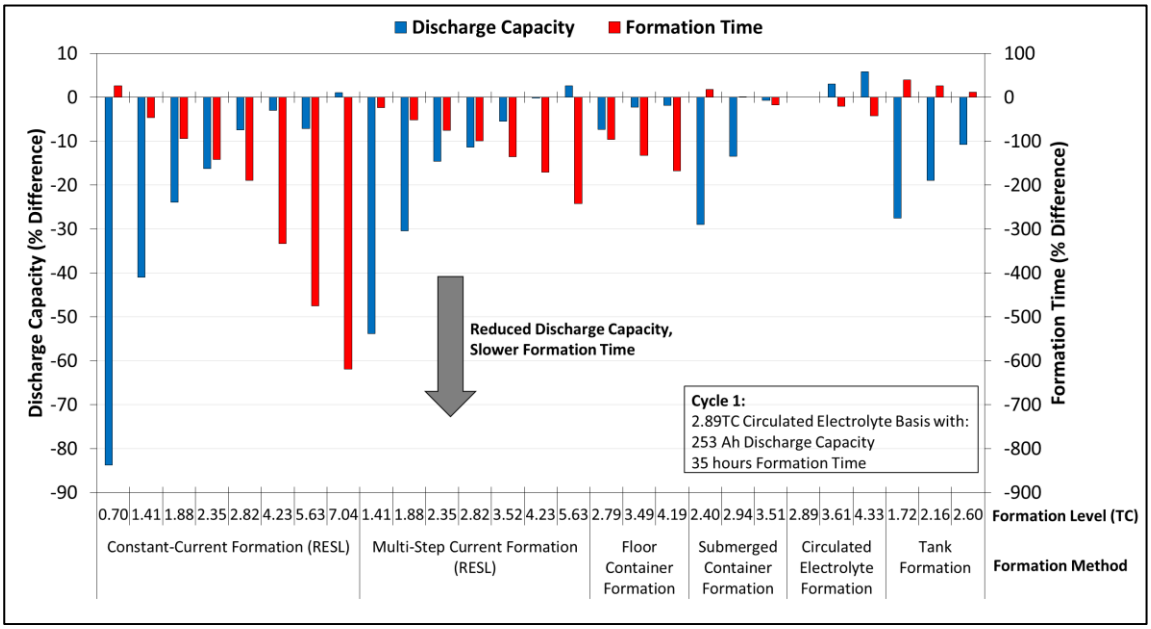

Figure 84 Differences in Discharge Capacity and Formation Time (Cycle 1) – UF Circulated Electrolyte Module Basis

As shown in Figure 84, there are no cells or modules which provide advantages over the UF circulated electrolyte module when considering both discharge capacity and formation time characteristics. As an example, the UF module formed using the submerged container formation method (i.e., 2.40TC) is shown to provide an advantage of 17.8 % with respect to the total formation time when compared to the circulated electrolyte UF module, but at the expense of a 28.9 % reduction in initial discharge capacity. Furthermore, it is clearly shown that the constant-current and multi-step current formation methods completed at the RESL, and the floor container formation at SBC are disadvantageous with respect to total formation time. Finally, it is interesting to note that the OF module formed using the tank formation method (i.e., 2.60TC) is shown to provide an advantage of 11.7 % with respect

to the total formation time when compared to the circulated electrolyte UF module, but only at the expense of a 10.7 % reduction in initial discharge capacity. Thus based on these results, it is recommended that formation levels higher than 2.60TC be formed and cycled using the tank formation method.

The advantages of the UF circulated electrolyte module with respect to discharge capacity are not limited to first discharge characteristics, as confirmed in Figure 85, which shows the differences in discharge capacity and formation time for the second deep-cycle.

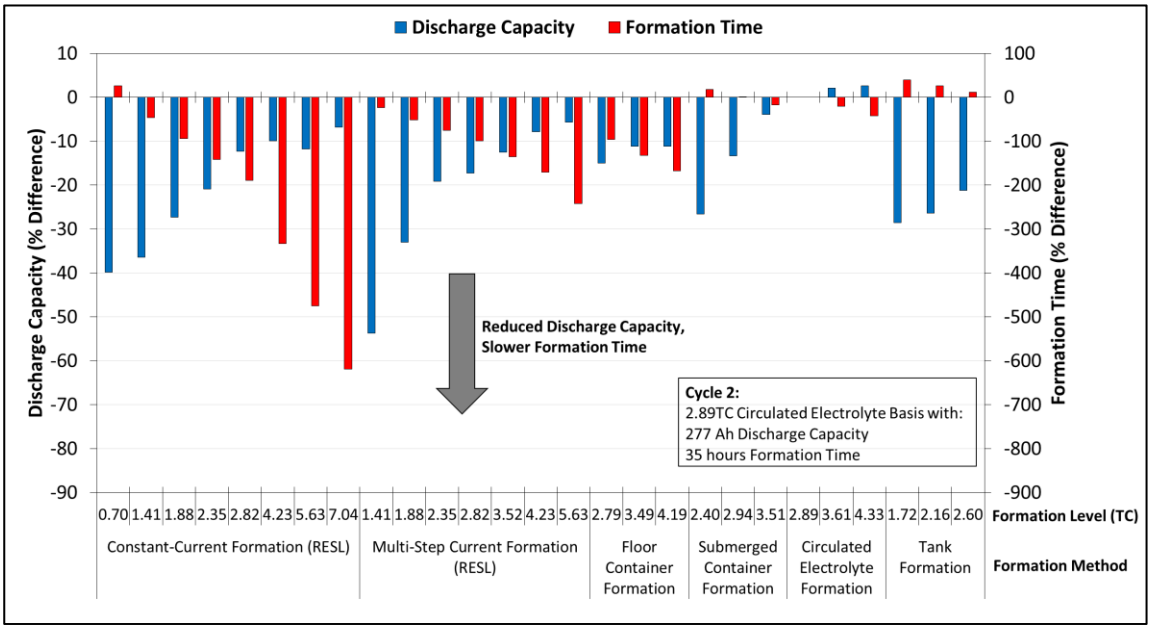

Figure 85 Differences in Discharge Capacity and Formation Time (Cycle 2) – UF Circulated Electrolyte Module Basis

As shown in Figure 85, discharge capacity differences for the second deep-cycle are consistent with the ones presented in Figure 84.

Specific Gravity Characteristics

The characteristic of specific gravity during deep-cycling operation is a difficult parameter to analyze due to the differences in formation procedures with respect to the electrolyte of the cells. Overall electrolyte SG values were found to be higher for the cells formed using the tank formation method when compared to the other three formation methods, as the cells were received in dry-charged conditions, which allowed for the complete volume of the cells to be filled with of 1.265 electrolyte SG. It was also shown that the overall electrolyte SG values increased during deep-cycling operation for the cells

which were formed using the submerged container formation method, circulated electrolyte formation method, and the UF cells of the tank formation method, while the electrolyte SG values for the remaining cells remained relatively constant. Finally, while a positive correlation was shown in phase 1 of this research project between the formation level and electrolyte SG values, this trend was shown to be reversed for the cells formed using the circulated electrolyte and tank formation methods, where it was the UF cells that had the highest electrolyte SG values during deep-cycling operation. With respect to the circulated electrolyte formation method, this discrepancy may be explained by the fact that the electrolyte which was used to balance the UF cells at end of formation had a higher H_2SO_4 concentration than the electrolyte which was used to balance the NF and OF cells. This in turn resulted in higher SG values for the UF cells. With respect to the tank formation method, this discrepancy can be explained by the fact that higher amounts of H_2SO_4 was released from the plates of the UF cells as they continued forming when compared to the NF and OF cells, cells which had previously been activated using the same electrolyte concentration. Thus, it can be stated that the formation method does influence the resulting values and trends of electrolyte SG during deep-cycling operation.

With respect to the SG profile of cycle 10, there were no significant differences between the different formation methods (no cycle 10 SG profiles were obtained for the cells formed using the floor container formation method, yet similar results would have been expected). Specifically, cell electrolyte SG values decreased during the first 4 hours of cycling (i.e., discharging process), and only started increasing during the CV phase of the charging process (see Table 13 – Step 5). However, it is believed that the SG values did increase at the start of the charging process, yet as the electrolyte samples were limited to being taken from the top of the cell, the increase in electrolyte SG was not noticeable until the gassing process became more pronounced (i.e., CV phase of the charging process). These results are in agreement with the electrolyte SG profile of the cells formed in phase 1 of this research project.

Internal Resistance Characteristics

Due to the differences in formation levels of the four different formation methods, the characteristic of internal resistance during deep-cycling operation is also difficult to compare between the 12 different modules. Nonetheless, a negative correlation was

confirmed between the formation level and overall IR resistance values for both the charging and discharging processes on the modules formed using the floor container, the submerged container, and the tank formation methods. This trend was not observed for the modules formed using the circulated electrolyte formation method, where it was instead shown that cells having received the highest amount of formation input (i.e., OF module) resulted in higher overall IR values. It is believed that these results were influenced by the aforementioned discrepancies in electrolyte SG values. Finally, for all modules which were shown to continue their formation process as a result of their respective deep-cycling operation, a correlation was observed with respect to their overall IR values, where they were shown to decrease with cycling iterations. Thus, with the exception of the circulated electrolyte formation method, it can be stated that the formation method does not influence the resulting values and trends of cell IR during deep-cycling operation.

Module Voltage Alignment

With respect to the voltage alignment the modules during deep-cycling operation, a positive correlation was observed between the formation level and alignment of the respective modules. Specifically, the OF floor container module (i.e., 4.19TC – Figure 53) was shown to have attained cell voltage alignment after the completion of five deep-cycles, the OF submerged container module (i.e., 3.51TC – Figure 61) was shown to have attained cell voltage alignment after the completion of two deep-cycles, and the OF circulated electrolyte module (i.e., 4.33TC – Figure 69) was shown to have maintained cell voltage alignment for all 10 deep-cycles. On the other hand, the OF tank formation module (i.e., 2.60TC – Figure 79) was not able to attain cell voltage alignment. Thus, it can be stated that the characteristic of module voltage alignment is a function of formation input, and not of formation method.

Optimal Formation Method

Following the performance analysis of the modules obtained using the four different formation methods, the second and third steps in determining the optimal formation method, as outlined in section 4.2.3, is comprised of applying weighting ratios to the normalized initial discharge capacity and DFE values of the 12 different module variations. Figure 86 shows the sum of these two values for all four formation methods. It is important to note

that as was the case in determining the optimal formation level in phase 1 of this research project, a weighting ratio of 70 % / 30 % was attributed to the initial discharge capacity and DFE values, respectively, as this ensured more importance was attributed to the initial discharge capacity of the cell, a necessary requirement for off-grid solar applications.

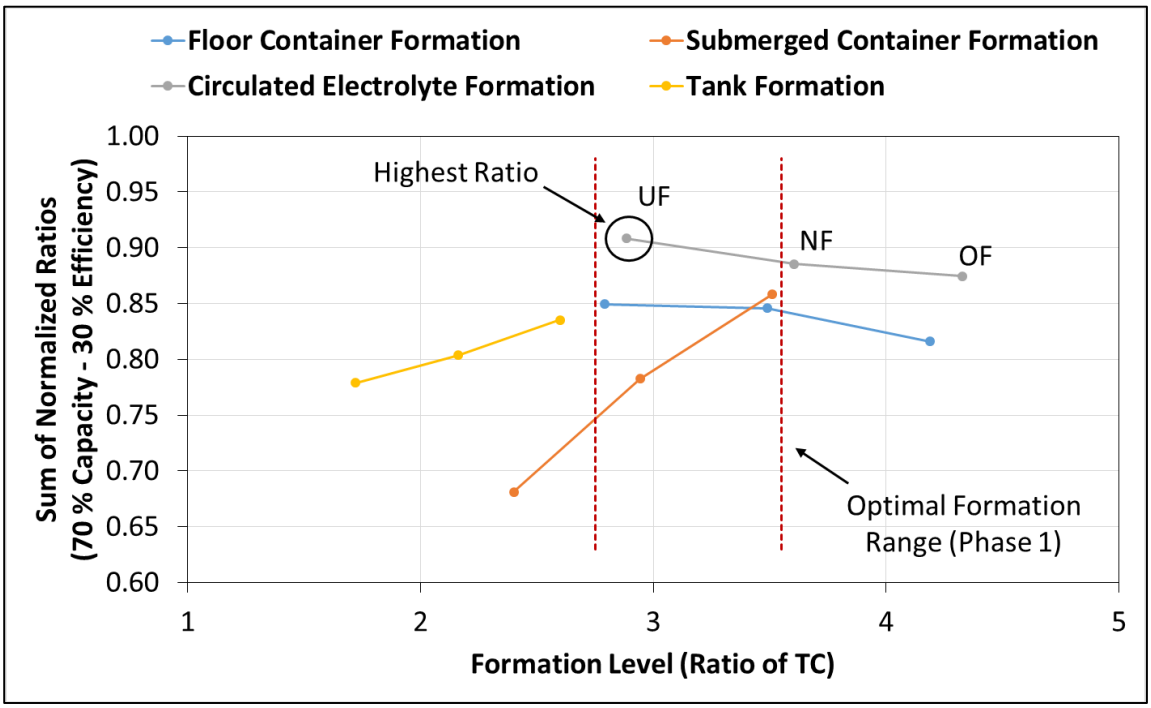

Figure 86 Sum of Normalized Initial Discharge Capacity and Discharge Formation Efficiency Values – Optimal Formation Method

Thus using the aforementioned weighting ratios, and as shown in Figure 86, the optimal formation method and level for off-grid solar applications was determined to be the UF level of the circulated electrolyte formation method (i.e., 2.89TC). This formation level falls within the recommended formation range of 2.75 to 3.55 times the theoretical capacity of the cell as was determined in phase 1 of this research project. As was shown in Figure 83, the UF circulated electrolyte module met its rated capacity output of 231 Ah on its initial discharge by obtaining a discharge capacity value of 253 Ah. Thus, client satisfaction would be ensured, while also providing a DFE of 12 % for the LAB manufacturer, slightly higher than the average DFE value of 11 % for the four formation methods.

In addition to having the best characteristics with respect to discharge capacity and DFE, the UF level of the circulated electrolyte formation method was shown to be clearly advantageous over the other three formation methods when considering the relationship

between discharge capacity and formation time (see Figure 84 and Figure 85). This advantage is a result of the ability of the circulated electrolyte formation method to maintain relatively constant electrolyte temperature and SG values during formation. Therefore based on the findings of this research project, it is recommended that SBC form ELG15 cells intended for off-grid solar applications using the circulated electrolyte formation method at their UF level of 2.89TC. By modifying their standard circulated electrolyte formation algorithm from the NF level to the UF level, it will save them time (i.e., 7.3 hours per formation) and energy, thus enabling a higher throughput, while still producing a good quality product.

Chapter 7: Conclusion

This thesis project was divided into two separate phases in order to address its main objective of determining the optimal formation level and method for the manufacturing of LABs intended for the growing off-grid solar storage market. This work resulted in three major research contributions:

1) A new method to determine best formation level according to performance, based on a comparison of initial discharge capacity and DFE (i.e., initial discharge capacity output of a cell divided by its formation capacity) values.
2) A new recommended formation range for LABs targeted for the off-grid solar market of 2.75 to 3.55 times the theoretical capacity of the cell. This range was found to be complementary to the range recommended in literature for conventional applications of 1.30 to 2.50 times the theoretical capacity of the cell. This is shown in Figure 44 (reproduced from section 5.3).

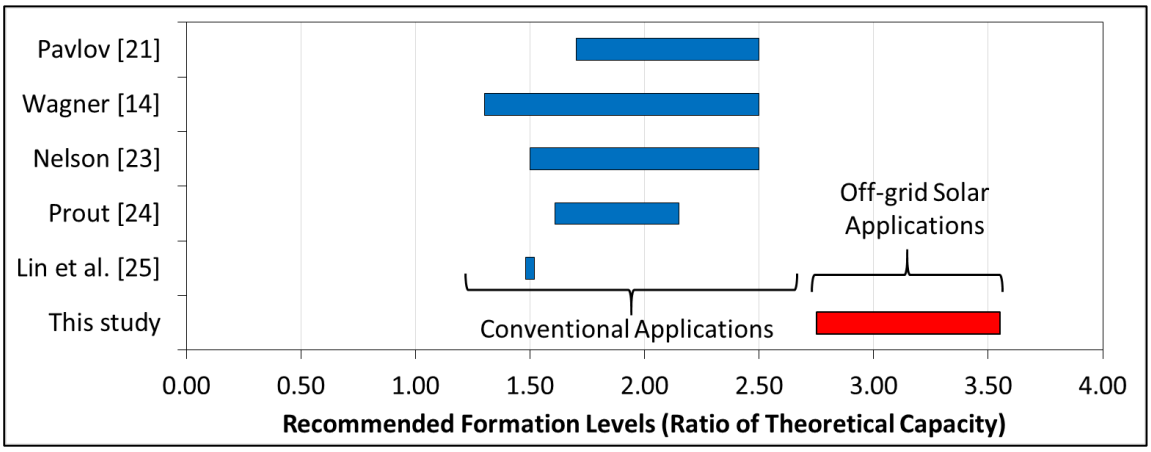

Figure 44 Comparison of Recommended Formation Levels

3) The experimental identification of a cell formed to a level of 2.89TC using the circulated electrolyte formation method at SBC as best for off-grid solar applications, meeting both client and manufacturer requirements.

In phase 1 of this research project, ELG15 LAB cells were formed and cycled at the RESL, allowing for all research parameters to be controlled, and with the objectives of identifying the optimal formation level and to study the impact of two different formation algorithms on subsequent cell performance. Specifically, using the container formation method, and with formation levels ranging from 0.70 to 7.04 times the theoretical capacity

of the cell, eight ELG15 cells were formed using the constant-current algorithm, while seven ELG15 cells were formed using the multi-step current algorithm. The deep-cycling results showed that the cells which received formation inputs ≤ 1.88TC performed better when formed using the constant-current formation algorithm than when formed using the multi-step current algorithm. Cells formed at a formation level ≥ 2.35TC were not subjected to this condition, where the multi-step current formation algorithm was shown to be advantageous over the constant-current formation algorithm due to its shortened formation duration, while providing comparable discharge capacity and DFE results. This discrepancy at relatively low formation levels was explained by the fact that the higher formation currents used in the multi-step current algorithm lowers the overall formation efficiency of the cells, a factor which is more evident at relatively low formation input values.

By applying a weighting ratio of 70 % / 30 % to the initial discharge capacity values and DFE values, respectively (i.e., ensuring more importance was attributed to the initial discharge capacity of the cell, a necessary requirement for off-grid solar applications), of the two different formation algorithms, the ideal formation level for this cell was determined to be between 2.75 and 3.55 times its theoretical capacity. This newly recommended formation range for off-grid solar applications was found to be complementary to the range recommended in literature for conventional applications of 1.30 to 2.50 times the theoretical capacity of the cell.

In phase 2 of this research project, ELG15 LAB cells were formed using four different formation methods at SBC, and subsequently cycled at the RESL with the objectives of identifying the optimal formation method for the LAB used in off-grid solar applications, and to determine the impact of these formation methods on the ideal formation level. Specifically, ELG15 cells were formed to three different formation levels per formation method, equivalent to 80 %, 100 %, and 120 % of the standard formation algorithm for each respective formation method. Subsequently, three cells per formation level (i.e., a module) were cycled simultaneously using a series configuration in order to mimic the S-480 battery. The deep-cycling results showed that the modules obtained using the circulated electrolyte formation method had the best performance results, while the modules obtained using the tank formation method had the worst performance results.

These initial results were not conclusive due to the differences in respective formation levels when comparing the four different methods used at SBC. These are clearly differentiated in Figure 16 (reproduced from section 4.2.1).

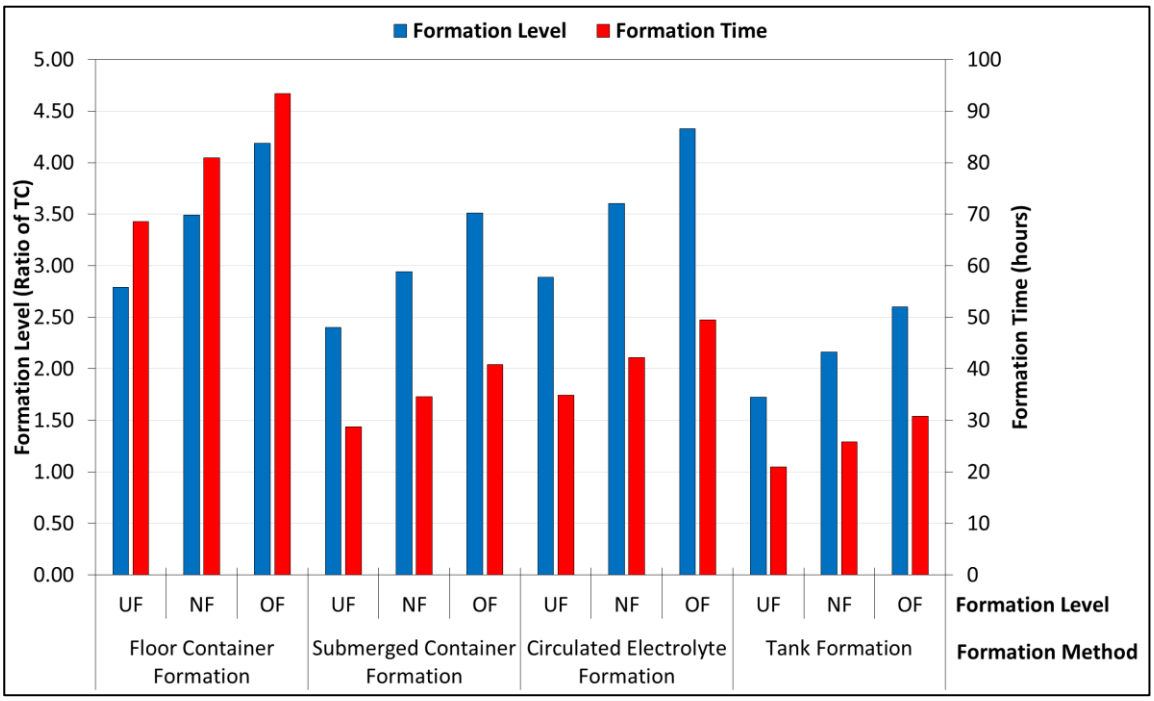

Figure 16 Comparison of Formation Levels and Times at SBC

Nonetheless, by comparing the initial discharge capacity results of the 12 different modules as a function of theoretical capacity, the modules obtained using the circulated electrolyte formation method still outperformed all other formation methods, including the cells formed in phase 1 of this research project, and showed no disadvantages with respect to total formation time when compared to the other formation methods.

By applying the recommended weighting ratio of 70 % / 30 % to the initial discharge capacity values and DFE values, respectively, the optimal formation method and level was determined to be the present UF formation level of the circulated electrolyte formation method at SBC (i.e., 2.89TC). This result was shown to be in agreement with the optimal formation range as determined in phase 1 of this research project. Advantages with respect to this formation method include a discharge step used to increase the overall amount of formed $PbSO_4$, and a reduced formation time due to its built-in ability to maintain relatively constant electrolyte temperature and SG values during formation.

Thus based on the aforementioned conclusions, it is recommended that SBC form ELG15 cells intended for the off-grid solar market using the circulated electrolyte formation method at their UF level of 2.89TC. This will require a change in Step 6 of their standard circulated electrolyte formation schedule, as shown in Table 22.

Table 22 SBC Circulated Electrolyte Formation Algorithm – Off-grid Solar Applications

Step #	Description	Duration
1	Electrolyte Filling	10 minutes
2	Soaking (1.250 SG Electrolyte)	30 minutes
3	Charge at 28.0 A	1 hour (i.e., 28 Ah)
4	Charge at 70.0 A	16 hours (i.e., 1120 Ah)
5	Charge at 46.7 A	1 hour (i.e., 47 Ah)
6	Charge at 70.0 A	6.7 hours (i.e., 469 Ah) **(NEW)**, reduced from 14 hours (i.e., 980 Ah)
7	Rest	5 minutes
8	Discharge at 37.3 A	4 hours (i.e., 149 Ah)
9	Rest	5 minutes
10	Charge at 70.0 A	5.5 hours (i.e., 385 Ah)

As shown in Table 22, modifying the duration of Step 6 will save 7.3 hours per formation, thus enabling a higher throughput, while producing the best product for off-grid solar applications. One is reminded that factors which influence the formation level include the thickness of the plates, the phase composition of the cured paste, the size of the particles which constitute the individual phases, and the current and voltage algorithms of formation. While the latter three factors have been discussed within this research project, these results have only been confirmed for a positive plate thickness of 4.32 mm.

In addition to these findings, it is recommended that formation levels higher than 3.51TC be formed at SBC using the submerged container formation method, due to the promising DFE results of this formation method. Also, due to the capability of this formation charger to discharge batteries, it is suggested that a discharge step be included in the formation algorithm as is the case for the circulated electrolyte formation algorithm. This would be expected to increase the initial discharge capacity values of the cells. With respect to the tank formation method, it is recommended ELG15 cell be formed using levels higher than 2.60TC, as the three modules obtained using this method were shown to be relatively under-formed compared to the other three formation methods.

Finally, recommendations pertaining to the improvement of this research project are as follows:

- That scanning electron microscope analysis be used to determine the β/α-PbO_2 ratio of the cells formed in phases 1 and 2 of this research project. This would provide additional information regarding the differences in formation characteristics.
- That internal cell temperatures and individual cell voltages be monitored during their formation process, which would provide additional information regarding the crystal structure of the formed PAM and NAM. This would also ensure proper temperature and voltage range for these cells during the formation process.
- That additional deep-cycles (i.e., 1000 cycles) be completed in order to study the impact of the different formation methods and levels on the cycle life of the LAB.
- That cells be formed to the same formation levels for each method at SBC, rather than a relative of the nominal manufacturing standards, in order to better compare the four different formation methods.
- That cells comprised of different plate thicknesses be formed in order to study the impact of this variable on the results of this research project.
- That a techno-economic analysis be completed taking into account the AC energy costs of the four different formation methods at SBC. This would provide additional information regarding the optimal formation method and level.

References

[1] International Energy Agency, Energy for All - Financing Access for the Poor, in: OECD/IEA (Ed.), Paris, 2011.

[2] R.K. Akikur, R. Saidur, H.W. Ping, K.R. Ullah, Comparative study of stand-alone and hybrid solar energy systems suitable for off-grid rural electrification: A review, Renewable and Sustainable Energy Reviews, 27 (2013) 738-752.

[3] A. Jossen, J. Garche, D.U. Sauer, Operation conditions of batteries in PV applications, Solar Energy, 76 (2004) 759-769.

[4] D. Pavlov, Chapter 3 - Formation of Lead-Acid Batteries and Structure of Positive and Negative Active Masses, in: D.A.J.R.G.T.M.D. Parker (Ed.) Valve-Regulated Lead-Acid Batteries, Elsevier, Amsterdam, 2004, pp. 37-108.

[5] D. Pavlov, Fundamentals of Lead–Acid Batteries, (2011) 29-114.

[6] W. Waag, D.U. Sauer, SECONDARY BATTERIES – LEAD– ACID SYSTEMS | State-of-Charge/Health, in: J. Garche (Ed.) Encyclopedia of Electrochemical Power Sources, Elsevier, Amsterdam, 2009, pp. 793-804.

[7] S. Piller, M. Perrin, A. Jossen, Methods for state-of-charge determination and their applications, Journal of Power Sources, 96 (2001) 113-120.

[8] R. Wagner, D.U. Sauer, Charge strategies for valve-regulated lead/acid batteries in solar power applications, Journal of Power Sources, 95 (2001) 141-152.

[9] A.C. Loyns, SECONDARY BATTERIES – LEAD– ACID SYSTEMS | Bipolar Batteries, in: J. Garche (Ed.) Encyclopedia of Electrochemical Power Sources, Elsevier, Amsterdam, 2009, pp. 750-754.

[10] D. Pavlov, Processes During Formation of Negative Battery Plates, (2011) 481-499.

[11] D. Pavlov, Processes After Formation of the Plates and During Battery Storage, (2011) 535-566.

[12] D. Pavlov, Curing of Battery Plates, (2011) 363-404.

[13] I. Dreier, F. Saez, P. Scharf, R. Wagner, Investigation on soaking and formation of lead/acid battery plates with different mass structure, Journal of Power Sources, 85 (2000) 117-130.

[14] R. Wagner, Secondary Batteries - Lead-Acid Systems | Curing and Formation, in: J. Garche (Ed.) Encyclopedia of Electrochemical Power Sources, Elsevier, Amsterdam, 2009, pp. 662-676.

[15] W. Boehnstedt, J.K. Whear, SECONDARY BATTERIES – LEAD– ACID SYSTEMS | Separators, in: J. Garche (Ed.) Encyclopedia of Electrochemical Power Sources, Elsevier, Amsterdam, 2009, pp. 620-631.

[16] D. Pavlov, H2SO4 Electrolyte – An Active Material in the Lead–Acid Cell, (2011) 117-148.

[17] D. Pavlov, SECONDARY BATTERIES – LEAD– ACID SYSTEMS | Electrolyte, in: J. Garche (Ed.) Encyclopedia of Electrochemical Power Sources, Elsevier, Amsterdam, 2009, pp. 610-619.

[18] P.T. Moseley, D.A.J. Rand, Chapter 1 - The Valve-regulated Battery — A Paradigm Shift in Lead-Acid Technology, in: D.A.J.R.G.T.M.D. Parker (Ed.) Valve-Regulated Lead-Acid Batteries, Elsevier, Amsterdam, 2004, pp. 1-14.

[19] D. Pavlov, Formation of Positive Lead–Acid Battery Plates, (2011) 443-479.

[20] N. Fan, C. Sun, D. Kong, Y. Qian, Chemical synthesis of PbO2 particles with multiple morphologies and phases and their electrochemical performance as the positive active material, Journal of Power Sources, 254 (2014) 323-328.

[21] D. Pavlov, Chapter 12 - Technology of Formation, in: D. Pavlov (Ed.) Lead-Acid Batteries: Science and Technology, Elsevier, Amsterdam, 2011, pp. 501-531.

[22] Trojan Battery Company, Trojan Industrial Line User's Guide, in, Santa Fe Springs, CA, 2012.

[23] D.W.H. Lambert, J.E. Manders, R.F. Nelson, K. Peters, D.A.J. Rand, M. Stevenson, Strategies for enhancing lead–acid battery production and performance, Journal of Power Sources, 88 (2000) 130-147.

[24] L. Prout, Aspects of Lead-Acid-Battery Technology .4. Plate Formation, Journal of Power Sources, 41 (1993) 195-219.

[25] M.T. Lin, Y.Y. Wang, C.C. Wan, Determination of Optimal Formation Conditions for Tubular Positive Electrodes of Lead-Acid-Batteries, Electrochimica Acta, 31 (1986) 565-571.

[26] D.U. Sauer, J. Garche, Optimum battery design for applications in photovoltaic systems — theoretical considerations, Journal of Power Sources, 95 (2001) 130-134.

[27] M.J. Weighall, Techniques for jar formation of valve-regulated lead–acid batteries, Journal of Power Sources, 116 (2003) 219-231.

[28] P. Kumar, K. Murthy, K. Sudarsanam, S. Vijayanand, An Exploratory Study on Electrolyte Circulation as a Means of Achieving Faster Formation of Lead Acid Batteries, International Journal of Electrochemical Science, 7 (2012) 1060-1070.

[29] V. Naidenov, U. Markov, Influence of ultrasonic waves on the formation of lead-acid batteries, Journal of Power Sources, 217 (2012) 236-242.

[30] F.B. Diniz, L.E.P. Borges, B.c.d.B. Neto, A comparative study of pulsed current formation for positive plates of automotive lead acid batteries, Journal of Power Sources, 109 (2002) 184-188.

[31] D. Pavlov, P. Nikolov, T. Rogachev, Influence of carbons on the structure of the negative active material of lead-acid batteries and on battery performance, Journal of Power Sources, 196 (2011) 5155-5167.

[32] S.W. Swogger, P. Everill, D.P. Dubey, N. Sugumaran, Discrete carbon nanotubes increase lead acid battery charge acceptance and performance, Journal of Power Sources, 261 (2014) 55-63.

[33] A. Moncada, M.C. Mistretta, S. Randazzo, S. Piazza, C. Sunseri, R. Inguanta, High-performance of PbO2 nanowire electrodes for lead-acid battery, Journal of Power Sources, 256 (2014) 72-79.

[34] D. Pavlov, Calculation of the Active Materials for Lead–Acid Cells, (2011) 607-622.

[35] P. Křivík, K. Micka, P. Bača, K. Tonar, P. Tošer, Effect of additives on the performance of negative lead-acid battery electrodes during formation and partial state of charge operation, Journal of Power Sources, 209 (2012) 15-19.

[36] J. Schiffer, D.U. Sauer, H. Bindner, T. Cronin, P. Lundsager, R. Kaiser, Model prediction for ranking lead-acid batteries according to expected lifetime in renewable energy systems and autonomous power-supply systems, Journal of Power Sources, 168 (2007) 66-78.

[37] R. Dufo-López, J.M. Lujano-Rojas, J.L. Bernal-Agustín, Comparison of different lead–acid battery lifetime prediction models for use in simulation of stand-alone photovoltaic systems, Applied Energy, 115 (2014) 242-253.

[38] D.U. Sauer, M. Bächler, G. Bopp, W. Höhe, J. Mittermeier, P. Sprau, B. Willer, M. Wollny, Analysis of the performance parameters of lead/acid batteries in photovoltaic systems, Journal of Power Sources, 64 (1997) 197-201.

[39] Surrette Battery Company, S-480 Spec Sheet, in, http://rollsbattery.com/public/specsheets/S-480.pdf, Accessed on 26/11/2014.

[40] Surrette Battery Company, Rolls Battery User Manual, in, http://support.rollsbattery.com/helpdesk/attachments/1073177, Last accessed on 10/02/2014.

[41] IEEE Standards Association, IEEE Guide for Selecting, Charging, Testing, and Evaluating Lead-Acid Batteries Used in Stand-Alone Photovoltaic (PV) Systems, in: IEEE Std 1361-2014 (Revision of IEEE Std 1361-2003), IEEE, New York, NY, 2014, pp. 1-39.

[42] P. Kurzweil, CAPACITORS | Electrochemical Double-Layer Capacitors, in: J. Garche (Ed.) Encyclopedia of Electrochemical Power Sources, Elsevier, Amsterdam, 2009, pp. 607-633.

[43] S. Abu-Sharkh, D. Doerffel, Rapid test and non-linear model characterisation of solid-state lithium-ion batteries, Journal of Power Sources, 130 (2004) 266-274.

[44] R. Wagner, SECONDARY BATTERIES – LEAD– ACID SYSTEMS | Electrode Design, in: J. Garche (Ed.) Encyclopedia of Electrochemical Power Sources, Elsevier, Amsterdam, 2009, pp. 599-609.

[45] D. Pavlov, Chapter 7 - Additives to the Pastes for Positive and Negative Battery Plates, in: D. Pavlov (Ed.) Lead-Acid Batteries: Science and Technology, Elsevier, Amsterdam, 2011, pp. 311-361.

[46] A. Kirchev, M. Perrin, E. Lemaire, F. Karoui, F. Mattera, Studies of the pulse charge of lead-acid batteries for PV applications: Part I. Factors influencing the mechanism of the pulse charge of the positive plate, Journal of Power Sources, 177 (2008) 217-225.

[47] Thermo Fisher Scientific Inc., dataTaker DT80, in, 2014.

[48] IEC, Stationary lead-acid batteries, in: Stationary lead-acid batteries - Part 11: Vented types - General requirements and methods of tests, IEC, Geneva, 2002.

[49] D. Pavlov, Lead Alloys and Grids. Grid Design Principles, (2011) 149-221.

[50] M. Barak, Electrochemical Power Sources: primary and secondary batteries, Institution of Engineering and Technology, 1980.

[51] American Elements, Lead Sponge, in, www.americanelements.com/lead-sponge.html, Accessed on 03/06/2015.

[52] A.K. Shukla, V. Ganesh Kumar, N. Munichandraiah, T.S. Srinath, A method to monitor valve-regulated lead acid cells, Journal of Power Sources, 74 (1998) 234-239.

[53] F. Huet, R.P. Nogueira, L. Torcheux, P. Lailler, Simultaneous real-time measurements of potential and high-frequency resistance of a lab cell, Journal of Power Sources, 113 (2003) 414-421.

[54] Continental Control Systems, Current Transformers, in, 2013.

[55] Continental Control Systems, WattNode Modbus, in, 2013.

[56] T. Beckwith, R. Marangoni, J. Lienhard, Mechanical Measurements, 6th ed., Prentice Hall, 2007.

[57] Arbin Instruments, Mits Pro User's Manual, in, 2013.

[58] OMEGA, Revised Thermocouple Reference Tables, TYPE T, in, http://www.omega.ca/temperature/Z/pdf/z207.pdf, n.d.

[59] Anton Paar, Portable Density Meter: DMA 35 - Specifications, in, http://www.anton-paar.com/us-en/products/details/portable-density-meter-dma-35/density-meter/, 2015.

[60] Fluke Inc., Fluke 87V Industrial Multimeter - Specs, in, http://en-us.fluke.com/products/digital-multimeters/fluke-87v-digital-multimeter.html#techspecs, 2015.

[61] Empro Shunts, Product Engineering FAQ, in, http://www.emproshunts.com/Products/Product-Engineering-FAQs.aspx, 2010.

[62] Thermo Fisher Scientific Inc., DT80 Technical Specifications, in, http://www.datataker.com/documents/specifications/TS-0059-F1%20-%20DT80.pdf, 2015.

[63] Digatron Power Electronics, INSTRUCTION MANUAL BCD80-8-375V, in, Shelton, Connecticut 2015.

[64] OHAUS, Ohaus SD Series, in, http://www.ohaus.ca/PU/SD200.htm, n.d.

[65] Surrette Battery Co. Ltd., Material Safety Data Sheet - Lead Acid Battery, in, 2014.

[66] Canadian Centre for Occupational Health and Safety, Battery Charging, in: OHS Answers Fact Sheets, Government of Canada, http://www.ccohs.ca/oshanswers/safety_haz/battery-charging.html, Last accessed on 16/03/2015.

[67] Surrette Battery Co. Ltd., Material Safety Data Sheet - Battery Acid, in, 2014.

Appendix A – Measurement Unit

A line diagram of the measurement unit is shown in Figure 13. Figure 14 and Figure 15 show the measurement unit as installed at SBC and an example of the measurement unit connected to the tank formation charger at SBC, respectively. As shown, this configuration allowed for the monitoring of a combined four DC channels using the DC 1 and DC 2 connection points (i.e., two channels each), and the monitoring of a combined two AC power inputs using the AC Voltage 1, AC Current 1, AC Voltage 2, and AC Current 2 connection points. These two DC connection points and four AC connection points were connected to the measuring equipment located inside the formation chargers by mean of appropriate electrical cables. Specifically, 300 V shielded cable with four twisted pairs was used to relay the DC measurements and the AC current measurements, while 600 V cable with four conductors was used to relay the AC voltage measurements.

DC values were measured using current shunts and voltage taps, and recorded using a dataTaker DT80 data logger. Current shunts, which have a known resistance, are used to measure current in a circuit by measuring the voltage drop across them, which is in turn proportional to the current flowing through it. Low-pass filtered voltage dividers (20:1 ratio) were used between the DC voltage measurements and the data logger, due to the data logger voltage limit of +/- 30 V [47], and resistor-capacitor (RC) circuits were used as low-pass filters to provide smoother DC current values to the data logger. Specifically, the filtered voltage dividers were comprised of two resistors (i.e., R_1 = 475 kΩ, R_2 = 24.9 kΩ) and one 47 µF capacitor, and provided a frequency cutoff of 0.14 Hz, while the RC circuits were comprised of a 1 kΩ resistor and a 220 µF capacitor, and provided a frequency cutoff of 0.72 Hz. Figure 87 shows the configuration of the filtered voltage dividers which were used to filter the DC voltage measurements, and the configuration of the RC circuits which were used to filter the DC current measurements.

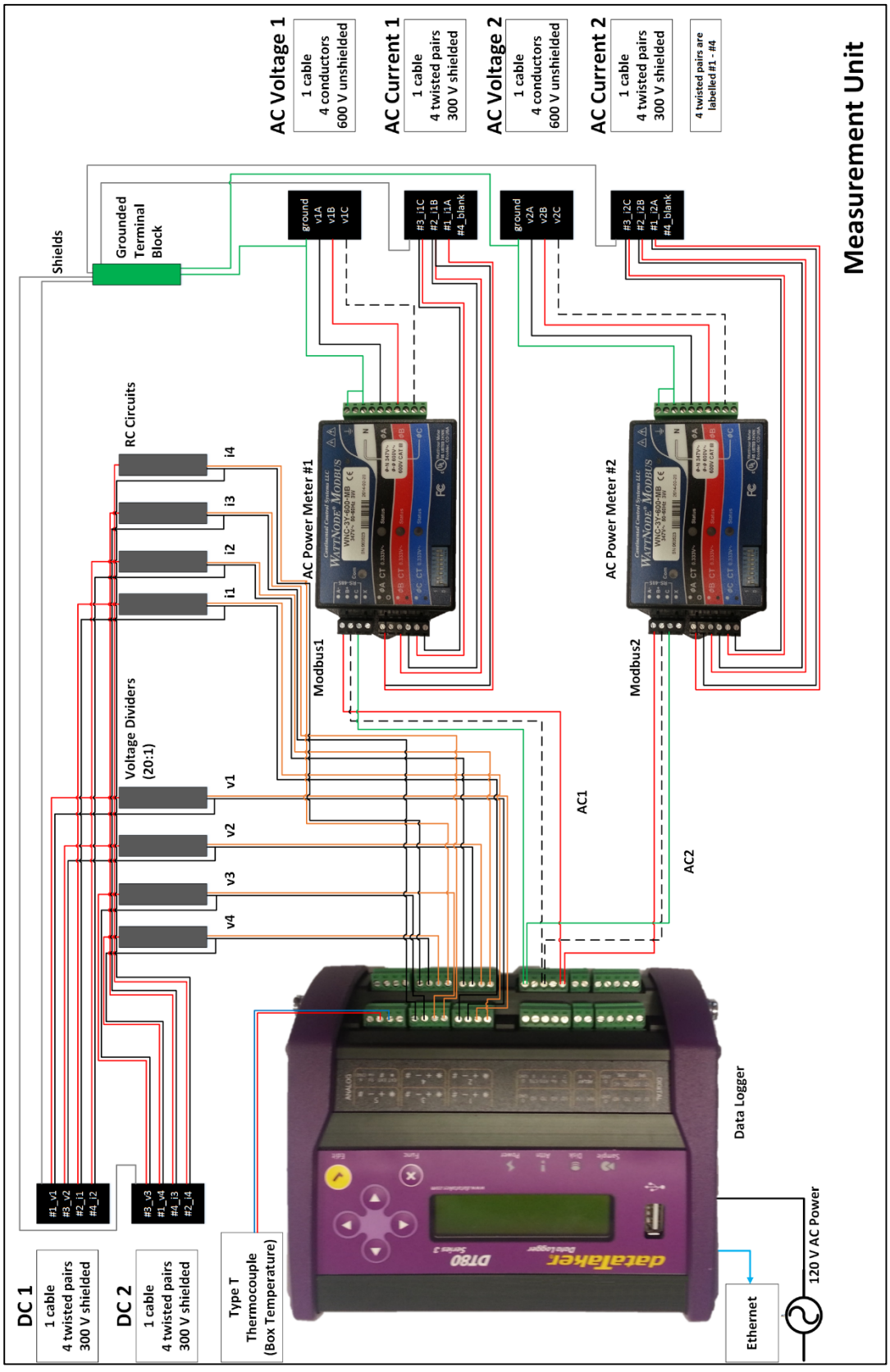

Figure 13 Line Diagram of Measurement Unit (Reproduced from section 4.2)

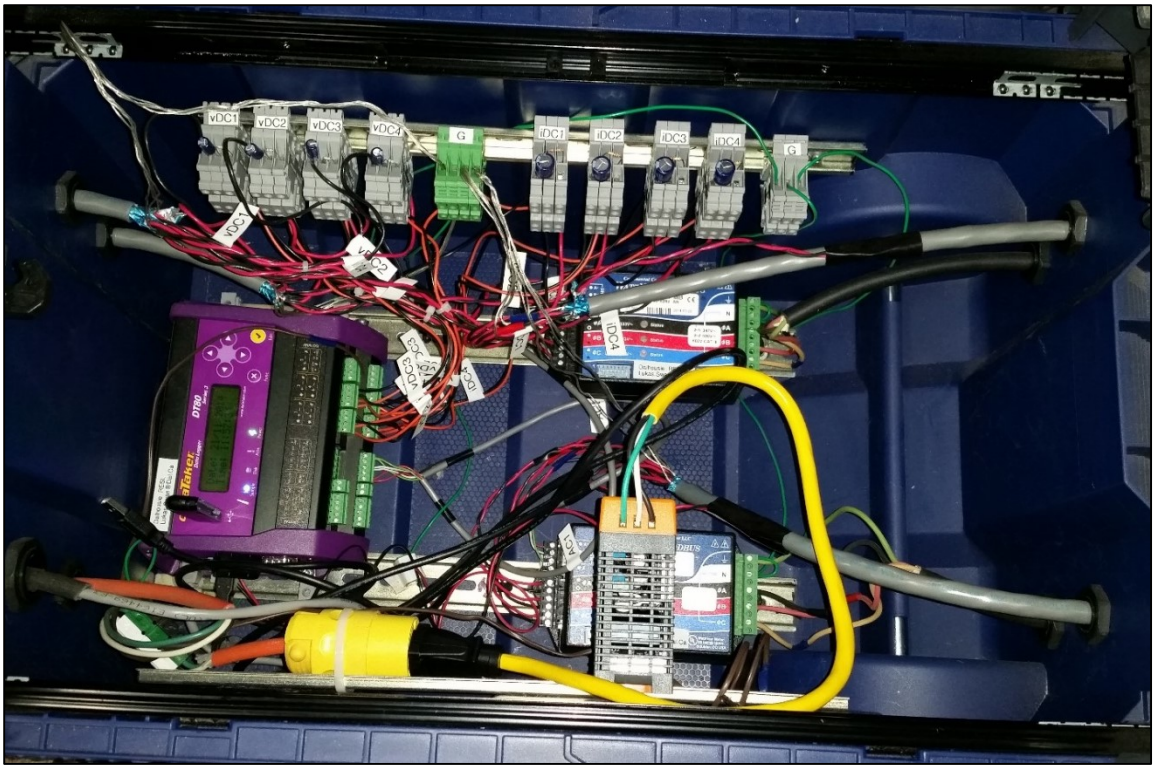

Figure 14 As-Built Measurement Unit (Reproduced from section 4.2)

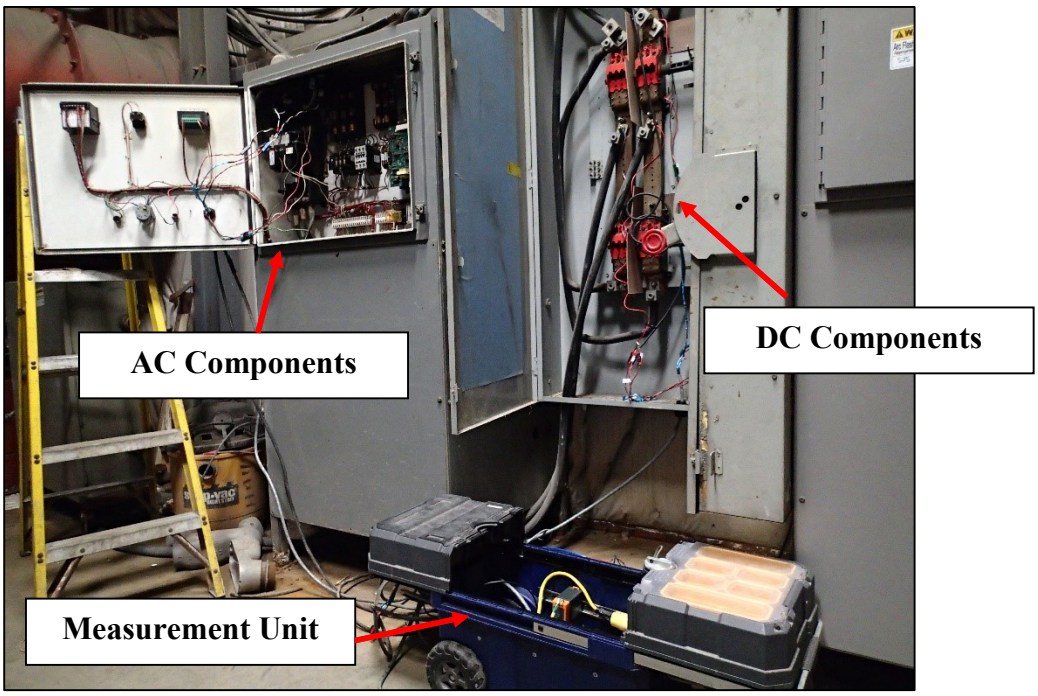

Figure 15 Measurement Unit and SBC Tank Formation Charger (Reproduced from section 4.2)

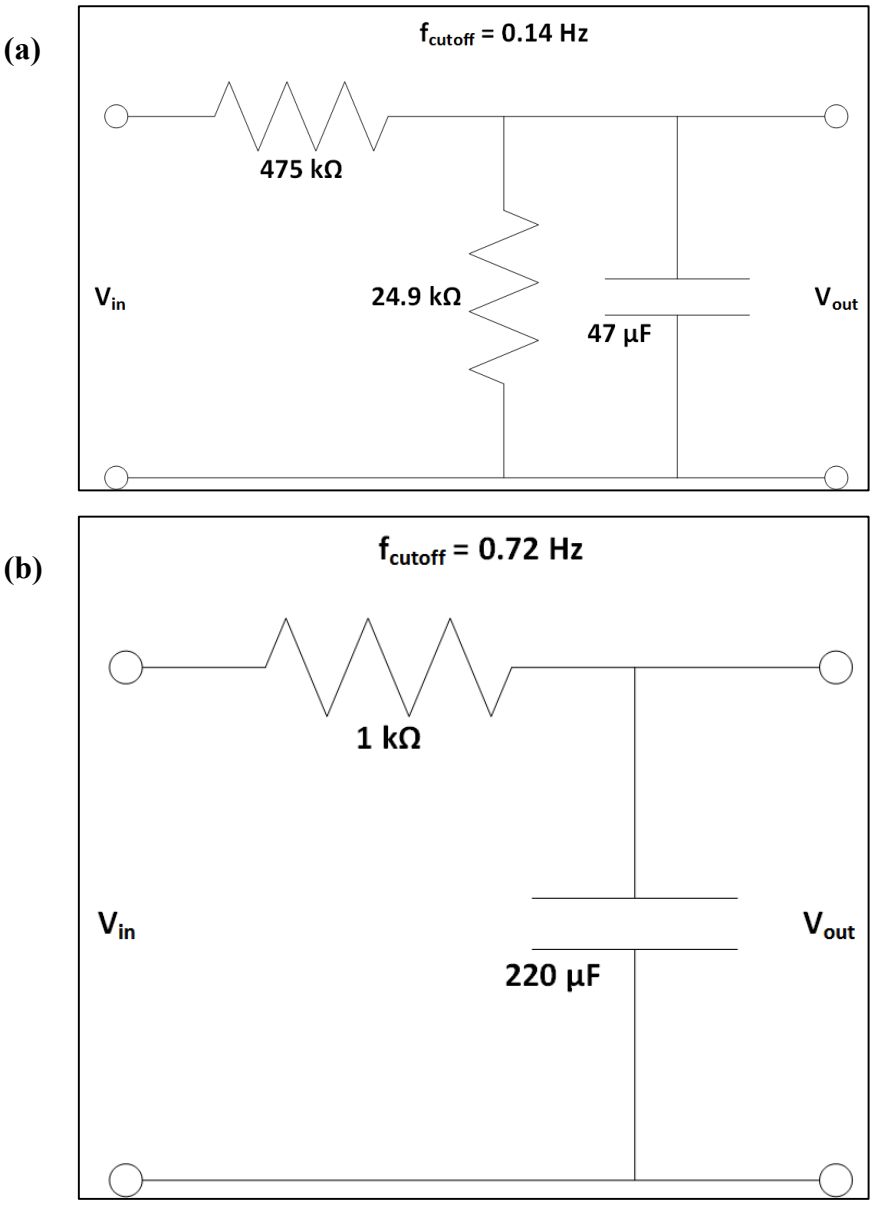

Figure 87 (a) Filtered Voltage Divider, (b) RC Circuit

AC current and voltage were measured using current transducers (CTs), and voltage taps, respectively, and recorded using the same data logger in conjunction with a WattNode AC power meter. CTs are used to measure current by providing a low-voltage output value, which is in turn proportional to the current flowing through it. In order to ensure accurate AC current measurements, the CTs were sized based on the magnitude of the current value for the specific formation charger, as the CTs are designed to provide a 333 mV voltage output at their rated full scale current [54]. The WattNode AC power meters, which convert

voltage, current, and true power measurements into a digital output read by the data logger through RS-485 communication, are rated for +/- 600 V and are line powered [55].

The shunts, CTs, and voltage taps were located directly inside the enclosure of each respective formation charger, whereas the voltage dividers/RC circuits, AC power meters, and the data logger were located inside the measurement unit near the formation charger of interest (see Figure 15).

The design of the measurement unit also included a grounded terminal block used to protect the equipment, a T-type thermocouple to measure the temperature of the unit, Ethernet capability to communicate with the data logger, 12 V AC to power the data logger, and shielded cables to avoid noise interference from other cables, thus providing more accurate readings.

Table 23 shows the DC output ratings of the four formation chargers, and the shunts which were used to measure their respective formation current, along with the AC input ratings of the four formation chargers, and the CTs which were used to measure their respective current. It should be noted that the AC input of all four formation chargers was comprised of three phases and ground.

Table 23 Formation Chargers DC Output and AC Input Ratings

	DC Output / AC Input Characteristics			
Formation Method	DC / AC Current (A)	DC / AC Voltage (V)	Current Shunt Rating (mV/A)	CT Rating (A)
Floor Container	0 – 100 / 35	12 – 280 / 600	50/100	50
Submerged Container	0 – 80 / 270	0 – 375 / 600	50/100	250
Circulated Electrolyte	0 – 300 / 120	0 – 150 / 600	50/500	250
Tank	0 – 600 / 134	0 – 200 / 575	50/500	250

Figure 88, Figure 89, Figure 90, and Figure 91, show the internal configurations of the floor container formation charger, the submerged container formation charger, the circulated electrolyte formation charger, and the tank formation charger, respectively, which were used to measure AC/DC formation inputs and outputs, respectively, of current and voltage.

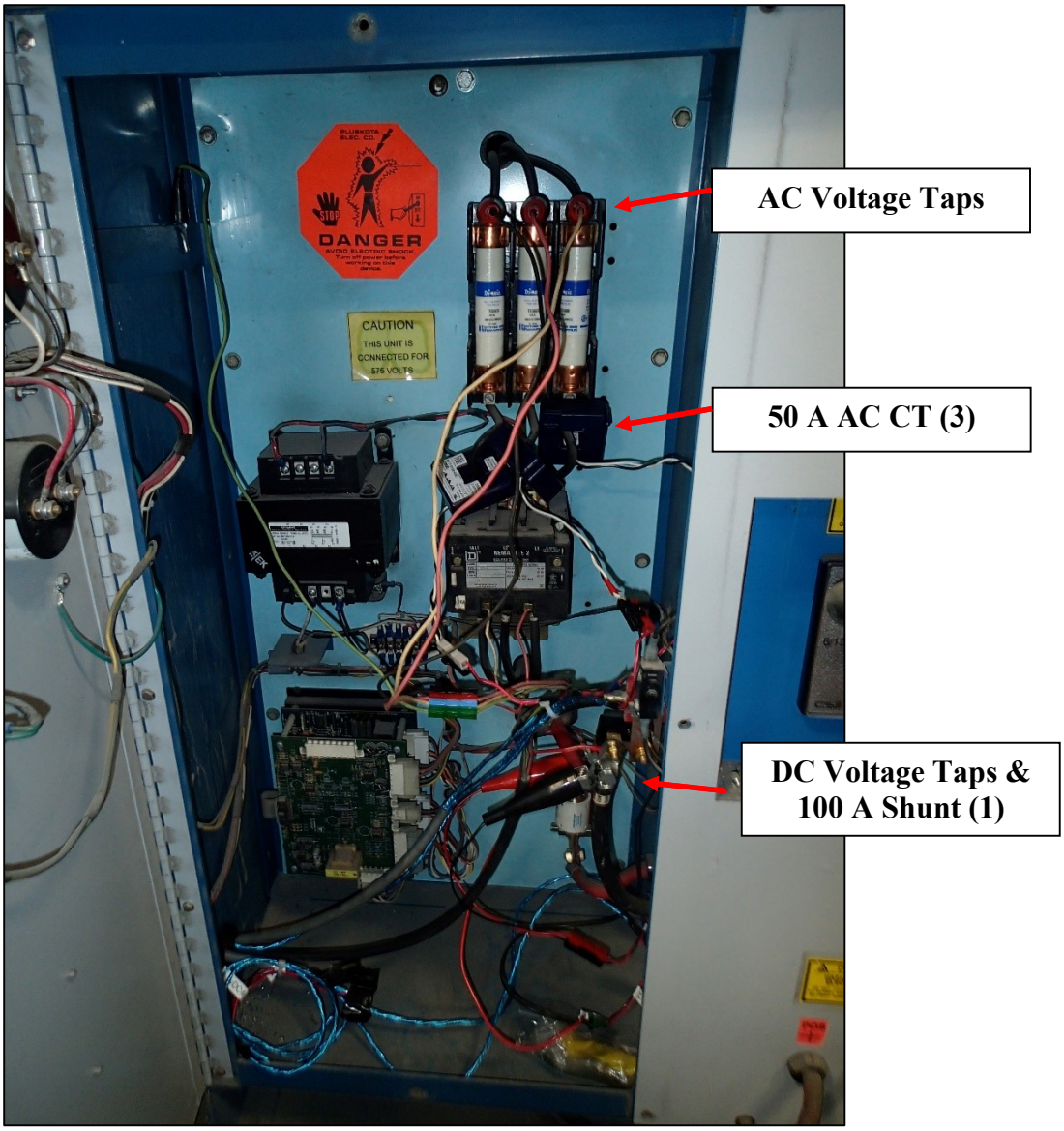

Figure 88 **SBC Floor Container Formation Charger – AC/DC Monitoring Configuration**

(a)

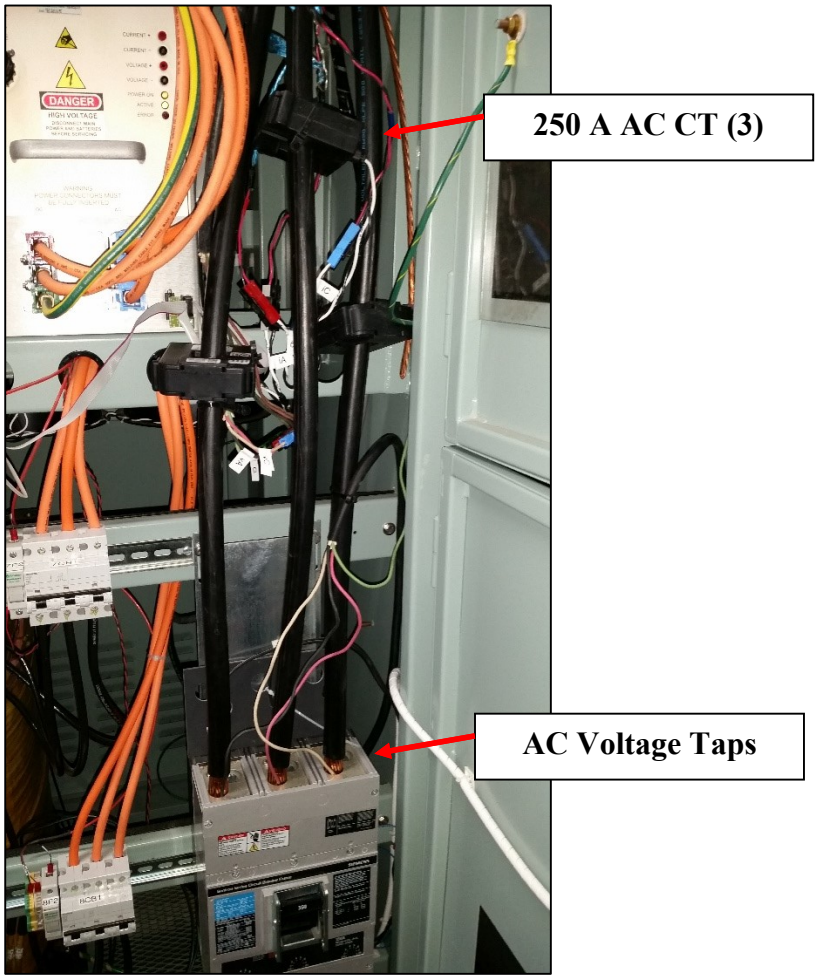

(b)

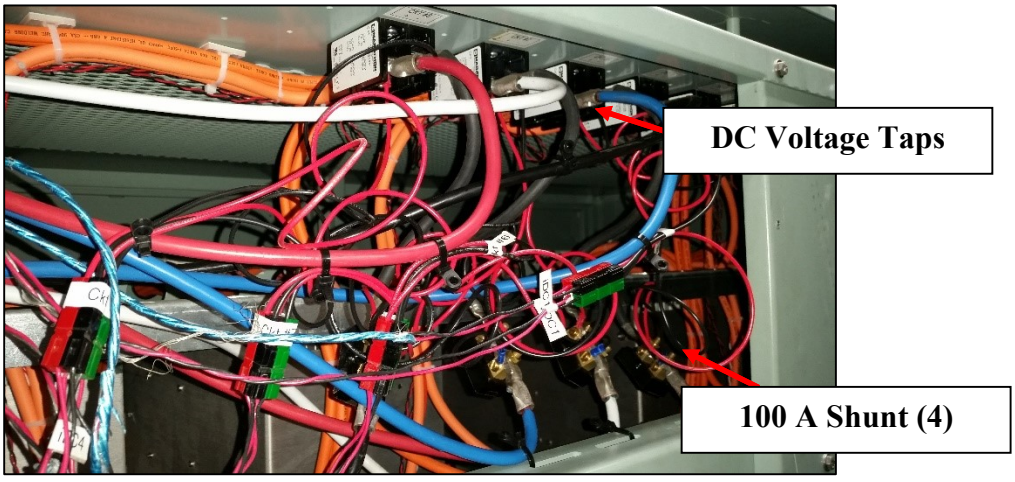

Figure 89 **SBC Submerged Container Formation Charger – (a) AC Monitoring Configuration, (b) DC Monitoring Configuration**

(a)

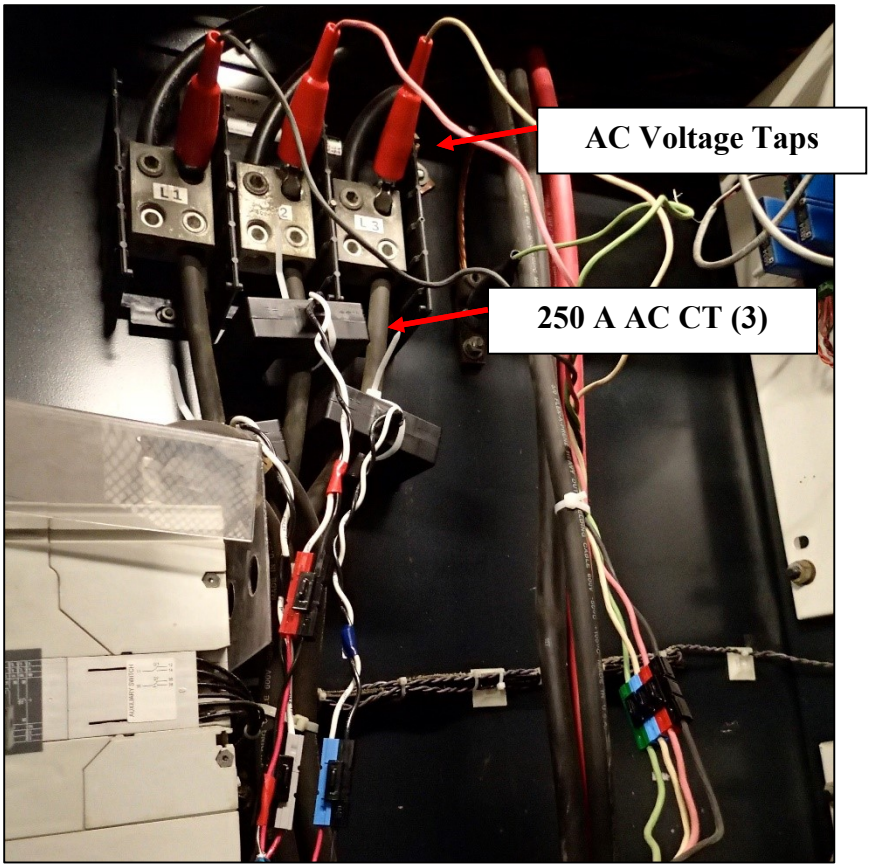

(b)

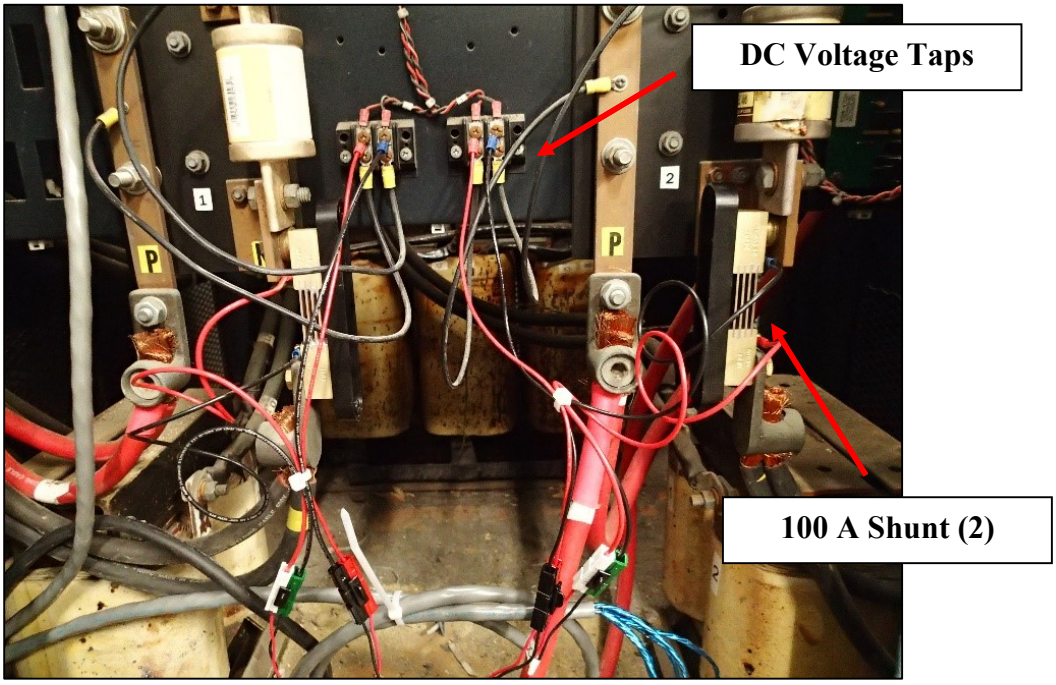

Figure 90 **SBC Circulated Electrolyte Formation Charger – (a) AC Monitoring Configuration, (b) DC Monitoring Configuration**

(a)

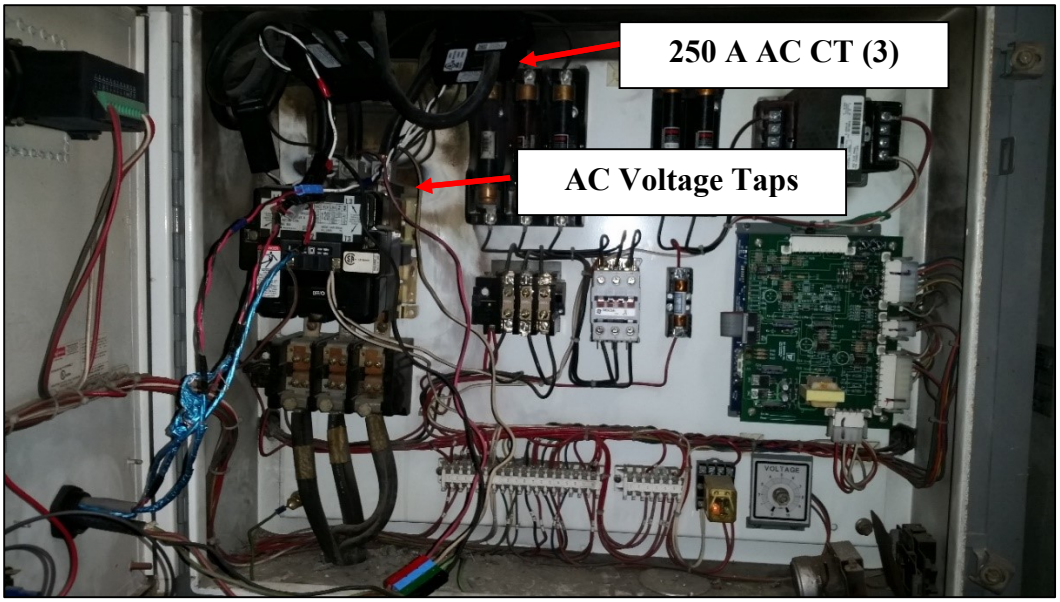

(b)

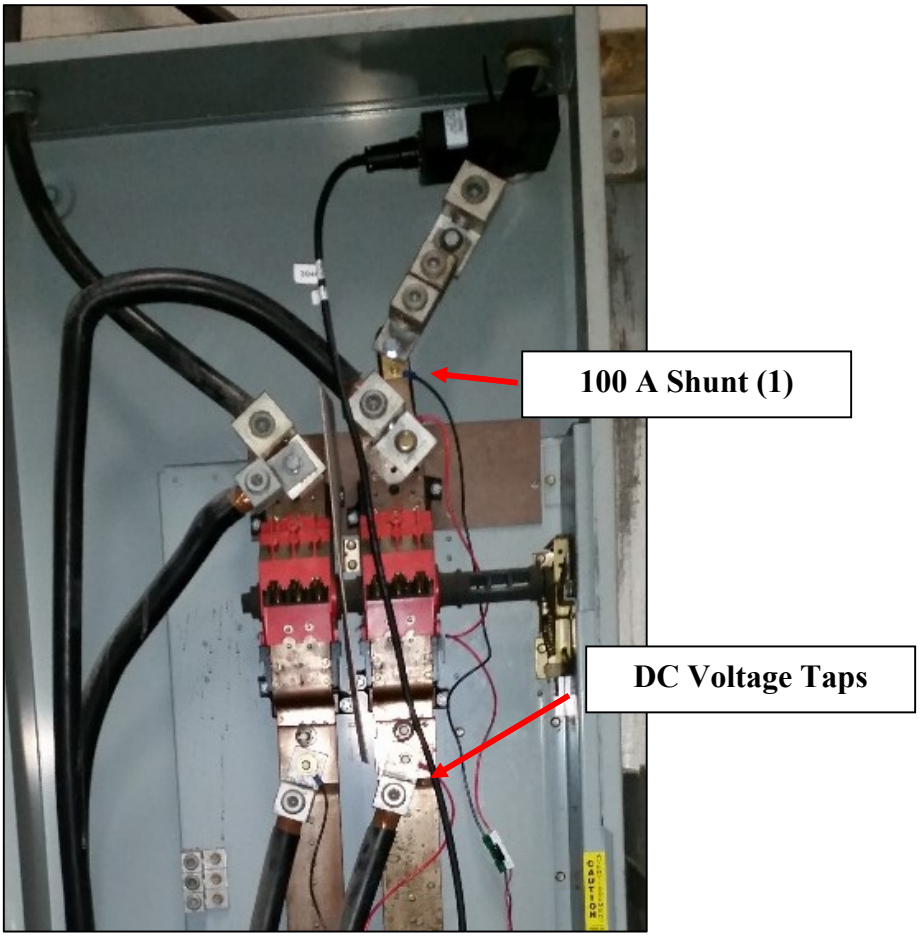

Figure 91 **SBC Tank Formation Charger – (a) AC Monitoring Configuration, (b) DC Monitoring Configuration**

Finally as an example, the dataTaker DT80 code written to monitor the circulated electrolyte formation charger at SBC is shown below.

```
' Code to Monitor Circulated Electrolyte Line at SBC
' By: Justin Deveau (deveau.jd@gmail.com)
' Copyright 2015 as part of the Renewable Energy Storage Laboratory

DELALLJOBS
BEGIN"SURRETTE"

' Sets up the DT80 to communicate with the WattNodes
PROFILE SERSEN_PORT BPS=19200
PROFILE SERSEN_PORT DATA_BITS=8
PROFILE SERSEN_PORT STOP_BITS=1
PROFILE SERSEN_PORT PARITY=NONE
PROFILE SERSEN_PORT FLOW=NONE
PROFILE SERSEN_PORT MODE=RS485
PROFILE SERSEN_PORT FUNCTION=MODBUS_MASTER

' Configuring CTs
'1modbus(AD1,R4:1603)=250
1modbus(AD2,R4:1603)=250

' Configures the time zone, and mains frequency
PROFILE LOCALE TIME_ZONE=-14400
PROFILE PARAMETERS P11=60

' Defining the statistical sub-schedule trigger
RS

' Defining schedule A & its trigger
RA"SurretteMonitoring"("B:",ALARMS:OV:100KB:W60,DATA:OV:50MB)1S
```

```
LOGONA
        ' Box Temperature
        5TT("BoxTemperature~degC",=10CV,LM,NA,AV)

        ' DC Measurements
        3HV("DC_3_Volt~V",=3CV,LM,20.30,AV)
        4HV("DC_4_Volt~V",=4CV,LM,20.32,AV)
        3*V("DC_3_Curr~A",=7CV,LM,-10,AV)
        4*V("DC_4_Curr~A",=8CV,LM,10,AV)

' Second WattNode (AC Measurements)

        ' Voltage Registers, and Frequency Register
        1MODBUS(AD2,R4:1017,MBF,MER,=200..208CV,W)
        200CV("AC_2_VoltAvgLN~V",AV)
        201CV("AC_2_VoltA~V",AV)
        202CV("AC_2_VoltB~V",AV)
        203CV("AC_2_VoltC~V",AV)
        204CV("AC_2_VoltAvgLL~V",AV)
        205CV("AC_2_VoltAB~V",AV)
        206CV("AC_2_VoltBC~V",AV)
        207CV("AC_2_VoltAC~V",AV)
        208CV("AC_2_Freq~Hz",AV)

        ' Energy Registers
        1MODBUS(AD2,R4:1001,MBF,MER,=210..211CV,W)
        210CV("AC_2_EnergySum~kWh",AV)
        211CV("AC_2_EnergyPosSum~kWh",AV)

        ' Power Registers
        1MODBUS(AD2,R4:1009,MBF,MER,=220..223CV,W)
        220CV("AC_2_PowerSum~W",AV)
        221CV("AC_2_PowerA~W",AV)
```

```
222CV("AC_2_PowerB~W",AV)
223CV("AC_2_PowerC~W",AV)

' Power Factor Register
1MODBUS(AD2,R4:1139,MBF,MER,=230..233CV,W)
230CV("AC_2_PowerFactorAvg~-",AV)
231CV("AC_2_PowerFactorA~-",AV)
232CV("AC_2_PowerFactorB~-",AV)
233CV("AC_2_PowerFactorC~-",AV)

' Apparent Power Registers, and Current Registers
1MODBUS(AD2,R4:1155,MBF,MER,=240..246CV,W)
240CV("AC_2_PowerAppSum~VA",AV)
241CV("AC_2_PowerAppA~VA",AV)
242CV("AC_2_PowerAppB~VA",AV)
243CV("AC_2_PowerAppC~VA",AV)
244CV("AC_2_CurrentA~A",AV)
245CV("AC_2_CurrentB~A",AV)
246CV("AC_2_CurrentC~A",AV)

' Reactive Power Registers
1MODBUS(AD2,R4:1147,MBF,MER,=250..253CV,W)
250CV("AC_2_PowerReacSum~VAR",AV)
251CV("AC_2_PowerReacA~VAR",AV)
252CV("AC_2_PowerReacB~VAR",AV)
253CV("AC_2_PowerReacC~VAR",AV)

' Demand Registers
1MODBUS(AD2,R4:1169,MBF,MER,=260..263CV,W)
260CV("AC_2_Demand~W",AV)
261CV("AC_2_DemandMin~W",AV)
262CV("AC_2_DemandMax~W",AV)
263CV("AC_2_DemandApp~W",AV)
```

```
' Creates a backup to the FTP Server
RB1H
        DO{COPYD start=new id=2 dest=ftp://[redacted]@resl-
9.me.dal.ca:21/Surrette/}

' Creates a backup to the USB drive
RC1H
        DO{COPYD start=new id=3 dest=A:}
END

RUNJOBONRESET"SURRETTE"
```

Appendix B – Measurement Uncertainty Analysis

The following will discuss the principal sources of measurement uncertainty for both phases of this research project. It is important to note that the general formula for uncertainty propagation, if $y = f(x)$, is equivalent to:

$$\delta y = \sqrt{\left(\frac{\partial y}{\partial x_1}\delta x_1\right)^2 + \left(\frac{\partial y}{\partial x_2}\delta x_2\right)^2 + \cdots + \left(\frac{\partial y}{\partial x_n}\delta x_n\right)^2} \qquad (n: 1) \qquad (8)$$

where δy and δx are the uncertainties of y and x, respectively [56].

Phase 1: Lead-acid Battery Formation Optimization – Laboratory Study

With respect to phase 1 of this research project, the principal sources of measurement uncertainty were attributed to the equipment which was used to form and cycle the ELG15 cells. Table 24 shows the principal equipment associated with phase 1 of this research project and their corresponding accuracy characteristics.

Table 24 Measurement Uncertainty Characteristics – Equipment Phase 1

Equipment	Accuracy	Full Scale Range (FSR)	Bias Uncertainty
Arbin BT-2000 Power-Cycler			
Voltage (V)	0.1 % of FSR [57]	20	0.02
Current (A)	0.1 % of FSR [57]	200	0.2
Aux Temperature Board (°C)	5 % of reading	N/A	5 %
T-Type Thermocouple (°C)	1.0 °C or 0.75 % of reading [58]	N/A	1.0
DMA 35 Density Meter (SG)	0.001 g/cm^3 [59]	3	0.1 %
Fluke 87V Multimeter (V)	0.05 % of reading + 1 [60]	N/A	Variable

As shown in Table 24, with respect to the Arbin power-cycler, an uncertainty of 0.02 V is attributed to the auxiliary measurement of voltage, while an uncertainty of 0.2 A is attributed to the measurement of current. Although these uncertainties are relatively insignificant (e.g., voltage: 0.02 V / 2.00 V = 1 %, current: 0.2 A / 60 A = 0.3 %), it should be noted that they will propagate as a result of the calculations associated to capacity (i.e., formation level, discharge/charge capacity, and DFE/coulombic efficiency), and IR.

Formation Level

With respect to the formation level of the cells formed using the Arbin power-cycler, each of the 15 cells are characterised with a different uncertainty due to the differences in

formation times and formation currents (i.e., constant-current vs. multi-step current formation algorithms). As an example, the uncertainty attributed to the formation level of cell 2.82TC$_a$ is derived below.

Firstly, its constant-current formation level, FL_{CC}, is defined as:

$$FL_{CC} = \frac{i_{cc} \times t_f}{TC} \tag{9}$$

where i_{cc} is the formation current (i.e., 20 A +/- 0.2 A) for the constant-current algorithm, t_f is the formation time, and *TC* is the theoretical capacity of the cell (i.e., 710 Ah). It should be noted that for the purpose of this research project, it was assumed that t_f had no uncertainty, while an uncertainty of 3 % (or +/- 21.3 Ah) was assumed for *TC*. This assumption was based on measurement data supplied by SBC. Thus, by applying equation (8) to equation (9), the FL_{CC} uncertainty for the cells formed using the constant-current algorithm, δFL_{CC}, was derived to be:

$$\delta FL_{CC} = \sqrt{\left(\frac{t_f}{TC} \times 0.2\ \text{A}\right)^2 + \left(\frac{i_{cc} \times t_f}{TC^2} \times 21.3\ \text{Ah}\right)^2} \tag{10}$$

Therefore, by using the formation time of 100 hours for cell 2.82TC$_a$, its FL_{CC} uncertainty was calculated to be +/- 0.09 (or 3.16 % of its formation level).

It is important to note that the equation defining the formation level of the cells formed using the multi-step current algorithm is different from the one presented in equation (9), as shown in equation (11):

$$FL_{MS} = \frac{\sum_{j=1}^{4}(i_{MS\_j} \times t_{f\_j})}{TC} \tag{11}$$

where FL_{MS} defines the multi-step current algorithm formation level, i_{MS_j} is the formation current, t_{f_j} is the formation time at said formation current, and *j* represents the four different formation steps which were shown in Table 4. Thus, the corresponding FL_{MS} uncertainty, δFL_{MS}, is represented by equation (12) (i.e., root sum square).

$$\delta FL_{MS} = \sqrt{\sum_{j=1}^{4}\left[\left(\frac{t_{f\_j}}{TC} \times 0.2\ \text{A}\right)^2 + \left(\frac{i_{MS\_j} \times t_{f\_j}}{TC^2} \times 21.3\ \text{Ah}\right)^2\right]} \tag{12}$$

Discharge/Charge Capacity

With respect to the discharge capacity of the cells, uncertainty is propagated due to the usage of equation (7), which was used to calculate the corrected discharge capacity of the

cells for a temperature basis of 25 °C. For clarity purposes, this equation is reproduced below.

$$C_{25\,^{\circ}\mathrm{C}} = C/[1 + \lambda(\theta - 25\ ^{\circ}\mathrm{C})] \tag{7}$$

where $C_{25\,^{\circ}\mathrm{C}}$ is the corrected capacity at 25 °C, C is the measured discharge capacity, λ is a factor based on the discharge rate, which in this case is equal to 0.006 due to the usage of a discharge current slower than the 3 hour rate, and θ is the cell temperature immediately prior to discharge. Thus, in order to calculate the uncertainty of $C_{25\,^{\circ}\mathrm{C}}$, the uncertainty of C and θ must first be determined.

With respect to the measured discharge capacity, the uncertainty varied per cell and cycle due to the differences in total discharging times. As an example, the uncertainty attributed to the measured discharge capacity for the first cycle of cell 2.82TC$_a$ is derived below. It should be noted that the pulses which were used to determine the IR of the cells were ignored for this analysis due to their relatively short duration.

Firstly, the measured discharge capacity is defined as:

$$C = i_D \times t_D \tag{13}$$

where i_D is the discharging current, and t_D is the discharging time. Again, it was assumed that t_D had no uncertainty. Thus, by applying equation (8) to equation (13), the C uncertainty, δC, was derived to be:

$$\delta C = t_D \times 0.2\ \mathrm{A} \tag{14}$$

Therefore, by using the cycle 1 discharge time of 3.77 hours for cell 2.82TC$_a$, its C uncertainty was calculated to be +/- 0.75 Ah (or 0.33 % of its measured discharge capacity).

With respect to the cell temperature immediately prior to discharge, the uncertainty was a function of the accuracy attributed to the T-type thermocouple, and the calibration of the auxiliary temperature board on the Arbin power-cycler. As stated in Table 24, the accuracy attributed to the thermocouple was determined to be +/- 1 °C, as this value was always larger than 0.75 % of any cell temperature reading. Furthermore, an average calibration accuracy of 5 % was assumed for the power-cycler with respect to its auxiliary temperature board. This assumption was based on a calibration verification performed using a Fluke 7102 Micro-Bath.

Thus, with the uncertainty characteristics of C and θ determined, the uncertainty of $C_{25\,^{\circ}\mathrm{C}}$, $\delta C_{25\,^{\circ}\mathrm{C}}$, was derived to be:

$$\delta C_{25\,^{\circ}\mathrm{C}} = \sqrt{\left(\frac{t_D \times 0.2\ \mathrm{A}}{1 + 0.006(\theta - 25)}\right)^2 + \left(\frac{-0.006C(1 + 0.05\theta)}{[1 + 0.006(\theta - 25)]^2}\right)^2} \quad (15)$$

Therefore, by using the cycle 1 discharge time of 3.77 hours for cell 2.82TC$_a$, its initial discharge temperature of 21.9 °C, and its measured discharge capacity of 230 Ah, its $C_{25\,^{\circ}\mathrm{C}}$ uncertainty was calculated to be +/- 3.10 Ah (or 1.32 % of its corrected discharge capacity).

With respect to the charge capacity of the cells, C_c, its uncertainty, δC_c, can be approximated by using equation (14), where t_D is instead replaced by t_C (i.e., charging time). It should be noted that is a conservative approximation, as it assumes the charging current to be constant.

Discharge Formation Efficiency and Coulombic Efficiency

With respect to the DFE and coulombic efficiency of the cells, uncertainty is propagated due to the discharge capacity values and the formation/charge capacity uncertainty values. As an example, the uncertainty attributed to the DFE of cell 2.82TC$_a$ is derived below.

Firstly, the *DFE* is defined as (reproduced from section 2.4):

$$DFE = \frac{C_{25\,^{\circ}\mathrm{C\_1}}}{i_{CC} \times t_f} \times 100\ \% \quad (5)$$

where $C_{25\,^{\circ}\mathrm{C\_1}}$ is the initial corrected discharge capacity. Thus, by applying equation (8) to equation (5), the *DFE* uncertainty, δDFE, was derived to be:

$$\delta DFE = \sqrt{\left(\frac{100 \times \delta C_{25\,^{\circ}\mathrm{C\_1}}}{i_{CC} \times t_f}\right)^2 + \left(\frac{100 \times t_f \times C_{25\,^{\circ}\mathrm{C\_1}} \times 0.2\ \mathrm{A}}{(i_{CC} \times t_f)^2}\right)^2} \quad (16)$$

Therefore, by using the respective values for cell 2.82TC$_a$, its *DFE* uncertainty was calculated to be +/- 0.19 % (or 1.66 % of its DFE).

The respective absolute values of uncertainty for formation level, discharge/charge capacity, and DFE/coulombic efficiency for all 15 cells formed and cycled in phase 1 of this research project were consistent. Thus, it can be stated that these aforementioned uncertainty characteristics are relatively insignificant. This is further highlighted in Figure 92.

Internal Resistance

With respect to the IR of the cells, uncertainty is propagated due to the usage of equation (6), reproduced below for clarity purposes.

$$DC\ IR = (e_2 - e_1)/(i_2 - i_1) \quad (6)$$

where e_2 and i_2 are voltage and current values immediately before the end of the pulse, respectively, and e_1 and i_1 are voltage and current values immediately before the beginning of the pulse, respectively. By applying equation (8) to equation (6), the *DC IR* uncertainty, $\delta DC\ IR$, was derived to be:

$$\delta DC\ IR = \sqrt{2 \times \left(\frac{0.02\ \text{V}}{(i_2 - i_1)}\right)^2 + 2 \times \left(\frac{0.2\ \text{A}\ (e_2 - e_1)}{(i_2 - i_1)^2}\right)^2} \quad (17)$$

As an example, the uncertainty attributed to the IR of cell 2.82TC_a at the 100 Ah discharging value for its first cycle can be calculated to be +/- 0.72 mΩ (or 76.7 % of the calculated IR value). This high uncertainty value is due to the uncertainty propagation of the voltage measurements logged by the Arbin power-cycler. Thus in order to justify the IR results presented in Chapters 5 and 6, a Fluke 87V Multimeter (i.e., high accuracy) was used to spot-check values of e_2 and e_1 when pulsing. Specifically, the *DC IR* uncertainty as based on the Fluke 87V Multimeter, $\delta DC\ IR_{Fluke}$, was derived to be:

$$\delta DC\ IR_{Fluke} = \sqrt{\left[\frac{(0.05\ \% \times e_2 + 0.001\ \text{V})}{(i_2 - i_1)}\right]^2 + \left[\frac{(0.05\ \% \times e_1 + 0.001\ \text{V})}{(i_2 - i_1)}\right]^2 + 2 \times \left[\frac{0.2\ \text{A}\ (e_2 - e_1)}{(i_2 - i_1)^2}\right]^2} \quad (18)$$

Thus by using equation (18), the uncertainty attributed to the IR of cell 2.82TC_a at the 100 Ah discharging value for its first cycle, as based on the Fluke 87V Multimeter, can be calculated to be +/- 0.07 mΩ (or 7.60 % of the calculated IR value). As per this significant reduction in uncertainty, it can be stated that the presented IR results are more confident than might first be thought based on the accuracy of the Arbin power-cycler. Comparable IR uncertainty values were obtained for all 15 cells formed and cycled in phase 1 of this research project.

Phase 2: Lead-acid Battery Formation Optimization – Industrial Study

With respect to phase 2 of this research project, the principal sources of measurement uncertainty were again attributed to the equipment which was used to form and cycle the ELG15 cells. Table 25 shows the principal equipment associated with phase 2 of this research project and their corresponding accuracy characteristics. The equipment already presented in Table 24 is omitted.

Table 25 Measurement Uncertainty Characteristics – Equipment Phase 2

Equipment	Accuracy	Full Scale Range (FSR)	Bias Uncertainty
Measurement Unit			
Voltage Dividers (V)	0.05 % of reading + 1	30	Variable
Empro Shunts (mV)	0.25 % of reading [61]	50	Variable
dataTaker DT80 Voltage (V)	0.10 % of reading +/- 0.01 % of FSR [62]	30 (voltage) / 3 (current)	Variable
Digatron Submerged Container Formation Charger (A)	0.5 % of FSR [63]	80	0.4
Ohaus SD200 Scale (kg)	0.1 [64]	200	0.1

The ratios of the voltage dividers (i.e., 20:1), as shown in Table 25, had the same accuracy values as the Fluke 87V Multimeter, due to the latter being used in their respective calibration process. Thus, the uncertainty with respect to the formation characteristic of voltage was due to the uncertainty values of the dataTaker DT80 and the Fluke 87V Multimeter. As an example, the uncertainty attributed to a formation voltage of 375 V (i.e., highest DC voltage rating) using the third voltage channel on the dataTaker DT80 (see Appendix A) is derived below.

Firstly, the formation voltage, V_f, is defined as:

$$V_f = V_d \times R \tag{19}$$

where V_d, is the divided formation voltage, and R is the voltage divider ratio (i.e., 20.30:1 for channel 3). Thus, by applying equation (8) to equation (19), the V_f uncertainty, δV_f, was derived to be:

$$\delta V_f = \sqrt{(R \times \delta\text{DT80})^2 + (V_d \times \delta\text{Fluke87V})^2} \tag{20}$$

where δDT80 and δFluke87V are the uncertainty characteristics of the dataTaker DT80 and the Fluke 87V Multimeter, respectively (see Table 25). Therefore by using the appropriate values, the V_f uncertainty can be calculated to be +/- 0.56 V (or 0.15 % of 375

V). Thus as a formation voltage of 375 V provides the largest uncertainty value, it can be stated that the uncertainty characteristic of formation voltage is relatively insignificant.

Formation Level

With respect to the formation level of the cells formed using the formation chargers at SBC, each of the four different formation methods are characterised with a different uncertainty due to the differences in formation times and formation currents. Thus, the formation level of the cells formed at SBC, FL_{SBC}, can be defined by equation (21).

$$FL_{SBC} = \frac{\sum_{j=1}^{n}(i_{SBC\_j} \times t_{f\_j})}{TC} \tag{21}$$

where for each respective formation charger, i_{SBC_j} is the formation current, t_{f_j} is the formation time at said formation current, and *n* is the number of formation steps (see section 4.2.1).

Likewise, the corresponding FL_{SBC} uncertainty, δFL_{SBC}, is represented by equation (22).

$$\delta FL_{SBC} = \sqrt{\sum_{j=1}^{n}\left[\left(\frac{t_{f\_j} \times \delta i\_SBC}{TC}\right)^2 + \left(\frac{i_{SBC\_j} \times t_{f\_j} \times 21.3\ \text{Ah}}{TC^2}\right)^2\right]} \tag{22}$$

where δi_SBC is the respective uncertainty attributed to the current measurement of the four different formation chargers. Specifically, with respect to the floor container, circulated electrolyte, and tank formation methods, δi_SBC is defined as shown in equation (23).

$$\delta i_{SBC} = SR(0.35\ \%\ \text{of reading} + 0.3\ \text{mV}) \tag{23}$$

where the shunt ratio, *SR*, is equivalent to 2 A/mV for the floor container formation charger, and 10 A/mV for the circulated electrolyte and tank formation chargers.

With respect to the submerged container formation charger, the uncertainty attributed to the current measurement is +/- 0.4 A, as shown in Table 25.

Discharge/Charge Capacity

With respect to the discharge and charge capacity of the cells, there are no differences in the derivation of uncertainty between phases 1 and 2 of this research project. Furthermore, absolute values of uncertainty with respect to the discharge/charge capacity values are in agreement with the cells formed in phase 1 of this research project.

Discharge Formation Efficiency and Coulombic Efficiency

With respect to the DFE/coulombic efficiency of the cells, there are no differences in the derivation of uncertainty between phases 1 and 2 of this research project. Furthermore, absolute values of uncertainty with respect to the DFE/coulombic efficiency values are in agreement with the cells formed in phase 1 of this research project.

Internal Resistance

With respect to the IR values of the cells, there are no differences in the derivation of uncertainty between phases 1 and 2 of this research project. Furthermore, absolute values of uncertainty with respect to the IR values are in agreement with the cells formed in phase 1 of this research project.

Effect of Measurement Uncertainty on Initial Discharge Capacity and Discharge Formation Efficiency Results

Figure 92 shows the initial discharge capacity and DFE results of the cells formed in phases 1 and 2 of this research project, with their respective uncertainty characteristics presented as error bars. It should be noted that this data, without uncertainty, was previously presented in Figure 83. Thus as shown in Figure 92, even with their uncertainty characteristics, the trends pertaining to the optimal formation level and method are still discernible. Thus, it is confirmed that the conclusions drawn in section 6.5 with respect to the main objective of this project are not impacted by the characteristics of uncertainty.

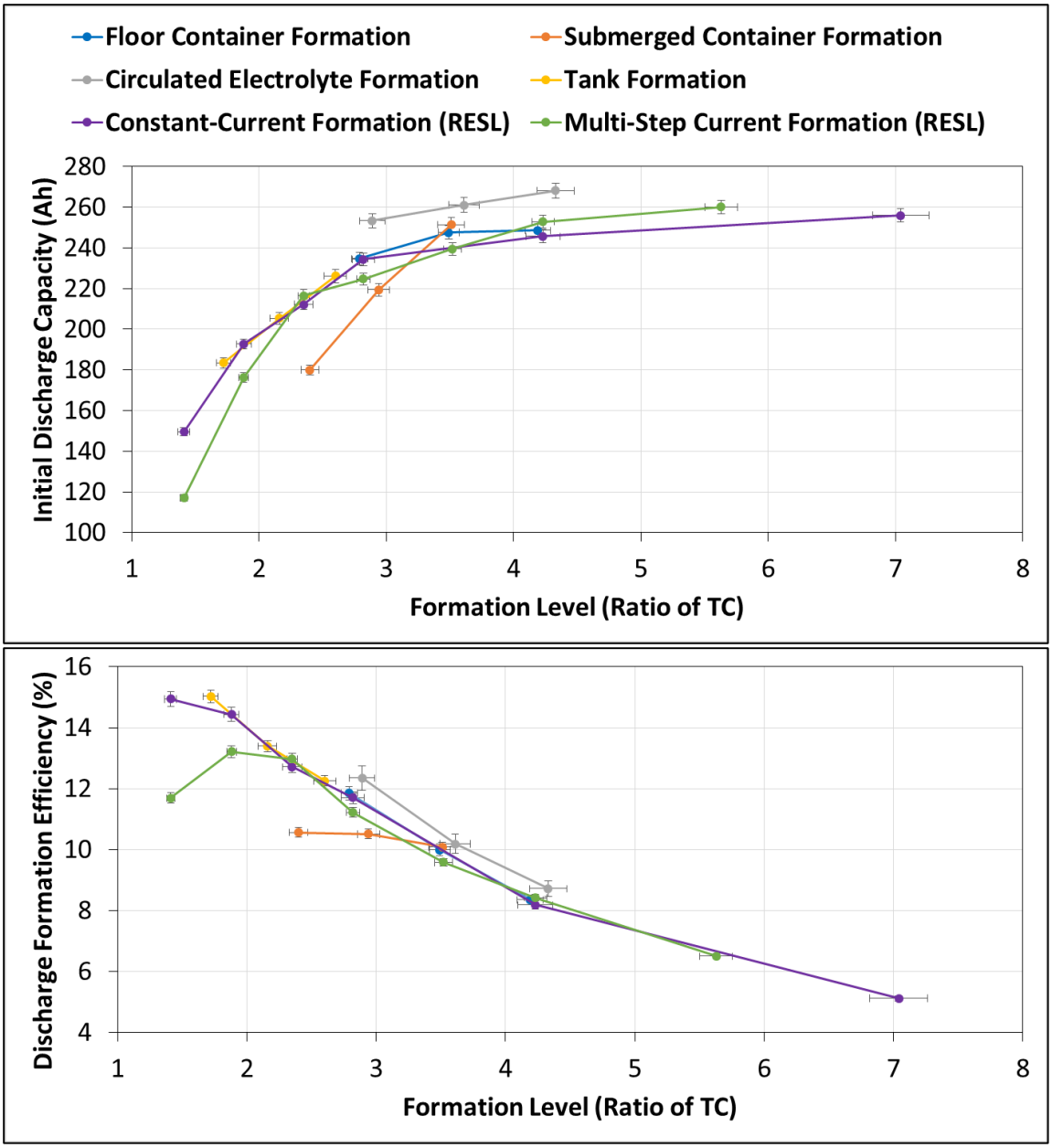

Figure 92 Initial Discharge Capacity and Discharge Formation Efficiency Results with Uncertainty Characteristics – Phases 1 and 2

Appendix C – Safety Assessment

A safety assessment was conducted with respect to both phases of this thesis project, where the necessary steps used to mitigate the identified safety risks are presented. Three safety categories were identified and analyzed for both phases, these being electrical, chemical, and physical safety risks.

Phase 1: Lead-acid Battery Formation Optimization – Laboratory Study

Electrical Safety Risks

With respect to the usage of the power-cycler, one must be aware of electrical safety risks, such as potentially dangerous voltages and currents. Specifically, the Arbin power-cycler has three channels each rated at 0-20 V and +/- 100 A. LABs, depending on their configuration, can also possess high voltage and current values. As such, measures were taken to mitigate risks related to short circuits and electrical shocks, which could in turn cause equipment damage, and could result in personal harm. A short circuit occurs when current travels along an unintended path where very low resistance is encountered, whereas an electrical shock can occur when contact is made with a grounded energy source [22].

The steps to mitigate electrical risks were as follows. The first line of defense was to create a line diagram of the proposed configuration when one was working with the power cycler and/or batteries. This line diagram, which had to be approved by the research supervisor before physical connection could be made, allowed for the immediate identification of potentially unsafe working conditions. Electrical risks were also mitigated by disconnecting all power sources from the batteries before work commenced, and if working on a large battery bank, batteries were disconnected from each other in order to reach safe voltage working levels. Safety glasses were worn at all times, and high voltage insulating gloves were worn when working on systems rated above 50 V. The following list of safety measures were also implemented when working with batteries to avoid electrical risks: watches, rings, etc. were removed, only tools with insulated handles were used, tools were not placed on top of batteries, circuit polarities were verified with a multi-meter before making connections, and sparks in the RESL were avoided.

Chemical Safety Risks

LABs also pose chemical safety risks. Specifically, one must be aware of the dangers related to lead, sulfuric acid, water electrolysis, and thermal run-away. Although lead and lead-dioxide are listed as carcinogens [65], there was limited exposure to these materials for this phase of the research project. On the other hand, one could be exposed to sulfuric acid when taking SG measurements, when watering or filling up batteries, or if electrolyte were to spill during battery handling. Watering is the periodical process of adding distilled water to the batteries, required as a result of water electrolysis [22]. Specifically, water electrolysis had to be considered during the processes of formation and cycling, as hydrogen gases are explosive in air concentrations over 4 % [66]. Thermal run-away is an extreme case of a battery overheating, which can lead to chemical fires.

The steps to avoid chemical risks were as follows. In order to avoid contact with sulfuric acid, protective clothing, googles, and lined rubber gloves and boots were used when taking SG measurements, or when watering batteries. To avoid electrolyte spills, batteries were kept in an upright position and were supported using straps. In the event that skin or eyes came in contact with electrolyte, the affected areas were to be flushed immediately with water. Specifically, the RESL is equipped with an eye wash station to be used in the event of eye contamination. In the event of a spill, the RESL is also equipped with a battery spill kit, which one can use to contain and neutralize the electrolyte before disposal. To mitigate the effect of water electrolysis, the cells were formed and cycled at the RESL in an area where two fans were used to exhaust air outdoors, thus ensuring sufficient ventilation. Furthermore, tubes were installed on top of the batteries during the formation process, which reduced the concentration of hydrogen in the air by recombining and condensing the gases as they exited the cells. The configuration used to mitigate the effects of water electrolysis is shown in Figure 6. The risk of thermal run-away was mitigated by using a battery cycling algorithm which limited the charging current and by monitoring the battery temperature. Additionally, built-in alarms within the power-cycler were used which triggered a full stop in operation if current values exceeded +/- 105 A, and/or temperature values exceeded 50 °C.

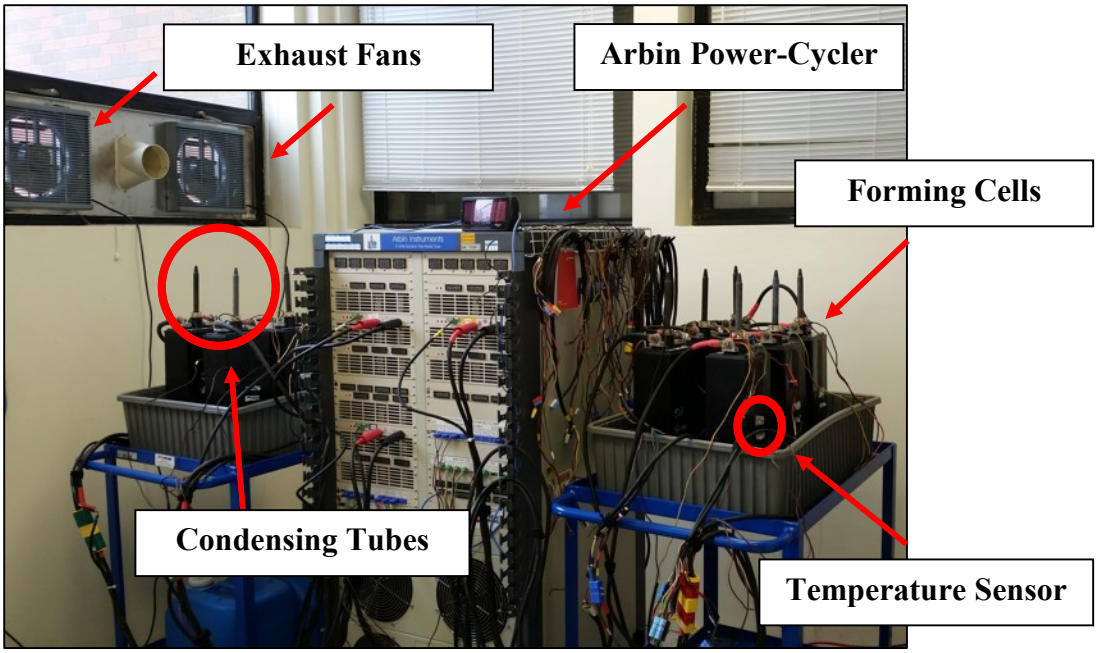

Figure 6 **Experimental Configuration for Cell Formation and Performance Cycling (RESL) (Reproduced from Chapter 4)**

Physical Safety Risks

Finally, the physical risks associated with batteries were considered. As was stated above, batteries can be heavy, with the ELG15 cell weighing 12.3 kg without electrolyte. As such, one must be aware of personal injury risks as a result of improper handling of batteries.

The steps used to avoid physical risks associated with the batteries were as follows. Proper footwear, in addition to using proper lifting techniques, were used when batteries were moved. In addition, batteries were placed on heavy-duty service carts, allowing them to be transported more efficiently in the RESL, or to the outside if deemed necessary. These service carts were labelled with their maximum weight capacity, so as to ensure they remained in good working order. Figure 93 shows a service cart load with strapped batteries, along with the location of the battery spill kit in the RESL.

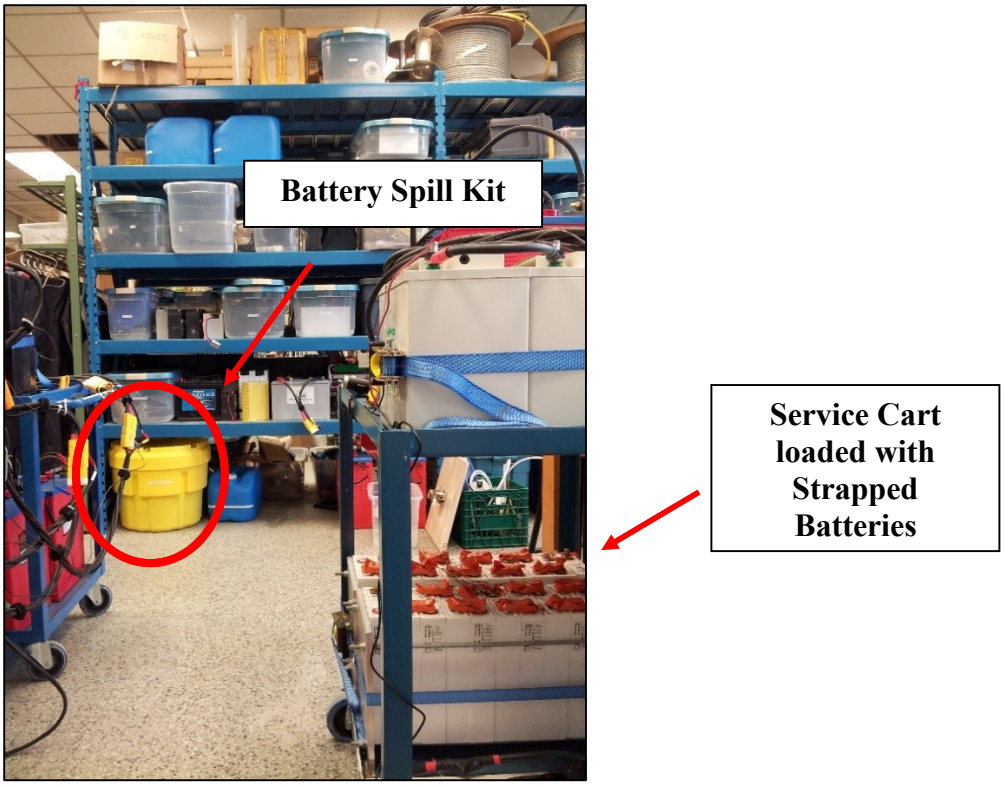

Figure 93 Service Cart and Battery Spill Kit (RESL)

Other Considerations

In addition to the mitigation steps outlined above, two other safety measures were employed at all times when work was completed in the RESL. First, the verification of work procedure was used to avoid potential human error. This procedure entails having someone else who not involved with the configuration at hand to visually inspect and approve it. Second, remote monitoring of the lab was made available to provide a real-time feed of the lab, in addition to providing access to the Arbin power-cycler.

Finally, the RESL is equipped with a fire extinguisher rated for fires of class B and C, and appropriate material safety data sheets.

Thus, as shown in this safety assessment, the RESL is well equipped to deal with potential electrical, chemical, and physical risks associated with the first phase of this research project.

Phase 2: Lead-acid Battery Formation Optimization – Industrial Study

Electrical Safety Risks

This phase of the project required the characterization of four different formation chargers at SBC. As the respective formation chargers have high AC and DC ratings (see Table 23), this phase of the project carried the same electrical risks which were identified for phase 1 of this project: short circuits and electrical shocks, albeit at a much higher danger threshold.

Electrical risks were mitigated by following all the steps which were highlighted in the safety assessment of phase 1. Furthermore, before the installation of any equipment, the necessary authorization was acquired from Mr. Ferron, SBC Plant Manager, who in turn asked the on-site electrician to assist with the installation if deemed necessary. The lead electrician ensured the installation of the equipment was completed in a safe and timely manner. Due to the high voltage and current ratings of the formation chargers, it was of utmost importance to disconnect the main power source of said formation charger before the installation of the monitoring and recording equipment. Furthermore, full arc-flash gear was used when installing equipment on the formation chargers.

Chemical Safety Risks

Chemical risks were also considered at the SBC manufacturing plant. While ones interaction with lead and lead-dioxide was limited within the workspace of the RESL, it had to be considered at SBC due to the small concentration of lead in the air. This is due to the on-site manufacturing of the positive and negative plates. Additionally, the tank formation method of the LABs causes some of the electrolyte to vaporize, which when inhaled, can cause severe irritation or damage to the mouth, nose, throat, and lungs [67]. Other chemical risks, such as electrolyte contamination, water electrolysis, and thermal run-away, are identical to the ones highlighted for phase 1 of this safety assessment.

Chemical risks with respect to electrolyte contamination and thermal run-away were mitigated by following the same steps which were highlighted for phase 1 of this safety assessment. Similarly to the RESL, in the event of electrolyte contamination or spills, SBC is also equipped with the necessary flushing stations and spill kits to neutralize the

electrolyte. Furthermore, risks associated to lead concentration in the air and electrolyte vapor were mitigated by using the appropriate respiratory protection.

Physical Safety Risks

As the formation of cells for this phase of the project was completed at SBC, there was a wider range of risks associated to physical safety. As such, in addition to considering the weight of the batteries, one had to be aware of forklifts, robots, and other battery manufacturing equipment. Figure 94 shows a robot which is used in the manufacturing process at SBC. As shown in the figure, physical safety risks can be attributed to the movement and range of the robot, and the load it carries.

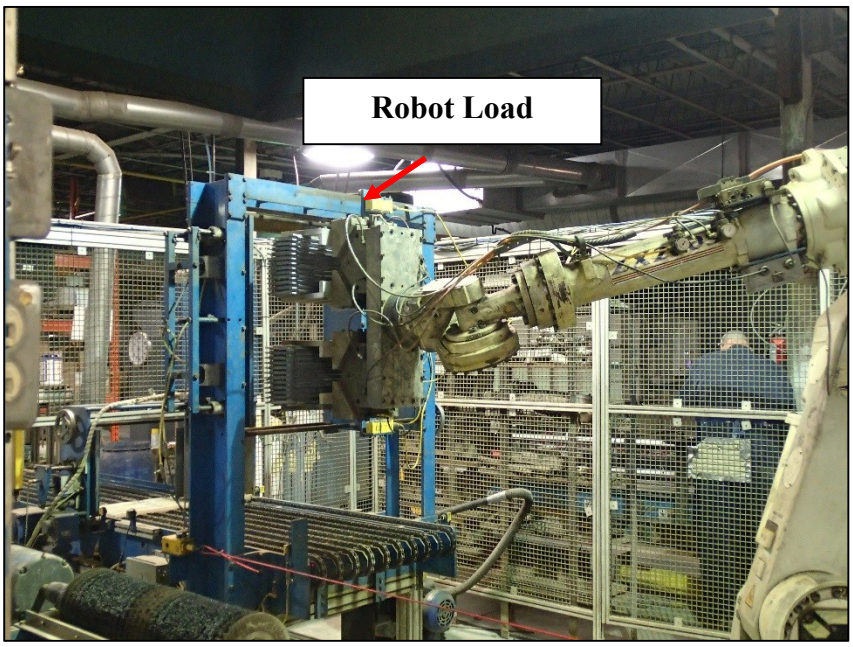

Figure 94 Battery Welding Robot (SBC)

The steps to avoid physical risks in the plant were as follows. Proper footwear, in addition to using proper lifting techniques were employed when batteries were moved. Risks associated to heavy machinery such as forklifts, robots, and other manufacturing equipment were mitigated by respecting the plant safety directives.

Other Considerations

In addition to the risk mitigation steps outlined above, the same verification of work procedure employed in the RESL was used at SBC to avoid potential human error.

Appendix D – S-480 Battery Data Sheet

Rolls

FLOODED DEEP CYCLE BATTERIES

S-480

6 VOLTS

CONTAINER:	High Density Polypropylene		
COVER:	High Density Polypropylene		
TERMINALS:	Flag M		
HANDLES:	Rope		

WEIGHT DRY:	37 kg	81	Lbs.
WEIGHT WET:	51 kg	113	Lbs.
LENGTH:	318 mm	12 1/2	Inches
WIDTH:	181 mm	7 1/8	Inches
HEIGHT:	425 mm	16 3/4	Inches

PLATE HEIGHT:	293 mm	11.550	Inches
PLATE WIDTH:	143 mm	5.625	Inches
THICKNESS (POSITIVE):	4.32 mm	0.170	Inches
THICKNESS (NEGATIVE):	3.05 mm	0.120	Inches

CELLS:	15 Plates/Cell	3	Cell
SEPARATOR THICKNESS:	2 mm	0.061	Inches
GLASS MAT INSULATION:	1 mm	0.02	Inches
ELECTROLYTE RESERVE: ABOVE PLATES	57 mm	2.25	Inches

COLD CRANK AMPS (CCA):	0°F / -17.8°C	1151
MARINE CRANK AMPS (MCA):	32°F / 0°C	1440
RESERVE CAPACITY (RC @ 25A):		814 Minutes

CAPACITY 375 AH

HOUR RATE:	SPECIFIC GRAVITY	CAPACITY / AMP HOUR	CURRENT / AMPS
@ 100 HOUR RATE	1.280	486	4.86
@ 72 HOUR RATE	1.280	459	6.38
@ 50 HOUR RATE	1.280	438	8.76
@ 24 HOUR RATE	1.280	386	16.09
@ 20 HOUR RATE	1.280	375	18.75
@ 15 HOUR RATE	1.280	352	23.45
@ 12 HOUR RATE	1.280	334	27.81
@ 10 HOUR RATE	1.280	319	31.88
@ 8 HOUR RATE	1.280	300	37.50
@ 6 HOUR RATE	1.280	278	46.25
@ 5 HOUR RATE	1.280	263	52.50
@ 4 HOUR RATE	1.280	244	60.94
@ 3 HOUR RATE	1.280	221	73.75
@ 2 HOUR RATE	1.280	191	95.63
@ 1 HOUR RATE	1.280	135	135.00

Amphere Hour capacity ratings based on specific gravities of 1.280. Reduce capacities 5% for 1.265 specific gravity and 10% for specific gravities of 1.250

CYCLE LIFE VS. DEPTH OF DISCHARGE

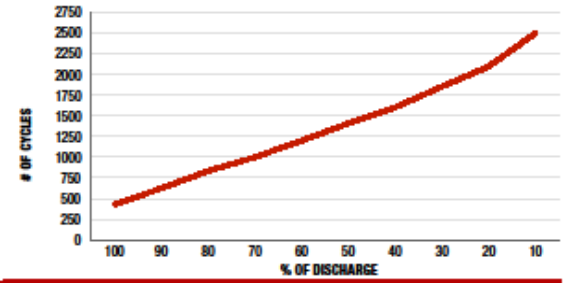

VOLTAGE VS. DEPTH OF DISCHARGE

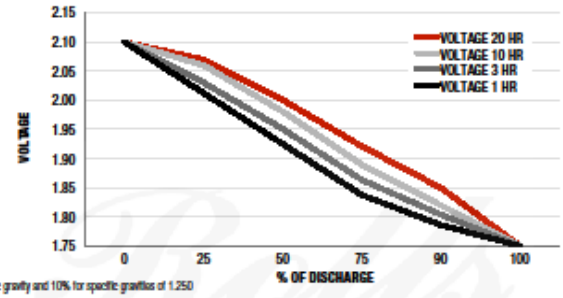

WWW.ROLLSBATTERY.COM

SURRETTE BATTERY COMPANY 1 STATION RD SPRINGHILL, NS CANADA B0M 1X0

SPEC 01

12/1/2013 REV. 1